Residual-Based Large Eddy Simulation of Turbulent Flows using Divergence-Conforming Discretizations

by

Christopher Joel Coley

B.S., University of Colorado, 2006

B.A., University of Colorado, 2006

M.S., Air Force Institute of Technology, 2011

A dissertation submitted to the

Faculty of the Graduate School of the

University of Colorado in partial fulfillment

of the requirements for the degree of

Doctor of Philosophy

Ann and H. J. Smead Aerospace Engineering Sciences

2017

The views expressed in this dissertation are those of the author and do not reflect the official policy or position of the United States Air Force, Department of Defense, or the United States Government.

This dissertation entitled
Residual-Based Large Eddy Simulation of Turbulent Flows using Divergence-Conforming Discretizations
written by Christopher Joel Coley
has been approved for Ann and H. J. Smead Aerospace Engineering Sciences

_____
John Evans

_____
Kenneth Jansen

_____
Carlos Felippa

_____
Peter Hamlington

_____
Yuri Bazilevs

Date _____

The final copy of this thesis has been examined by the signatories, and we find that both the content and the form meet acceptable presentation standards of scholarly work in the above mentioned discipline.

Coley, Christopher Joel (Ph.D., Aerospace Engineering Sciences)

Residual-Based Large Eddy Simulation of Turbulent Flows using Divergence-Conforming Discretizations

Dissertation directed by Assistant Professor John Evans

In this dissertation, a class of methods which combines divergence-conforming discretizations with residual-based subgrid modeling for large eddy simulation of turbulent flows is introduced. These methods fall within two frameworks: residual-based variational multiscale methods and residual-based eddy viscosities. These methods utilize variationally-consistent formulations for the fine-scale velocities in order to construct subgrid-scale models based on the coarse-scale residual. The result is an LES methodology that responds naturally to spatially- and temporally-varying turbulence. Numerical results demonstrate that these new methods demonstrate proper behavior for homogeneous turbulence and outperform classical LES models for transitional flows and wall-bounded turbulent flows. Furthermore, the resulting formulations contain no "tunable" parameters, and thus extend generally across various classes of flow.

Additionally, a differential variational multiscale method in which the unresolved fine-scales are approximated element-wise using a discontinuous Galerkin method is presented and examined. Stability and convergence results for the methodology as applied to the scalar transport problem are established, and it is proven that the method exhibits optimal convergence rates in the SUPG norm and is robust with respect to the Péclet number if the discontinuous subscale approximation space is sufficiently rich. The method is applied to isogeometric NURBS discretizations of steady and unsteady transport problems, and the corresponding numerical results demonstrate that the method is stable and accurate in the advective limit even when low-order discontinuous subscale approximations are employed. Based on these promising results, a class of differential subgrid vortex models for large eddy simulation of turbulent flows is proposed.

Finally, the underlying discretization utilized by the simulations here offers the opportunity

to develop efficient new geometric multigrid linear solvers. In this regard, a geometric multigrid methodology for the solution of matrix systems associated with isogeometric compatible discretizations of the generalized Stokes and Oseen problems is presented. The methodology provably yields a pointwise divergence-free velocity field independent of the number of pre-smoothing steps, post-smoothing steps, grid levels, or cycles in a V-cycle implementation. The methodology relies upon Scwharz-style smoothers in conjunction with specially defined overlapping subdomains that respect the underlying topological structure of the generalized Stokes and Oseen problems. Numerical results in both two- and three-dimensions demonstrate the robustness of the methodology through the invariance of convergence rates with respect to grid resolution and flow parameters for the generalized Stokes problem as well as the generalized Oseen problem, provided it is not advection-dominated.

Dedication

To my wife Hannah

Acknowledgements

First, I am thankful to my advisor, Professor John Evans, for giving me the opportunity to investigate a problem of personal interest and for his guidance over the years. I also want to thank my committee members, Professors Kenneth Jansen, Carlos Felippa, Peter Hamlington, and Yuri Bazilevs for their comments and suggestions, which contributed to the quality of this work. Many of the numerical results in this dissertation were obtained using the Janus and Summit computational resources administered in part by the University of Colorado and funded by the National Science Foundation. Without access to these supercomputing resources, I would not have been able to complete my work in a timely manner.

I am grateful to have had the opportunity to work in a great research lab with a group of great people. I want to thank all of my fellow CMG Lab-mates for everything I have learned from them over the years and for all the great times we had outside of the lab. I extend a special thanks to Ryan Aronson, who helped me considerably with implementation of the Sigma, Vreman, and WALE models and for producing many useful and interesting animations and visualizations from the simulation data. Ryan's help was invaluable.

I thank my parents for encouraging me from an early age to be a lifelong learner and for teaching me the value of discipline.

Last, but certainly not least, I thank my wife Hannah for her unwavering love and support through this entire process.

Contents

Chapter

List of Tables

Table

List of Figures

Figure

Chapter 1

Introduction

1.1 Motivation

Large eddy simulation (LES) has been a successful methodology for simulating turbulence, but challenges still remain which have so far prevented LES from becoming a mature technology for complex engineering flow analysis. LES has been demonstrated to perform adequately for flows at low Reynolds numbers and with basic geometries and physics. However, the currently available subgrid-scale models are inadequate for many classes of flows, such as for transitional flows [21, 69, 116, 113, 135], rotational flows [10, 54, 113, 129, 135], flows with a reverse energy cascade (backscatter) [114, 113], relaminarization [113], and flows that include aeroacoustics [104, 113, 115], mixing [142, 144], and chemical reactions [117, 144]. In spite of these issues, the simple Smagorinsky model and its variants are still probably the most widely used models in LES today. This speaks loudly about the inability of newer subgrid-scale models to resolve the aforementioned problems inherent in LES. In addition to the deficiencies present in current subgrid-scale models, the use of filters in LES is also associated with many difficulties, including the need for inhomogeneous non-commutative filters for wall-bounded flows and the use of complex filtered quantities in compressible flows [11].

Variational multiscale (VMS) methods for turbulence modeling seek to address the shortcomings of LES. In VMS methods, filtering is replaced with variational projections and modeling

is limited to the fine scales. Some of the motivations behind the development of VMS for turbulence modeling include the desire to perform scale separation *a priori* (whereas traditional filtering performs this separation *a posteriori*) [86], and to retain numerical consistency in the coarse-scale equations. Thus far, early attempts at using VMS methods to provide LES-like turbulence modeling show promise [11, 86, 87, 88], and this is an active area of research where there is still much to be gained.

Divergence-conforming B-spline discretizations[1] have recently arisen as an attractive candidate for the spatial discretization of fluid flow problems [33, 59, 61, 63, 64, 62, 124]. These discretizations comprise a discrete Stokes complex [36, 57, 66] and may be interpreted as smooth generalizations of Raviart-Thomas-Nédélec finite elements [107, 120]. When applied to incompressible flow problems, divergence-conforming discretizations produce pointwise divergence-free velocity fields and hence exactly satisfy mass conservation. As a result, they preserve the balance law structure of the incompressible Navier-Stokes equations, and in particular, they properly conserve mass, linear and angular momentum, energy, vorticity, enstrophy (in the two-dimensional setting), and helicity (in the three-dimensional setting) in the inviscid limit [64]. These discretizations have been shown to provide excellent accuracy and stability in the direct numerical simulation (DNS) of incompressible viscous flow [61, 63, 64] and have recently been applied to Cahn-Hilliard flow [136], turbulent flow [45, 132], and fluid-structure interaction [96] where improved results were attained in comparison with state-of-the-art discretization procedures.

Despite the promise that divergence-conforming discretizations can deliver improved accuracy for the simulation of incompressible turbulent flows, the introduction of efficient linear solution strategies is critical for divergence-conforming discretizations to develop into a mature technology. So far, very little research has been conducted in the area of efficient linear solvers. In fact, only the performance of Krylov subspace methods in conjunction with block preconditioners has been investigated in prior work [46, 47]. However, the inherent structure of divergence-conforming

[1] Depending on context, divergence-conforming B-spline discreizations may also be referred to as isogeometric compatible discretizations, isogeometric discrete differential forms, structure-preserving discretizations, or curl-conforming discretizations.

discretizations offers the opportunity to develop geometric multigrid methods based on Schwarz-style smoothers [53] in conjunction with specially-defined overlapping subdomains that respect the underlying topological structure of the generalized Stokes and Oseen problems [44].

The goals of the current research are twofold: first, to arrive at an LES methodology for turbulent flows that is robust across a wide range of flow regimes, and second, to introduce an optimally-efficient linear solution procedure for divergence-conforming discretizations of incompressible fluid flow. Toward the first goal, a new turbulence modeling framework has been developed which leverages residual-based turbulence modeling with divergence-conforming discretizations of the incompressible Navier-Stokes equations. Within this framework, various subgrid models have been implemented and analyzed. It is demonstrated that the resulting methodology not only performs as well as classical LES methods for homogeneous turbulence, where LES is currently demonstrated to perform well, but also performs well where classical LES methods fail to perform adequately, such as for transitional flows and wall-bounded flows. Furthermore, this methodology contains no "tunable" parameters, and thus extends generally across various classes of flow.

1.2 Research Objectives and Contributions

With the completion of this dissertation, the following research objectives have been obtained.

(1) Quasi-static and dynamic residual-based variational multiscale subgrid models for simulation of turbulent flows using divergence-conforming discretizations have been implemented and analyzed.

(2) Quasi-static and dynamic residual-based eddy viscosity subgrid models for simulation of turbulent flows using divergence-conforming discretizations have been implemented and analyzed.

(3) Performance of the above-mentioned modeling methodologies have been evaluated for the problems of forced homogeneous turbulence, decay of homogeneous turbulence, Taylor-

Green vortex flow and turbulent channel flow. It is demonstrated that the turbulence modeling methodologies introduced in this research perform as well as classical LES methodologies for homogeneous turbulence problems and outperform existing LES methodologies for transitional flows and wall-bounded flows.

(4) Differential variational multiscale subgrid models for scalar transport utilizing discontinuous Galerkin subscales have been developed, analyzed, and demonstrated. These models are demonstrated to be accurate, displaying optimal convergence rates with respect to mesh refinement, and robust with regard to the advective limit and geometry. It is demonstrated that lowest-order discontinuous subscale approximations are sufficient to stabilize high-order coarse-scale approximations in the context of isogeometric analysis. These results provide optimism that development of discontinuous subscale approaches for LES-type turbulence modeling is a worthwhile pursuit.

(5) Differential variational multigrid subgrid models for simulation of turbulent flows using divergence-conforming discretizations have been introduced.

(6) A geometric multigrid method using Schwarz smoothers on overlapping subdomains which respect the divergence-free constraint have been developed and demonstrated for the generalized Stokes and Oseen problems. It is proven that the methodology yields a pointwise divergence-free velocity field independent of the number of pre-smoothing steps, post-smoothing steps, grid levels, or cycles in a V-cycle implementation. Furthermore, the methdology is found to exhibit convergence rates independent of the grid resolution and flow parameters for the generalized Stokes problem and the Oseen problem, so long as it is not advection-dominated.

1.3 Structure of the Dissertation

The structure of the remainder of this dissertation is as follows. Chapter 2 introduces the incompressible Navier-Stokes equations, including the Galerkin method for the incompressible Navier-Stokes equations and the treatment of weakly-enforced Dirichlet boundary conditions. In Chapter 3, divergence-conforming discretizations are presented and the B-spline spaces which are used for discretization in this work are described. Chapter 4 discusses filtering of the incompressible Navier-Stokes equations and the classical LES approaches which have been developed within this paradigm. This is followed by a discussion of residual-based variational multiscale methods for LES in Chapter 5 and residual-based eddy viscosity models in Chapter 6. Chapter 7 presents numerical results which demonstrate the performance of the residual-based VMS and RBEV models. In Chapter 8, a differential variational multiscale method utilizing discontinuous subscales for scalar transport is presented. Chapter 9 describes an efficient linear solver for divergence-conforming discretizations in the form of a geometric multigrid method. Finally, in Chapter 10, conclusions are drawn and future work is discussed.

Chapter 2

Incompressible Navier-Stokes Equations

In this chapter, the incompressible Navier-Stokes equations are introduced, first in strong form, then in weak form. From the weak form, we derive the Galerkin formulation. We end the chapter with a discussion of weak enforcement of Dirichlet boundary conditions.

2.1 The Strong Form of the Incompressible Navier-Stokes Equations

We consider the incompressible Navier-Stokes equations subject to homogeneous Dirichlet boundary conditions. For $d \in \mathbb{Z}_+$, let $\Omega \subset \mathbb{R}^d$ denote an open, Lipschitz bounded domain, let Γ denote the boundary of Ω, and let $T \in \mathbb{R}_+$. Given $\nu \in \mathbb{R}_+$, $\mathbf{f} : \Omega \times (0,T) \to \mathbb{R}^d$, and $\mathbf{u}_0 : \Omega \to \mathbb{R}^d$, the strong form of the Navier-Stokes problem then reads as follows: Find $\mathbf{u} : \overline{\Omega} \times [0,T] \to \mathbb{R}^d$ and $p : \Omega \times (0,T) \to \mathbb{R}$ such that

$$\begin{aligned} \tfrac{\partial \mathbf{u}}{\partial t} + \mathbf{u} \cdot \nabla \mathbf{u} - \nu \Delta \mathbf{u} + \nabla p &= \mathbf{f} \qquad \text{for } (\mathbf{x}, t) \in \Omega \times (0,T) \\ \nabla \cdot \mathbf{u} &= 0 \qquad \text{for } (\mathbf{x}, t) \in \Omega \times (0,T) \\ \mathbf{u} &= \mathbf{0} \qquad \text{for } (\mathbf{x}, t) \in \Gamma \times (0,T) \\ \mathbf{u}|_{t=0} &= \mathbf{u}_0 \qquad \text{for } \mathbf{x} \in \Omega \end{aligned} \tag{2.1}$$

where $\mathbf{u}$ denotes the velocity field, p denotes the pressure field, ν denotes the kinematic viscosity, $\mathbf{f}$ denotes the force per unit mass, and $\mathbf{u}_0$ denotes the initial velocity field. The velocity field is

uniquely specified by the Navier-Stokes problem while the pressure field is unique up to a constant.

In order to simplify later discussion, we define the differential operator associated with the Navier-Stokes equations $\mathcal{L}_{NS}$ as

$$\mathcal{L}_{NS}\mathbf{U} \equiv \begin{bmatrix} \nabla \cdot \mathbf{u} \\ \mathbf{u}_{,t} + \nabla \cdot (\mathbf{u} \otimes \mathbf{u}) + \nabla p - \nu \nabla^2 \mathbf{u} \end{bmatrix}, \tag{2.2}$$

where $\mathbf{U} = [\mathbf{u}, p]^T$.

2.2 The Weak Form of the Incompresible Navier-Stokes Equations

We now state a weak formulation for the incompressible Navier-Stokes equations. We strictly consider the case of homogeneous Dirichlet boundary conditions without loss of generality. Before proceeding, we must first define suitable velocity and pressure test spaces:

$$\mathbf{H}_0^1(\Omega) := \left\{ \mathbf{v} \in \mathbf{H}^1(\Omega) : \mathbf{v} = \mathbf{0} \text{ on } \Gamma \right\}$$
$$L_0^2(\Omega) := \left\{ q \in L^2(\Omega) : \int_\Omega q d\Omega = 0 \right\}.$$

We also assume that $\sigma, \nu \in \mathbb{R}_+$, $\mathbf{a} \in \mathbf{H}_0^1(\Omega)$, and $\mathbf{f} \in \mathbf{L}^2(\Omega)$. With these assumptions in hand, the weak form of the incompressible Navier-Stokes equations is stated as follows: Find $\mathbf{u} \in \mathbf{H}_0^1(\Omega)$ and $p \in L_0^2(\Omega)$ such that

$$a(\mathbf{v}; \mathbf{u}) - b(\mathbf{v}, p) + b(\mathbf{u}, q) = \ell(\mathbf{v}) \tag{2.3}$$

for all $\mathbf{v} \in \mathbf{H}_0^1(\Omega)$ and $q \in L_0^2(\Omega)$ where

$$a(\mathbf{v}; \mathbf{u}) := \int_\Omega \mathbf{v} \cdot \frac{\partial \mathbf{u}}{\partial t} \, d\Omega + \int_\Omega \mathbf{v} \cdot (\mathbf{u} \cdot \nabla \mathbf{u}) \, d\Omega + \int_\Omega \nu \nabla \mathbf{v} : \nabla \mathbf{u} \, d\Omega$$

$$b(\mathbf{v}, p) := \int_\Omega (\nabla \cdot \mathbf{v}) \, p \, d\Omega$$

$$\ell(\mathbf{v}) := \int_\Omega \mathbf{v} \cdot \mathbf{f} \, d\Omega$$

2.3 The Galerkin Method

To discretize in space using a mixed Galerkin formulation, we first must specify finite-dimensional approximation spaces for the velocity and pressure fields. We denote these spaces as $\mathbf{V}_h \subset \mathbf{H}_0^1(\Omega)$ and $\mathrm{Q}_h \subset L_0^2(\Omega)$ respectively, but we defer the discussion of suitable approximation spaces to Chapter 3. With approximation spaces defined, the mixed Galerkin formulation of the incompressible Navier-Stokes equations is stated as follows: Find $\mathbf{u}_h \in \mathbf{V}_h$ and $p_h \in \mathrm{Q}_h$ such that

$$a(\mathbf{v}_h; \mathbf{u}_h) - b(\mathbf{v}_h, p_h) + b(\mathbf{u}_h, q_h) = \ell(\mathbf{v}_h) \tag{2.4}$$

for all $\mathbf{v}_h \in \mathbf{V}_h$ and $q_h \in \mathrm{Q}_h$. It should be noted that the velocity and pressure approximation spaces may not be arbitrarily selected. Instead, they should be chosen such that the Babuška-Brezzi inf-sup condition is satisfied [7, 23]. We later select isogeometric divergence-conforming discretizations for spatial discretization which indeed satisfy such a condition.

When $\mathbf{V}_h$ is sufficiently refined so as to resolve all length scales down to the Kolmogorov scale, $\mathbf{u}_h$ represents the DNS solution. However, when this is not the case, then there are unresolved fine scales in the simulation and $\mathbf{u}_h$ is inaccurate. The accuracy of this solution can be improved by modeling the effect of the unresolved scales on the resolved scales. One approach to accomplish this is the variational multiscale method, which is introduced in Chapter 5.

2.4 Weak Enforcement of Dirichlet Boundary Conditions

The no-slip boundary condition, $\mathbf{u} \times \mathbf{n} = \mathbf{0}$ where $\mathbf{n}$ is the outward facing normal to Γ, leads to the formation of boundary layers for wall-bounded flows. High mesh resolution is required near boundary layers to accurately represent associated sharp layers, so when the no-slip condition is strongly enforced in a mixed Galerkin formulation, inaccurate flow field approximations are obtained for insufficiently-resolved boundary layer meshes. It has recently been shown that superior results can be achieved by imposing the no-penetration boundary condition strongly and the no-slip boundary condition weakly using a combination of upwinding and Nitsche's method [14, 15]. With

such an approach, we first specify finite-dimensional velocity and pressure approximation spaces as before, but we only require that the corresponding discrete velocity fields satisfy $\mathbf{v} \cdot \mathbf{n} = 0$. That is, we specify $\mathbf{V}_h \subset \mathbf{H}^1_n(\Omega) = \left\{\mathbf{v} \in \mathbf{H}^1(\Omega) : \mathbf{v} \cdot \mathbf{n} = 0 \text{ on } \Gamma\right\}$ and $\mathrm{Q}_h \subset L^2_0(\Omega)$. The corresponding formulation for the incompressible Navier-Stokes equations is then stated as: Find $\mathbf{u}_h \in \mathbf{V}_h$ and $p_h \in \mathrm{Q}_h$ such that

$$a_h(\mathbf{v}_h; \mathbf{u}_h) - b(\mathbf{v}_h, p_h) + b(\mathbf{u}_h, q_h) = \ell(\mathbf{v}_h) \tag{2.5}$$

for all $\mathbf{v}_h \in \mathbf{V}_h$ and $q_h \in \mathrm{Q}_h$ where

$$a_h(\mathbf{v}_h; \mathbf{u}_h) := a(\mathbf{v}_h, \mathbf{u}_h) - \int_\Gamma \nu \mathbf{v}_h \cdot \nabla_{\mathbf{n}} \mathbf{u}_h \, d\Gamma - \int_\Gamma \nu \nabla_{\mathbf{n}} \mathbf{v}_h \cdot \mathbf{u}_h \, d\Gamma + \int_\Gamma \frac{C_I \nu}{h} \mathbf{v}_h \cdot \mathbf{u}_h \, d\Gamma.$$

Above, h is the wall-normal element mesh size and C_I is a positive constant that must be chosen sufficiently large to ensure coercivity of $a_h(\cdot;\cdot)$. Appropriate values for the constant C_I can be obtained by solving element-wise eigenvalue problems or by appealing to analytical upper bounds for the trace inequality [60].

In order to impose non-homogeneous tangential Dirichlet (prescribed-slip) boundary conditions, we instead solve [64]

$$a_h(\mathbf{v}_h; \mathbf{u}_h) - b(\mathbf{v}_h, p_h) + b(\mathbf{u}_h, q_h) = \ell_h(\mathbf{v}_h) \tag{2.6}$$

where

$$\ell_h(\mathbf{v}_h) := \ell(\mathbf{v}_h) - \int_\Gamma \nu \nabla_{\mathbf{n}} \mathbf{v}_h \cdot \mathbf{u}_{BC}(t) \; d\Gamma + \int_\Gamma \frac{C_I \nu}{h} \mathbf{v}_h \cdot \mathbf{u}_{BC}(t) \; d\Gamma, \tag{2.7}$$

where $\mathbf{u}_{BC}(t)$ is the prescribed velocity at the wall. We choose to weakly enforce Dirichlet boundary conditions for the incompressible Navier-Stokes equations throughout this work. This not only leads to more accurate numerical results [14, 15], but it also ensures proper solution behavior in the limit of zero viscosity [63, 64].

Chapter 3

Divergence-conforming Discretizations and Compatible B-splines

Up to this point, we have yet to specify suitable velocity and pressure approximation spaces for the incompressible Navier-Stokes problem. In this chapter, we present a particular selection of velocity and pressure approximation spaces which is not only inf-sup stable but also yields pointwise divergence-free discrete velocity fields. Before doing so, however, we first introduce the so-called Stokes complex, which succinctly captures the fundamental theorem of calculus and expresses the differential relationships between potential, velocity, and pressure fields.

3.1 The Stokes Complex

The Stokes complex [57, 66] is a cochain complex of the form

$$0 \longrightarrow \Phi \xrightarrow{\vec{\nabla}} \boldsymbol{\Psi} \xrightarrow{\vec{\nabla}\times} \mathbf{V} \xrightarrow{\vec{\nabla}\cdot} \mathrm{Q} \longrightarrow 0 \tag{3.1}$$

in the three-dimensional setting where

$$\Phi := H_0^1(\Omega) \qquad \boldsymbol{\Psi} := \left\{ \boldsymbol{\psi} \in \mathbf{L}^2(\Omega) : \vec{\nabla} \times \boldsymbol{\psi} \in \mathbf{H}^1(\Omega) \text{ and } \boldsymbol{\psi} \times \mathbf{n} = \mathbf{0} \text{ on } \Gamma \right\}$$
$$\mathbf{V} := \mathbf{H}_n^1(\Omega) \qquad \mathrm{Q} := L_0^2(\Omega)$$

are infinite-dimensional spaces of scalar potential fields, vector potential fields, velocity fields, and pressure fields. The Stokes complex is a smoothed version of the classical L^2 de Rham complex, and when the domain $\Omega \subset \mathbb{R}^3$ is simply connected with simply connected boundary, the Stokes complex

is exact. This means that every pressure field may be represented as the divergence of a velocity field, every divergence-free velocity field may be represented as the curl of a vector potential field, and every curl-free vector potential field may be represented as the gradient of a scalar potential field. An analogous two-dimensional Stokes complex also exists, though for brevity, the interested reader is referred to [57] for more details.

It has been shown in previous works that the Stokes complex endows the incompressible Navier-Stokes problem with important underlying topological structure. In particular, the infinite-dimensional inf-sup condition may be derived from the complex [57]. As such, there is impetus for developing finite-dimensional approximations of the Stokes complex. Such discrete complexes are referred to as discrete Stokes complexes, and when these complexes are endowed with special commuting projection operators, they form the following commuting diagram with the Stokes complex:

$$\begin{array}{ccccccccccc} 0 & \longrightarrow & \Phi & \xrightarrow{\vec{\nabla}} & \boldsymbol{\Psi} & \xrightarrow{\vec{\nabla}\times} & \mathbf{V} & \xrightarrow{\vec{\nabla}\cdot} & \mathrm{Q} & \longrightarrow & 0 \\ & & \downarrow{\scriptstyle \Pi_\phi} & & \downarrow{\scriptstyle \Pi_\psi} & & \downarrow{\scriptstyle \Pi_v} & & \downarrow{\scriptstyle \Pi_q} & & \\ 0 & \longrightarrow & \Phi_h & \xrightarrow{\vec{\nabla}} & \boldsymbol{\Psi}_h & \xrightarrow{\vec{\nabla}\times} & \mathbf{V}_h & \xrightarrow{\vec{\nabla}\cdot} & \mathrm{Q}_h & \longrightarrow & 0 \end{array} \tag{3.2}$$

where Φ_h, $\boldsymbol{\Psi}_h$, $\mathbf{V}_h$, and Q_h are discrete scalar potential, vector potential, velocity, and pressure spaces and $\Pi_\phi : \Phi \to \Phi_h$, $\Pi_\psi : \boldsymbol{\Psi} \to \boldsymbol{\Psi}_h$, $\Pi_v : \mathbf{V} \to \mathbf{V}_h$, and $\Pi_q : \mathrm{Q} \to \mathrm{Q}_h$ are the aforementioned commuting projection operators. Remarkably, when $\mathbf{V}_h$ and Q_h are selected as velocity and pressure approximation spaces in a mixed Galerkin formulation of the incompressible Navier-Stokes problem, the resulting approximation scheme is *inf-sup stable and free of spurious oscillations* and the *returned discrete velocity solution will be pointwise divergence-free* [61, 63]. Thus any velocity/pressure discretization which is inherited from a discrete Stokes complex is referred to as a "divergence-conforming" discretization. Both of the aforementioned properties are a direct consequence of the commuting diagram above, and for the sake of completeness, we prove the second property below.

Lemma 3.1.1 Assume that the discrete velocity and pressure spaces $\mathbf{V}_h$ and Q_h are associated with a discrete complex which commutes with the Stokes complex. Suppose $\mathbf{v}_h \in \mathbf{V}_h$ satisfies

$b(\mathbf{v}_h, q_h) = 0$ for every $q_h \in \mathrm{Q}_h$. Then $\nabla \cdot \mathbf{v}_h = 0$ pointwise.

Proof Let $q_h = \nabla \cdot \mathbf{v}_h$. Then $\|\nabla \cdot \mathbf{v}_h\|^2_{L^2(\Omega)} = b(\mathbf{v}_h, q_h) = 0$ and the desired result follows.

While we have demonstrated the benefit of using velocity and pressure spaces coming from a discrete Stokes complex, we have not yet described how to arrive at such spaces. In order to do so, we turn to the use of so-called isogeometric compatible B-spline discretizations, which are the focus of the next two sections.

3.2 Univariate and Multivariate B-splines

The basic building blocks of isogeometric compatible B-spline discretizations, like any isogeometric analysis technology, are B-splines [49]. B-splines are piecewise polynomial functions, but unlike C^0-continuous finite elements, B-splines may exhibit high levels of continuity. Univariate B-splines are constructed by first specifying a polynomial degree k, a number of basis functions n, and an open knot vector $\Xi = \{\xi_0, \xi_1, \ldots, \xi_{n+p+1}\}$, a non-decreasing vector of knots ξ_i such that the first and last knot are repeated $p+1$ times. We assume without loss of generality that the first and last knot are 0 and 1, respectively, such that the domain of the knot vector is $(0, 1)$. With a knot vector in hand, univariate B-spline basis functions are defined recursively through the Cox-deBoor formula:

$$\hat{N}_{i,p}(\xi) := \frac{\xi - \xi_i}{\xi_{i+p} - \xi_i} \hat{N}_{i,p-1}(\xi) + \frac{\xi_{i+p+1} - \xi}{\xi_{i+p+1} - \xi_{i+1}} \hat{N}_{i+1,p-1}(\xi) \quad \text{for } p > 0$$

$$\hat{N}_{i,0}(\xi) := \begin{cases} 1 & \xi_i \leq \xi < \xi_{i+1} \\ 0 & \text{elsewhere.} \end{cases}$$

Figure 3.1 shows example sets of unvariate B-spline basis functions. We can alternatively define B-splines not from the knot vector itself, but instead a vector of unique knot values $\boldsymbol{\zeta} = \{\zeta_1, \zeta_2, \ldots, \zeta_{n_k}\}$ and a regularity vector $\boldsymbol{\alpha} = \{\alpha_1, \alpha_2, \ldots, \alpha_{n_k}\}$ such that the B-splines have α_j continuous derivatives across ζ_j. By construction, $\alpha_1 = \alpha_{n_k} = -1$. We will later employ the convention $\boldsymbol{\alpha} - 1 = \{-1, \alpha_2 - 1, \ldots, \alpha_{n_k - 1} - 1, -1\}$.

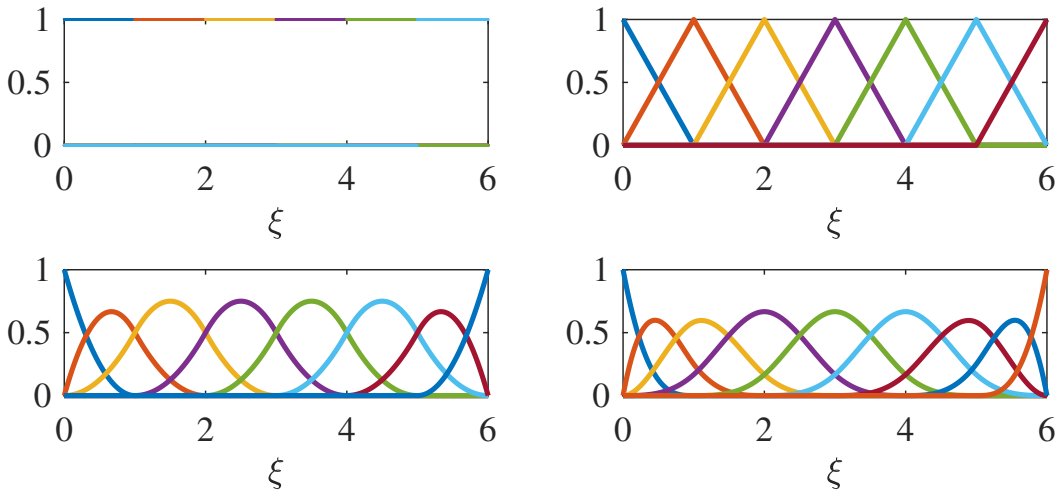

Figure 3.1: Maximal continuity univariate B-spline basis functions of varying polynomial degree associated with a vector of unique knot values $\boldsymbol{\zeta} = \{0, 1, 2, 3, 4, 5, 6\}$: $p = 0$ (upper left), $p = 1$ (upper right), $p = 2$ (lower left), and $p = 3$ (lower right).

Given a set of knot vectors and polynomial degrees, multivariate B-spline basis functions are obtained through a tensor-product of univariate B-spline basis functions

$$\hat{N}_{\mathbf{i},\mathbf{p}}(\boldsymbol{\xi}) := \prod_{k=1}^{d} \hat{N}_{i_k,p_k}(\xi_k)$$

where $\mathbf{i} = (i_1, i_2, \ldots, i_d)$ and $\mathbf{p} = (p_1, p_2, \ldots, p_d)$. We denote the corresponding space of multidimensional B-splines over the parametric domain $\hat{\Omega} = (0, 1)^d$ as

$$S^{p_1,p_2,\ldots,p_d}_{\boldsymbol{\alpha}_1,\boldsymbol{\alpha}_2,\ldots,\boldsymbol{\alpha}_d}(\mathcal{M}_h) := \left\{ f : \hat{\Omega} \to \mathbb{R} \;\middle|\; f(\boldsymbol{\xi}) = \sum_{\mathbf{i}} a_{\mathbf{i}} \hat{N}_{\mathbf{i},\mathbf{p}}(\boldsymbol{\xi}) \right\},$$

where $\boldsymbol{\alpha}_j$ is the regularity vector associated with the j^{th} direction where $j = 1, \ldots, d$ and $\boldsymbol{\mathcal{M}}_h$ is the parametric mesh defined by the vectors of unit knot values in each parameteric direction. Note that the space is fully characterized by the polynomial degrees, regularity vectors, and parametric mesh as indicated by the notation. For ease of notation, however, we drop the dependence on the parameteric mesh and instead use $S^{p_1,p_2,\ldots,p_d}_{\boldsymbol{\alpha}_1,\boldsymbol{\alpha}_2,\ldots,\boldsymbol{\alpha}_d} = S^{p_1,p_2,\ldots,p_d}_{\boldsymbol{\alpha}_1,\boldsymbol{\alpha}_2,\ldots,\boldsymbol{\alpha}_d}(\mathcal{M}_h)$ in what follows.

3.3 Isogeometric Compatible B-splines

We are now in a position to define isogeometric compatible B-splines. Their definition is made possible through the observation that the derivative of univariate B-splines of degree k are univariate B-splines of degree $k-1$. Since multivariate B-splines are tensor-products of univariate B-splines, the aforementioned property naturally generalizes to higher dimension, allowing us to build a discrete Stokes complex of B-spline spaces [57, 35]. We first define such a discrete Stokes complex in the parametric domain $\hat{\Omega} = (0,1)^d$ for both $d = 2$ and $d = 3$ before constructing a discrete Stokes complex in the physical domain of interest using a set of structure-preserving push-forward/pull-back operators.

In the two-dimensional setting, we define the following B-spline spaces over the unit square:

$$\begin{aligned}
\hat{\Psi}_h &:= \left\{ \hat{\psi}_h \in S^{p_1,p_2}_{\boldsymbol{\alpha}_1,\boldsymbol{\alpha}_2} : \hat{\psi}_h = 0 \text{ on } \hat{\Gamma} \right\} \\
\hat{\mathbf{V}}_h &:= \left\{ \hat{\mathbf{v}}_h \in S^{p_1,p_2-1}_{\boldsymbol{\alpha}_1,\boldsymbol{\alpha}_2-1} \times S^{p_1-1,p_2}_{\boldsymbol{\alpha}_1-1,\boldsymbol{\alpha}_2} : \hat{\mathbf{v}}_h \cdot \mathbf{n} = 0 \text{ on } \hat{\Gamma} \right\} \\
\hat{\mathrm{Q}}_h &:= \left\{ \hat{q}_h \in S^{p_1-1,p_2-1}_{\boldsymbol{\alpha}_1-1,\boldsymbol{\alpha}_2-1} : \int_{\hat{\Omega}} \hat{q}_h d\hat{\Omega} = 0 \right\},
\end{aligned}$$

where $\hat{\Psi}_h$ is the B-spline space of streamfunctions, $\hat{\mathbf{V}}_h$ is the B-spline space of flow velocities, and $\hat{\mathrm{Q}}_h$ is the B-spline space of pressures. These discrete spaces are endowed with B-spline basis functions $\{\hat{N}^{\psi}_i\}_{i=1}^{n_\psi}$, $\{\hat{\mathbf{N}}^{v}_i\}_{i=1}^{n_v}$, and $\{\hat{N}^{p}_i\}_{i=1}^{n_q}$, respectively, where n_ψ is the number of streamfunction basis functions, n_v is the number of velocity basis functions, and n_q is the number of pressure basis functions, all of which can be inferred from the chosen polynomial degrees and knot vectors. One can readily show that these spaces form the following discrete Stokes complex:

$$0 \longrightarrow \hat{\Psi}_h \xrightarrow{\vec{\nabla}^{\perp}} \hat{\mathbf{V}}_h \xrightarrow{\vec{\nabla}\cdot} \hat{\mathrm{Q}}_h \longrightarrow 0. \tag{3.3}$$

Provided the functions in the B-spline pressure space are at least C^0-continuous, there exists a set of commuting projection operators that make the above discrete complex commute with the Stokes complex. Thus, we refer to the spaces $\hat{\Psi}_h$, $\hat{\mathbf{V}}_h$, and $\hat{\mathrm{Q}}_h$ as compatible B-spline spaces. As mentioned previously, if we select $\hat{\mathbf{V}}_h$ and $\hat{\mathrm{Q}}_h$ as velocity and pressure approximation spaces in a mixed Galerkin formulation of the incompressible Navier-Stokes equations, then the resulting

scheme yields a pointwise divergence-free velocity field. The degrees of freedom associated with compatible B-splines are associated with the geometrical entries of the underlying control mesh. This is graphically illustrated in Figure 3.2, which shows that streamfunction degrees of freedom are associated with control points, velocity degrees of freedom are associated with (and aligned normal to) control edges, and pressure degrees of freedom are associated with control cells. Each degree of freedom corresponds to a particular basis function, and to visualize these basis functions, we have selected four degrees of freedom in Figure 3.2 and visualized the respective basis functions in Figure 3.3[1] .

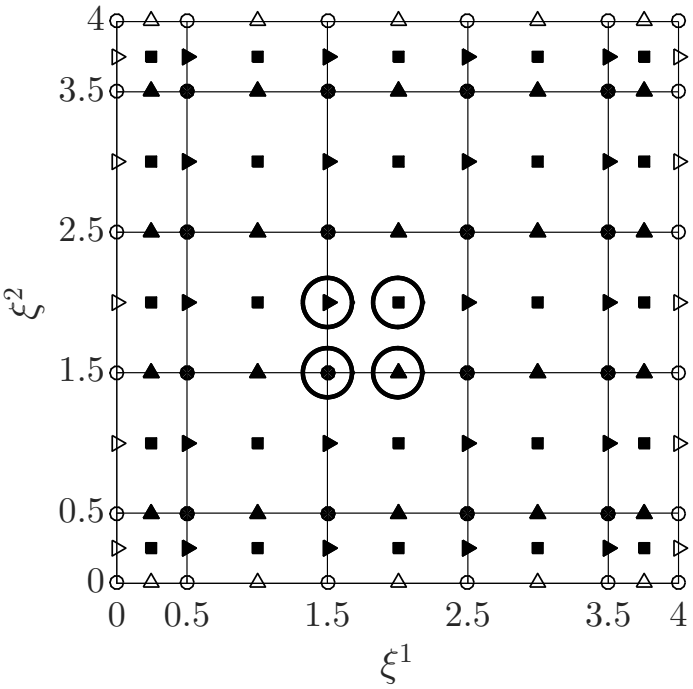

Figure 3.2: Control mesh and degrees of freedom for maximal continuity compatible B-splines of degree $k_1 = k_2 = 2$ associated with vectors of unique knot values $\boldsymbol{\zeta}_1 = \boldsymbol{\zeta}_2 = \{0, 1, 2, 3, 4\}$. Filled circles (●) denote streamfunction degrees of freedom, triangles (▶, ▲) denote velocity degrees of freedom, and filled squares (■) denote pressure degrees of freedom. Hollow markers indicate degrees of freedom associated with boundary conditions.

[1] Note that the pressure basis function we have highlighted does not have zero average over the parametric domain. In practice, we enforce this constraint using a Lagrange multiplier rather than to the individual pressure basis functions.

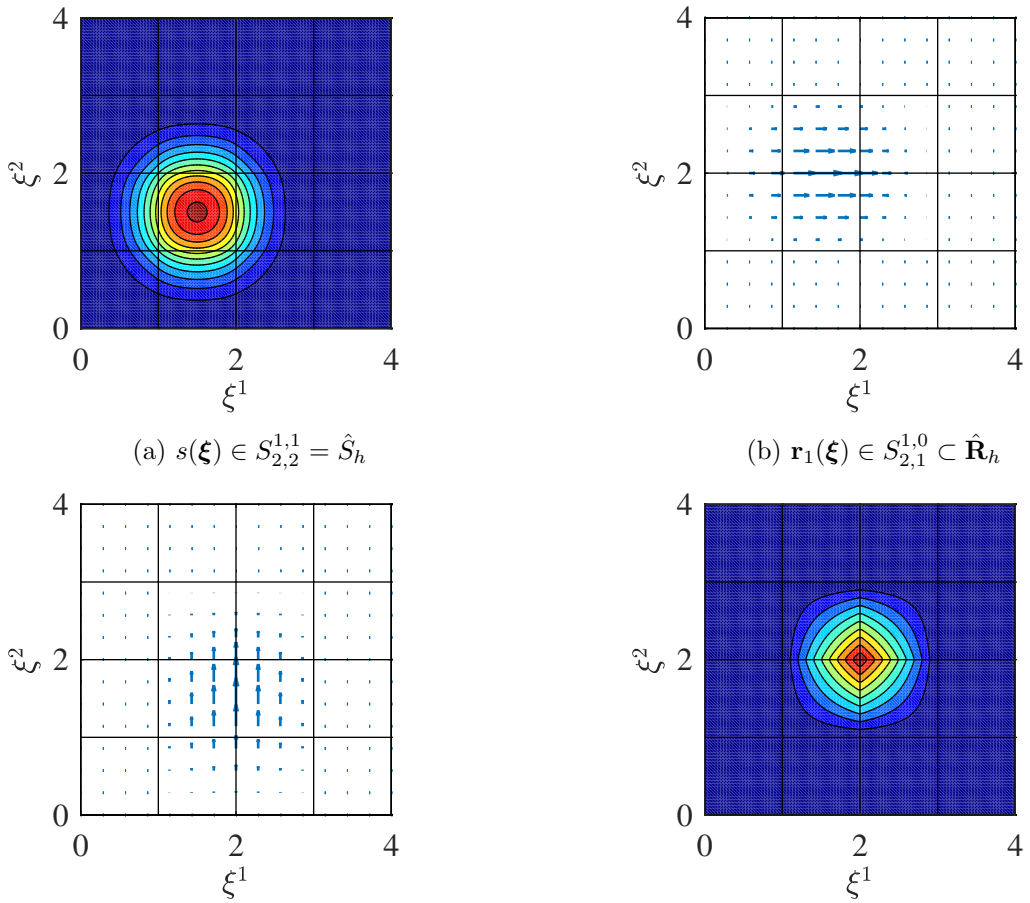

(a) $s(\boldsymbol{\xi}) \in S^{1,1}_{2,2} = \hat{S}_h$

(b) $\mathbf{r}_1(\boldsymbol{\xi}) \in S^{1,0}_{2,1} \subset \hat{\mathbf{R}}_h$

(c) $\mathbf{r}_2(\boldsymbol{\xi}) \in S^{0,1}_{1,2} \subset \hat{\mathbf{R}}_h$

(d) $w(\boldsymbol{\xi}) \in S^{0,0}_{1,1} = \hat{W}_h$

Figure 3.3: Streamfunction (upper left), velocity (upper right and lower left), and pressure (lower right) basis functions associated with the circled degrees of freedom in Figure 3.2.

In the three-dimensional setting, we define the following B-spline spaces over the unit cube:

$$\hat{\Phi}_h := \left\{ \hat{\phi}_h \in S^{p_1,p_2,p_3}_{\boldsymbol{\alpha}_1,\boldsymbol{\alpha}_2,\boldsymbol{\alpha}_3} : \hat{\phi}_h = 0 \text{ on } \hat{\Gamma} \right\}$$

$$\hat{\boldsymbol{\Psi}}_h := \left\{ \hat{\boldsymbol{\psi}}_h \in S^{p_1-1,p_2,p_3}_{\boldsymbol{\alpha}_1-1,\boldsymbol{\alpha}_2,\boldsymbol{\alpha}_3} \times S^{p_1,p_2-1,p_3}_{\boldsymbol{\alpha}_1,\boldsymbol{\alpha}_2-1,\boldsymbol{\alpha}_3} \times S^{p_1,p_2,p_3-1}_{\boldsymbol{\alpha}_1,\boldsymbol{\alpha}_2,\boldsymbol{\alpha}_3-1} : \hat{\boldsymbol{\psi}}_h \times \mathbf{n} = \mathbf{0} \text{ on } \hat{\Gamma} \right\}$$

$$\hat{\mathbf{V}}_h := \left\{ \hat{\mathbf{v}}_h \in S^{p_1,p_2-1,p_3-1}_{\boldsymbol{\alpha}_1,\boldsymbol{\alpha}_2-1,\boldsymbol{\alpha}_3-1} \times S^{p_1-1,p_2,p_3-1}_{\boldsymbol{\alpha}_1-1,\boldsymbol{\alpha}_2,\boldsymbol{\alpha}_3-1} \times S^{p_1-1,p_2-1,p_3}_{\boldsymbol{\alpha}_1-1,\boldsymbol{\alpha}_2-1,\boldsymbol{\alpha}_3} : \hat{\mathbf{v}}_h \cdot \mathbf{n} = 0 \text{ on } \hat{\Gamma} \right\}$$

$$\hat{\mathrm{Q}}_h := \left\{ \hat{q}_h \in S^{p_1-1,p_2-1,p_3-1}_{\boldsymbol{\alpha}_1-1,\boldsymbol{\alpha}_2-1,\boldsymbol{\alpha}_3-1} : \int_{\hat{\Omega}} \hat{q}_h d\hat{\Omega} = 0 \right\},$$

where $\hat{\Phi}_h$ is the B-spline space of scalar potentials, $\hat{\boldsymbol{\Psi}}_h$ is the B-spline space of vector potentials, $\hat{\mathbf{V}}_h$ is the B-spline space of flow velocities, and $\hat{\mathrm{Q}}_h$ is the B-spline space of pressures. These discrete spaces are endowed with the basis functions $\{\hat{N}^{\phi}_i\}_{i=1}^{n_\phi}$, $\{\hat{\mathbf{N}}^{\psi}_i\}_{i=1}^{n_\psi}$, $\{\hat{\mathbf{N}}^{v}_i\}_{i=1}^{n_v}$, and $\{\hat{N}^{p}_i\}_{i=1}^{n_q}$, respectively,

where n_ϕ is the number of scalar potential basis functions, n_ψ is the number of vector potential basis functions, n_v is the number of velocity basis functions, and n_q is the number of pressure basis functions, all of which can be inferred from the chosen polynomial degrees and knot vectors. Once again, one can show that the above spaces form the following discrete Stokes complex:

$$0 \longrightarrow \hat{\Phi}_h \xrightarrow{\vec{\nabla}} \hat{\mathbf{\Psi}}_h \xrightarrow{\vec{\nabla}\times} \hat{\mathbf{V}}_h \xrightarrow{\vec{\nabla}\cdot} \hat{\mathrm{Q}}_h \longrightarrow 0. \tag{3.4}$$

Provided the functions in the B-spline pressure space are at least C^0-continuous, there exists a set of commuting projection operators that make the above discrete complex commute with the Stokes complex.

Heretofore, we have discussed how to construct compatible B-splines in the parametric domain. To define compatible B-splines in the physical domain Ω, we need to first define a piece-wise smooth bijective mapping $\mathbf{F} : \hat{\Omega} \to \Omega$. This mapping can be defined using Non-Uniform Rational B-splines (NURBS), for instance, as is commonly done in the isogeometric analysis community [49], although this is certainly not the only way to define this mapping. With this mapping in hand, we define two-dimensional compatible B-spline spaces in the physical domain via the relations

$$\begin{aligned}
\Psi_h &:= \left\{ \psi_h \in \Psi : \psi_h \circ \mathbf{F} \in \hat{\Psi}_h \right\} \\
\mathbf{V}_h &:= \left\{ \mathbf{v}_h \in \mathbf{V} : \det(\mathbf{J})\, \mathbf{J}^{-1} \mathbf{v}_h \circ \mathbf{F} \in \hat{\mathbf{V}}_h \right\} \\
\mathrm{Q}_h &:= \left\{ q_h \in \mathrm{Q} : \det(\mathbf{J})\, q_h \circ \mathbf{F} \in \hat{\mathrm{Q}}_h \right\},
\end{aligned}$$

and three-dimensional compatible B-spline spaces via the relations

$$\begin{aligned}
\Phi_h &:= \left\{ \phi_h \in \Phi : \phi_h \circ \mathbf{F} \in \hat{\Phi}_h \right\} \\
\mathbf{\Psi}_h &:= \left\{ \boldsymbol{\psi}_h \in \mathbf{\Psi} : \mathbf{J}^{-T} \boldsymbol{\psi}_h \circ \mathbf{F} \in \hat{\mathbf{\Psi}}_h \right\} \\
\mathbf{V}_h &:= \left\{ \mathbf{v}_h \in \mathbf{V} : \det(\mathbf{J})\, \mathbf{J}^{-1} \mathbf{v}_h \circ \mathbf{F} \in \hat{\mathbf{V}}_h \right\} \\
\mathrm{Q}_h &:= \left\{ q_h \in \mathrm{Q} : \det(\mathbf{J})\, q_h \circ \mathbf{F} \in \hat{\mathrm{Q}}_h \right\},
\end{aligned}$$

where $\mathbf{J} = \partial_{\boldsymbol{\xi}} \mathbf{F}$ is the Jacobian of the parametric mapping. Corresponding basis functions in the physical domain are defined via pushes-forward of the basis functions in the parametric domain, and we denote the discrete velocity basis functions as $\{\mathbf{N}_i^v\}_{i=1}^{n_v}$ and the basis functions for other

quantities in analogous fashion. It is easily shown that the compatible B-spline spaces in the physical domain also comprise a discrete complex which commutes with the Stokes complex. The compatible B-splines in the physical domain are referred to as isogeometric compatible B-splines, as they are built from B-splines, the basis building blocks of geometric modeling, and they are defined on the exact geometry of the problem of interest.

Chapter 4

Filtering, Eddy Viscosity, and Classical LES Approaches

Large eddy simulation was first proposed in 1963 for use in atmospheric simulation [128], and early applications were also in this area [52, 103]. About a decade after its initial introduction, LES for engineering-related problems was first explored by Deardorff [51] and Schumann [125]. Early applications of LES were in simple flows, such as homogeneous turbulence, mixing layers, and plane channel flows. However, as computer technology improved and computing power increased, the number of LES applications also grew [144]. The popularity of LES has increased as it provides higher accuracy than Reynolds-Averaged Navier Stokes (RANS) [121] methods but also lower cost than DNS.

There are four conceptual steps in LES. The first is to decompose the velocity into a resolved component and an unresolved (or residual) component, where the resolved component of the velocity represents the large eddies. This can be accomplished either through filtering or variational projections. Next, the equations for the evolution of the resolved velocity field are derived from the Navier-Stokes equations. These equations will contain some effect of the residual motion. The third step is to obtain closure by modeling the residual motion, which is usually accomplished by using eddy-viscosity models, variational multiscale concepts, or a combination of both. In the final step, the resulting equations are solved numerically for the resolved velocity [118]. In this chapter, the classical LES paradigm, where scale separation is accomplished through filtering and the residual motion is modeled using an eddy viscosity, and several such models are described. It should be

noted that in the scale-separation step, the filter width is typically taken to be equal to the grid spacing. When this is the case, it is appropriate to refer to the residual component as a subgrid component. Although it is not necessary for the filter width and grid spacing to coincide, for the purposes of this dissertation, it will be assumed that they do, and thus the term "subgrid" will be used in lieu of "residual" throughout.

4.1 The Filtered Navier-Stokes Equations

In the classical LES setting, scale splitting of the velocity is performed through a filtering operation and the subgrid stresses are modeled using eddy-viscosity models. In these filtered equations, a subgrid stress tensor arises as a result of the subgrid-scale motion [102]. The simplest, and most common approach to modeling the subgrid stress tensor is through the use of an eddy-viscosity model.

The Navier-Stokes operator for the filtered Navier-Stokes equations can be written as

$$\bar{\mathcal{L}}_{NS}\bar{\mathbf{U}} \equiv \begin{bmatrix} \nabla \cdot \bar{\mathbf{u}} \\ \bar{\mathbf{u}}_{,t} + \nabla \cdot (\bar{\mathbf{u}} \otimes \bar{\mathbf{u}}) + \nabla \bar{p} - \nu \nabla^2 \bar{\mathbf{u}} + \nabla \cdot \boldsymbol{\tau}_r \end{bmatrix}, \tag{4.1}$$

where here the barred terms indicate the filtered velocity and pressure fields and $\boldsymbol{\tau}_r$, the so-called residual-stress tensor, is an additional term resulting from the filtering operation that must now be modeled. This residual-stress tensor accounts for the transfer of momentum caused by turbulent eddies. In eddy-viscosity models, this effect is modeled by an effective eddy viscosity, analogous to how a molecular viscosity is used to model the momentum transfer caused by molecular diffusion. This modeling takes the form

$$\boldsymbol{\tau}_r = 2\nu_t \boldsymbol{S}, \tag{4.2}$$

where the rate of strain tensor is given by

$$S_{ij} = \frac{1}{2}\left(\frac{\partial \bar{u}_i}{\partial x_j} + \frac{\partial \bar{u}_j}{\partial x_i}\right). \tag{4.3}$$

Substituting (4.2) and (4.3) into (4.1) gives a modified form of the Navier-Stokes operator such

that

$$\bar{\mathcal{L}}_{NS}\bar{\mathbf{U}} \equiv \begin{bmatrix} \nabla \cdot \bar{\mathbf{u}} \\ \bar{\mathbf{u}}_{,t} + \nabla \cdot (\bar{\mathbf{u}} \otimes \bar{\mathbf{u}}) + \nabla \bar{p} - \nabla \cdot 2\nu_{\text{eff}} \nabla \bar{\mathbf{u}} \end{bmatrix}, \tag{4.4}$$

where it is recognized that the effect of modeling the subgrid motion with an eddy viscosity is such that an effective viscosity ν_{eff} can be defined as

$$\nu_{\text{eff}} = \nu + \nu_t. \tag{4.5}$$

4.2 Eddy-viscosity Models

The concept of an eddy viscosity was first proposed by Boussinesq [20] and was initially utilized in LES by Smagorinsky [128]. In this work, Smagorinsky assumed the eddy viscosity to be a constant. Lilly further developed the concept of the eddy viscosity and, borrowing from mixing length theory [119], determined a form for the eddy viscosity as a function of the grid size and rate of strain tensor [103]. This basic model for the eddy viscosity has come to be known as the Smagorinsky (or the Smagorinsky-Lilly) model for eddy viscosity. This model depends on the so-called Smagorinsky constant, which is assumed to be constant for a given flow, but varies in value depending on the type of flow. Despite its simplicity, the Smagorinsky eddy-viscosity model has proven to be quite successful, especially for flows with isotropic turbulence.

Despite being one of the most popular subgrid-scale models, the Smagorinsky eddy-viscosity model has its shortcomings. First of all, the Smagorinsky constant needs to be tuned for different flows. Secondly, the Smagorinsky constant in reality should not be constant throughout a flow, and needs to be modified whenever the turbulence is decaying or damped, such as near walls [111]. A third deficiency is that the Smagorinsky model is known to be overly-dissipative for transitional flows [144]. In order to address these deficiencies, dynamic eddy-viscosity models have been proposed. Some of these models use *ad-hoc* damping and intermittency functions, but perhaps the most successful has been the model proposed by Germano [69]. In this *dynamic* Smagorinsky model, the Smagorinsky "constant" is computed locally in space and time during the simulation.

This is accomplished by recognizing an algebraic identity between the subgrid-scale stresses at two different filtered levels and the resolved turbulent stresses. The result of this relationship is an eddy viscosity that vanishes in laminar flow and at solid boundaries, and has the correct asymptotic behavior in the near-wall region of turbulent boundary layers [69]. Despite these positive attributes, the dynamic Smagorinsky model still has its deficiencies. The eddy viscosity that results from the Germano identity can oftentimes vary wildly in time and space, and can even be negative. These problems are typically overcome by performing some sort of averaging, enforcing positive values for the eddy viscosity, or employing other techniques [39, 70, 141]. Also, implementation of the model can be difficult, as it involves the use of a test filter, which poses its own set of unique challenges [111].

In contrast to dynamic models, a different approach to addressing the aforementioned deficiencies with the classical Smagorinsky model is to utilize a subgrid scale model that relies on an operator other than the rate of strain tensor. By choosing an appropriate operator, it is possible to design a method that has favorable characteristics, including damping in areas of low turbulence, such as in regions of laminar or transitional flow and near walls, without resorting to complicated filtering operations. Three examples of such models include the Wall-adapting Local Eddy Viscosity (WALE) [110], Vreman [137], and Sigma [109] models. While these models have been demonstrated to provide performance comparable to the dynamic Smagorinsky model for some classes of flow [110, 137, 109, 143], they still have their deficiencies. For example, the WALE model does not appropriately "turn off" in laminar flows with three-dimensional velocity gradients. Additionally, both the WALE and Vreman models both fail to properly damp the eddy viscosity for axisymmetric expansion and flows with solid rotation [109]. Furthermore, none of the models mentioned here can properly account for backscatter, and they all feature a constant in their formulation which must still be tuned for various classes of flow.

4.3 Considered Eddy-Viscosity Models

Eddy viscosity models can be written in a general form as

$$\nu_t = (C\Delta)^2 \,\mathrm{OP}, \tag{4.6}$$

where C is some constant, Δ is an associated length scale (usually the filter width or grid spacing), and OP represents some operator that is chosen to give the method favorable characteristics. In this work, we consider four eddy-viscosity models: Smagorinsky, WALE, Vreman, and Sigma models.

4.3.1 Smagorinsky Eddy-Viscosity Model

In the Smagorinsky eddy-viscosity model, the eddy viscosity is calculated as [103]

$$\nu_t = (C_s\Delta)^2 \left|\boldsymbol{S}\right|, \tag{4.7}$$

where Δ is the filter width, $\boldsymbol{S}$ is the rate of strain tensor, and C_s is the Smagorinsky constant. For homogeneous isotropic turbulence, a value of $C_s = 0.18$ has been shown to perform satisfactorily, but smaller values have been required for other applications [69].

4.3.2 Wall-adapting Local Eddy Viscosity Model

In the WALE model, the traceless symmetric part of the square of the velocity gradient tensor is used as an operator rather than the rate of strain tensor. This operator is chosen as it goes naturally to zero near the wall without the use of any damping functions nor dynamic procedure. Using this operator, the eddy viscosity is calculated as [110]

$$\nu_t = (C_w\Delta)^2 \frac{\left(S^d_{ij}S^d_{ij}\right)^{\frac{3}{2}}}{\left(S_{ij}S_{ij}\right)^{\frac{5}{2}} + \left(S^d_{ij}S^d_{ij}\right)^{\frac{5}{4}}}, \tag{4.8}$$

where the traceless symmetric part of the square of the velocity gradient tensor $\boldsymbol{S}^d$ is

$$S^d_{ij} = \frac{1}{2}\left(g^2_{ij} + g^2_{ij}\right) - \frac{1}{3}\delta_{ij}g^2_{kk}, \tag{4.9}$$

δ_{ij} is the Kronecker delta symbol, the velocity gradient tensor $\boldsymbol{g}$ is defined as

$$g_{ij} = \frac{\partial \bar{u}_i}{\partial x_j}, \tag{4.10}$$

Δ is the filter width, $\boldsymbol{S}$ is the rate of strain tensor, and C_w is a constant. In the original work which introduced the model, a value of C_w in the range $0.55 \leq C_w \leq 0.60$ was reported for homogeneous turbulence [110], but later studies by the authors suggest a lower value of $C_w = 0.325$ is more appropriate [1]. In general, the optimal value for C_w varies based on several factors including the flow problem considered and even the mesh size of the simulation [110].

4.3.3 Vreman Model

In the Vreman model, an alternative operator is used which is designed to produce very low dissipation in transitional and near-wall regions. The eddy viscosity is calculated as [137]

$$\nu_t = 2.5 C_s^2 \sqrt{\frac{B_\beta}{\alpha_{ij}\alpha_{ij}}}, \tag{4.11}$$

with

$$\alpha_{ij} = \frac{\partial \bar{u}_j}{\partial x_i}, \tag{4.12}$$

$$\beta_{ij} = \Delta_m^2 \alpha_{mi} \alpha_{mj}, \tag{4.13}$$

$$B_\beta = \beta_{11}\beta_{12} - \beta_{12}^2 + \beta_{11}\beta_{33} - \beta_{13}^2 + \beta_{22}\beta_{33} - \beta_{23}^2, \tag{4.14}$$

and C_s is the Smagorinsky constant.

4.3.4 Sigma Model

In the Sigma model, the subgrid stress is related to the singular values of the resolved velocity gradient tensor. The operator of this model is constructed to deliver zero subgrid stress in cases of two-component or two-dimensional flow as well as in cases of pure axisymmetric or isotropic contraction/expansion. Furthermore, it has a cubic behavior near solid boundaries and thus naturally damps near walls. The eddy viscosity is calculated as [109]

$$\nu_t = (C_\sigma \Delta)^2 \mathcal{D}_\sigma, \tag{4.15}$$

with

$$\mathcal{D}_\sigma = \frac{\sigma_3 (\sigma_1 - \sigma_2)(\sigma_2 - \sigma_3)}{\sigma_1^2}, \tag{4.16}$$

where $\sigma_1 \geq \sigma_2 \geq \sigma_3 \geq 0$ are the three singular values of the velocity gradient tensor, $\boldsymbol{g}$. The value of the constant, C_σ must be tuned based on the flow problem, the grid resolution, and numerics, but a value of $C_\sigma = 1.35$ has been reported to provide results comparable to the classical Smagorinsky model for homogeneous isotropic turbulence [109].

Chapter 5

Residual-based Variational Multiscale Models for Structure-preserving LES

5.1 Projection and Variational Multiscale Models

The possibility of developing an LES formulation using VMS for subgrid-scale modeling of incompressible turbulent flows was first discussed in [86]. The main idea was to use variational projections rather than filtered equations and to confine modeling to the fine scales. In this work, the solution space is divided into three components: a coarse (or large) scale, a resolved fine (or small) scale, and an unresolved fine scale. In making this three-way split, it is recognized that the unresolved fine scale affects the resolved fine scale and the resolved fine scale affects the coarse scale. After this scale separation is performed, the effect of the Reynolds stress on the fine scales is modeled through an eddy-viscosity, inspired by the classical Smagorinsky model, but which is applied only to the fine scales. This methodology diminishes the role of the Smagorinsky constant in producing dissipation in favor of dissipation effects associated with velocity fluctuations and, as a result, yields correct asymptotic behavior at walls and reduces damping of resolved structures as compared to the classical Smagorinsky LES [86]. Additionally, limiting modeling to the fine-scale equations retains numerical consistency of the coarse-scale equations, which is important for the underlying numerical method to achieve optimal convergence. This version of the VMS method for turbulence modeling was studied in [87, 88] and is demonstrated to work very well for homogeneous

isotropic flows and fully-developed turbulent channel flows.

One deficiency of the original VMS method is that the energy transfer to unresolved modes is too small when the discretization is very coarse. In order to address this, a residual-based VMS formulation for LES of incompressible turbulent flows was presented in [11]. This approach models the fine scales as a function of the coarse scale residual, thus avoiding any *ad hoc* devices, such as eddy viscosities, and captures all scales consistently. The method presented in [11] first splits the exact solution into coarse and fine scales and substitutes this splitting of the solution into the Navier-Stokes equations. Next, this equation is projected onto the coarse- and fine-scale subspaces. When the splitting of the solution is performed such that the cutoff for the coarse scales resides in the inertial subrange, an LES interpretation of the method is applicable. The fine-scale solution is related to the residual of the coarse-scale solution through the action of a fine-scale Green's operator [82] that acts on the residual of the coarse-scale solution. The action of the fine-scale Green's operator is then approximated as the product of the element-wise stabilization parameter τ [32, 79, 80, 130] and the local coarse-scale residual.

This turbulence modeling methodology was implemented with a NURBS discretization of the unsteady Navier-Stokes equations and the resulting method was demonstrated to perform admirably for the test cases of forced isotropic turbulence and fully-developed turbulent channel flow [11]. One advantage of the residual-based VMS method is that the magnitude of the fine-scale solution scales with the residual of the coarse-scale solution. As a result, the subgrid modeling "turns off" naturally for laminar flows and the method reverts to DNS when there is sufficient grid resolution. These features are particularly attractive for predictive simulation of turbulent flows in engineering applications, because in many cases the flow regime at a given location in space is often not known *a priori*, yet the flow solution needs to be computed with sufficient accuracy. The residual-based VMS formulation for LES has been successfully used to simulate a number of challenging turbulent-flow test cases [16, 10]. While these results show much promise, it is also argued that improved sugbrid modeling can yield even better results.

Traditionally, in the methods described above, the fine-scale problem is not solved outright.

Rather, the objective is to solve the coarse-scale problem, but it is recognized that the fine-scale problem influences the coarse-scale solution. As such, once the fine-scale problem has been parameterized in terms of the coarse-scale solution, it is substituted back into or statically condensed out of the coarse-scale problem. The net result is that only one problem, expressed entirely in terms of the coarse scale solution must be solved. In contrast to this approach, there is the option to solve the approximate fine-scale problem outright and use the solution in the coarse-scale problem. One method that uses this approach is the method of subgrid vortices. Before describing the method of subgrid vortices, we formally introduce the variational multiscale method and the resulting fine-scale problem.

5.2 The Variational Multiscale Method

The VMS method was originally introduced in [80] in order to identify the origins of stabilized finite element methods and it was quickly realized that the VMS method provides a theoretical framework for incorporating missing fine-scale effects into numerical problems governing coarse-scale behavior [11, 80, 82, 86, 89]. Construction of the variational multiscale method is simple: decompose the solution to a partial differential equation into a sum of coarse-scale and fine-scale components, determine the fine-scale component analytically in terms of the coarse-scale component, and solve for the coarse-scale component numerically. The above scale decomposition is uniquely specified by identifying a projector from the space of all scales onto the coarse-scale subspace. As a consequence, the coarse-scale component is *a priori* guaranteed to best-fit the solution in a variational sense.

To proceed forward, we must first define finite-dimensional, coarse-scale test spaces $\bar{\mathbf{V}} \subset \mathbf{V}$ and $\bar{Q} \subset Q$ and corresponding continuous, linear projection operators $\mathbf{P}_v : \mathbf{V} \to \bar{\mathbf{V}}$ and $\mathbf{P}_q : Q \to \bar{Q}$. The projection operator $\mathbf{P}_v$ naturally splits the test space into coarse-scale and fine-scale components as exhibited by the decomposition

$$\mathbf{V} = \bar{\mathbf{V}} \oplus \mathbf{V}'$$

where $\mathbf{V}' = \ker(\mathbf{P}_v)$ is the infinite-dimensional, fine-scale test space. Consequently, each test function $\mathbf{v} \in \mathbf{V}$ is uniquely represented as the sum of a coarse-scale test function $\bar{\mathbf{v}} = \mathbf{P}_v\mathbf{v} \in \bar{\mathbf{V}}$ and a fine-scale test function $\mathbf{v}' = \mathbf{v} - \bar{\mathbf{v}} \in \mathbf{V}$. Associated with the coarse-scale test space is a corresponding set of trial functions of the form $\bar{\mathbf{S}} = \bar{\mathbf{g}} + \bar{\mathbf{V}}$ where $\bar{\mathbf{g}} \in \mathbf{S}$ satisfies the non-homogeneous Dirichlet boundary condition $\bar{\mathbf{g}}|_{\Gamma_D} = \mathbf{g}$. This inspires a similar split of the set of trial functions into coarse-scale and fine-scale components:

$$\mathbf{S} = \bar{\mathbf{S}} + \mathbf{S}'$$

where $\mathbf{S}'$ is the infinite-dimensional set of fine-scale trial functions. Therefore, the solution to the problem $\mathbf{u} \in \mathbf{S}$ and is uniquely represented as the sum of a coarse-scale component $\bar{\mathbf{u}} = \bar{\mathbf{g}} + \mathbf{P}_v\mathbf{u} \in \bar{\mathbf{S}}$ and a fine-scale component $\mathbf{u}' = \mathbf{u} - \bar{\mathbf{u}} \in \mathbf{S}'$. Since the coarse-scale trial functions satisfy the required non-homogeneous boundary condition, the fine-scale trial functions satisfy homogeneous boundary conditions, and thus we have $\mathbf{S}' = \mathbf{V}'$. Following the same treatment for the test space Q, we can define a set of trial functions for the pressure W such that $W = \bar{W} + W'$ and $W' = Q'$.

Heretofore, we have discussed how to split the solution to the problem into coarse-scale and fine-scale components, but we have not discussed how to obtain said components via a numerical method. To do so, we simply use the decompositions $\mathbf{V} = \bar{\mathbf{V}} \oplus \mathbf{V}'$ and $Q = \bar{Q} \oplus Q'$ and bilinearity to perform a scale splitting of the problem. To do this, we first define space-time sets of trial functions as

$$\mathbf{S}_T := C([0,T]; \mathbf{S}) \tag{5.1}$$

which is the set of continuous functions $\mathbf{u} : [0,T] \to \mathbf{S}$ with

$$\max_{0 \le t \le T} \|\mathbf{u}(t)\|_{H^1(\Omega)} < \infty,$$

and

$$W_T := C([0,T]; W) \tag{5.2}$$

which is the set of continuous functions $p : [0,T] \to W$ with

$$\max_{0\leq t\leq T} \|p(t)\|_{L^2(\Omega)} < \infty.$$

The corresponding variational problem takes the form: Find $\bar{\mathbf{u}} \in C\left([0,T];\bar{\mathbf{S}}\right)$, $\mathbf{u}' \in C\left([0,T];\mathbf{S}'\right)$, $\bar{p} \in C\left([0,T];\bar{W}\right)$, and $p' \in C\left([0,T];W'\right)$ such that

$$a(\bar{\mathbf{v}};\bar{\mathbf{u}}+\mathbf{u}') - b(\bar{\mathbf{v}},\bar{p}+p') + b(\bar{\mathbf{u}}+\mathbf{u}',\bar{q}) = \ell(\bar{\mathbf{v}}) \tag{5.3}$$

for all $\bar{\mathbf{v}} \in \bar{\mathbf{V}}$, $\bar{q} \in \bar{Q}$ and almost every $t \in (0,T)$ and

$$a(\mathbf{v}';\bar{\mathbf{u}}+\mathbf{u}') - b(\mathbf{v}',\bar{p}+p') + b(\bar{\mathbf{u}}+\mathbf{u}',q') = \ell(\mathbf{v}') \tag{5.4}$$

for all $\mathbf{v}' \in \mathbf{S}'$, $q' \in Q'$ and almost every $t \in (0,T)$. The coarse-scale problem is given by (5.3), whereas (5.4) is referred to as the fine-scale problem. This is the split variational problem that relates the effect of the fine scales on the coarse scales and vice-versa. It should be noted that at this point, the VMS method is *exact*. However, solving for the coarse-scale solution depends on a method for solving the infinite-dimensional fine-scale equation. Since this is, in general, intractable, some form of modeling for the fine-scale method must be employed. Thus, developing suitable subgrid-scale models for the VMS method is of utmost importance.

By relating the subgrid scales to the resolved scales, it is shown that the subgrid scale solution is related to the *residual* of the resolved scales [80, 82]. In particular, for divergence-conforming discretizations, the fine-scale problems for $\mathbf{u}' \in \mathcal{S}'$ and $p' \in \mathcal{W}'$ can be solved in terms of the so-called coarse-scale residual of the momentum equation[1] :

$$\mathbf{u}' = \mathcal{G}'_{\text{vel}}\left(\text{Res}_m\left(\bar{\mathbf{u}},\bar{p}\right)\right) \tag{5.5}$$

$$p' = \mathcal{G}'_{\text{press}}\left(\text{Res}_m\left(\bar{\mathbf{u}},\bar{p}\right)\right), \tag{5.6}$$

where $\mathcal{G}'_{\text{vel}}$ and $\mathcal{G}'_{\text{press}}$ represent fine-scale Green's operators [48, 80, 82] and

$$\text{Res}_m\left(\bar{\mathbf{u}},\bar{p}\right) := \mathbf{f} - \frac{\partial\bar{\mathbf{u}}}{\partial t} + \bar{\mathbf{u}}\cdot\nabla\bar{\mathbf{u}} - \nu\Delta\bar{\mathbf{u}} + \nabla\bar{p}. \tag{5.7}$$

[1] Note in general the fine-scale velocity and pressure depend on the coarse-scale residual of both the momentum and continuity equations. However, for divergence-conforming discretizations, the coarse-scale residual of the continuity equation is zero by design.

In order to solve (5.6), we need to employ suitable approximations for the fine-scale Green's operators $\mathcal{G}'_{\text{vel}}$ and $\mathcal{G}'_{\text{press}}$. This is addressed in the next section. By inserting the resulting solution for $\mathbf{u}'$ and p' back into the coarse-scale problem, a final finite-dimensional system for the coarse-scale solution $\bar{\mathbf{u}} \in \bar{\mathbf{S}}$ and $\bar{p} \in \bar{W}$ is achieved.

The primary issue associated with the variational multiscale method is that $\mathbf{V}'$ and Q' are infinite-dimensional spaces and thus solving the fine-scale problem is an intractable task. Fortunately, for most problems of interest, it is sufficient to approximate the effect of the fine-scales on the coarse-scale solution in order to produce stable and accurate numerical solutions [48]. This motivates the need to pursue effective approaches for modeling the fine-scale problem.

5.3 The Fine-scale Problem

We now present the fine-scale problem for the variational multiscale incompressible Navier-Stokes problem, including some candidate approximations for solving the fine-scale problem. First, we assume that the fine-scale problem can be localized to an element. The physical interpretation of this assumption is that the subgrid scales do not transfer mass between elements. With this assumption in mind, the element-wise fine-scale problem for a given element can be stated:

$$\begin{aligned}
\frac{\partial \mathbf{u}'}{\partial t} + \nabla \cdot (\bar{\mathbf{u}} \otimes \mathbf{u}' + \mathbf{u}' \otimes \bar{\mathbf{u}} + \mathbf{u}' \otimes \mathbf{u}') - \nu \Delta \mathbf{u}' + \nabla p' &= \text{Res}_m (\bar{\mathbf{u}}, \bar{p}) \quad && \text{for } (\mathbf{x}, t) \in \Omega_e \times (0, T) \\
\nabla \cdot \mathbf{u}' &= 0 && \text{for } (\mathbf{x}, t) \in \Omega_e \times (0, T) \\
\mathbf{u}' &= \mathbf{0} && \text{for } (\mathbf{x}, t) \in \Gamma_e \times (0, T) \\
\mathbf{u}'|_{t=0} &= \mathbf{u}'_0 && \text{for } \mathbf{x} \in \Omega_e
\end{aligned} \tag{5.8}$$

The relationships in (5.6) inspire two candidate *algebraic* approximations to (5.8). In the first approximation, denoted the *quasi-static* approximation, the fine-scale solution is solved at a given time step based on the coarse-scale momentum residual at that time step. In an alternative approximation, denoted the *dynamic* approximation, the time derivative of the fine-scale solution

is retained in hopes of improving the approximation [43]. These approximations are

$$\text{Quasi-static:} \quad \tau_{qs}^{-1}\mathbf{u}' = \frac{\partial \mathbf{u}'}{\partial t} + \nabla \cdot \left(\bar{\mathbf{u}} \otimes \mathbf{u}' + \mathbf{u}' \otimes \bar{\mathbf{u}} + \mathbf{u}' \otimes \mathbf{u}'\right) - \nu \Delta \mathbf{u}' \tag{5.9}$$

$$\text{Dynamic:} \quad \tau_{d}^{-1}\mathbf{u}' = \nabla \cdot \left(\bar{\mathbf{u}} \otimes \mathbf{u}' + \mathbf{u}' \otimes \bar{\mathbf{u}} + \mathbf{u}' \otimes \mathbf{u}'\right) - \nu \Delta \mathbf{u}', \tag{5.10}$$

where τ_{qs}^{-1} and τ_{d}^{-1} are algebraic operators associated with the quasi-static and dynamic approximations, respectively. In order to define these operators, it is first recognized that these operators represent time scales for their respective fine-scale approximations. We then turn to dimensional analysis in order to find appropriate forms for these operators. The time scale τ must depend on h, ν, and $\bar{\mathbf{u}}$. Thus, we identify both advective and diffusive time scales:

$$\text{Advective:} \quad \tau_{\text{adv}} = \frac{h}{C_I \left|\bar{\mathbf{u}}\right|}$$

$$\text{Diffusive:} \quad \tau_{\text{diff}} = \frac{h^2}{C_{II}\nu},$$

where C_I is typically chosen to be 2 and C_{II} can be determined from inverse estimates [95]. We also seek an additional time scale related to the unsteadiness of the problem. One option which has its origins in stabilized methods [85, 126] is to relate the time scale to the time step size used in the numerical discretization:

$$\tau_{\text{uns}} = \frac{\Delta t}{C_{III}}, \tag{5.11}$$

where again C_{III} is a constant and is typically chosen to be 2. While this formulation for τ_{uns} has been demonstrated to be effective when Δt is sufficiently large, its dependency on time step size means τ_{uns} vanishes as the time step is decreased. For explicit schemes which may rely on very small time steps in order to satisfy the CFL condition, this can lead to an ineffective or unstable [79] method. In order to address these issues, we propose an alternative formation for τ_{uns} which relies on the unsteadiness of the flow solution rather than the time step:

$$\tau_{\text{uns}} = \frac{\left|\bar{\mathbf{u}}_n\right|}{\left|\bar{\mathbf{u}}_{n+1} - \bar{\mathbf{u}}_n\right|} \frac{\Delta t}{C_{III}}, \tag{5.12}$$

where $\bar{\mathbf{u}}_{n+1}$ and $\bar{\mathbf{u}}_n$ represent the coarse-scale solution at the next and the current time steps, respectively. Although we present this alternate formulation for τ_{uns}, we use the classical formulation given by (5.11) herein.

Having defined appropriate time scales related to the advection, diffusion, and unsteadiness of the flow, we can now define appropriate formulations for τ_{sq} and τ_d:

$$\tau_{sq} = \left(\tau_{\text{uns}}^{-2} + \tau_{\text{adv}}^{-2} + \tau_{\text{diff}}^{-2}\right)^{-1/2} \tag{5.13}$$

$$\tau_d = \left(\tau_{\text{adv}}^{-2} + \tau_{\text{diff}}^{-2}\right)^{-1/2}. \tag{5.14}$$

Utilizing (5.13) and (5.14) in conjunction with (5.9) and (5.9), respectively, then defines our approximation to the fine-scale problem. We choose to solve the fine-scale problem using the method of subgrid vortices.

5.4 Method of Subgrid Vortices

The method of subgrid vortices is based on the application of the VMS method to divergence-conforming discretizations of the Navier-Stokes equations. In this method, a reduced fine-scale velocity problem with homogeneous boundary conditions is solved over each element using a discrete approximation of the divergence-free fine-scale space. The basis for the fine-scale velocity is constructed as the curl of the (divergence-free) fine-scale vector potential space, where the vector potential space is represented with Bernstein polynomials. The physical interpretation of each of these basis functions is a set of single vortical filaments, or *subgrid vortices*.

When this basis is naïvely constructed, a discretization of polynomial order k_f and dimension d will contain $(k_f - 1)^d$ linearly-dependent subgrid vortices. In order to construct an analysis-suitable basis of linearly-independent functions, an eigenvalue decomposition of the element stiffness matrix is conducted. The eigenvectors corresponding to non-zero eigenvalues then provide the basis used to solve for the fine-scale velocity. This set of eigenvectors represents a set of subgrid vortices residing in each element, organized by their energy content. Furthermore, it is recognized that

the stabilization parameter τ represents a time scale related to the dissipation rate of the subgrid vortical energy. This interpretation of the method elucidates the connection between the underlying mathematics and the physical representation of the subgrid model. While the method of subgrid vortices was first imagined as a VMS method for turbulence modeling, since it explicitly calculates a fine-scale velocity, it can also be used with residual-based eddy viscosity models, which are introduced in the next chapter.

5.5 Considered Residual-based Variational Multiscale Models

We utilize the fine-scale approximations in (5.9) and (5.10) along with the fine-scale problem (5.8) in order to define a class of residual-based variational multiscale models for structure-preserving LES.

5.5.1 Quasi-static Variational Multiscale Model

In the quasi-static VMS model, we approximate the fine-scale velocity using the fine-scale approximation (5.9). The resulting problem is a Darcy problem with diffusivity τ_{qs}^{-1} driven by the momentum residual of the coarse-scale solution. This has the form

$$\begin{aligned} \tau_{qs}^{-1}\mathbf{u}' + \nabla p' &= -\mathrm{Res}_m\left(\bar{\mathbf{u}}, \bar{p}\right) \quad \text{over} \quad \Omega_e \\ \nabla \cdot \mathbf{u}' &= 0 \quad \text{over} \quad \Omega_e, \end{aligned} \tag{5.15}$$

subject to the boundary conditions

$$\begin{aligned} \mathbf{u}' \cdot \mathbf{n} &= 0 \quad \text{on} \quad \partial\Omega_e \\ \int_{\Omega_e} p' &= 0 \quad \text{over} \quad \Omega_e, \end{aligned} \tag{5.16}$$

$\mathbf{n}$ is the normal vector on element boundaries. In the quasi-static VMS model, the fine-scale velocity is solved instantaneously at each time step and thus does not take into consideration any time evolution of the fine-scale velocity.

The fine-scale problem described in (5.15) is solved using the method of subgrid vortices. The approximate fine-scale problem is approximated element-by-element using a diverence-conforming

discretization of degree k_f. This has the effect of representing the fine scales using subgrid vortical structures.

5.5.2 Dynamic Variational Multiscale Model

In the dynamic VMS model, we approximate the fine-scale velocity using the fine-scale approximation (5.10). The resulting problem is a Darcy problem with diffusivity τ_d^{-1} driven by the momentum residual of the coarse-scale solution. This has the form

$$\begin{aligned} \frac{\partial \mathbf{u}'}{\partial t} + \tau_d^{-1}\mathbf{u}' + \nabla p' &= -\mathrm{Res}_m\left(\bar{\mathbf{u}}, \bar{p}\right) \quad \text{over} \quad \Omega_e \\ \nabla \cdot \mathbf{u}' &= 0 \quad \text{over} \quad \Omega_e, \end{aligned} \tag{5.17}$$

subject to the same boundary conditions as (5.16). As with the quasi-static VMS model, the method of subgrid vortices is used in order to solve (5.17).

5.5.3 Coarse-scale Governing Equation

Given either of the models above, we can substitute the resulting fine-scale solution back into (5.3) in order to arrive at an approximation for the coarse-scale solution. In doing so, we make the following assumptions: 1) the effect of unsteadiness and diffusion of the fine-scale velocity on the coarse scales is negligible and 2) the effect of the fine-scale pressure on the coarse scales is negligible. These assumptions may be linked to the choice of projection operators for the velocity and pressure fields as made precise in [89, 132]. The resulting coarse-scale governing equation is

$$a_{\mathrm{VMS}}(\bar{\mathbf{v}}; \bar{\mathbf{u}}, \mathbf{u}') - b(\bar{\mathbf{v}}, \bar{p}) + b(\bar{\mathbf{u}}, \bar{q}) = \ell(\bar{\mathbf{v}}), \tag{5.18}$$

where

$$a_{\mathrm{VMS}}(\bar{\mathbf{v}}; \bar{\mathbf{u}}, \mathbf{u}') := \int_\Omega \bar{\mathbf{v}} \cdot \frac{\partial \bar{\mathbf{u}}}{\partial t}\, d\Omega + \int_\Omega \bar{\mathbf{v}} \cdot \left(\left(\bar{\mathbf{u}} + \mathbf{u}'\right) \cdot \nabla \left(\bar{\mathbf{u}} + \mathbf{u}'\right)\right)\, d\Omega + \int_\Omega \nu \nabla \bar{\mathbf{v}} : \nabla \bar{\mathbf{u}}\, d\Omega.$$

Chapter 6

Residual-based Eddy-viscosity Models for Structure-preserving LES

6.1 Residual-based Eddy-viscosity Models

Residual-based eddy-viscosity (RBEV) models, first introduced in [111], borrow ideas from the classical eddy-viscosity models and the residual-based VMS formulation. In the RBEV model, the effect of the subgrid scales is expressed as an eddy viscosity that acts on the coarse scales. In contrast to the Smagorinsky eddy viscosity model, where the eddy viscosity is proportional to the grid size and the rate of strain tensor, in the RBEV model, the eddy viscosity is proportional to the fine-scale velocity and the grid size. In order to calculate the fine-scale velocity, the RBEV model utilizes the VMS formulation in order to provide an approximate expression for the fine-scale velocity field as an algebraic operator τ times the residual of the coarse-scale velocity. Since the eddy viscosity is proportional to the fine-scale velocity, and the fine-scale velocity is proportional to the coarse-scale velocity residual, this lends a natural dynamic behavior to the RBEV model.

The RBEV model has much in common with the original VMS method [80] and the more recent residual-based VMS methods [11], but there are two important distinctions. In the original VMS method [80], there is a three-way split of the solution space and modeling is confined to the fine scales. In the RBEV model, there is a two-way split of the solution space and the eddy viscosity is applied to the coarse scales. When compared to residual-based VMS methods [11],

the difference is in the utilization of the fine-scale solution. In the VMS method, an expression is found for the fine-scale solution which is then substituted into the coarse-scale problem. In the RBEV model, the fine-scale velocity is used to construct an eddy viscosity model for the coarse-scale equations. The RBEV model has been tested in predicting the decay of incompressible and compressible homogeneous turbulence and was shown to be more accurate than the dynamic Smagorinsky model [111].

6.2 Considered Residual-based Eddy Viscosity Models

To contrast the variational multiscale models presented in Chapter 5, we also consider residual-based eddy viscosity models. In these RBEV models, we seek to capture the effect of the subgrid scale turbulent motion through an eddy viscosity that acts on the coarse scales as in (4.5). For the RBEV model, the eddy viscosity has the form [111]

$$\nu_t = \bar{C} h \left| \mathbf{u}' \right|, \tag{6.1}$$

where h represents the grid spacing and $\mathbf{u}'$ denotes the fine-scale velocity. For the constant $\bar{C}$, we make the claim that the subgrid approximation represents all turbulent motion at length scales smaller than the grid resolution, and thus set the constant to $\bar{C} = 0.074$ [111]. We utilize the fine-scale approximations in (5.9) and (5.10) along with the fine-scale problem (5.8) in order to define a class of residual-based eddy-viscosity models for structure-preserving LES.

6.2.1 Quasi-static Residual-based Eddy Viscosity Model

In the quasi-static RBEV model, we approximate the fine-scale velocity using the fine-scale approximation (5.9). The resulting problem is the same fine-scale velocity problem (5.15) as the quasi-static VMS model. After the fine-scale velocity is computed, the result is substituted into (6.1) in order to produce the quasi-static RBEV model.

6.2.2 Dynamic Residual-based Eddy Viscosity Model

The dynamic RBEV model follows closely from the quasi-static RBEV model. As in that case, the eddy viscosity is represented as in (6.1). In comparison to the quasi-static RBEV model, we approximate the fine-scale velocity using the fine-scale approximation (5.10). The resulting problem is the same fine-scale velocity problem (5.17) as the dynamic VMS model. The resulting fine-scale velocity is then used to calculate an eddy viscosity, resulting in the dynamic RBEV model.

Chapter 7

Numerical Results for a Selection of Turbulent Flows

In this chapter, we present numerical results for a series of turbulent flow simulations which demonstrate the performance of the residual-based VMS and RBEV models. The flow problems chosen here reflect several classes of flows, including homogeneous turbulence, transitional flows, and wall-bounded flows. Results for the residual-based VMS and RBEV models are compared to classical LES models. Prior to presenting these numerical results, a brief description of the software used for these simulations is provided.

7.1 Implementation of a Parallel Divergence-conforming B-spline Framework

In order to evaluate the performance of the VMS and RBEV models presented here, an accurate and efficient unsteady incompressible Navier-Stokes solver using using divergence-conforming discretizations was written. It was required that the simulation software scale efficiently in order to test problems up to the limit of DNS and, additionally, be flexible enough to accommodate many different subgrid models for evaluation and study. With these goals in mind, a custom divergence-conforming discretization code was purpose-built, written in C++, in order to support the current research.

The software developed here was modeled after a sequential divergence-conforming three-

dimensional unsteady incompressible Navier-Stokes solver used for DNS simulations in [57]. Considerable changes were introduced to the software in order to add subgrid-scale models and to parallelize the code. The resulting code uses the Crank-Nicolson [50] method to discretize the viscous terms and a multi-step Adams-Bashforth [9] method to discretize the nonlinear advective terms. A vector potential representation of the velocity field is used in order to provide an efficient method for solving the Navier-Stokes equations. At each time step, the program uses a vector potential expression to convert a discrete generalized Stokes system from a mixed problem into a positive semi-definite problem of Maxwell type, which is solved using the Jacobi-preconditioned conjugate gradient method [57]. The solution is evolved in time using a second-order Adams-Bashforth multi-step method [9].

The code developed here can accommodate many different LES turbulence models, including traditional eddy-viscosity, VMS, RBEV, and differential subgrid vortex models. At this time, the classical Smagorinsky, WALE, Vreman, Sigma, VMS (quasi-static and dynamic), and RBEV (quasi-static and dynamic) models have all been implemented. For the classical Smagorinsky, WALE, Vreman, and Sigma models, it is necessary to calculate the velocity gradient components in order to construct each model's respective subgrid stress operator. In contrast to standard finite element codes, calculating the velocity gradients is a straightforward task for the code developed here as the framework of the code makes arbitrary-order derivatives of the basis functions readily available. On the other hand, implementation of VMS and RBEV models requires the calculation of a fine-scale velocity, which is accomplished by solving a fine-scale problem over each element using the method of subgrid vortices.

In order to accomplish this, a two-step process is carried out at each time step. First, the coarse-scale problem is solved with the approximated value of the fine-scale velocity field at the current time step. Second, the fine-scale velocity field for the next time step is calculated based on the residual of the coarse-scale velocity field of the current time step. At time $t = 0$, the fine-scale velocity field is initialized to $\mathbf{u}' = \mathbf{0}$. Solving the local fine-scale problem over each element is made efficient by exploiting the homogeneous boundary conditions for each fine-scale element problem.

As such, the local system is assembled and solved only over the internal degrees of freedom on each element. After this reduced system is formed, an eigenvalue decomposition of the system is performed and the system is solved using a basis consisting of the eigenvectors associated with non-zero eigenvalues.

Parallelization of the code is provided through the Message Passing Interface (MPI), with the Portable, Extensible Toolkit for Scientific Computation (PETSc) [8] handling most of the implementation details. Furthermore, PETSc data types are used for management of the vectors and matrices associated with solving the system for the coarse-scale problem, and PETSc's Krylov solver is used for solving the system at each time step. In contrast, the fine-scale element problems are solved using LAPACK [2]. Domain decomposition is performed by METIS [100] by providing a graph of the element connectivity to its multilevel recursive-bisection routine. Since the fine-scale problem is solved over elements, these operations are completely localized on each process and do not add any additional computational expense in the form of inter-process communication. The resulting code is a highly efficient, scalable framework able to utilize various subgrid-scale models for solving the unsteady Navier-Stokes equations using a divergence-conforming discretization.

In order to demonstrate the parallel efficiency of the code, a series of tests were conducted. For these tests, the Taylor-Green vortex flow problem was solved and the simulation was run for 300 time steps. The baseline case considered is 64^3 elements using 24 processes. The problem is then scaled in a way such that the amount of work per process is kept roughly constant. This results in problem sizes of 81^3 elements and 102^3 elements run with 48 and 96 processes, respectively. Solutions using both no subgrid model and the dynamic VMS model are tested. A summary of the test cases is described in Table 7.1, where the dynamic VMS model is labeled as "D-VMS". It is clear from these results that the code exhibits acceptable scalability. Simulations involving the subgrid modeling show slightly worse scalability than simulations without subgrid modeling. This is partially explained by the fact that even though the calculations involved with the subgrid modeling is completely local on each process, these calculations still add considerable amount of additional work per time step. Thus, any load imbalancing (which cannot be completely eliminated

in the isogeometric analysis setting) leads to reduced parallel efficiency. Another factor in the degredation of scalability is in the linear algebra. Specifically, the problem with the dynamic VMS models require more iterations of the solver in order to solve the solution at each time step. Thus, in order to provide a more accurate measure of scalability, the amount of work for each problem should be kept the same by using the same number of iterations of the solver at each time step regardless of which subgrid model is used.

Table 7.1: Parallel efficiency

Model	Problem size	Processes used	Wall-time	Parallel efficiency
no model	262114	24	0:38	–
no model	531441	48	0:40	0.950
no model	1061208	96	0:43	0.884
D-VMS	262114	24	4:57	–
D-VMS	531441	48	5:11	0.955
D-VMS	1061208	96	6:53	0.719

In addition to these scalability results, a "stress test" was performed to determine the limits of the code's scalability, even if the code is not scaled optimally in these limits. To date, the code has been demonstrated on domains of up to 256^3 elements, which corresponds to a system of over 51 million degrees of freedom.

7.2 Numerical results

In this section, numerical results that demonstrate the efficacy of the proposed turbulent simulation method for a set of benchmark turbulent problems are presented. A suite of test problems were chosen in order to evaluate the performance of the VMS and RBEV models across a wide range of flows, including homogeneous turbulence, transitional flow, and wall-bounded turbulent flow. Homogeneous turbulence is represented with both forced homogeneous turbulence at $Re_\lambda = 233$ and decay of homogeneous turbulence at an initial $Re_\lambda = 233$. These two simulations are considered to be two parts of one flow problem. First, turbulence is created and sustained through forcing, then the forcing is removed and the turbulence is allowed to decay. This approach to modeling

homogeneous turbulence is taken here since it reflects the conditions under which turbulence is experienced in flows of engineering interest, where regions of homogeneous turbulence are generated upstream by some mechanism.

Results for the forced and decaying homongeneous turbulence problems using the VMS and RBEV models are compared with results using no model (under-resolved DNS) and the classical Smagorinsky model. Transitional flow is represented with Taylor-Green vortex flow at $Re = 1600$ and wall-bounded turbulent flow is represented by turbulent channel flow at $Re_\tau = 395$. The classical Smagorinsky model is ill-suited for these last two problems, so results for the WALE, Vreman, and Sigma models are also compared for these cases. For all the simulations which follow, the following constants were used for their respective models: $C_s = 0.18$, $C_w = 0.325$, $C_\sigma = 1.35$. These simulations were all performed using the software described in the previous section. For the purpose of presenting results here, k and k_f refer to the polynomial order to which the coarse- and fine-scale velocity discrete spaces are complete.

7.2.1 Forced Homogeneous Turbulence at $Re_\lambda = 233$

The study of homogeneous turbulence allows for the study of the energy transfer from the large scales to the small scales without any interference from any mechanisms such as wall damping or energy input in intermediate scales. For these reasons, homogeneous turbulence has become a fundamental flow for the study of turbulence. By adding a forcing which acts on the lowest modes to homogeneous turbulence, it is possible to achieve a higher Reynolds number and to gather longer statistics than what is possible for decaying homogeneous turbulence. As such, we begin our evaluation of our proposed turbulence methodology with this problem. We consider forced homogeneous turbulence at Taylor microscale Reynolds number $Re_\lambda = 233$. The domain in physical space is $\Omega = (2\pi)^3$ with periodic boundary conditions in all directions. The kinematic viscosity is set to $\nu = \frac{1}{150}$ in order to establish the Taylor microscale Reynolds number of $Re = 233$. Forced homogeneous turbulence is simulated as specified in [11] by supplying a constant power

input in the lowest modes. The forcing at a given time is given by

$$f(x) = \sum_{\substack{\boldsymbol{\kappa} \\ |\kappa_i|<\kappa_f \\ \boldsymbol{\kappa}\neq\mathbf{0}}} \frac{P_{in}}{2E_{\kappa_f}} \hat{\mathbf{u}}_{\boldsymbol{\kappa}} \exp\left(i\boldsymbol{\kappa}\cdot\mathbf{x}\right), \tag{7.1}$$

where $i = \sqrt{-1}$, $P_{in} = 62.8436001234$ is the fixed power input,

$$E_{\kappa_f} = \frac{1}{2} \sum_{\substack{\boldsymbol{\kappa} \\ |\kappa_i|<\kappa_f \\ \boldsymbol{\kappa}\neq\mathbf{0}}} \hat{\mathbf{u}}_{\boldsymbol{\kappa}} \cdot \hat{\mathbf{u}}_{\boldsymbol{\kappa}} \tag{7.2}$$

is the kinetic energy contained in the lowest modes, and

$$\hat{\mathbf{u}}_{\boldsymbol{\kappa}} = \frac{1}{|\Omega|} \int_{\Omega} \mathbf{u}^h(\mathbf{x}) \exp\left(-i\boldsymbol{\kappa}\cdot\mathbf{x}\right) d\Omega \tag{7.3}$$

are the Fourier coefficients of the velocity field. These Fourier coefficients $\hat{\mathbf{u}}_{\boldsymbol{\kappa}}$ are computed for each $\boldsymbol{\kappa}$ that satisfies $|\kappa_i| < \kappa_f, i = 1, 2, 3$ and κ_f is chosen to be 3. Note that this specification of the forcing inputs power into a box with dimensions defined by κ_f in each direction, rather than a sphere with radius κ_f, as was used in [101]. As such, the turbulence in the lowest modes is not isotropic, although the structure of the highest and intermediate scales is unaffected. Also, this alternative specification for the forcing leads to a higher Reynolds number than what is reported in [11, 101]. The integrals in (7.3) are calculated using quadrature rather than fast Fourier transforms because only a few modes are required.

The simulation is initialized to a random velocity field with zero fine-scale velocity and is allowed to advance in time until the dissipation reaches equilibrium with the power input. The time step used is $\Delta t = 0.0125h$, where h is the grid spacing. After the simulation reaches equilibrium, data samples are collected for 15 eddy turnover times (T_{ett}) with samples separated by $0.5T_{\text{ett}}$. Velocity components are sampled at the knots. Forced homoegeneous turbulence at $Re_\lambda = 233$ was computed using the VMS and RBEV models presented earlier and compared to the classical Smagorinsky eddy viscosity model.

The quantities of interest are the energy spectrum and the two-point third-order structure function. The energy spectrum function $E(\kappa)$ is calculated as the integral of the velocity spectrum

$\mathbf{\Phi}(\boldsymbol{\kappa})$ over the surface of a sphere of radius $\kappa = |\boldsymbol{\kappa}|$:

$$E(\kappa) = \oint \frac{\mathbf{\Phi}(\boldsymbol{\kappa}) \cdot \mathbf{\Phi}(\boldsymbol{\kappa})}{2} dS(\kappa), \tag{7.4}$$

where $S(\kappa)$ is the surface of the sphere and $\mathbf{\Phi}(\boldsymbol{\kappa})$ is calculated as the Fourier transform of the two-point velocity correlation [118].

The two-point third-order structure function is defined as

$$S_3(r) = \left\langle (u_i(\boldsymbol{x} + \boldsymbol{r}) - u_i(\boldsymbol{x}))^3 \right\rangle, \tag{7.5}$$

where $u_i(\boldsymbol{x})$ is a velocity component at a position $\boldsymbol{x}$ parallel to a relative displacement $\boldsymbol{r}$. Here, $\langle \cdot \rangle$ implies ensemble average. In the inertial subrange, S_3 scales like r for fully-developed, locally isotropic turbulence [118]. Thus, a simulation which accurately represents the energy transfer in the inertial subrange is accompanied by an accurate representation of S_3.

First, in order to provide an overall impression of the performance of all of the considered models, the energy spectra for simulations with $h = \frac{\pi}{16}$, $k = 2$ and $k_f = 1$ are presented in Fig. 7.1. This solution is intentionally under-resolved and thus serves as a representative case that allows the performance of the various methods to be compared. The reference line represents the $-\frac{5}{3}$ power law. It is apparent that without any sort of subgrid-scale modeling, the solution suffers from energy pileup in the higher modes. However, both of the dynamic models show great improvement over the no-model case and demonstrate excellent agreement with the $-\frac{5}{3}$ law in the inertial subrange and through the cutoff wavenumber. Comparing the Smagorinsky model to the dynamic residual-based models highlights the fact that the Smagorinsky model is overly dissipative for this case[1] . In contrast to the dynamic residual-based models, the quasi-static methods suffer from energy pileup and it appears that that neither of these models are very effective for this problem. This is due to the small time step used, which is required to satisfy the CFL, but has the unfortunate effect of rendering τ_{qs} too small such that the fine scales are not properly activated in the simulation.

[1] It is acknowledged that superior results for the Smagorinsky model can be achieved if a smaller C_s is chosen, however this would render the model under-dissipative for the second part of this simulation when the forcing is turned off. This highlights the need for models that can respond dynamically to turbulence which varies in space and time.

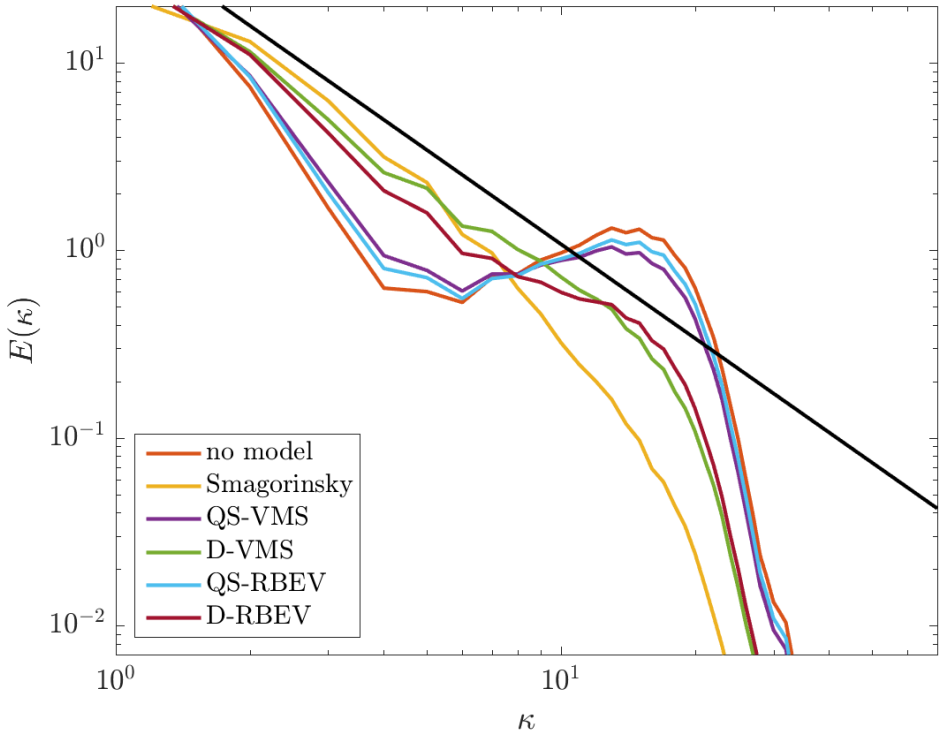

Figure 7.1: Energy spectra for simulation of forced homogeneous turbulence with $k = 2$, $k_f = 1$, and $h = \frac{\pi}{16}$ and reference line with $-\frac{5}{3}$ slope. Comparison of subgrid-scale models (no model, Smagorinsky LES, quasi-static VMS (QS-VMS), dynamic VMS (D-VMS), quasi-static RBEV (QS-RBEV), and dynamic RBEV (D-RBEV)).

We next present the two-point third-order structure function for the same simulation in Fig. 7.2. Only the Smagorinsky and dynamic residual-based models are presented since it is already clear from the energy spectra that the quasi-static models are ineffective here. The results reinforce what was observed in the energy spectra. Namely, we see that the dynamic residual-based models properly capture the energy transfer in the inertial subrange, whereas the Smagorinsky model is overly-dissipative.

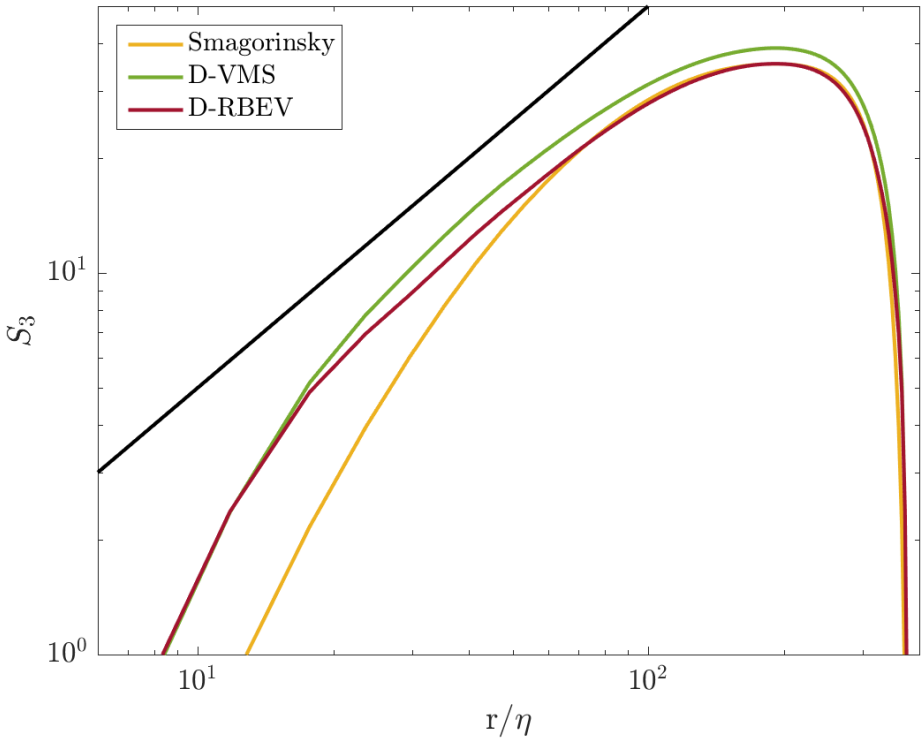

Figure 7.2: Two-point third-order structure function for simulation of forced homogeneous turbulence with $k = 2$, $k_f = 1$, and $h = \frac{\pi}{16}$. Comparison of subgrid-scale models (Smagorinsky LES, dynamic VMS (D-VMS), and dynamic RBEV (D-RBEV)).

The next set of results demonstrate consistency of the dynamic residual-based models with respect to mesh refinement. In Fig. 7.3 the energy spectra for the dynamic VMS and dynamic RBEV models are presented for $k = 2$, $k_f = 1$, and various mesh sizes. Both results show good agreement with the DNS, although the dynamic VMS model is superior to the dynamic RBEV model. Both dynamic models show some energy pileup for the coarsest mesh which goes away as the mesh is refined. For $h = \frac{\pi}{16}$ and smaller, the dynamic VMS accurately matches the DNS up to the cutoff wavenumber. In contrast, the dynamic RBEV model shows some slight energy pileup for $h = \frac{\pi}{16}$ and is slightly over-diffuse, even for $h = \frac{\pi}{32}$.

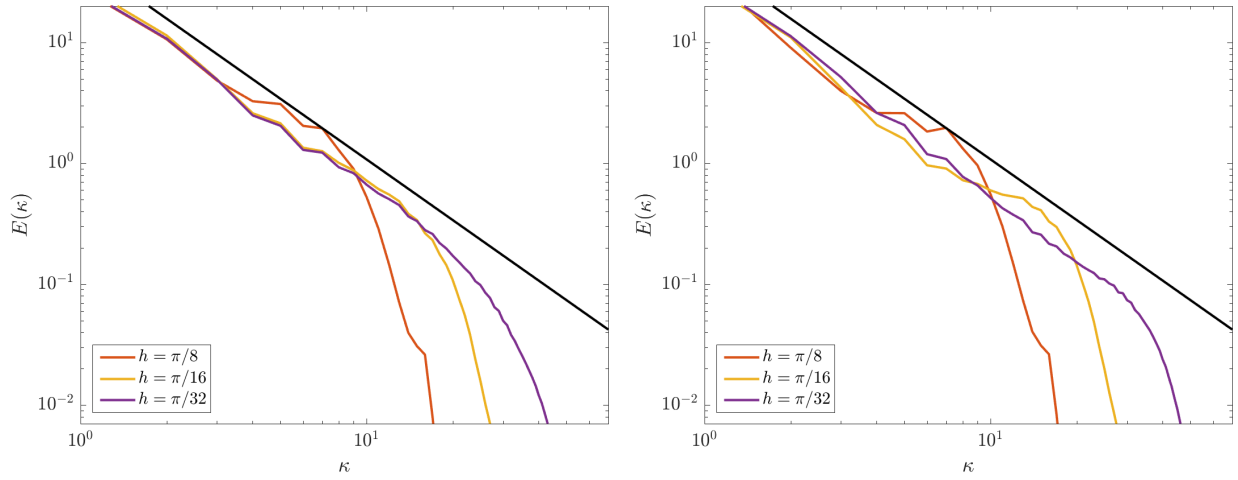

(a) Dynamic VMS

(b) Dynamic RBEV

Figure 7.3: Energy spectra for simulation of forced homogeneous turbulence under mesh refinement with $k = 2$ and $k_f = 1$ and reference line with $-\frac{5}{3}$ slope.

Next, results for degree elevation of the basis are presented. In Fig. 7.4 the energy spectra for the dynamic VMS and dynamic RBEV models are presented for $h = \frac{\pi}{16}$ and various coarse-scale and fine-scale polynomial orders. From these results, we can make two observations. The first observation is that linear coarse scales are insufficient for the dynamic VMS model. It appears that at least quadratics are required to get enough resolution for the subgrid-scale model to produce the proper dissipation. In contrast, the eddy viscosity, and thus the dissipation, of the dynamic RBEV model is related only to the magnitude of the fine-scale velocity, so it is not sensitive to the coarse-scale polynomial order. The second observation is that neither model is very sensitive to the polynomial order of the fine scales. We obtain equally impressive results for $k_f = 1$ as we do for $k_f = 2$. This is very encouraging, as it suggests that the model can be kept computationally efficient by utilizing the lowest-order basis for the fine scales.

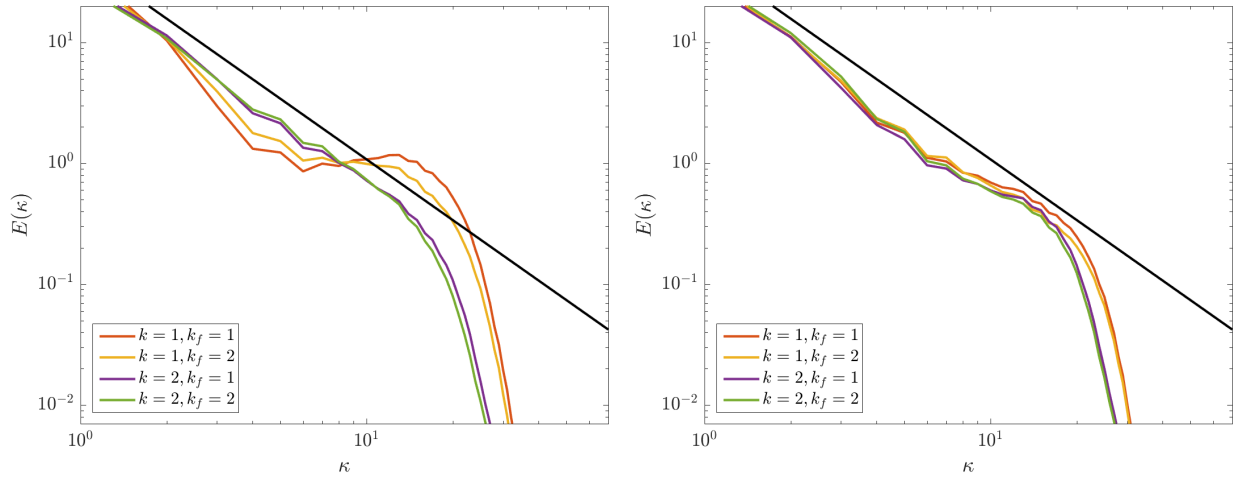

(a) Dynamic VMS (b) Dynamic RBEV

Figure 7.4: Energy spectra for simulation of forced homogeneous turbulence under degree elevation with $h = \frac{\pi}{16}$ and reference line with $-\frac{5}{3}$ slope.

7.2.2 Decay of Homogeneous Turbulence at Initial $Re_\lambda = 233$

We next present results for the decay of homogeneous turbulence. The problem is initialized by running the forced homogeneous turbulence simulation previously described until the dissipation reaches equilibrium with the power input. This ensures that the solution has fully-developed, homogeneous turbulence with proper correlations in the coarse- and fine-scale velocity fields. At this point, designated $t = 0$ for this simulation, the forcing is turned off and the simulation is advanced in time and allowed to naturally decay. The domain in physical space is $\Omega = (2\pi)^3$ with periodic boundary conditions in all directions. The kinematic viscosity is set to $\nu = \frac{1}{150}$. The time step used is $\Delta t = 0.0125h$, where h is the grid spacing. The solution is advanced for 4.46 seconds, during which time 28 data samples are taken. Velocity components are sampled at the knots. The decay of homogeneous turbulence was computed using the VMS and RBEV models presented earlier and compared to the classical Smagorinsky eddy viscosity model.

Only results for the dynamic residual-based models are presented here. Since quasi-static models were determined to be ineffective for the forced homogeneous turbulence, they are not

further explored here in the context of decaying homogeneous turbulence. Additionally, results for the Smagorinsky model are not presented here, since it is already widely established that the Smagorinsky model is well suited for decaying homogeneous turbulence[2] .

The energy spectra for the dynamic VMS model at both the initial time and a later stage ($t = 4.45$) are presented in Fig. 7.5 for $k = 1, 2$, $k_f = 1$, and $h = \frac{\pi}{16}$. Again, the reference line represents the $-\frac{5}{3}$ power law. It is clear that the model properly transfers energy from the large scales to the small scales without any energy pileup. Even for $k = 1$, where the model experienced energy pileup for the forced homogeneous turbulence, here the energy is able to properly transfer between scales and dissipate away. For this problem, unlike for the forced homogeneous turbulence, it appears that the dynamic VMS method is effective even with $k = 1$.

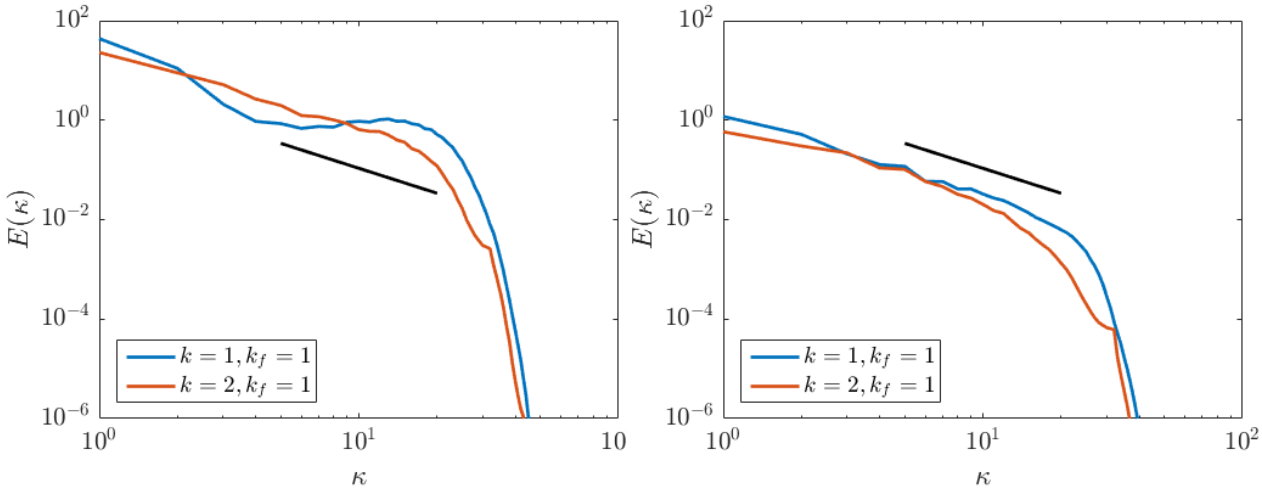

(a) Initial time ($t = 0$)

(b) Later time ($t = 4.45$)

Figure 7.5: Kinetic energy spectra for simulation of decaying homogeneous turbulence with varying coarse-scale degrees, $k_f = 1$, and $h = \frac{\pi}{16}$ and reference line with $-\frac{5}{3}$ slope. Dynamic VMS model.

Next, the energy spectra for the dynamic RBEV model at both the initial time and a later stage ($t = 4.45$) are presented in Fig. 7.6 for $k = 1, 2$, $k_f = 1$, and $h = \frac{\pi}{16}$. As was the case with the dynamic VMS model, the dynamic RBEV model properly transfers energy from the large scales to the small scales without any energy pileup.

[2] The Smagorinsky model was constructed and tuned to perform well for this problem!

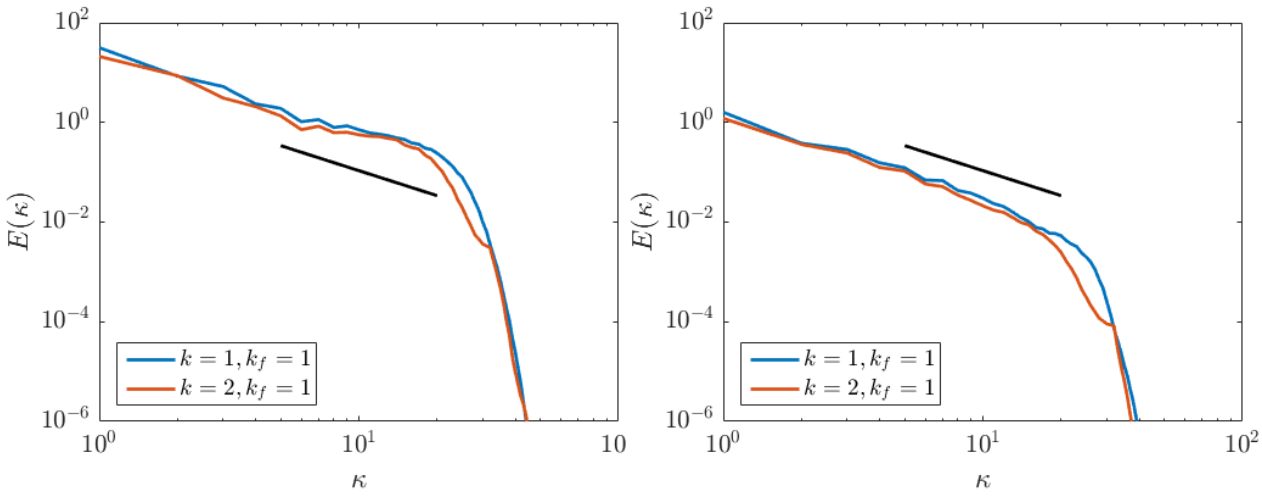

(a) Initial time ($t = 0$)

(b) Later time ($t = 4.45$)

Figure 7.6: Kinetic energy spectra for simulation of decaying homogeneous turbulence with varying coarse-scale degrees, $k_f = 1$, and $h = \frac{\pi}{16}$ and reference line with $-\frac{5}{3}$ slope. Dynamic RBEV model.

7.2.3 Taylor-Green Vortex at $Re = 1600$

Three-dimensional Taylor-Green vortex flow is one of the simplest systems in which to study the generation of small scales through vortex stretching and the energy dissipation from the resulting turbulence. The initial condition of Taylor-Green vortex flow is laminar and consists of purely two-dimensional streamlines, but for all time $t > 0$, the flow is three-dimensional. As the solution is evolved in time, vortex stretching causes the generation of small-scale motion and eventual transition into turbulence. The initial conditions for this flow are

$$\mathbf{u}_0(x, y, z) = \begin{bmatrix} \sin(x)\cos(y)\cos(z) \\ -\sin(x)\sin(y)\cos(z) \\ 0 \end{bmatrix}. \tag{7.6}$$

The initial condition can be visualized in Fig. 7.7. The flow is periodic in all three spatial directions in the domain $\Omega = (0, 2\pi)^3$ and, due to inherent symmetries in the flow, can be modeled within a computational domain of $\Omega^h = (0, \pi)^3$ with impermeable stress-free boundaries. At low Reynolds numbers ($Re < 400$), the flow is anisotropic for all time, but as Reynolds number increases,

the flow experiences increased isotropy [21].

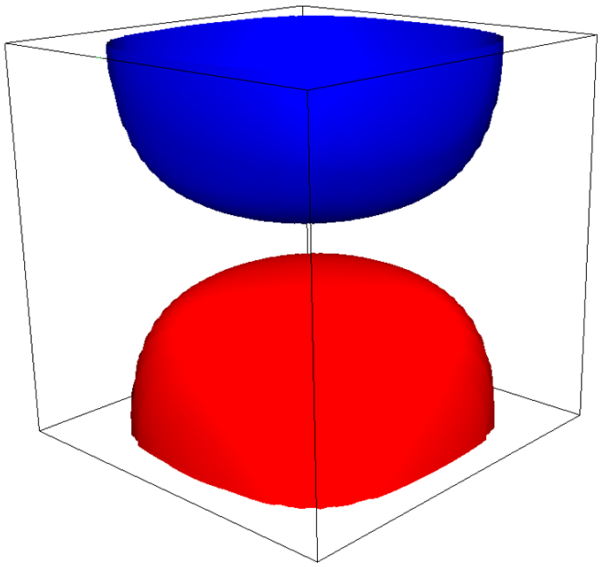

Figure 7.7: Isosurfaces of enstrophy colored by z-component of vorticity for Taylor-Green Vortex flow at $t = 0s$

Taylor-Green vortex flow at $Re = 1600$ was simulated and results are presented here. The simulation is initialized as in (7.6) and the simulation is advanced for 10 seconds, which is enough time for the flow to develop and transition into fully turbulent flow. A time step size of $\Delta t = 0.125h$ is used in all simulations. The flow is solved using the VMS and RBEV models presented earlier and are compared to the classical Smagorinsky, WALE, Vreman, and Sigma eddy viscosity models and to Fourier-based DNS results using 256^3 modes [21, 133].

The quantities of interest are the time history of the kinetic energy and of the kinetic energy dissipation rate, the Q-criterion, and the energy spectrum for the solution at the final time instance of the simulation. The kinetic energy, E_k, of the flow is given by

$$E_k(t) = \frac{1}{\Omega}\int_\Omega \frac{\mathbf{u}(t)\cdot\mathbf{u}(t)}{2} d\Omega. \tag{7.7}$$

The kinetic energy dissipation rate, ϵ, can be computed as the time derivative of E_k:

$$\epsilon = -\frac{dE_k}{dt}. \tag{7.8}$$

For incompressible flow, the kinetic energy dissipation rate is directly related to the enstrophy, ε:

$$\epsilon = 2\nu\varepsilon, \tag{7.9}$$

where the enstrophy is computed as

$$\varepsilon = \frac{1}{\Omega}\int_{\Omega} \frac{\boldsymbol{\omega}\cdot\boldsymbol{\omega}}{2} d\Omega, \tag{7.10}$$

where $\boldsymbol{\omega} = \nabla \times \mathbf{u}$ is the vorticity. For LES, application of (7.9) to the resolved velocity field results in the *resolved dissipation rate*. This represents the amount of kinetic energy dissipation that is present in the coarse scales. The difference of the *total dissipation rate* and the *resolved dissipation rate* allows for the calculation of the *model dissipation rate*, which gives a measure of how much dissipation a particular subgrid scale model provides.

The Q-criterion represents the local balance between vorticity magnitude and shear strain rate, and identifies vorticies as regions where the vorticity magnitude is greater than the magnitude of the rate of strain. The Q-criterion is calculated as [91]

$$Q = \frac{1}{2}\left(|\mathbf{\Omega}|^2 - |\mathbf{S}|^2\right), \tag{7.11}$$

where $\Omega_{ij} = \frac{1}{2}\left(\frac{\partial \bar{u}_i}{\partial x_j} - \frac{\partial \bar{u}_j}{\partial x_i}\right)$.

Before presenting the results for the residual-based models, we first present a comparison of classical eddy-viscosity models. First, the time histories of the kinetic energy is presented for simulations with $h = \frac{\pi}{16}$ and $k = 2$ in Fig. 7.8. All of the models appear to predict the same time evolution of the kinetic energy, and actually demonstrate a decrease in performance from the no-model baseline case. All of the models are overly dissipative, and depart from the DNS from the very beginning of the simulation. This suggests that all of the models are active even at the beginning of the simulation when the solution is purely laminar.

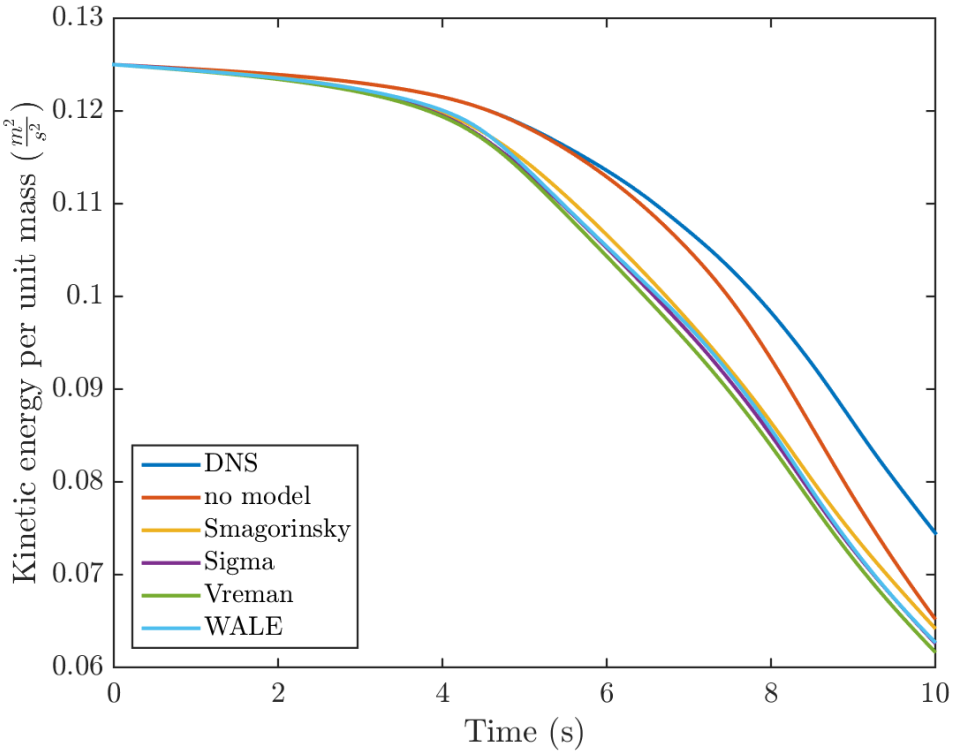

Figure 7.8: Time history of kinetic energy for simulation of Taylor-Green vortex with $k = 2$ and $h = \frac{\pi}{16}$. Comparison of subgrid-scale models (no model, Smagorinsky, Sigma, Vreman, WALE with DNS [21].

We now turn our attention to the total dissipation rate for the same set of simulations, presented in Fig. 7.9. All of the eddy-viscosity models show roughly the same characteristics: too much dissipation for all time, beginning at the onset of the simulation, a local maxima at the midpoint of the simulation, and a prediction of the peak dissipation approximately one second earlier than the DNS data. In all cases, the prediction with the model is further from the DNS than the no-model baseline. It is clear that none of the operators used in these models properly reduce the eddy viscosity in three-dimensional laminar flow.

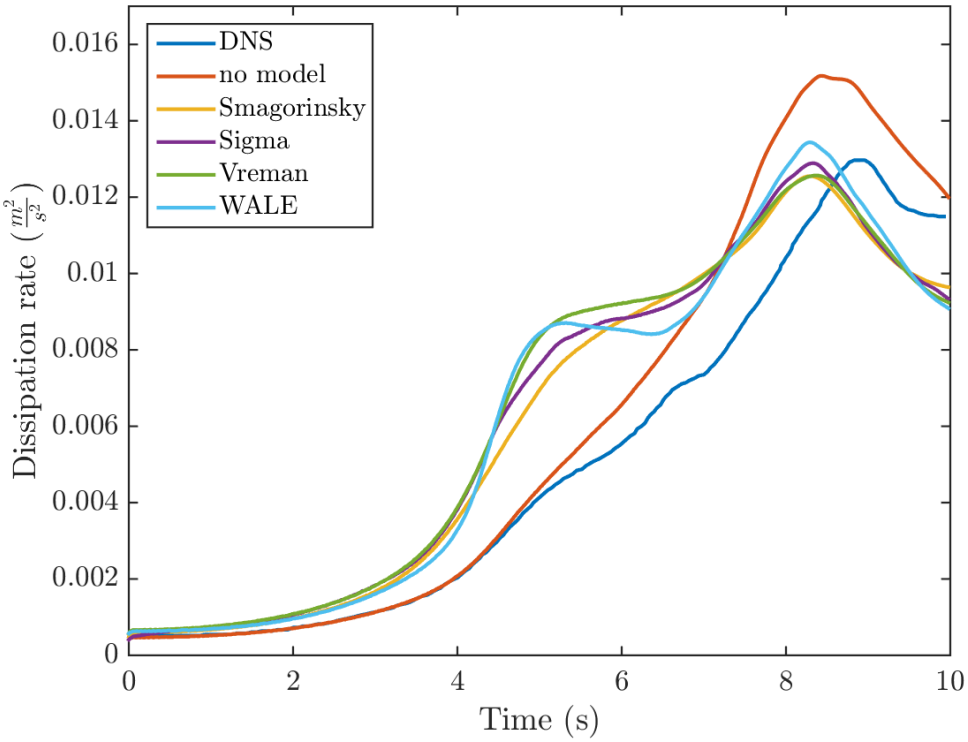

Figure 7.9: Time history of total dissipation rate for simulation of Taylor-Green vortex with $k = 2$ and and $h = \frac{\pi}{16}$. Comparison of subgrid-scale models (no model, Smagorinsky, Sigma, Vreman, WALE with DNS [21].

We can further elucidate the various models' response to turbulence production and transition by examining the resolved and model dissipation rates. The time histories of both of these parameters for the same set of simulations are presented in Fig. 7.10. Between the four models, there is not very much difference in the resolved dissipation. The model dissipation reflects the same characterstics that were observed with the total dissipation. At $t = 0$, all of the models have non-zero model dissipation[3] .

[3] Interestingly, these models all exhibit more model dissipation than resolved dissipation for almost all time.

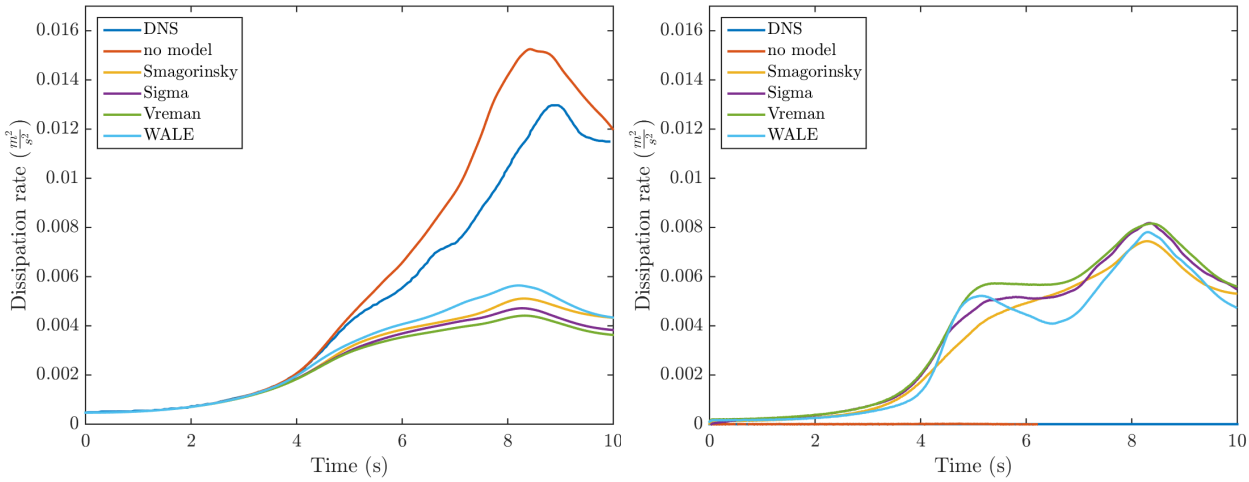

(a) Resolved dissipation

(b) Model dissipation

Figure 7.10: Time history of resolved and model dissipation for simulation of Taylor-Green vortex with $k = 2$ and $h = \frac{\pi}{16}$. Comparison of subgrid-scale models (no model, Smagorinsky Sigma, Vreman, WALE with DNS [21].

In the next set of results, we evaluate the performance of the residual-based models. Since the Sigma, Vreman, and WALE models did not show marked improvement over the Smagorinsky model, we have selected the Smagorinsky model as a representative eddy-viscosity model by which to measure the residual-based models. First, the time histories of the kinetic energy is presented for simulations with $h = \frac{\pi}{16}$, $k = 2$ and $k_f = 1$ in Fig. 7.11. From the figure, it is clear that all of the residual-based models outperform the Smagorinsky model. Furthermore, the dynamic models are more accurate than the quasi-static models. Since the Smagorinsky model has no mechanism to reduce the eddy viscosity in laminar flows, it departs from the DNS solution very early in the simulation. All of the residual-based models depart from the DNS at roughly the same point in time, later than the Smagorinsky model, indicating that in all four cases, the model is appropriately "turned off" when the solution lacks subgrid-scale activity. Interestingly, at later times, both of the quasi-static residual-based models become overly dissipative. Although both dynamic models have lower kinetic energy than the DNS after the midpoint in the simulation, by the late times both models match the DNS in terms of the dissipation rate.

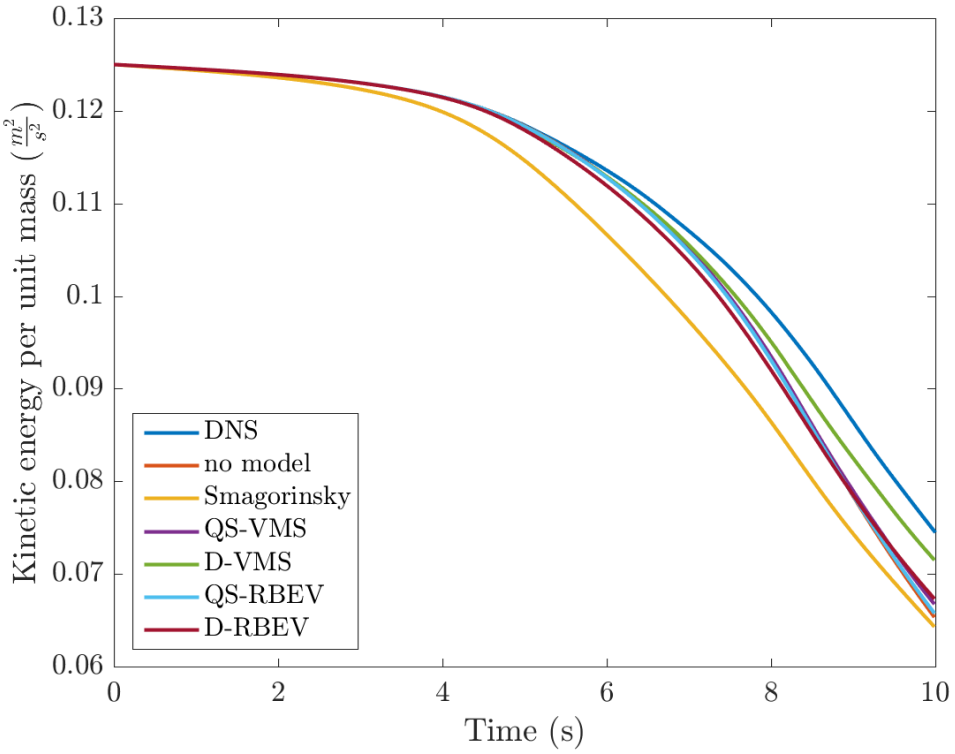

Figure 7.11: Time history of kinetic energy for simulation of Taylor-Green vortex with $k = 2$, $k_f = 1$, and $h = \frac{\pi}{16}$. Comparison of subgrid-scale models (no model, Smagorinsky LES, quasi-static VMS (QS-VMS), dynamic VMS (D-VMS), quasi-static RBEV (QS-RBEV), and dynamic RBEV (D-RBEV)) with DNS [21].

We once again turn our attention to the total dissipation rate for the same set of simulations, presented in Fig. 7.12. First, we observe that the quasi-static models are fairly ineffective and do not show any improvement from the no-model baseline until after the time of peak dissipation. After this point, the subgrid-scale activity has developed to the point that the coarse-scale residual grows large enough for the quasi-static models to activate, despite the extremely low value of τ_{qs} resulting from the small time step. The dynamic RBEV model shows much improvement over the quasi-static models, but is overly dissipative for all time. The dynamic VMS model, on the other hand, shows the closest agreement to the DNS for all time. The dynamic VMS model even predicts the proper maximum total dissipation, although it arrives at this point in the simulation early.

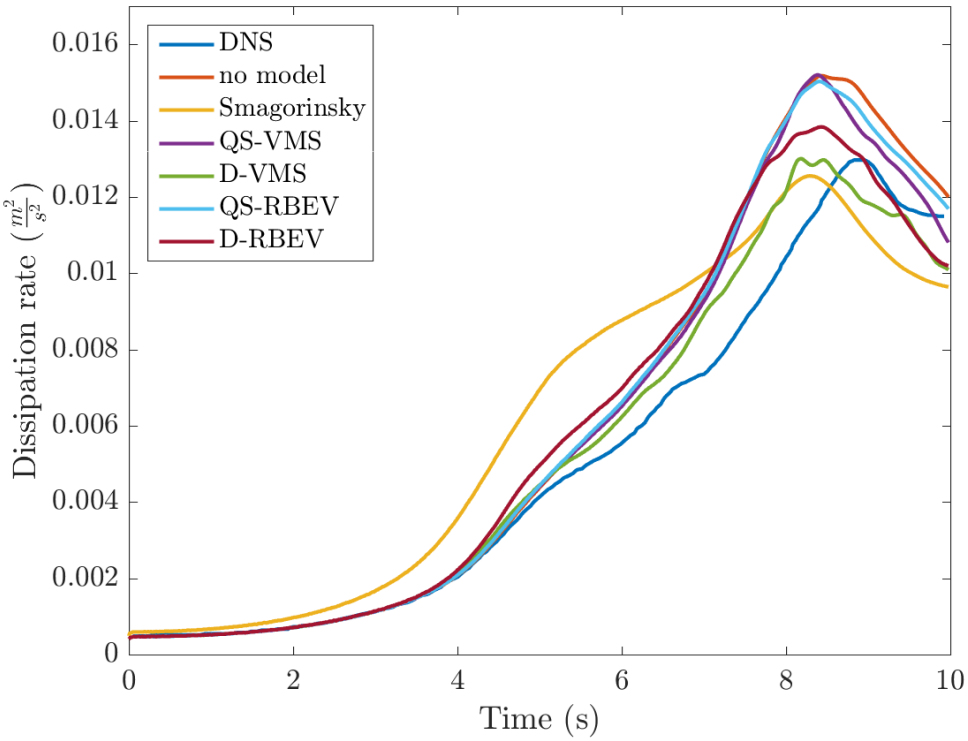

Figure 7.12: Time history of total dissipation rate for simulation of Taylor-Green vortex with $k = 2$, $k_f = 1$, and $h = \frac{\pi}{16}$. Comparison of subgrid-scale models (no model, Smagorinsky LES, quasi-static VMS (QS-VMS), dynamic VMS (D-VMS), quasi-static RBEV (QS-RBEV), and dynamic RBEV (D-RBEV)) with DNS [21].

In order to better understand how these residual-based models respond to turbulence production and transition, we again examine the resolved and model dissipation rates. The time histories of both of these parameters for the same set of simulations are presented in Fig. 7.13. It is clear that the quasi-static models are not activated until very late in the simulation, and even then they produce very little modeling. The two dynamic models show similar performance.

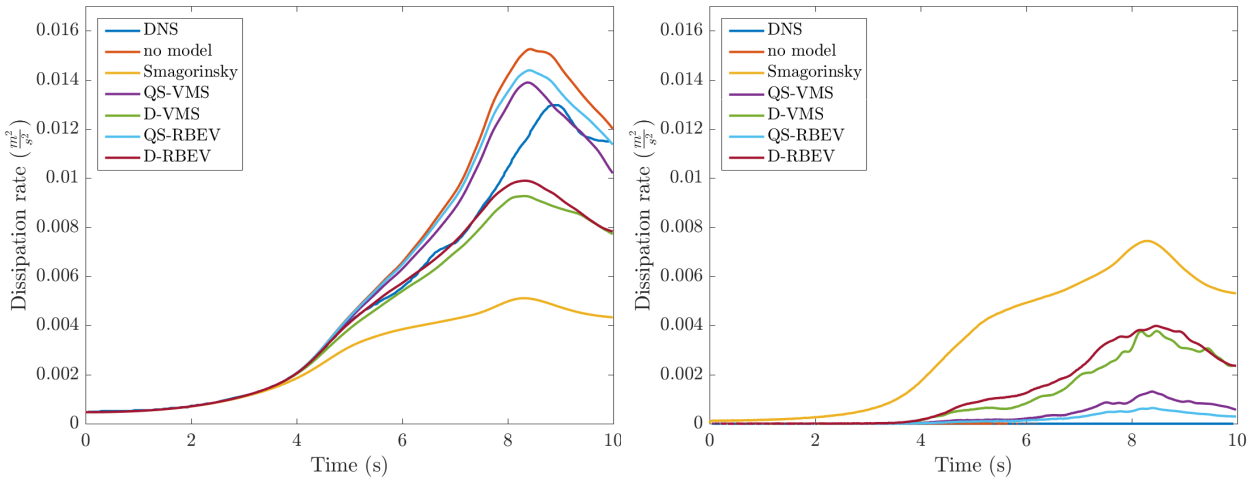

(a) Resolved dissipation

(b) Model dissipation

Figure 7.13: Time history of resolved and model dissipation for simulation of Taylor-Green vortex with $k = 2$, $k_f = 1$, and $h = \frac{\pi}{16}$. Comparison of subgrid-scale models (no model, Smagorinsky LES, quasi-static VMS (QS-VMS), dynamic VMS (D-VMS), quasi-static RBEV (QS-RBEV), and dynamic RBEV (D-RBEV)) with DNS [21].

In Fig. 7.14, we present the kinetic energy spectrum for the various models at the end time of the simulation. This occurs shortly after the point of maximum dissipation, so the solution is fully turbulent with structures encompassing the full range of turbulent scales present. The reference line has a slope of -1.98, as reported in [21]. From the spectra, it is clear that the dynamic models and the Smagorinsky model exhibit the expected energy cascade[4] . The quasi-static models demonstrate some slight energy pileup in the higher modes.

[4] At this point, the flow is essentially a "box of turbulence," so the Smagorinsky model performs well. Note, however, that it has lower energy overall due to its overly-dissipative nature at earlier times.

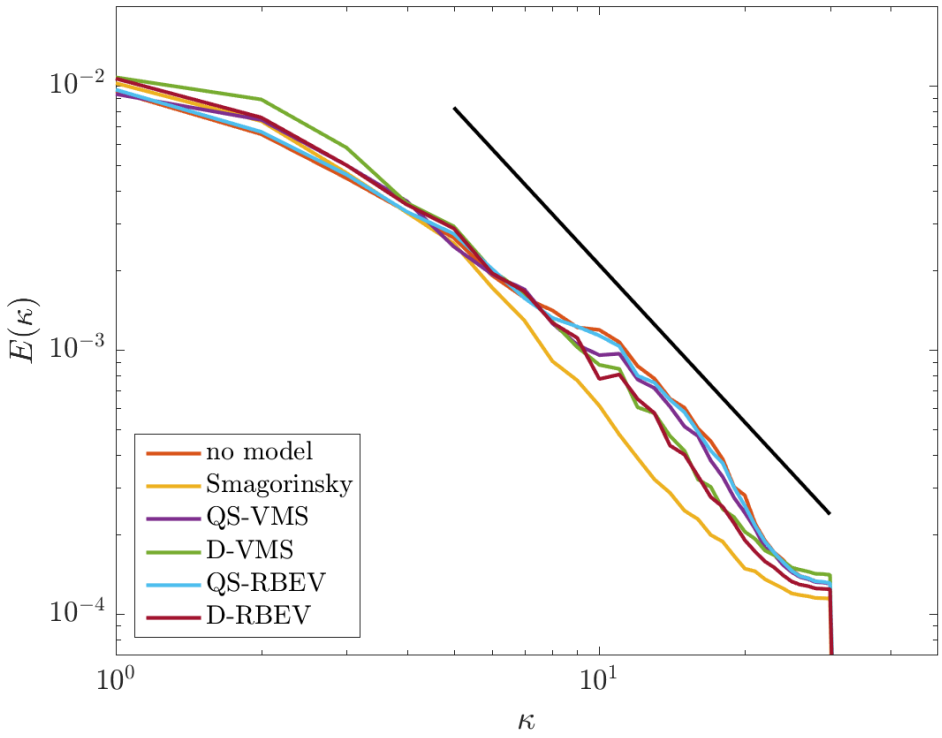

Figure 7.14: Energy spectra for simulation of Taylor-Green vortex with $k = 2$, $k_f = 1$, and $h = \frac{\pi}{16}$ and reference line with -1.98 slope. Comparison of subgrid-scale models (no model, Smagorinsky LES, quasi-static VMS (QS-VMS), dynamic VMS (D-VMS), quasi-static RBEV (QS-RBEV), and dynamic RBEV (D-RBEV)).

Another way to compare the performance of the models is to look at the character of the vortical structures present in the various solutions. Contours of $Q = 1$ colored by vorticity at a late time shortly after the time of maximum dissipation ($t = 9.57$) for the Smagorinsky and dynamic VMS models are compared in Fig. 7.15. Compared to the dynamic VMS model, the Smagorinsky model damps out the smallest turbulent structures. Only the larger vortical structures, with lower vorticity, remain. In contrast, the dynamic VMS model more accurately predicts turbulent structures in the smallest length scales that can be represented on the mesh.

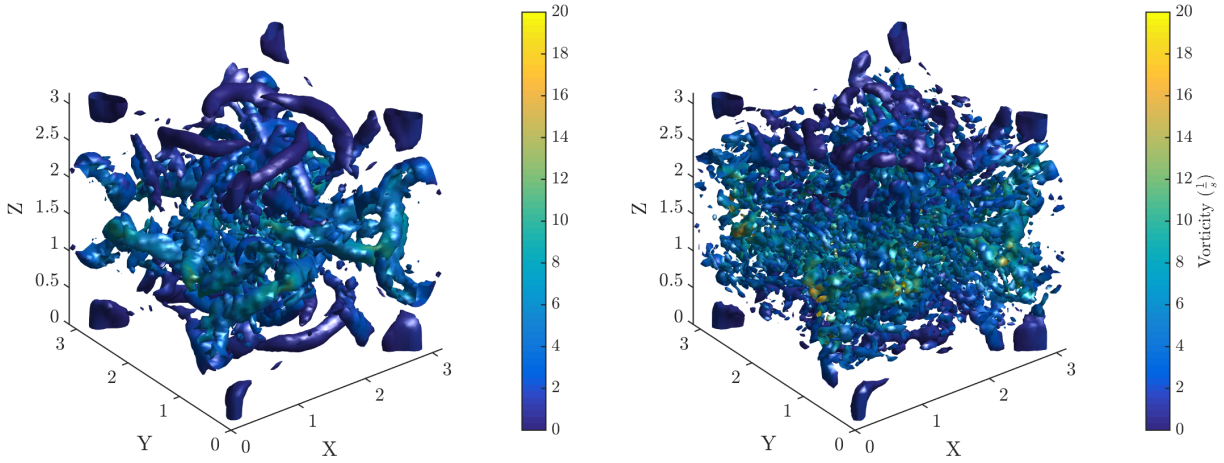

(a) Smagorinsky model.

(b) Dynamic VMS model.

Figure 7.15: Contours of $Q = 1$ colored by vorticity for simulation of Taylor-Green votex with $k = 2$, $k_f = 1$, and $h = \frac{\pi}{16}$. Comparison of Smagorinsky LES and dynamic VMS models.

We once again turn our attention to consistency of the residual-based models with respect to mesh refinement and polynomial elevation. We limit our presentation in this regard to the dynamic models since they demonstrated the best performance for the Taylor-Green vortex. First, we examine consistency of the methods with respect to mesh refinement. In Fig. 7.16, the time histories of the total, resolved, and model dissipation for the dynamic VMS and RBEV models are presented for various mesh sizes. It is clear here that as the mesh is refined, the total dissipation rate for both models converge to the DNS solution. This is accompanied by an appropriate increase in the resolved dissipation rate as well as a corresponding decrease in the model dissipation rate. It is also noted that the dynamic VMS model outperforms the dynamic RBEV model for both coarse and fine meshes.

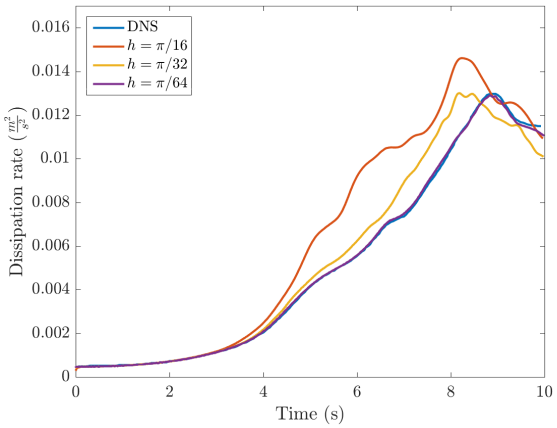

(a) Total dissipation rate. Dynamic VMS model.

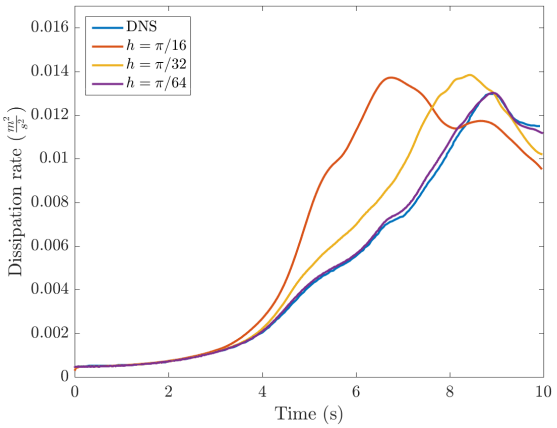

(b) Total dissipation rate. Dynamic RBEV model.

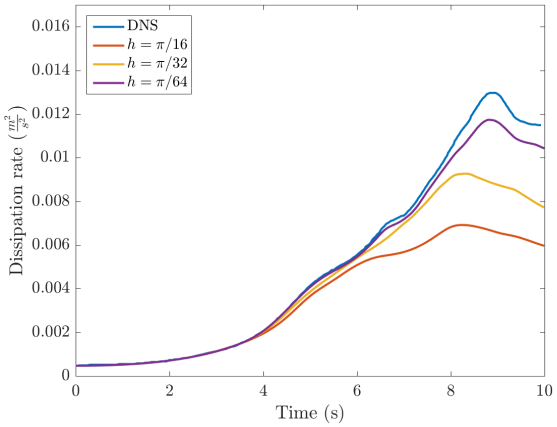

(c) Resolved dissipation rate. Dynamic VMS model.

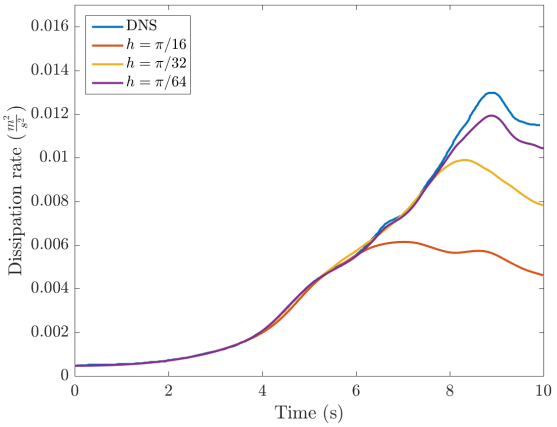

(d) Resolved dissipation rate. Dynamic RBEV model.

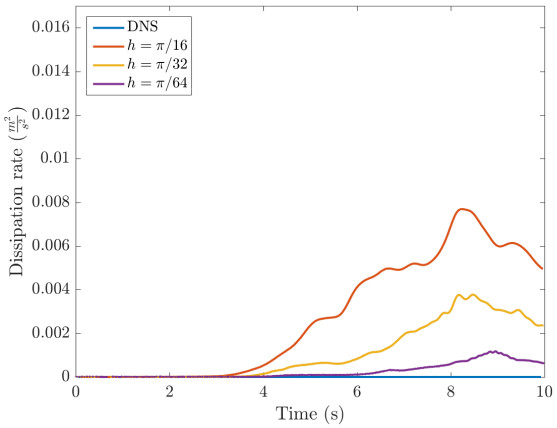

(e) Model dissipation rate. Dynamic VMS model.

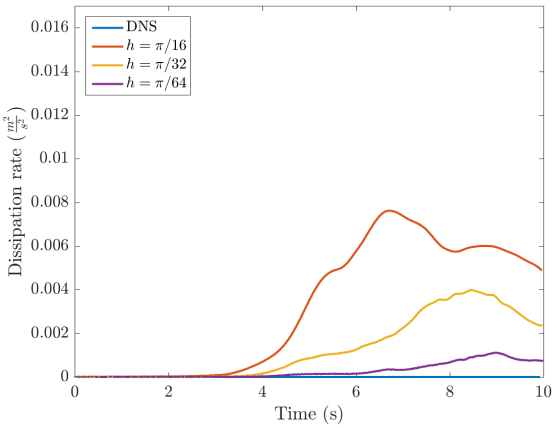

(f) Model dissipation rate. Dynamic RBEV model.

Figure 7.16: Time history of total, resolved, and model dissipation for simulation of Taylor-Green vortex under mesh refinement with $k = 2$ and $k_f = 1$.

Now we demonstrate the effect of coarse- and fine-scale degree elevation. The time histories of the total, resolved, and model dissipation for the dynamic VMS and RBEV models are presented for various coarse- and fine-scale polynomial degrees in Fig. 7.17. The same trends that were observed for homogeneous turbulence are seen here. First, the dynamic RBEV model shows effectiveness with $k = 1$, while the dynamic VMS model shows improved results with $k = 2$ compared to $k = 1$. Second, coarse-scale polynomial order is more influential in the results than fine-scale polynomial order. For the dynamic RBEV model, there is essentially no difference observed for $k_f = 1$ or $k_f = 2$, regardless of coarse-scale polynomial degree. For the dynamic VMS model, there is an observable but minute improvement in the prediction by using a higher fine-scale order. However, this effect is less pronounced as the coarse-scale order is elevated.

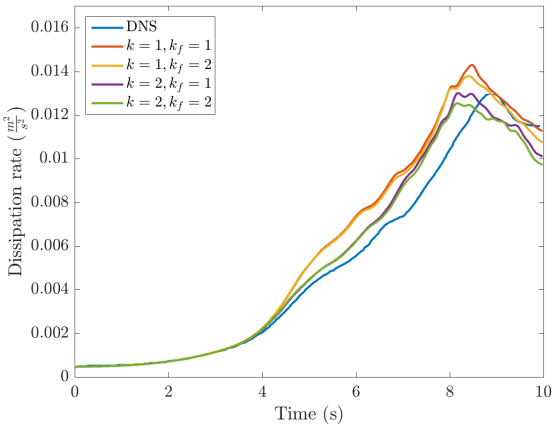

(a) Total dissipation rate. Dynamic VMS model.

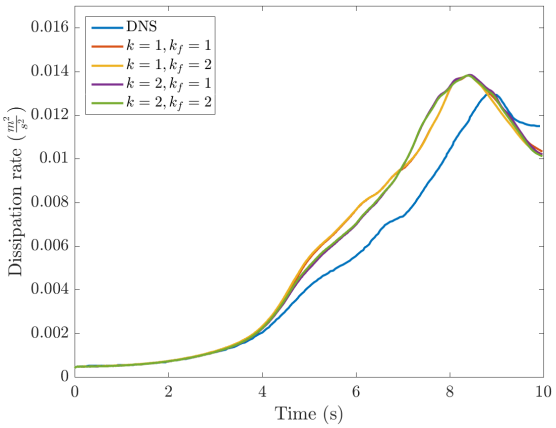

(b) Total dissipation rate. Dynamic RBEV model.

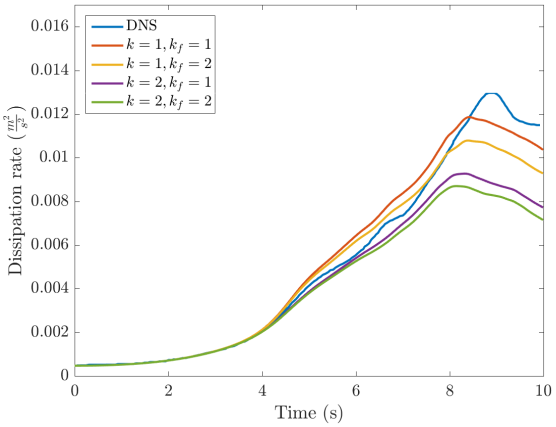

(c) Resolved dissipation rate. Dynamic VMS model.

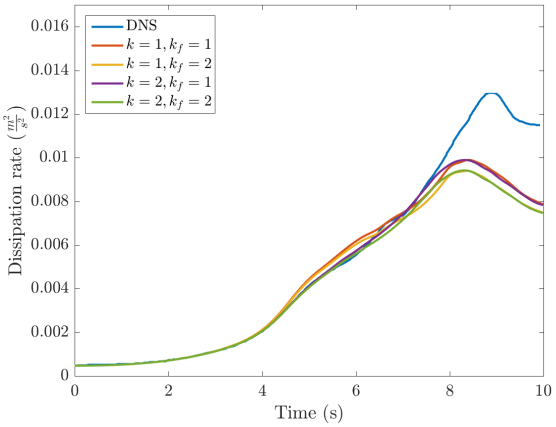

(d) Resolved dissipation rate. Dynamic RBEV model.

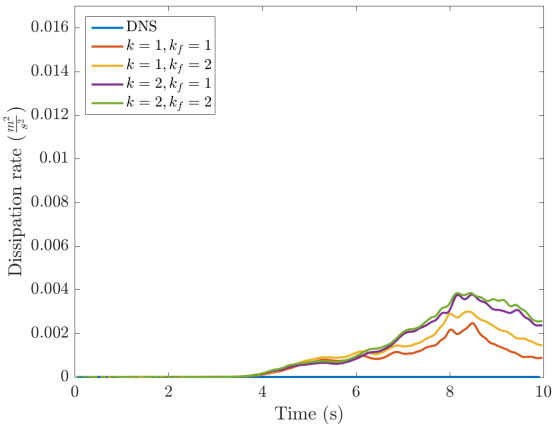

(e) Model dissipation rate. Dynamic VMS model.

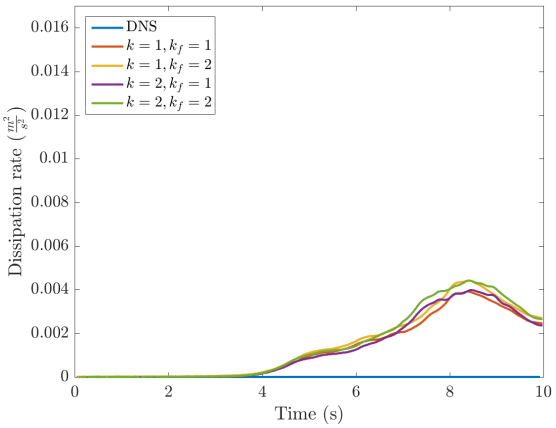

(f) Model dissipation rate. Dynamic RBEV model.

Figure 7.17: Time history of total, resolved, and model dissipation for simulation of Taylor-Green vortex under degree elevation with $h = \frac{\pi}{16}$.

Contours of $Q = 1$ colored by vorticity are plotted alongside the magnitude of the fine scale velocity for the dynamic VMS model in Fig. 7.18. Solutions at an early time ($t = 0.25$), an intermediate time ($t = 4.66$) and a late time shortly after the time of maximum dissipation ($t = 9.57$) are presented in order to provide a comparison of the character of the solutions during various phases of transition from laminar to turbulent flow. It is clear that the fine scales grow in amplitude as expected in regions where more small-scale turbulent structures develop and the fine scale velocities remain low in amplitude where only large-scale structures that can be resolved by the mesh are present.

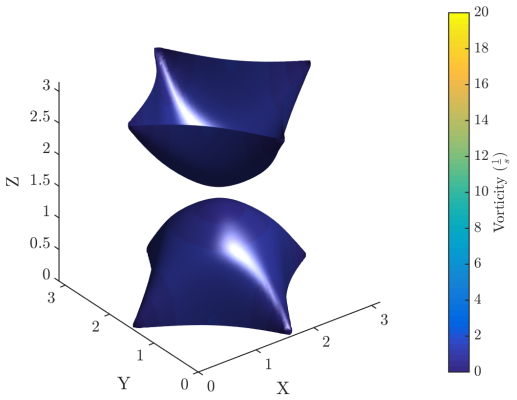

(a) Contours of $Q = 1$ at $t = 0.25$. Dynamic VMS model.

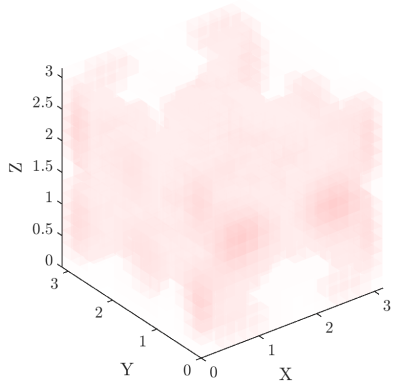

(b) Fine scales at $t = 0.25$. Dynamic VMS model.

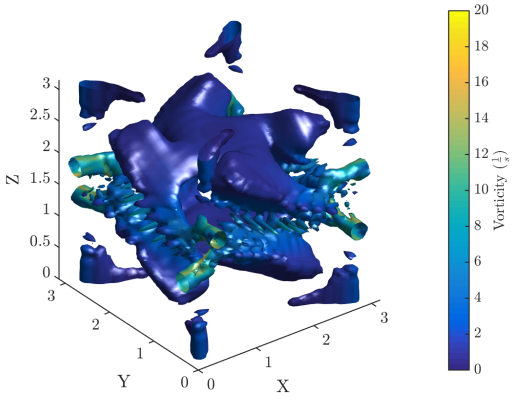

(c) Contours of $Q = 1$ at $t = 4.66$. Dynamic VMS model.

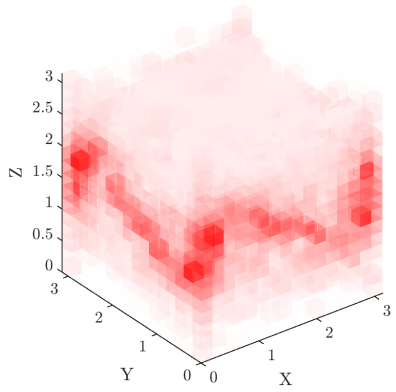

(d) Fine scales at $t = 4.66$. Dynamic VMS model.

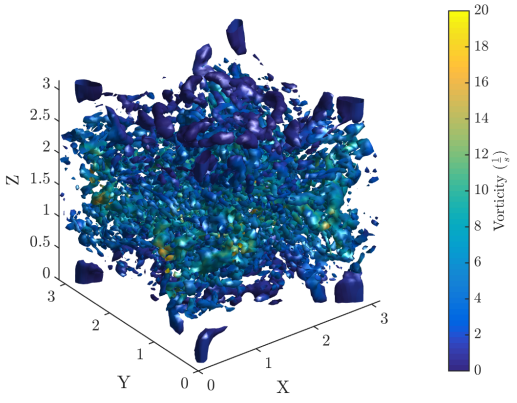

(e) Contours of $Q = 1$ at $t = 9.57$. Dynamic VMS model.

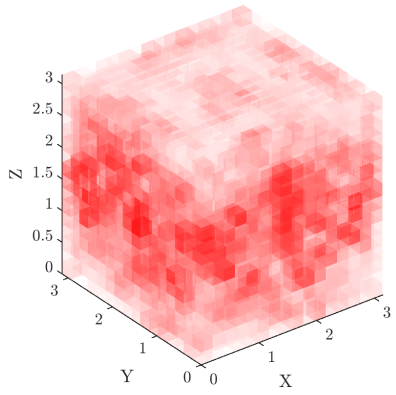

(f) Fine scales at $t = 9.57$. Dynamic VMS model.

Figure 7.18: Q-criterion contours colored by vorticity and magnitude of fine scale velocity for simulation of Taylor-Green votex with $k = 2$, $k_f = 1$, and $h = \frac{\pi}{16}$.

Up until now, the quasi-static residual-based models have been demonstrated to be ineffective as a result of the small time step used rendering τ_{qs} so small as to essentially "turn off" the fine scales in the model. In order to explore the possibility of eliminating the sensitivity of τ_{sq} to the time step, we now consider the quasi-static VMS model using τ_{qs} defined using the alternate formulation for τ_{uns} given by (5.12). The total dissipation rate for the quasi-static VMS model using both formulations of τ_{uns} is plotted in Fig. 7.19. Here, it is clear that the alternate formulation for τ_{uns} has the effect of bringing the total dissipation rate closer to the DNS.

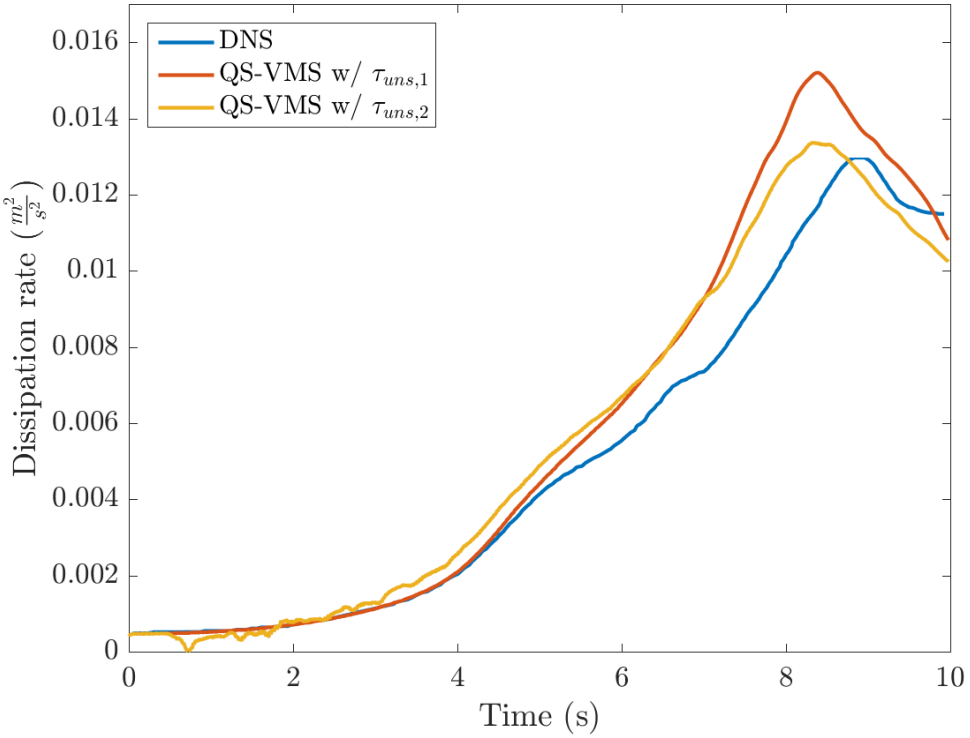

Figure 7.19: Time history of total dissipation rate for simulation of Taylor-Green vortex with $k = 2$, $k_f = 1$, and $h = \frac{\pi}{16}$. Comparison of quasi-static VMS model using τ_{uns} defined by (5.11) and by (5.12) with DNS [21].

By examining the resolved and model dissipation rates for the two formulations of τ_{uns} (presented in Fig. 7.20), it is clear that the alternate formulation for τ_{uns} is effective in activating the fine scales. The result is an increase in the model dissipation rate and a corresponding decrease in

the resolved dissipation rate.

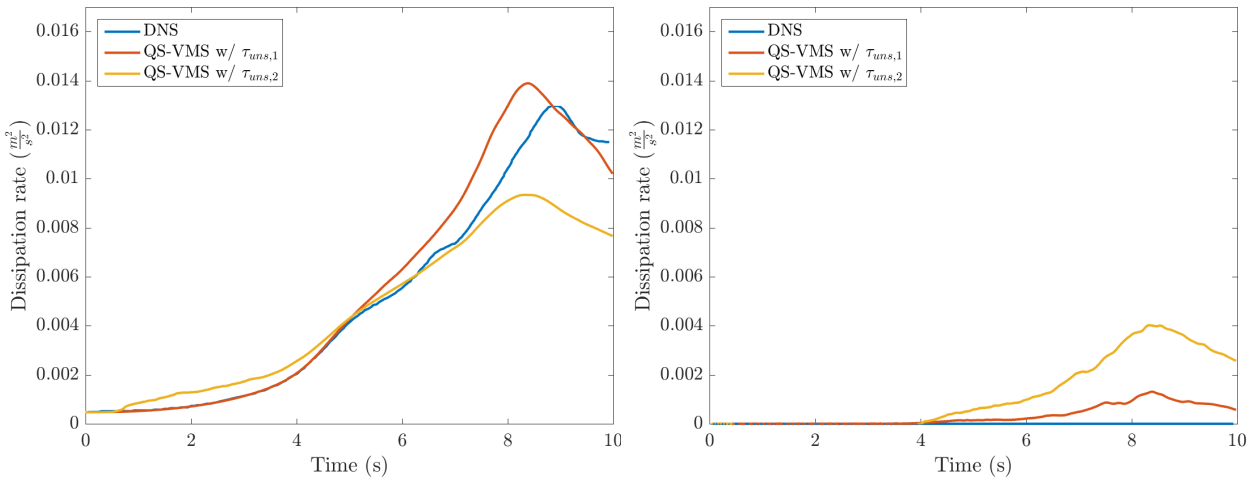

(a) Resolved dissipation

(b) Model dissipation

Figure 7.20: Time history of resolved and model dissipation for simulation of Taylor-Green vortex with $k = 2$, $k_f = 1$, and $h = \frac{\pi}{16}$. Comparison of quasi-static VMS model using τ_{uns} defined by (5.11) and by (5.12) with DNS [21].

In order to better evaluate the effectiveness of the quasi-static VMS model using the alternate formulation for τ_{uns}, we now compare the results to those of the dynamic VMS model. The total dissipation rate for the two models are compared in Fig. 7.21 and a comparison of the resolved and model dissipations rates are presented in Fig. 7.22. From these figures, it is clear that the quasi-static VMS model using the alternate formulation of τ_{uns} provides results similar to the dynamic VMS model.

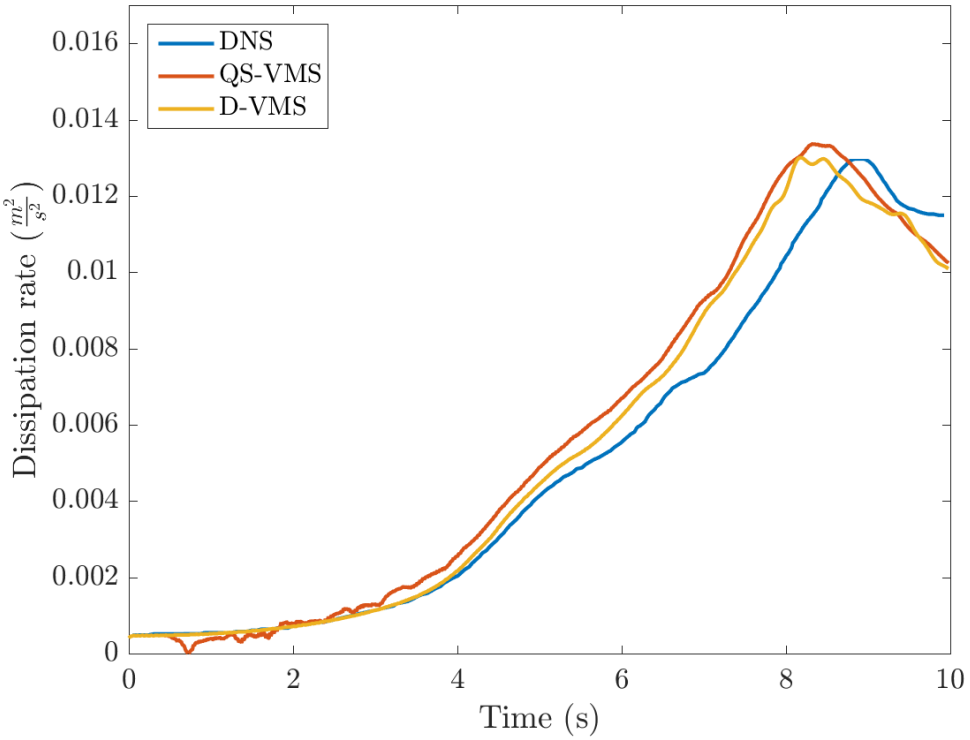

Figure 7.21: Time history of total dissipation rate for simulation of Taylor-Green vortex with $k = 2$, $k_f = 1$, and $h = \frac{\pi}{16}$. Comparison of dynamic VMS model (D-VMS) and quasi-static VMS model using τ_{uns} defined by (5.12) (QS-VMS) with DNS [21].

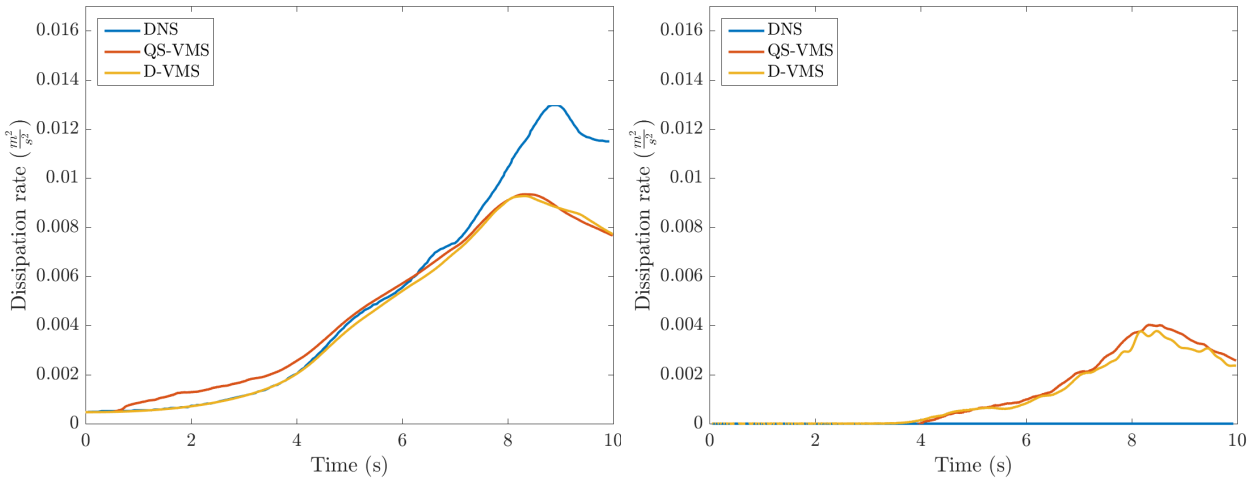

(a) Resolved dissipation

(b) Model dissipation

Figure 7.22: Time history of resolved and model dissipation for simulation of Taylor-Green vortex with $k = 2$, $k_f = 1$, and $h = \frac{\pi}{16}$. Comparison of dynamic VMS model (D-VMS) and quasi-static VMS model using τ_{uns} defined by (5.12) (QS-VMS) with DNS [21].

7.2.4 Turbulent Channel Flow at $Re_\tau = 395$

The next numerical example is turbulent channel flow at $Re_\tau = 395$, where Re_τ is the Reynolds number based on the friction velocity and the channel half width. Near the regions of the channel walls, the turbulence is damped as the velocity must necessarily go to zero at the wall. This provides a challenging flow for classical LES models since the velocity gradients do not go to zero at the wall. The simulation domain is rectangular with dimensions $2\pi \times 2 \times \frac{2\pi}{3}$ in the streamwise, wall-normal, and spanwise directions, respectively. In the streamwise and spanwise directions, periodic boundary conditions are applied, and at the wall ($y = \pm 1$), no-slip Dirichlet boundary conditions are imposed such that the no-penetration condition is strongly enforced and the no-tangential velocity condition is weakly enforced. Uniform grid spacing in the wall-normal direction is utilized (no grid stretching) so that the weak boundary condition acts as a variationally-consistent wall model [14]. The domain is illustrated in Fig. 7.23. The flow is driven by a constant pressure gradient, f_x, acting in the streamwise direction. In order to achieve a Reynolds number of $Re_\tau = 395$, the forcing is set to $f_x = 1.47200 \times 10^{-4}$ and the kinematic viscosity is set to $\nu = 3.372040 \times 10^{-3}$.

The solution is initialized with no mean streamwise flow and random fluctuations in all three velocity components. A time step of $\Delta t = 0.0125 h_x$ is used, where h_x is the grid spacing in the streamwise direction. The solution is advanced in time until the dissipation reaches equilibrium with the pressure forcing. After this time, the solution is advanced for 10 flow-through times and the velocity fields are sampled at the mesh knots every $0.5s$. The flow is solved using the VMS and RBEV models presented earlier and the statistics of interest are compared to the classical Smagorinsky, WALE, Vreman, and Sigma eddy viscosity models and to DNS data of Moser et al. using a semi-spectral simulation with $256 \times 193 \times 192\times$ modes [106].

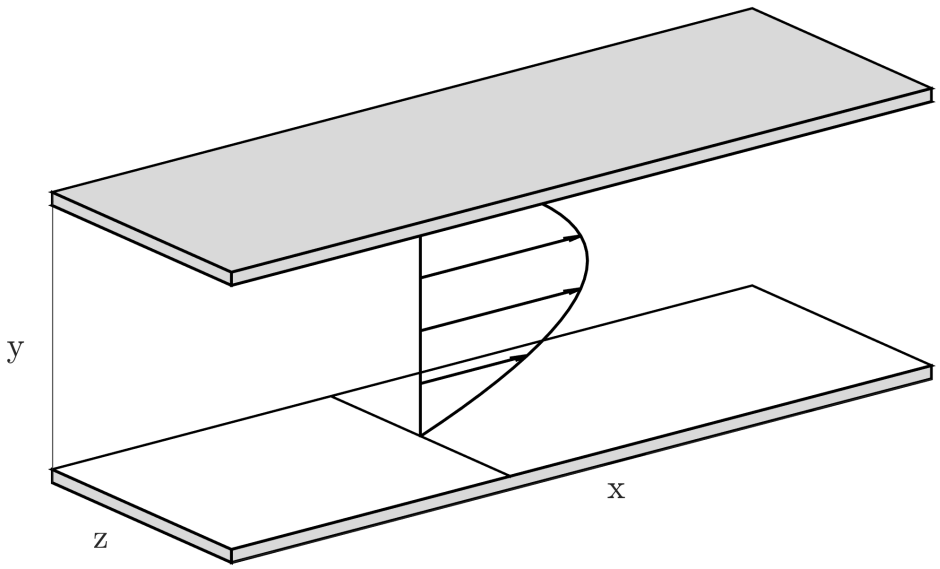

Figure 7.23: Setup for the turbulent channel flow problem.

The statistics of interest are the mean streamwise velocity, the root-mean-square velocity fluctuations, and the Q-criterion. Given a discrete sampling of the velocity field, the root-mean-square velocity fluctuation for a given velocity component u at a specified location in the field $\mathbf{x}$ is

calculated as

$$u_{rms}(\mathbf{x}) = \sqrt{\frac{1}{n}\sum_{n}\left(u(\mathbf{x},t) - \langle u(\mathbf{x})\rangle\right)^2}, \tag{7.12}$$

where n is the number of time samples of the velocity field. Statistics are obtained by averaging the sampled velocity fields in the streamwise and spanwise directions as well as time. All results are presented in non-dimensional wall units. The non-dimensional distance to the wall y^+ and the non-dimensional velocity u^+ are calculated as

$$y^+ = \frac{yu_\tau}{\nu}, \quad u^+ = \frac{u}{u_\tau}, \tag{7.13}$$

where u_τ is the friction velocity and is calculated as

$$u_\tau = \sqrt{\frac{\tau_w}{\rho}}, \tag{7.14}$$

where ρ is the fluid density and τ_w is the wall shear stress. When the no-slip boundary is strongly enforced, the wall shear stress is calculated in the usual way:

$$\tau_w = \mu\left(\frac{\partial u}{\partial y}\right)_{y=0}, \tag{7.15}$$

where μ is the dynamic viscosity of the fluid. With weakly-enforced no-slip boundary conditions, however, the *effective wall shear stress* is equal to the wall shear stress from (7.15) plus an additional wall shear stress term that accounts for the possible non-zero velocity at the wall [64]. The effective wall shear stress is then calculated as

$$\tau_{w,\text{eff}} = \tau_w + \mu\frac{C_I|u(y=0)|}{h}. \tag{7.16}$$

As was done for the Taylor-Green vortex, we first present a comparison of classical eddy-viscosity models. In Fig. 7.24, the mean streamwise velocity is presented for simulations with $k = 1$ and 32^3 unstretched elements. The no-model baseline case under-predicts the mean flow, but does a good job of capturing the right characteristics of the velocity profile (as indicated by a correct matching of the slope of u^+). None of the eddy-viscosity models predict the slope of u^+ as accurately as the baseline case, although the WALE, Vreman, and Sigma models are all

an improvement over the Smagorisnky model. The Vreman model is close in slope and value in the channel center, but is overly dissipative near the wall. In contrast, the WALE, Sigma, and Smagorinsky models are all overly dissipative in the channel center, with the Smagorinsky model the most dissipative.

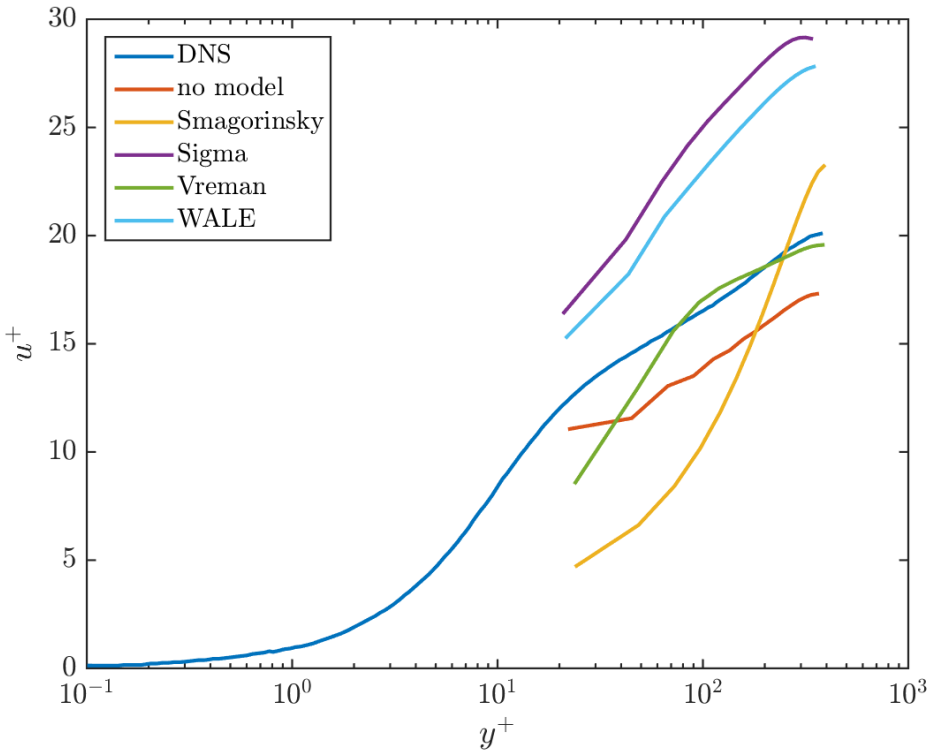

Figure 7.24: Mean streamwise velocity for simulation of turbulent channel flow with $k = 1$ and 32^3 unstretched elements. Comparison of subgrid-scale models (no model, Smagorinsky, Sigma, Vreman, WALE, with DNS [106].

Next we examine the root-mean-square velocity fluctuations. Figure 7.25 presents the root-mean-square velocity fluctuations for the streamwise, spanwise, and wall-normal velocity components[5] . Here, the no-model baseline case provides the closest prediction for all of the velocity fluctuations. The Vreman model once again is demonstrated to provide a reasonable match to the DNS data in the channel center, but is overly dissipative near the wall. The WALE and Sigma

[5] The DNS data for the root-mean-square velocity fluctuations is recreated here by digitizing the plots from [11]. There, the curves do not show the oscillations present in the curves presented here. These oscillations are merely an artifact of the digitzation process.

models show somewhat better agreement, but still do not provide a very good match. For these models, u_{rms} is over-predicted, v_{rms} is under-predicted, especially close to the wall, and w_{rms} does not have the proper character. The Smagorinsky model is excessively diffusive and obliterates almost all of the fluctuations in the flow.

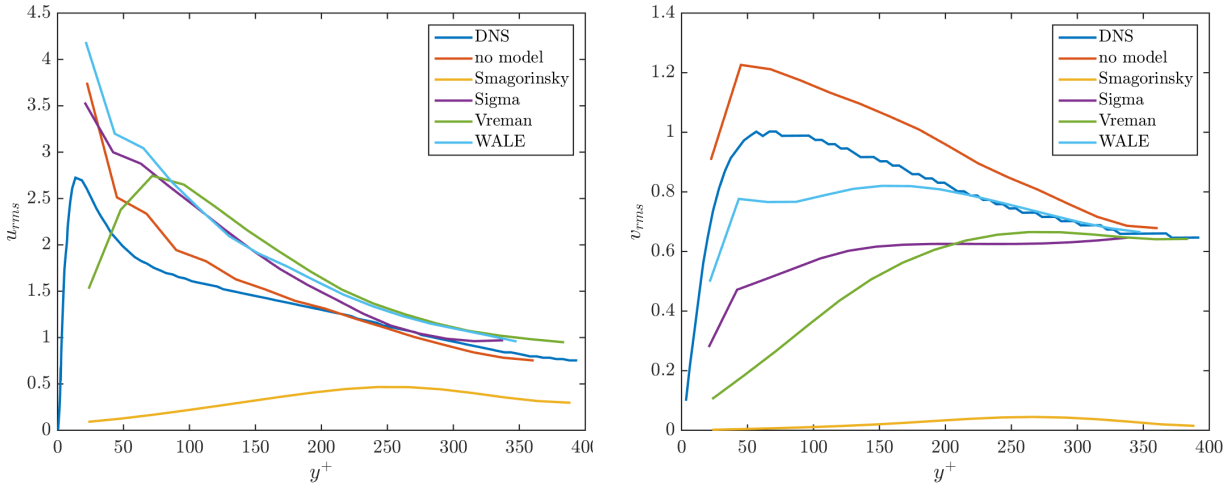

(a) u_{rms}

(b) v_{rms}

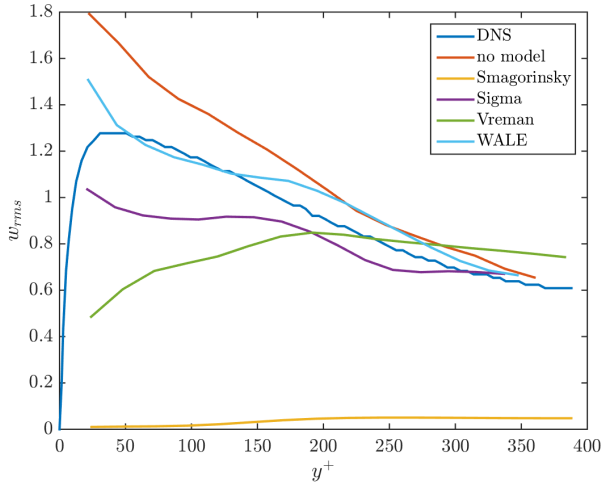

(c) w_{rms}

Figure 7.25: Root-mean-square velocity fluctuations for simulation of turbulent channel flow with $k = 1$ and 32^3 unstretched elements. Comparison of subgrid-scale models (no model, Smagorinsky, Sigma, Vreman, WALE, with DNS [106].

Contours for $Q = 0.1$ colored by streamwise velocity for the four LES models are presented

in Fig. 7.26. Similar characteristics that were observed from the root-mean-square velocity fluctuations are also present here. Namely, it is once again clear that the Smagorinsky model is overly dissipative, as the solution for this model damps out almost all of the vortical structures in the flow. The Vreman model is also overly dissipative, supporting only large-scale vortical structures. In contrast, the Sigma and WALE models support increasingly smaller turbulent structures. We also see that all of the models have a higher peak centerline velocity than $\langle u \rangle = 1.1$ as predicted by the DNS [106].

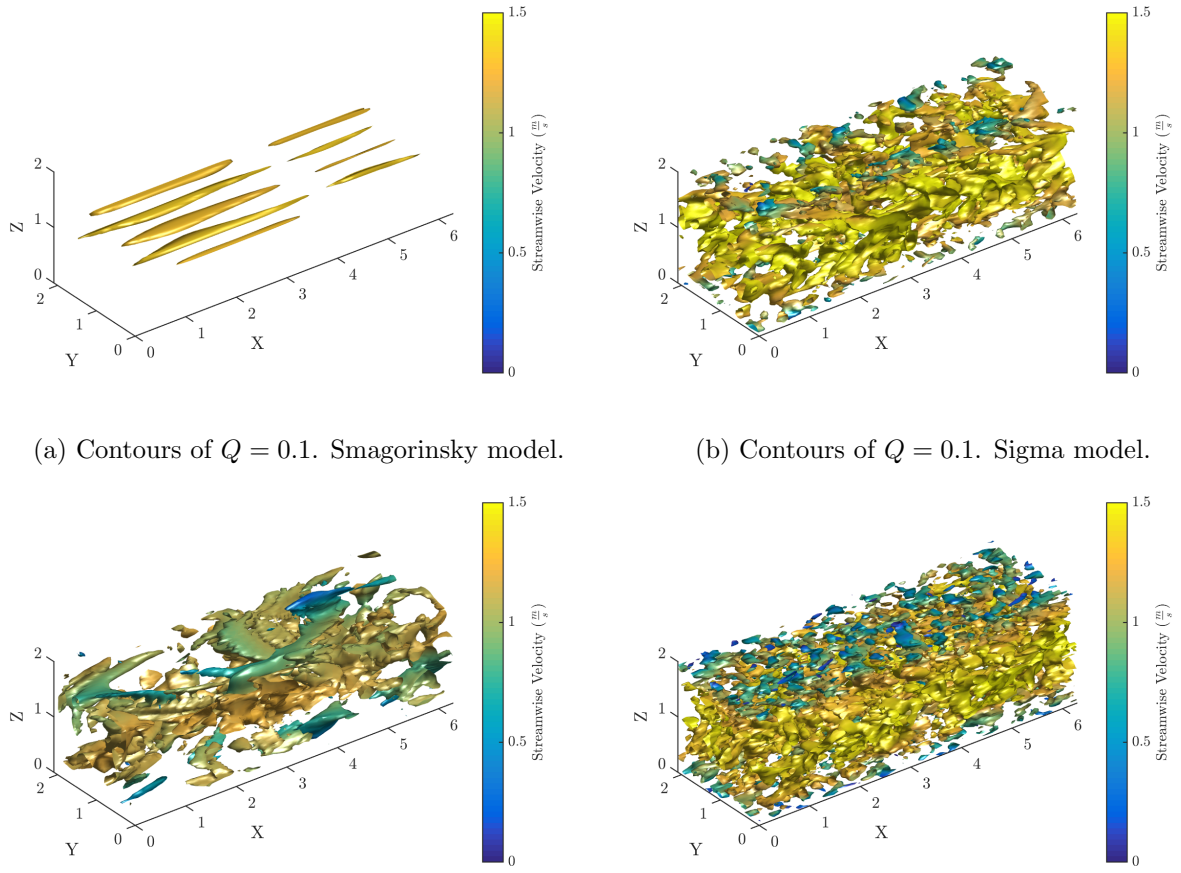

(a) Contours of $Q = 0.1$. Smagorinsky model.

(b) Contours of $Q = 0.1$. Sigma model.

(c) Contours of $Q = 0.1$. Vreman model.

(d) Contours of $Q = 0.1$. WALE model.

Figure 7.26: Q-criterion contours colored by streamwise velocity for simulation of turbulent channel flow with $k = 1$ and 32^3 unstretched elements. Comparison of subgrid-scale models (Smagorinsky, Sigma, Vreman, and WALE).

We now examine the performance of the residual-based models. First, the mean streamwise velocity is presented for simulations with $k = 1$, $k_f = 1$, and 16^3 unstretched elements in Fig. 7.27. Note that this mesh is even coarser than the mesh used to compare the eddy-viscosity models. Since none of the eddy-viscosity models considered provided very accurate results using 32^3 unstretched elements, it is certainly not expected that any of them will provide reasonable results for this mesh, which is even coarser. However, the results for the Smagorinsky model are plotted alongside those for the residual-based models in order to provide a point of reference. Also note that in the figure, the data for the no-model baseline case is obscured by the data for the quasi-static residual-based models. As has been the case for homogeneous turbulence and the Taylor-Green vortex, we see that the quasi-static models using the classical definition for τ_{qs} are rendered ineffective due to the small time step required to respect the CFL condition. The dynamic VMS model is shown once again to be ineffective for $k = 1$, whereas the dynamic RBEV model shows marked improvement over the baseline case. Although the dynamic RBEV model provides the most accurate approximation of the mean streamwise velocity in the center of the channel, closer to the wall it is overly dissipative and the entire velocity curve for this model has the wrong curvature. Considering how poor the classical eddy-viscosity models performed on the finer mesh, it is remarkable that the residual-based eddy-viscosity model performs so well for this problem.

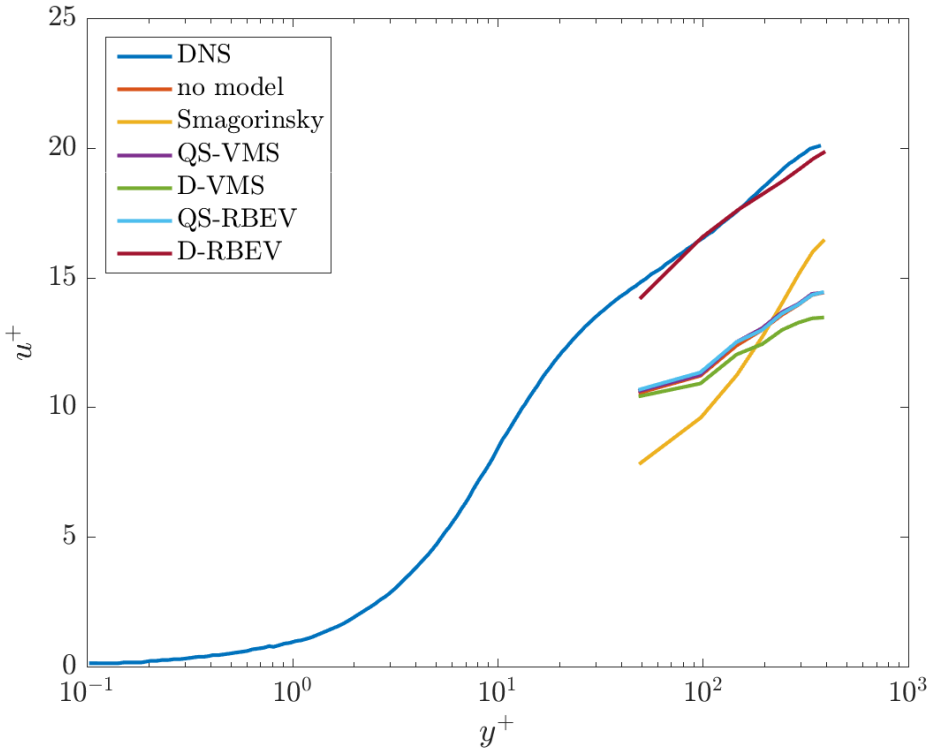

Figure 7.27: Mean streamwise velocity for simulation of turbulent channel flow with $k = 1$, $k_f = 1$, and 16^3 unstretched elements. Comparison of subgrid-scale models (no model, Smagorinsky LES, quasi-static VMS (QS-VMS), dynamic VMS (D-VMS), quasi-static RBEV (QS-RBEV), and dynamic RBEV (D-RBEV)) with DNS [106].

Next we examine the root-mean-square velocity fluctuations. Figure 7.28 presents the root-mean-square velocity fluctuations for the streamwise, spanwise, and wall-normal velocity components. From these figures, we observe that the dynamic RBEV model is overly dissipative, as the velocity fluctuations are reduced much too aggressively near the wall, and the overall shape of the fluctuation curves have the wrong character. The dynamic VMS model seems to show an improvement in the wall-normal velocity fluctuations near the middle of the channel, but the solution diverges closer to the wall. This suggests that, although the dynamic VMS model did not affect the mean-flow prediction much, it is activated to some degree in providing some subgrid-scale modeling.

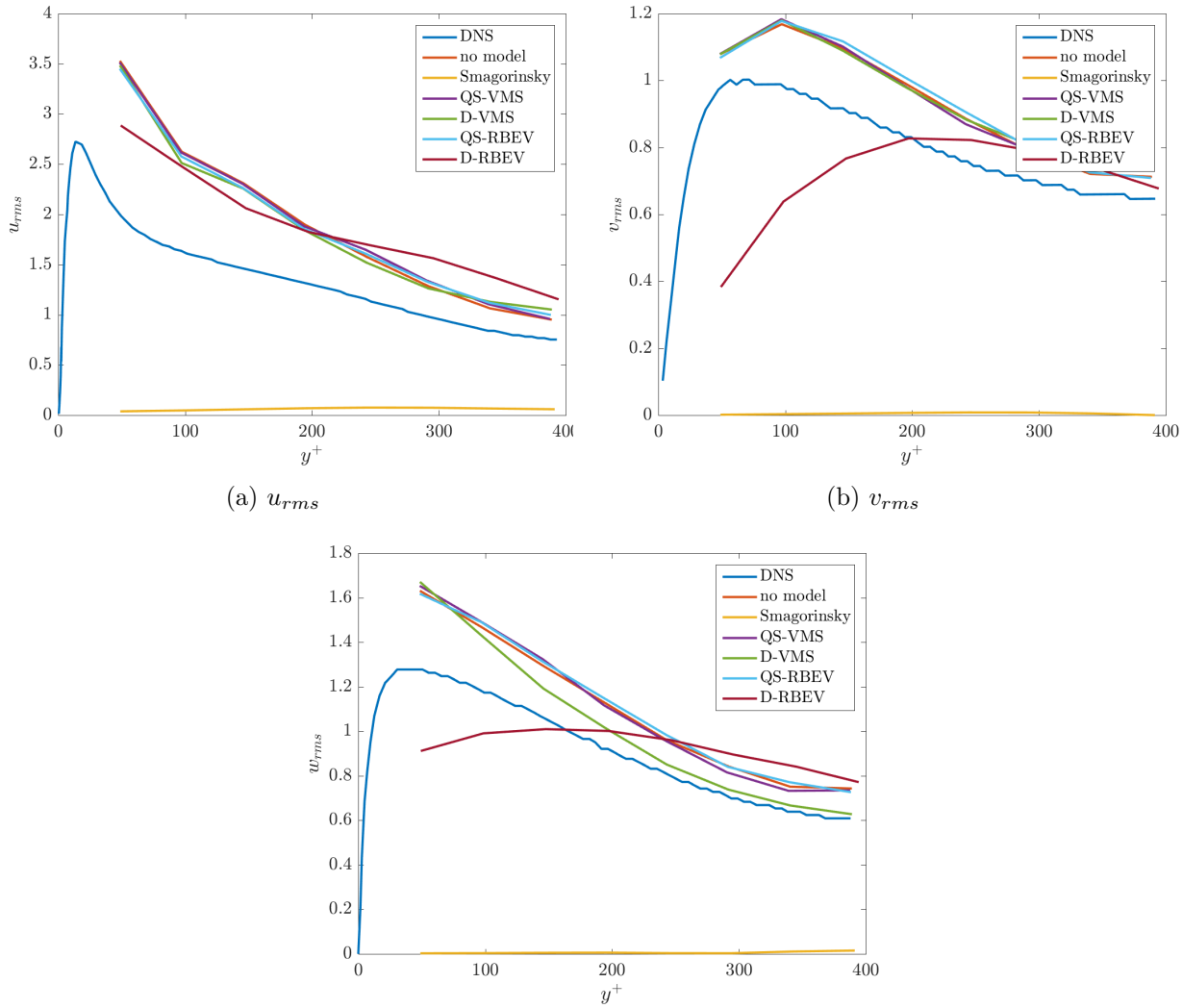

(a) u_{rms}

(b) v_{rms}

(c) w_{rms}

Figure 7.28: Root-mean-square velocity fluctuations for simulation of turbulent channel flow with $k = 1$, $k_f = 1$, and 16^3 unstretched elements. Comparison of subgrid-scale models (no model, Smagorinsky LES, quasi-static VMS (QS-VMS), dynamic VMS (D-VMS), quasi-static RBEV (QS-RBEV), and dynamic RBEV (D-RBEV)) with DNS [106].

Next, the mean streamwise velocity is presented for simulations with $k = 2$, $k_f = 1$, and 16^3 unstretched elements in Fig. 7.29. Compared to the $k = 1$ case, we observe that that no-model baseline case shows closer agreement to the DNS case. However, the quasi-static models are still rendered ineffective due to the small time step. Likewise, the Smagorinsky model does not show much, if any, improvement. In contrast, both of the dynamic residual-based models perform

admirably. Although the dynamic RBEV model provides the most accurate approximation of the mean streamwise velocity in the center of the channel, closer to the wall it is overly dissipative and the entire velocity curve for this model has the wrong curvature. In contrast, the dynamic VMS model has the correct slope and curvature except for very close to the wall, although it slightly under-predicts the mean velocity.

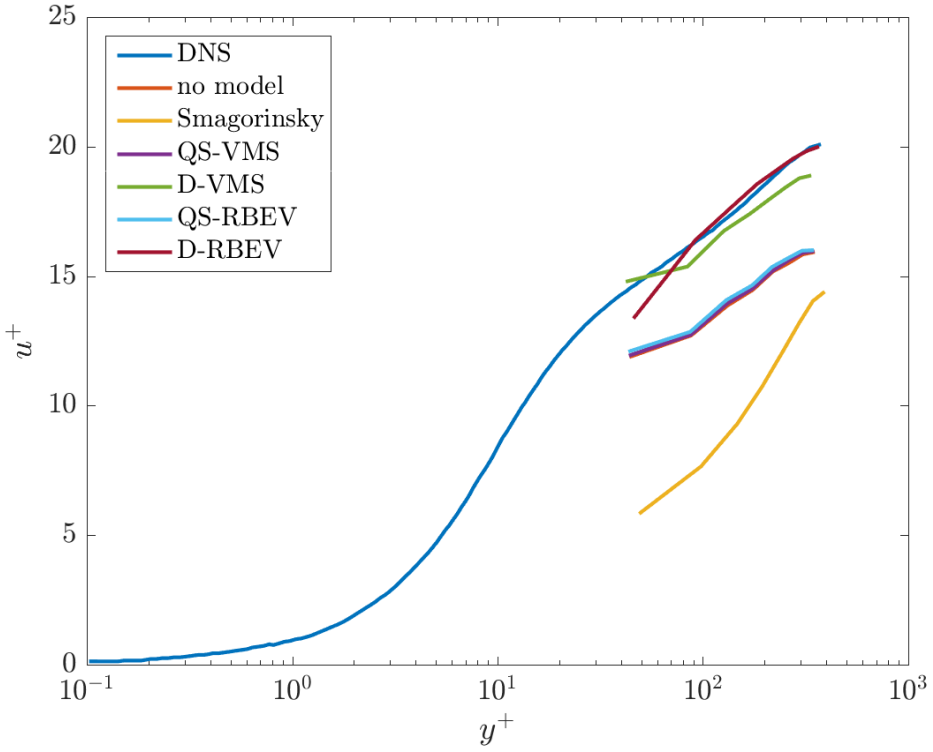

Figure 7.29: Mean streamwise velocity for simulation of turbulent channel flow with $k = 2$, $k_f = 1$, and 16^3 unstretched elements. Comparison of subgrid-scale models (no model, Smagorinsky LES, quasi-static VMS (QS-VMS), dynamic VMS (D-VMS), quasi-static RBEV (QS-RBEV), and dynamic RBEV (D-RBEV)) with DNS [106].

We now turn our attention to the root-mean-square velocity fluctuations. Figure 7.30 presents the root-mean-square velocity fluctuations for the streamwise, spanwise, and wall-normal velocity components. From these figures, we observe that the dynamic VMS model provides the best prediction of the streamwise and spanwise fluctuations. The dynamic RBEV model does not show much improvement in the prediction of the root-mean-square velocity fluctuations and continues

to be overly dissipative, especially close to the wall.

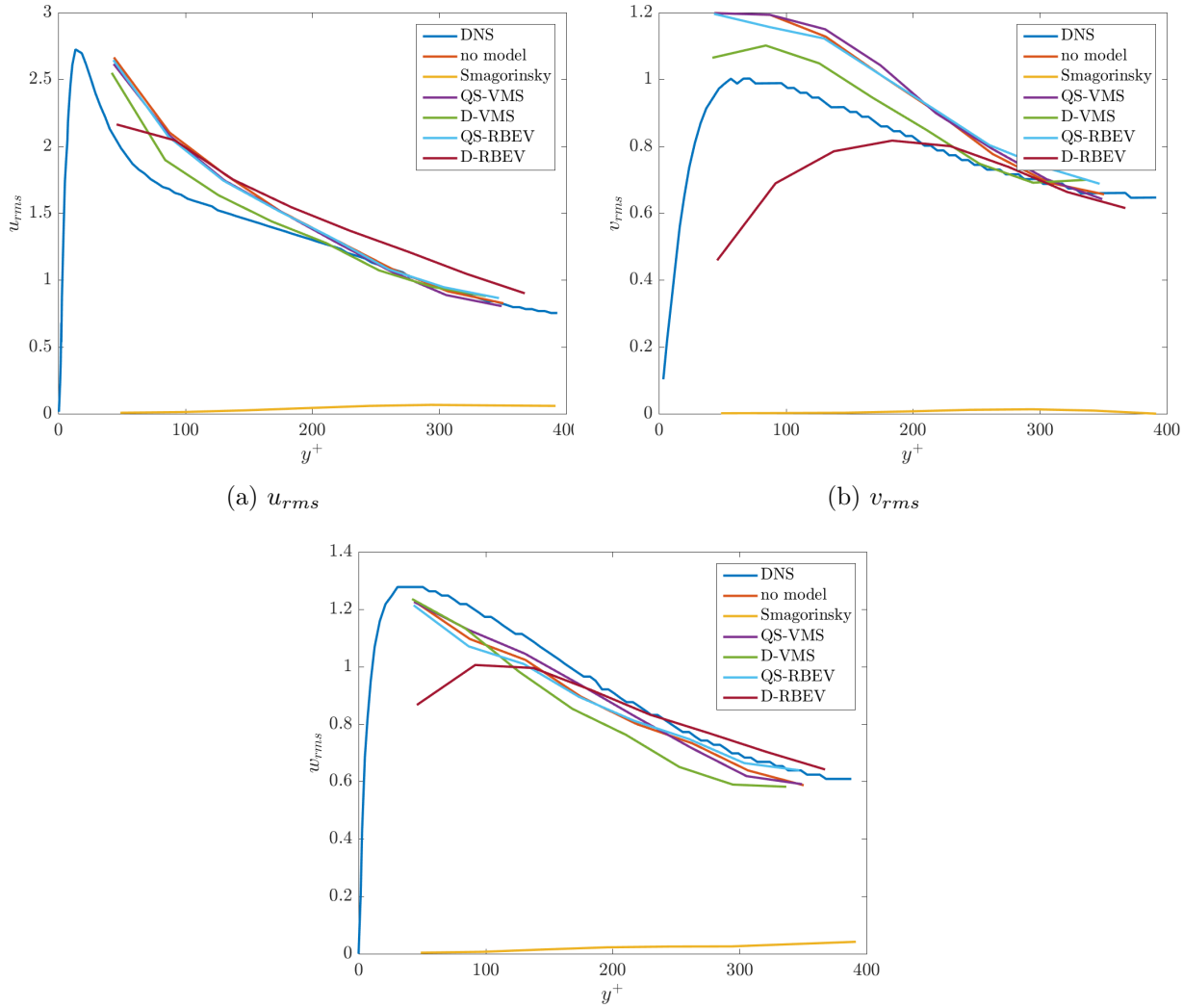

(a) u_{rms}

(b) v_{rms}

(c) w_{rms}

Figure 7.30: Root-mean-square velocity fluctuations for simulation of turbulent channel flow with $k = 2$, $k_f = 1$, and 16^3 unstretched elements. Comparison of subgrid-scale models (no model, Smagorinsky LES, quasi-static VMS (QS-VMS), dynamic VMS (D-VMS), quasi-static RBEV (QS-RBEV), and dynamic RBEV (D-RBEV)) with DNS [106].

Finally, contours for $Q = 0.1$ colored by streamwise velocity for the dynamic residual-based models are presented in Fig. 7.31. From the figure we see that the dynamic RBEV model is more dissiptative than the dynamic VMS model. We also observe that the dynamic VMS model has a lower peak centerline velocity and higher streamwise velocity gradient near the wall than the

dynamic RBEV model.

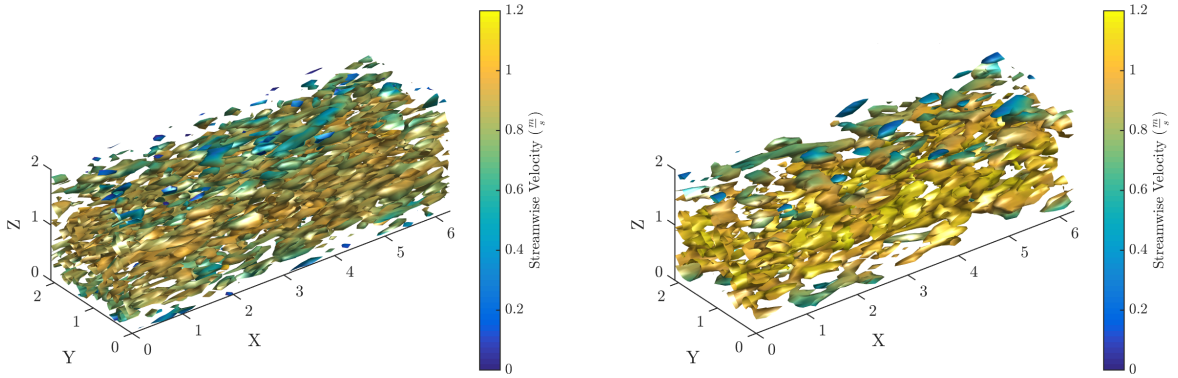

(a) Contours of $Q = 0.1$. Dynamic VMS model.

(b) Contours of $Q = 0.1$. Dynamic RBEV model.

Figure 7.31: Q-criterion contours colored by streamwise velocity for simulation of turbulent channel flow with $k = 2$, $k_f = 1$, and 16^3 unstretched elements. Comparison of subgrid-scale models (dynamic VMS and dynamic RBEV).

Chapter 8

Variational Multiscale Modeling with Discontinuous Subscales for Scalar Transport

Recall that the primary challenge in the variational multiscale method is determining the fine-scale component in terms of the coarse-scale component. Namely, the problem governing the behavior of the fine-scales is infinite-dimensional and nearly as difficult to solve as the original problem of interest. Consequently, in practice, the fine-scale problem must be approximated. The simplest approximations are based on algebraic models which express the fine-scale component in terms of an algebraic expression of the coarse-scale residual. In fact, classical stabilization approaches such as the streamline upwind Petrov Galerkin (SUPG) method [32], the Galerkin Least Squares (GLS) method [83, 84], and the Douglas-Wang method [55] may be viewed as algebraic models. While these models have proven to be quite successful in capturing the mean effect of the unresolved fine-scales on coarse-scale behavior, they typically are unable to account for higher-order moments of fine-scale components [38]. For example, it has been shown that algebraic models yield inaccurate representations of the subgrid stress tensor for turbulent incompressible flows [138].

A more accurate approximation of the fine-scale problem may be obtained using differential models wherein a model differential equation is solved for the fine-scale component. Perhaps the simplest differential model is the method of residual-free bubbles [24, 30, 25, 29, 122]. In this approach, the fine-scale solution space is approximated by the space of bubbles over each element. This yields an element-wise problem which can then be solved for the fine-scale solution field over

the element. It should be noted that these element-wise problems are still infinite-dimensional, so they must in turn be solved using a numerical method. Moreover, the fine-scale solution over each element exhibits multiscale features including the presence of boundary layers over element boundaries, so any proposed method must be able to account for such features. In prior work, researchers have turned to Galerkin's method to solve these problems with either (i) polynomial bubble functions and subgrid viscosity [27, 72] or (ii) piecewise polynomial functions over Shiskin submeshes [28, 26]. The first approach leads to a simple implementation, though the exact value of the required subgrid viscosity is problem-dependent and polynomial bubble functions are unable to accurately represent layers. The second approach leads to a more complex implementation, but it is better able to accurately capture boundary layer phenomena.

In this chapter, we examine an alternative approach, which we refer to henceforth as the method of discontinuous subscales, in which the fine-scales in the method of residual-free bubbles are approximated element-wise using a discontinuous Galerkin method [4]. As the discontinuous subscales are not required to meet the residual-free bubble boundary conditions in a strong sense, they are able to represent layers without resorting to a complicated submesh. Herein, we employ the symmetric interior penalty method to approximate diffusive fluxes and the upwind method to approximate advective fluxes on element boundaries in the element-wise fine-scale problems [3, 127]. This yields a stable methodology for transport and incompressible fluid flow even in the advective limit, though it should be mentioned that alternative discontinuous Galerkin methods may be employed [41, 42, 108]. To examine the effectiveness of the method of discontinuous subscales, we conduct a theoretical stability and convergence analysis of the method as applied to the scalar transport problem. Though the scalar transport problem is linear, it exhibits multiscale behavior in the form of boundary and internal layers and thus serves as a simplified vehicle to study the more complicated Navier-Stokes equations. Through our analysis, we find that the method of discontinuous subscales exhibits optimal convergence rates and is robust with respect to the Péclet number if the discontinuous subscale approximation space is sufficiently rich. We further explicitly identify the required richness in the context of affine finite elements. We finish this chapter by applying

the method to isogeometric discretizations [81] of steady and unsteady transport problems. Our motivation for examining isogeometric discretizations is that they exhibit improved stability and accuracy properties as compared with classical finite elements when applied to difficult transport [13], laminar and turbulent fluid flow [11, 61, 63, 132], and fluid-structure interaction [12] applications. Surprisingly, we find that the method of discontinuous subscales is stable and accurate in the advective limit even when lowest-order discontinuous subscale approximations are employed as a companion fine-scale model for an isogeometric discretization.

It should be mentioned that the method of discontinuous subscales is related to many other multiscale methods in the literature, and in particular, it is closely aligned with the discontinuous residual-free bubble method of Sangalli [123], the multiscale discontinuous Galerkin method of Hughes *et al.* [18, 34, 90], and the parameter-free variational multiscale method of Cottrell [48]. In the discontinuous residual-free bubble method, one also employs a discontinuous Galerkin method to approximate fine-scale solution behavior, though alternative boundary conditions are employed at the element boundaries. Moreover, no theoretical stability or convergence results exist for the method. In the multiscale discontinuous Galerkin method, variational multiscale analysis and an interscale transfer operator are employed to essentially reduce the computational complexity of a discontinuous Galerkin method to that of a continuous Galerkin method. While the multiscale discontinuous Galerkin method has a firm theoretical foundation, it is fairly difficult to implement, and it is not possible to employ different polynomial degrees for the coarse- and fine-scale components in the method. The parameter-free variational multiscale method is perhaps most closely aligned with the method of discontinuous subscales. In this approach, the discontinuous Galerkin method is employed to approximate the so-called fine-scale Green's function as opposed to the residual-free bubble directly. No theoretical stability or convergence results exist for the parameter-free variational multiscale method, though we believe that the analysis carried out here can be easily extended to this approach.

In this chapter we first provide an overview of the scalar transport problem, and then we introduce the method of residual-free bubbles and the method of discontinuous subscales. We next

present a theoretical analysis of the method of discontinuous subscales and we apply the method to a selection of steady and unsteady scalar transport problems. Finally, we present a pair of differential VMS models for the simulation of turbulent flows using divergence-conforming discretizations.

8.1 The Governing Equations of Scalar Transport

We limit our discussion in this chapter to the scalar transport problem, also referred to as the advection-diffusion or drift-diffusion problem in the literature. Though we consider both steady and unsteady transport throughout, we only state the strong and weak forms of the unsteady problem here as the corresponding forms for the steady problem are implied. With the above in mind, the strong form of the unsteady scalar transport problem reads as follows: Find $u : \overline{\Omega} \times [0, T) \to \mathbb{R}$ such that

$$\begin{aligned} \frac{\partial u}{\partial t} + \boldsymbol{a} \cdot \nabla u - \nabla \cdot (\kappa \nabla u) &= f \qquad \text{in } \Omega \times (0, T) \\ u &= g \qquad \text{on } \Gamma_D \times (0, T) \\ \kappa \nabla u \cdot \boldsymbol{n} &= h \qquad \text{on } \Gamma_N \times (0, T) \\ u &= u_0 \qquad \text{in } \Omega \times \{0\} \end{aligned} \tag{8.1}$$

where $\Omega \subset \mathbb{R}^d$ is the spatial domain of the problem, d is the number of spatial dimensions, Γ is the boundary of the domain, Γ_D is the Dirichlet part of the boundary, Γ_N is the Neumann part of the boundary, $\boldsymbol{n}$ is the unit outward boundary normal, u is the scalar being transported, $\boldsymbol{a} : \Omega \to \mathbb{R}^d$ is the advective velocity, $\kappa : \Omega \to \mathbb{R}_+$ is the diffusivity, $f : \Omega \to \mathbb{R}$ is the applied forcing, $g : \Gamma_D \to \mathbb{R}$ is the prescribed Dirichlet data, $h : \Gamma_N \to \mathbb{R}$ is the prescribed Neumann data, and $u_0 : \Omega \to \mathbb{R}$ is the prescribed initial data. In order for the scalar transport problem to be well-posed, we require that $\Gamma = \overline{\Gamma_D \cap \Gamma_N}$ and that $a_n = \boldsymbol{a} \cdot \boldsymbol{n} \geq 0$ on Γ_N. Note that to simplify our presentation, we have assumed that the advective velocity, diffusivity, forcing, and prescribed data are all independent of time. We further assume throughout that these quantities are all smooth and that the advective velocity is divergence-free.

To establish a weak form of the unsteady scalar transport problem, we must first define a

test space and set of trial functions. With this in mind, let

$$\mathcal{V} := \left\{ v \in H^1(\Omega) : v|_{\Gamma_D} = 0 \right\} \tag{8.2}$$

and

$$\mathcal{S} := \left\{ u \in H^1(\Omega) : u|_{\Gamma_D} = g \right\} \tag{8.3}$$

denote the time-instantaneous test space and set of trial functions, respectively, where $H^1(\Omega)$ is the Sobolev space of square-integrable functions with square-integrable derivatives. We further define the space-time set of trial functions as

$$\mathcal{S}_T := C([0,T];\mathcal{S}) \tag{8.4}$$

which is the set of continuous functions $u : [0,T] \to \mathcal{S}$ with:

$$\max_{0 \le t \le T} \|u(t)\|_{H^1(\Omega)} < \infty.$$

The weak form of the unsteady advection-diffusion problem then reads as follows: Find $u \in \mathcal{S}_T$ such that $u(\cdot,0) = u_0(\cdot)$ and:

$$\int_\Omega \frac{\partial u}{\partial t} v - \int_\Omega u \boldsymbol{a} \cdot \nabla v + \int_\Omega \kappa \nabla u \cdot \nabla v + \int_{\Gamma_N} a_n u v = \int_\Omega f v + \int_{\Gamma_N} h v \tag{8.5}$$

for all $v \in \mathcal{V}$ and almost every $t \in (0,T)$. It is well-known that the strong and weak forms of the advection-diffusion problem admit a unique solution that depends smoothly on the prescribed data [65].

To simplify our later discussion, we define the following operator:

$$\mathcal{L}_{AD} := \frac{\partial}{\partial t} + \boldsymbol{a} \cdot \nabla - \nabla \cdot \kappa \nabla \tag{8.6}$$

Note that $\mathcal{L}_{AD}$ is precisely the differential operator associated with the unsteady scalar transport problem.

8.2 Residual-Free Bubbles and the Method of Discontinuous Subscales

Now that we have defined the governing equations for scalar transport, we are ready to present the method of discontinuous subscales. Before doing so, however, we first review the residual-free bubble method.

8.2.1 Differential Fine-scale Modeling with Residual-free Bubbles

Assume that we have a decomposition of the spatial domain into a mesh of elements $\mathcal{M} = \{\Omega_K\}_{K=1}^{n_{el}}$ satisfying $\overline{\cup_K \Omega_K} = \overline{\Omega}$. We associate the decomposition with the finite element mesh in the finite element setting, and we associate the decomposition with the Bézier mesh in the context of isogeometric analysis [19]. In the residual-free bubble approach [24, 30, 25], we simply replace the fine-scale test space and set of trial functions in the variational multiscale method by the space of H^1-conforming bubbles over each element:

$$\mathcal{V}'_{bubble} = \mathcal{S}'_{bubble} := \left\{ v \in \mathcal{V} : v \in H_0^1(\Omega_K) \text{ for each element } \Omega_K \subset \Omega \right\}. \tag{8.7}$$

Since the functions in $\mathcal{V}'_{bubble}$ and $\mathcal{S}'_{bubble}$ are zero-valued on the boundary of each element, the fine-scale problem applies element-by-element. Thus, we have

$$\int_{\Omega_K} \frac{\partial \left(\bar{u} + u'\right)}{\partial t} v' - \int_{\Omega_K} \left(\bar{u} + u'\right) \boldsymbol{a} \cdot \nabla v' + \int_{\Omega_K} \kappa \nabla \left(\bar{u} + u'\right) \cdot \nabla v' = \int_{\Omega_K} f v' \tag{8.8}$$

for every $v' \in H_0^1(\Omega_K)$ and each element $\Omega_K \subset \Omega$. By integration-by-parts, the above implies the following element-wise problem:

$$\begin{aligned} \mathcal{L}_{AD} u'_K &= \text{Res}\left(\bar{u}\right) \text{ in } \Omega_K \\ u'_K &= 0 \text{ on } \Gamma_K, \end{aligned} \tag{8.9}$$

where $u'_K = u'|_{\Omega_K}$ and Γ_K is the boundary of the element Ω_K. Residual-free bubbles are defined as the functions u'_K which satisfy the above problem strongly.

Note that the governing equations for the residual-free bubbles are still infinite-dimensional. While these equations are easier to solve than the fine-scale problem associated with the variational

multiscale method, they are still nearly as difficult to solve as the original scalar transport problem. Thus, in practice, one must turn to a numerical method to approximate the residual-free bubbles. Additionally, the residual-free bubbles exhibit multiscale behavior such as boundary layers, so any method must be able to account for such behavior. As previously mentioned, a number of approaches have been proposed in prior work based on the continuous Galerkin method. While these approaches have been shown to be closely related to the SUPG method, they exhibit complex features such as problem-dependent subgrid diffusivity [27] or advection-aligned Shishkin subgrid meshes [26] in order to overcome the advective instabilities associated with the continuous Galerkin method and to account for the multiscale features in the residual-free bubbles. We instead turn to another means of approximating the residual-free bubbles in the next subsection.

8.2.2 Approximation of the Residual-free Bubbles with Discontinuous Subscales

Recall that the residual-free bubbles exhibit the same sorts of multiscale phenomena as the solution to the scalar transport problem, including boundary layers along element boundaries. This inspires us to weaken the enforcement of element-wise homogeneous Dirichlet boundary conditions via a discontinuous Galerkin methodology. We refer to this approach as the method of discontinuous subscales as the corresponding residual-free bubble approximations are discontinuous between adjacent elements.

To set the stage, we need to first define a finite-dimensional test space and set of trial functions for the discontinuous subscales. As with the method of residual-free bubbles, these two sets collapse to the same space, and we simply require that the test and trial functions are H^1-conforming over each element. We denote the discontinuous subscale approximation space over element Ω_K as $\mathcal{V}'_{disc,K} = \mathcal{S}'_{disc,K} \subset H^1(\Omega_K)$ and the approximation space over the entire domain as

$$\mathcal{V}'_{disc} = \mathcal{S}'_{disc} := \left\{ v \in L^2(\Omega) : v|_{\Omega_K} \in \mathcal{V}'_{disc,K} \text{ for every } \Omega_K \in \mathcal{M} \right\}. \tag{8.10}$$

There are many potential candidates for the discontinuous subscale approximation space, and we consider polynomial basis functions of a particular degree later in this paper.

It remains now to discretize the governing residual-free bubble equation using our discontinuous subscale approximation space. We turn to a discontinuous Galerkin method in which the symmetric interior penalty method is employed to approximate the diffusive fluxes on element boundaries and the upwind method is employed to approximate the advective fluxes on element boundaries [127]. This approach is known to be stable even in the advective limit, and it results in the following element-wise problem

$$\begin{aligned} &\int_{\Omega_K} \frac{\partial u'}{\partial t} v' - \int_{\Omega_K} u' \boldsymbol{a} \cdot \nabla v' + \int_{\Omega_K} \kappa \nabla u' \cdot \nabla v' \\ &+ \int_{\Gamma_K} u' v' a_n^+ - \int_{\Gamma_K} \kappa \nabla u' \cdot \boldsymbol{n} v' - \int_{\Gamma_K} u' \kappa \nabla v' \cdot \boldsymbol{n} + \int_{\Gamma_K} \frac{C_{pen} \kappa}{h_K} u' v' = \int_{\Omega_K} \mathrm{Res}\left(\bar{u}\right) v' \end{aligned} \tag{8.11}$$

for every $v' \in \mathcal{V}'_{disc,K}$ where $a_n^+ = (\boldsymbol{a} \cdot \boldsymbol{n})^+ = \max\{\boldsymbol{a} \cdot \boldsymbol{n}, 0\}$. Above, h_K indicates a measure of the size of element Ω_K (e.g., h_K could be the diameter of the smallest ball encompassing the element), and $C_{pen} > 0$ is a stabilization parameter that must be specifically chosen such that the resulting methodology is stable. It should be noted that the exact value of the stabilization parameter should depend on both the coarse-scale and discontinuous subscale approximation spaces, and we discuss how to choose the stabilization parameter in the next section.

At this juncture, we have arrived at a fully specified method. However, we should highlight a few modifications that yield a more robust and streamlined methodology. First of all, we have found that the optional inclusion of an artificial diffusivity κ_{art} in the subscale governing equation generally improves stability as well as the conditioning of the resulting linear system. Guidelines for how to choose the artificial diffusivity are provided in the next section. Second of all, we have found that neglecting the influence of the subscale solution field in the unsteady and diffusive terms appearing in the coarse-scale governing equation also improves stability. It should be mentioned that these terms also vanish if the projection operator is specially chosen as observed in previous works [89]. Finally, one may choose to ignore the time-history of the subscale solution field by removing the time-derivative of the subscales appearing in the subscale governing equation. This approach, which we refer to as the quasi-static model, leads to a simpler implementation than the corrresponding dynamic model. However, both the dynamic and quasi-static models exhibit nearly

the same computational cost. It should be noted that the dynamic and quasi-static labels are inspired by the Dynamic Subscales (DSS) and Quasi-Static Subscales (QSS) methods of Codina *et al.* [43], though the DSS and QSS methods do not attempt to solve for the residual-free bubbles.

Collecting all of our governing equations together, we obtain the following:

Coarse-scale Governing Equation:

$$\int_\Omega \frac{\partial \bar{u}}{\partial t}\bar{v} - \int_\Omega \left(\bar{u}+u'\right)\boldsymbol{a}\cdot\nabla\bar{v} + \int_\Omega \kappa\nabla\bar{u}\cdot\nabla\bar{v} + \int_{\Gamma_N} a_n\bar{u}\bar{v} = \int_\Omega f\bar{v} + \int_{\Gamma_N} h\bar{v} \qquad \text{for all } \bar{v}\in\bar{\mathcal{V}} \tag{8.12}$$

Dynamic Discontinuous Subscale Model:

$$\int_{\Omega_K} \frac{\partial u'}{\partial t}v' - \int_{\Omega_K} u'\boldsymbol{a}\cdot\nabla v' + \int_{\Omega_K}\left(\kappa+\kappa_{art}\right)\nabla u'\cdot\nabla v' + \int_{\Gamma_K} u'v'a_n^+ - \int_{\Gamma_K}\kappa\nabla u'\cdot\boldsymbol{n}v' - \int_{\Gamma_K} u'\kappa\nabla v'\cdot\boldsymbol{n} + \int_{\Gamma_K}\frac{C_{pen}\kappa}{h_K}u'v' = \int_{\Omega_K}\mathrm{Res}\left(\bar{u}\right)v' \qquad \text{for all } v'\in\mathcal{V}'_{disc,K} \text{ and } \Omega_K\in\mathcal{M} \tag{8.13}$$

Quasi-static Discontinuous Subscale Model:

$$\int_{\Omega_K} u'\boldsymbol{a}\cdot\nabla v' + \int_{\Omega_K}\left(\kappa+\kappa_{art}\right)\nabla u'\cdot\nabla v'\cdot\boldsymbol{n} + \int_{\Gamma_K} u'v'a_n^+ - \int_{\Gamma_K}\kappa\nabla u'\cdot\boldsymbol{n}v' - \int_{\Gamma_K} u'\kappa\nabla v'\cdot\boldsymbol{n} + \int_{\Gamma_K}\frac{C_{pen}\kappa}{h_K}u'v' = \int_{\Omega_K}\mathrm{Res}\left(\bar{u}\right)v' \qquad \text{for all } v'\in\mathcal{V}'_{disc,K} \text{ and } \Omega_K\in\mathcal{M} \tag{8.14}$$

The governing semi-discrete equations may be discretized in time using any particular time-integrator of interest, yielding a linear system to be solved at each time-step. Note that in both the dynamic and quasi-static discontinuous subscale models, the subscale solution fields on each element are decoupled. Consequently, an element-wise static condensation procedure can be employed to remove the subscale degrees-of-freedom from the discrete system at each time-step, yielding a reduced linear system for the coarse-scale solution field [140]. Moreover, as the subscale solution fields on each element are decoupled, this reduced linear system has exactly the same sparsity pattern as that associated with either Galerkin's method or the SUPG method.

8.3 Analysis of the Method of Discontinuous Subscales

Now that we have presented our methodology for solving the scalar transport problem, we establish stability and convergence results. To simplify exposition, we deal solely with the steady advection-diffusion problem with homogeneous Dirichlet boundary conditions. With this in mind, let us define the group vector space $\boldsymbol{\mathcal{V}}^h = \overline{\mathcal{V}} \times \mathcal{V}'_{disc}$, the group variables $\mathbf{U}^h = (\bar{u}, u') \in \boldsymbol{\mathcal{V}}^h$ and $\mathbf{V}^h = (\bar{v}, v') \in \boldsymbol{\mathcal{V}}^h$, the group bilinear form

$$\mathbf{B}\left(\mathbf{U}^h, \mathbf{V}^h\right) := \bar{B}(\bar{u}, \bar{v}) + \bar{C}(u', \bar{v}) + C'(\bar{u}, v') + B'(u', v') \tag{8.15}$$

where

$$\begin{aligned}
\bar{B}(\bar{u}, \bar{v}) &:= -\int_\Omega \bar{u}\boldsymbol{a} \cdot \nabla \bar{v} + \int_\Omega \kappa \nabla \bar{u} \cdot \nabla \bar{v} \\
\bar{C}(u', \bar{v}) &:= -\sum_{K=1}^{n_{el}} \int_{\Omega_K} u' \boldsymbol{a} \cdot \nabla \bar{v} \\
C'(\bar{u}, v') &:= \sum_{K=1}^{n_{el}} \int_{\Omega_K} v' \left(\boldsymbol{a} \cdot \nabla \bar{u} - \nabla \cdot (\kappa \nabla \bar{u})\right) \\
B'(u', v') &:= \sum_{K=1}^{n_{el}} \left(-\int_{\Omega_K} u' \boldsymbol{a} \cdot \nabla v' + \int_{\Omega_K} \left(\kappa + \kappa_{art}\right) \nabla u' \cdot \nabla v' + \int_{\Gamma_K} u' v' a_n^+ \right. \\
&\quad \left. - \int_{\Gamma_K} \kappa \nabla u' \cdot \boldsymbol{n} v' - \int_{\Gamma_K} u' \kappa \nabla v' \cdot \boldsymbol{n} + \int_{\Gamma_K} \frac{C_{pen}\kappa}{h_K} u' v' \right),
\end{aligned}$$

and the group linear form

$$\mathbf{L}\left(\mathbf{W}^h\right) := \bar{L}(\bar{v}) + L'(v') \tag{8.16}$$

where

$$\begin{aligned}
\bar{L}(\bar{v}) &:= \int_\Omega f \bar{v} \\
L'(v') &:= \int_\Omega f v'.
\end{aligned}$$

With the above notation established, our discrete problem is as follows: Find $\mathbf{U}^h \in \boldsymbol{\mathcal{V}}^h$ such that for all $\mathbf{V}^h \in \boldsymbol{\mathcal{V}}^h$

$$\mathbf{B}\left(\mathbf{U}^h, \mathbf{V}^h\right) = \mathbf{L}\left(\mathbf{V}^h\right). \tag{8.17}$$

Throughout, we assume that $\overline{\mathcal{V}}$ is a finite-dimensional space of continuous piecewise polynomial or tensor-product polynomial functions of degree k defined over a given mesh $\mathcal{M}$ of simplices (triangles and tetrahedra) or parallelotopes (quadrilaterals and hexahedra). We also assume that $\mathcal{V}'_{disc}$ is a finite dimensional-space of discontinuous piecewise polynomial or tensor-product polynomials of degree k_f defined over the same mesh $\mathcal{M}$. While our analysis only strictly covers the setting of affinely-mapped finite elements, it easily extends to the more general settings of curvilinear finite elements and isogeometric analysis.

Throughout this section, we make use of the classical Lebesgue spaces $L^q(D)$ endowed with the norm $\|\cdot\|_{L^q(D)}$ where $1 \leq q \leq \infty$ and $D \subset \mathbb{R}^d$ is a generic open domain for integer $d \geq 1$. We will also utilize the Sobolev spaces $W^{k,q}(D)$ for k a non-negative integer and $1 \leq q \leq \infty$, endowed with the norm

$$\|u\|_{k,q,D} := \left(\sum_{\alpha_1+\ldots+\alpha_d \leq k} \left\| \frac{\partial^{\alpha_1}}{\partial x_1^{\alpha_1}} \cdots \frac{\partial^{\alpha_d}}{\partial x_d^{\alpha_d}} u \right\|^2_{L^q(D)} \right)^{1/2} \tag{8.18}$$

and semi-norm

$$|u|_{k,q,D} := \left(\sum_{\alpha_1+\ldots+\alpha_d = k} \left\| \frac{\partial^{\alpha_1}}{\partial x_1^{\alpha_1}} \cdots \frac{\partial^{\alpha_d}}{\partial x_d^{\alpha_d}} u \right\|^2_{L^q(D)} \right)^{1/2}. \tag{8.19}$$

In the setting when $q = 2$, the Sobolev spaces $W^{k,q}(D)$ become $H^k(D)$ and we use the simplified notation $\|\cdot\|_{k,D} \equiv \|\cdot\|_{k,2,D}$ and $|\cdot|_{k,D} \equiv |\cdot|_{k,2,D}$. Sobolev norms are defined over boundaries of open domains in an analogous manner.

To proceed forward, we must make certain assumptions regarding the form of the penalty constant C_{pen} and the artificial diffusivity κ_{art}. In particular, we assume the following:

Assumption 1: *The penalty constant C_{pen} satisfies $C_{pen} \geq 8C_{trace}$ where $C_{trace} > 0$ is a sufficiently large positive constant such that*

$$\|\bar{v}\|^2_{0,\Gamma_K} \leq \frac{C_{trace}}{h_K} \|\bar{v}\|^2_{0,\Omega_K} \quad \text{and} \quad \|\nabla \bar{v} \cdot \boldsymbol{n}\|^2_{0,\Gamma_K} \leq \frac{C_{trace}}{h_K} |\bar{v}|^2_{1,\Omega_K}$$
$$\|v'\|^2_{0,\Gamma_K} \leq \frac{C_{trace}}{h_K} \|v'\|^2_{0,\Omega_K} \quad \text{and} \quad \|\nabla v' \cdot \boldsymbol{n}\|^2_{0,\Gamma_K} \leq \frac{C_{trace}}{h_K} |v'|^2_{1,\Omega_K}$$

for every $\bar{v} \in \overline{\mathcal{V}}$, $v' \in \mathcal{V}'_{disc}$, and element $\Omega_K \in \mathcal{M}$.

Assumption 2: *The artificial diffusivity* κ_{art} *takes the form*

$$\kappa_{art} = C_{art}\left(\max\left\{\frac{\|\boldsymbol{a}\|_{0,\infty,\Omega_K}}{h_K}, \frac{C_{inv}\kappa}{h_K^2}\right\}\right)^{-1}\|\boldsymbol{a}\|^2_{\infty,\Omega_K}$$

where $C_{art} \geq 0$ *is an arbitrary non-negative constant and* $C_{inv} > 0$ *is a sufficiently large positive constant such that*

$$|\bar{v}|^2_{1,\Omega_K} \leq \frac{C_{inv}}{h_K^2}\|\bar{v}\|^2_{0,\Omega_K} \quad \text{and} \quad \|\Delta\bar{v}\|^2_{0,\Omega_K} \leq \frac{C_{inv}}{h_K^2}|\bar{v}|^2_{1,\Omega_K}$$
$$|v'|^2_{1,\Omega_K} \leq \frac{C_{inv}}{h_K^2}\|v'\|^2_{0,\Omega_K} \quad \text{and} \quad \|\Delta v'\|^2_{0,\Omega_K} \leq \frac{C_{inv}}{h_K^2}|v'|^2_{1,\Omega_K}$$

for every $\bar{v} \in \overline{\mathcal{V}}$, $v' \in \mathcal{V}'_{disc}$, *and element* $\Omega_K \in \mathcal{M}$.

One can readily find the trace and inverse constants associated with Assumptions 1 and 2 by solving element-wise eigenproblems. Alternatively, explicit bounds for these constants are available both in the setting of finite elements and isogeometric analysis [13, 60, 74, 139].

The following result shows that the group bilinear form is coercive, and hence the group variable solution is unique.

Theorem 8.3.1 The coercivity result

$$\mathbf{B}(\mathbf{V}^h, \mathbf{V}^h) \geq \frac{1}{4}\left(\kappa|\bar{v}|^2_{1,\Omega} + \sum_{K=1}^{n_{el}}\left(\left(\kappa + \kappa_{art}\right)|v'|^2_{1,\Omega_K} + \frac{C_{pen}\kappa}{h_K}\|v'\|^2_{0,\Gamma_K} + \|a_n^{1/2}v'\|^2_{0,\Gamma_K}\right)\right)$$

holds for all $\mathbf{V}^h \in \boldsymbol{\mathcal{V}}^h$ provided Assumption 1 is satisfied.

Proof For the coarse-scale bilinear form, we evaluate

$$\begin{aligned}
\bar{B}(\bar{v}, \bar{v}) &= -\int_\Omega \bar{v}\boldsymbol{a}\cdot\nabla\bar{v} + \int_\Omega \kappa\nabla\bar{v}\cdot\nabla\bar{v} \\
&= -\int_\Omega \frac{1}{2}\nabla\cdot\left(\boldsymbol{a}\bar{v}^2\right) + \kappa|\bar{v}|^2_{1,\Omega} \qquad \text{(by the product rule)} \\
&= \kappa|\bar{v}|^2_{1,\Omega}. \qquad \text{(by the divergence theorem)} \qquad (8.20)
\end{aligned}$$

Similarly, for the fine-scale bilinear form, we evaluate

$$\begin{aligned} B'(v',v') &= \sum_{K=1}^{n_{el}} \Bigg(-\int_{\Omega_K} v'\boldsymbol{a}\cdot\nabla v' + \int_{\Omega_K} (\kappa+\kappa_{art})\,\nabla v'\cdot\nabla v' + \int_{\Gamma_K} v'v'a_n^+ \\ &\quad - \int_{\Gamma_K} \kappa\nabla v'\cdot\boldsymbol{n}v' - \int_{\Gamma_K} v'\kappa\nabla v'\cdot\boldsymbol{n} + \int_{\Gamma_K} \frac{C_{pen}\kappa}{h_K} v'v' \Bigg) \\ &= \sum_{K=1}^{n_{el}} \Bigg((\kappa+\kappa_{art})\,|v'|^2_{1,\Omega_K} + \frac{C_{pen}\kappa}{h_K}\|v'\|^2_{0,\Gamma_K} \\ &\quad - \int_{\Omega_K} \frac{1}{2}\nabla\cdot\left(\boldsymbol{a}\left(v'\right)^2\right) + \int_{\Gamma_K} a_n^+\left(v'\right)^2 - 2\int_{\Gamma_K}\kappa\nabla v'\cdot\boldsymbol{n}v' \Bigg) \\ &= \sum_{K=1}^{n_{el}} \Bigg((\kappa+\kappa_{art})\,|v'|^2_{1,\Omega_K} + \frac{C_{pen}\kappa}{h_K}\|v'\|^2_{0,\Gamma_K} \\ &\quad - \int_{\Gamma_K} \frac{1}{2}a_n\left(v'\right)^2 + \int_{\Gamma_K} a_n^+\left(v'\right)^2 - 2\int_{\Gamma_K}\kappa\nabla v'\cdot\boldsymbol{n}v' \Bigg) \\ &= \sum_{K=1}^{n_{el}} \left((\kappa+\kappa_{art})\,|v'|^2_{1,\Omega_K} + \frac{C_{pen}\kappa}{h_K}\|v'\|^2_{0,\Gamma_K} + \frac{1}{2}\|a_n^{1/2}v'\|^2_{0,\Gamma_K} - 2\int_{\Gamma_K}\kappa\nabla v'\cdot\boldsymbol{n}v' \right). \end{aligned} \tag{8.21}$$

For the bilinear forms coupling the coarse-scales and fine-scales, we evaluate

$$\begin{aligned} \bar{C}(v',\bar{v}) + C'(\bar{v},v') &= -\sum_{K=1}^{n_{el}} \int_{\Omega_K} v'\nabla\cdot(\kappa\nabla\bar{v}) \\ &= \sum_{K=1}^{n_{el}} \left(\int_{\Omega_K} \kappa\nabla\bar{v}\cdot\nabla v' - \int_{\Gamma_K}\kappa\nabla\bar{v}\cdot\boldsymbol{n}v' \right). \end{aligned} \tag{8.22}$$

To continue, we recognize that, for every element $\Omega_K \in \mathcal{M}$,

$$\left| \int_{\Gamma_K} \kappa\nabla v'\cdot\boldsymbol{n}v' \right| \leq \frac{1}{2}\left(\frac{h_K}{4C_{trace}}\kappa\|\nabla v'\cdot\boldsymbol{n}\|^2_{0,\Gamma_K} + \frac{4C_{trace}}{h_K}\kappa\|v'\|^2_{0,\Gamma_K} \right)$$

by Young's inequality, and

$$\left| \int_{\Gamma_K} \kappa\nabla v'\cdot\boldsymbol{n}v' \right| \leq \frac{1}{2}\left(\frac{1}{4}\kappa|v'|^2_{1,\Omega_K} + \frac{4C_{trace}}{h_K}\kappa\|v'\|^2_{0,\Gamma_K} \right) \tag{8.23}$$

by the trace inequality. By a similar argument, we have

$$\left| \int_{\Gamma_K} \kappa\nabla\bar{v}\cdot\boldsymbol{n}v' \right| \leq \frac{1}{2}\left(\frac{1}{4}\kappa|\bar{v}|^2_{1,\Omega_K} + \frac{4C_{trace}}{h_K}\kappa\|v'\|^2_{0,\Gamma_K} \right) \tag{8.24}$$

for every element $\Omega_K \in \mathcal{M}$. Finally, by Young's inequality, we have

$$\left| \int_{\Omega_K} \kappa\nabla\bar{v}\cdot\nabla v' \right| \leq \frac{1}{2}\left(\kappa|\bar{v}|^2_{1,\Omega_K} + \kappa|v'|^2_{1,\Omega_K} \right) \tag{8.25}$$

for every element $\Omega_K \in \mathcal{M}$. Collecting our results contained in (8.20)-(8.25), we obtain

$$\begin{aligned}
\bar{B}(\bar{v},\bar{v}) &= \kappa|\bar{v}|^2_{1,\Omega} && (8.26)\\
B'(v',v') &\geq \sum_{K=1}^{n_{el}} \Bigg((\kappa+\kappa_{art})\,|v'|^2_{1,\Omega_K} + \frac{C_{pen}\kappa}{h_K}\|v'\|^2_{0,\Gamma_K} + \frac{1}{2}\|a_n^{1/2}v'\|^2_{0,\Gamma_K} \\
&\quad -\frac{1}{4}\kappa|v'|^2_{1,\Omega_K} - \frac{4C_{trace}}{h_K}\kappa\|v'\|^2_{0,\Gamma_K}\Bigg) && (8.27)\\
\bar{C}(v',\bar{v}) + C'(\bar{v},v') &\geq -\sum_{K=1}^{n_{el}} \frac{1}{2}\Big(\kappa|\bar{v}|^2_{1,\Omega_K} + \kappa|v'|^2_{1,\Omega_K} \\
&\quad +\frac{1}{4}\kappa|\bar{v}|^2_{1,\Omega_K} + \frac{4C_{trace}}{h_K}\kappa\|v'\|^2_{0,\Gamma_K}\Bigg) && (8.28)
\end{aligned}$$

The desired expression follows by adding the above inequalities and invoking Assumption 1. ∎

The coercivity result provided in Theorem 4.1 ensures that the group variable solution is unique, but it does not ensure that the corresponding methodology is stable. In fact, note that in the limit $\kappa \to 0$, the coercivity result suggests that the methodology loses control of the coarse-scale solution entirely. However, we are able to show that the methodology satisfies a different notion of stability, namely inf-sup stability, in this limit. To proceed forward, let us define the norm

$$\begin{aligned}
\|\mathbf{V}^h\|^2_S &:= \kappa|\bar{v}|^2_{1,\Omega} + \sum_{K=1}^{n_{el}} \left((\kappa+\kappa_{art})\,|v'|^2_{1,\Omega_K} + \frac{C_{pen}\kappa}{h_K}\|v'\|^2_{0,\Gamma_K} + \|a_n^{1/2}v'\|^2_{0,\Gamma_K}\right) \\
&\quad + \sum_{K=1}^{n_{el}} \|\tau_K^{1/2}\mathcal{P}'_K\left(\boldsymbol{a}\cdot\nabla\left(\bar{v}+v'\right)\right)\|^2_{0,\Omega_K} && (8.29)
\end{aligned}$$

for every $\mathbf{V}^h \in \boldsymbol{\mathcal{V}}^h$ where $\mathcal{P}'_K$ is the L^2-projector onto the space of discontinuous subscales $\mathcal{V}'_{disc,K}$ on element $\Omega_K \in \mathcal{M}$ and τ_K is the element-wise constant

$$\tau_K := C_\tau \left(\max\left\{ \frac{\|\boldsymbol{a}\|_{0,\infty,\Omega_K}}{h_K}, \frac{C_{inv}\kappa}{h_K^2} \right\} \right)^{-1}$$

where $C_\tau > 0$ is an arbitrary positive constant. With the above norm defined, we have the following inf-sup stability result.

Theorem 8.3.2 The inf-sup stability result

$$\inf_{\mathbf{U}^h \in \boldsymbol{\mathcal{V}}^h} \sup_{\mathbf{V}^h \in \boldsymbol{\mathcal{V}}^h} \frac{\mathbf{B}(\mathbf{U}^h,\mathbf{V}^h)}{\|\mathbf{U}^h\|_S \|\mathbf{V}^h\|_S} \geq \beta > 0$$

holds provided Assumptions 1 and 2 are satisfied where β is a positive constant independent of the problem parameters $\boldsymbol{a}$ and κ and the mesh size $h = \max_K h_K$.

Proof Let $\mathbf{U}^h = (\bar{u}, u')$ be an arbitrary member of $\boldsymbol{\mathcal{V}}^h$. It suffices to show that there exists some $\mathbf{V}^h = (\bar{v}, v') \in \boldsymbol{\mathcal{V}}^h$ such that $\mathbf{B}(\mathbf{U}^h, \mathbf{V}^h) \geq \beta \|\mathbf{U}^h\|_S \|\mathbf{V}^h\|_S$. In this direction, let $z' \in \mathcal{V}'_{disc}$ be defined such that $z'|_{\Omega_K} = \tau_K \mathcal{P}'_K \left(\boldsymbol{a} \cdot \nabla \left(\bar{u} + u'\right)\right)$. Note that we have the following inequalities bounding the element-wise L^2-norm of z':

$$\begin{aligned}
\|z'\|_{0,\Omega_K} &\leq \tau_K \|\boldsymbol{a} \cdot \nabla \left(\bar{u} + u'\right)\|_{0,\Omega_K} \\
&\leq \tau_K \|\boldsymbol{a}\|_{0,\infty,\Omega_K} |\bar{u} + u'|_{1,\Omega_K} \\
&\leq \tau_K C_{inv}^{1/2} h_K^{-1} \|\boldsymbol{a}\|_{0,\infty,\Omega_K} \|\bar{u} + u'\|_{0,\Omega_K} \\
&\leq C_\tau C_{inv}^{1/2} \|\bar{u} + u'\|_{0,\Omega_K} \\
&\leq C_\tau C_{inv}^{1/2} \left(\|\bar{u}\|_{0,\Omega_K} + \|u'\|_{0,\Omega_K}\right), \qquad (8.30)
\end{aligned}$$

the element-wise L^2-norm of the gradient of z':

$$\begin{aligned}
\kappa^{1/2} |z'|_{1,\Omega_K} &\leq \kappa^{1/2} C_{inv}^{1/2} h_K^{-1} \|z'\|_{0,\Omega_K} \\
&= \tau_K^{1/2} \kappa^{1/2} C_{inv}^{1/2} h_K^{-1} \|\tau_K^{-1/2} z'\|_{0,\Omega_K} \\
&\leq C_\tau^{1/2} \|\tau_K^{1/2} \mathcal{P}'_K \left(\boldsymbol{a} \cdot \nabla \left(\bar{u} + u'\right)\right)\|_{0,\Omega_K}, \qquad (8.31)
\end{aligned}$$

again the element-wise L^2-norm of the gradient of z':

$$\begin{aligned}
\kappa_{art}^{1/2} |z'|_{1,\Omega_K} &\leq \kappa_{art}^{1/2} C_{inv}^{1/2} h_K^{-1} \|z'\|_{0,\Omega_K} \\
&= \tau_K^{1/2} \kappa_{art}^{1/2} C_{inv}^{1/2} h_K^{-1} \|\tau_K^{-1/2} z'\|_{0,\Omega_K} \\
&= \tau_K C_\tau^{-1/2} C_{art}^{1/2} \|\boldsymbol{a}\|_{0,\infty,\Omega_K} C_{inv}^{1/2} h_K^{-1} \|\tau_K^{-1/2} z'\|_{0,\Omega_K} \\
&\leq C_\tau^{1/2} C_{art}^{1/2} C_{inv}^{1/2} \|\tau_K^{1/2} \mathcal{P}'_K \left(\boldsymbol{a} \cdot \nabla \left(\bar{u} + u'\right)\right)\|_{0,\Omega_K}, \qquad (8.32)
\end{aligned}$$

the element-wise L^2-norm of the trace of z':

$$\begin{aligned}
\|a_n^{1/2} z'\|_{0,\Gamma_K} &\leq \|\boldsymbol{a}\|_{0,\infty,\Omega_K}^{1/2} \|z'\|_{0,\Gamma_K} \\
&\leq C_{trace}^{1/2} h_K^{-1/2} \|\boldsymbol{a}\|_{0,\infty,\Omega_K}^{1/2} \|\tau_K \mathcal{P}_K' \left(\boldsymbol{a} \cdot \nabla \left(\bar{u} + u'\right)\right) \|_{0,\Omega_K} \\
&\leq \tau_K^{1/2} C_{trace}^{1/2} h_K^{-1/2} \|\boldsymbol{a}\|_{0,\infty,\Omega_K}^{1/2} \|\tau_K^{1/2} \mathcal{P}_K' \left(\boldsymbol{a} \cdot \nabla \left(\bar{u} + u'\right)\right) \|_{0,\Omega_K} \\
&\leq C_\tau^{1/2} C_{trace}^{1/2} \|\tau_K^{1/2} \mathcal{P}_K' \left(\boldsymbol{a} \cdot \nabla \left(\bar{u} + u'\right)\right) \|_{0,\Omega_K}, \qquad (8.33)
\end{aligned}$$

again the element-wise L^2-norm of the trace of z':

$$\begin{aligned}
C_{pen}^{1/2} h_K^{-1/2} \kappa^{1/2} \|z'\|_{0,\Gamma_K} &\leq C_{pen}^{1/2} C_{trace}^{1/2} h_K^{-1} \kappa^{1/2} \|z'\|_{0,\Omega_K} \\
&= \tau_K^{1/2} C_{pen}^{1/2} C_{trace}^{1/2} h_K^{-1} \kappa^{1/2} \|\tau_K^{-1/2} z'\|_{0,\Omega_K} \\
&\leq C_\tau^{1/2} C_{pen}^{1/2} C_{trace}^{1/2} C_{inv}^{-1/2} \|\tau_K^{1/2} \mathcal{P}_K' \left(\boldsymbol{a} \cdot \nabla \left(\bar{u} + u'\right)\right) \|_{0,\Omega_K} \qquad (8.34)
\end{aligned}$$

and the element-wise L^2-norm of the normal derivative trace of z':

$$\begin{aligned}
h_K^{1/2} \kappa^{1/2} \|\nabla z' \cdot \boldsymbol{n}\|_{0,\Gamma_K} &\leq C_{trace}^{1/2} \kappa^{1/2} |z'|_{1,\Omega_K} \\
&\leq C_{inv}^{1/2} C_{trace}^{1/2} h_K^{-1} \kappa^{1/2} \|z'\|_{0,\Omega_K} \\
&= \tau_K^{1/2} C_{inv}^{1/2} C_{trace}^{1/2} h_K^{-1} \kappa^{1/2} \|\tau^{-1/2} z'\|_{0,\Omega_K} \\
&\leq C_\tau^{1/2} C_{trace}^{1/2} \|\tau_K^{1/2} \mathcal{P}_K' \left(\boldsymbol{a} \cdot \nabla \left(\bar{u} + u'\right)\right) \|_{0,\Omega_K}. \qquad (8.35)
\end{aligned}$$

We need one more inequality for z'. Notably, observe:

$$\begin{aligned}
\|\tau_K^{1/2} \mathcal{P}_K' \left(\boldsymbol{a} \cdot \nabla z'\right) \|_{0,\Omega_K} &\leq \tau_K^{1/2} \|\boldsymbol{a}\|_{0,\infty,\Omega_K} |z'|_{1,\Omega_K} \\
&\leq \tau_K^{1/2} C_{inv}^{1/2} h_K^{-1} \|\boldsymbol{a}\|_{0,\infty,\Omega_K} \|z'\|_{0,\Omega_K} \\
&= \tau_K^{1/2} C_{inv}^{1/2} h_K^{-1} \|\boldsymbol{a}\|_{0,\infty,\Omega_K} \|\tau_K \mathcal{P}_K' \left(\boldsymbol{a} \cdot \nabla \left(\bar{u} + u'\right)\right) \|_{0,\Omega_K} \\
&\leq \tau_K C_{inv}^{1/2} h_K^{-1} \|\boldsymbol{a}\|_{0,\infty,\Omega_K} \|\tau_K^{1/2} \mathcal{P}_K' \left(\boldsymbol{a} \cdot \nabla \left(\bar{u} + u'\right)\right) \|_{0,\Omega_K} \\
&\leq C_\tau C_{inv}^{1/2} \|\tau_K \mathcal{P}_K' \left(\boldsymbol{a} \cdot \nabla \left(\bar{u} + u'\right)\right) \|_{0,\Omega_K}. \qquad (8.36)
\end{aligned}$$

Let us define $\mathbf{Z}^h = (0, z')$. Note immediately that as a consequence of the above inequalities, the following inequality holds:

$$\|\mathbf{Z}^h\|_S \leq C_z \|\mathbf{U}^h\|_S \qquad (8.37)$$

where

$$C_z = \sqrt{C_\tau \left(1 + C_{trace} + C_{trace} C_{pen} C_{inv}^{-1} + C_{art} C_{inv} + C_\tau C_{inv}\right)}. \tag{8.38}$$

We now seek a lower bound for the quantity $\mathbf{B}(\mathbf{U}^h, \mathbf{Z}^h)$. We observe that

$$\begin{aligned}
\mathbf{B}(\mathbf{U}^h, \mathbf{Z}^h) &= B'(u', z') + C'(\bar{u}, z') \\
&= \sum_{K=1}^{n_{el}} \Big(- \int_{\Omega_K} u' \boldsymbol{a} \cdot \nabla z' + \int_{\Omega_K} (\kappa + \kappa_{art}) \nabla u' \cdot \nabla z' + \int_{\Gamma_K} u' z' a_n^+ \\
&\quad - \int_{\Gamma_K} \kappa \nabla u' \cdot \boldsymbol{n} z' - \int_{\Gamma_K} u' \kappa \nabla z' \cdot \boldsymbol{n} + \int_{\Gamma_K} \frac{C_{pen}\kappa}{h_K} u' z' \\
&\quad + \int_{\Omega_K} z' \left(\boldsymbol{a} \cdot \nabla \bar{u} - \nabla \cdot (\kappa \nabla \bar{u}) \right) \Big) \\
&= \sum_{K=1}^{n_{el}} \Big(\int_{\Omega_K} \boldsymbol{a} \cdot \nabla \left(\bar{u} + u' \right) z' + \int_{\Omega_K} (\kappa + \kappa_{art}) \nabla u' \cdot \nabla z' \\
&\quad - \int_{\Gamma_K} u' z' a_n^- - \int_{\Gamma_K} \kappa \nabla u' \cdot \boldsymbol{n} z' - \int_{\Gamma_K} u' \kappa \nabla z' \cdot \boldsymbol{n} + \int_{\Gamma_K} \frac{C_{pen}\kappa}{h_K} u' z' \\
&\quad - \int_{\Omega_K} z' \left(\nabla \cdot (\kappa \nabla \bar{u}) \right) \Big).
\end{aligned} \tag{8.39}$$

We deal with each of the expressions appearing above one-by-one. First, we note that, by definition

$$\begin{aligned}
\int_{\Omega_K} \boldsymbol{a} \cdot \nabla \left(\bar{u} + u' \right) z' &= \tau_K \int_{\Omega_K} \boldsymbol{a} \cdot \nabla \left(\bar{u} + u' \right) \mathcal{P}'_K \left(\boldsymbol{a} \cdot \nabla \left(\bar{u} + u' \right) \right) \\
&= \| \tau_K^{1/2} \mathcal{P}'_K \left(\boldsymbol{a} \cdot \nabla \left(\bar{u} + u' \right) \right) \|_{0,\Omega_K}^2.
\end{aligned} \tag{8.40}$$

For the next term, we have

$$\begin{aligned}
\left| \int_{\Omega_K} \kappa \nabla u' \cdot \nabla z' \right| &\leq \kappa |u'|_{1,\Omega_K} |z'|_{1,\Omega_K} \\
&\leq C_\tau^{1/2} \kappa^{1/2} |u'|_{1,\Omega_K} \| \tau_K^{1/2} \mathcal{P}'_K \left(\boldsymbol{a} \cdot \nabla \left(\bar{u} + u' \right) \right) \|_{0,\Omega_K} \\
&\leq C_\tau^{1/2} \left(\frac{\kappa}{2\gamma_1} |u'|_{1,\Omega_K}^2 + \frac{\gamma_1}{2} \| \tau_K^{1/2} \mathcal{P}'_K \left(\boldsymbol{a} \cdot \nabla \left(\bar{u} + u' \right) \right) \|_{0,\Omega_K}^2 \right)
\end{aligned} \tag{8.41}$$

where $\gamma_1 > 0$ is an arbitrarily chosen positive number. In analogous fashion, we have

$$\left| \int_{\Omega_K} \kappa_{art} \nabla u' \cdot \nabla z' \right| \leq C_\tau^{1/2} C_{art}^{1/2} C_{inv}^{1/2} \left(\frac{\kappa_{art}}{2\gamma_2} |u'|_{1,\Omega_K}^2 + \frac{\gamma_2}{2} \| \tau_K^{1/2} \mathcal{P}'_K \left(\boldsymbol{a} \cdot \nabla \left(\bar{u} + u' \right) \right) \|_{0,\Omega_K}^2 \right) \tag{8.42}$$

$$\left| \int_{\Gamma_K} u' z' a_n^- \right| \leq C_\tau^{1/2} C_{trace}^{1/2} \left(\frac{1}{2\gamma_3} \| a_n^{1/2} u' \|_{0,\Gamma_K}^2 + \frac{\gamma_3}{2} \| \tau_K^{1/2} \mathcal{P}'_K \left(\boldsymbol{a} \cdot \nabla \left(\bar{u} + u' \right) \right) \|_{0,\Omega_K}^2 \right) \tag{8.43}$$

$$\left|\int_{\Gamma_K}\frac{C_{pen}\kappa}{h_K}u'z'\right| \leq C_\tau^{1/2}C_{pen}^{1/2}C_{trace}^{-1/2}C_{inv}^{-1/2}\left(\frac{C_{pen}\kappa}{2\gamma_4 h_K}\|u'\|_{0,\Gamma_K}^2+\frac{\gamma_4}{2}\|\tau_K^{1/2}\mathcal{P}_K'\left(\boldsymbol{a}\cdot\nabla\left(\bar{u}+u'\right)\right)\|_{0,\Omega_K}^2\right), \tag{8.44}$$

where again $\gamma_2,\gamma_3,\gamma_4>0$ are arbitrarily chosen positive numbers. The remaining terms require slightly more care. For the first remaining term, we have

$$\begin{aligned}\left|\int_{\Gamma_K}\kappa\nabla u'\cdot\boldsymbol{n}z'\right| &\leq \left(C_{pen}^{-1/2}h_K^{1/2}\kappa^{1/2}\|\nabla u'\cdot\boldsymbol{n}\|_{0,\Gamma_K}\right)\left(C_{pen}^{1/2}\kappa^{1/2}h_K^{-1/2}\|z'\|_{0,\Gamma_K}\right)\\ &\leq \left(C_{trace}^{1/2}C_{pen}^{-1/2}\kappa^{1/2}|u'|_{1,\Omega_K}\right)\left(C_{pen}^{1/2}\kappa^{1/2}h_K^{-1/2}\|z'\|_{0,\Gamma_K}\right)\\ &\leq \left(\kappa^{1/2}|u'|_{1,\Omega_K}\right)\left(C_{pen}^{1/2}\kappa^{1/2}h_K^{-1/2}\|z'\|_{0,\Gamma_K}\right)\\ &\leq C_\tau^{1/2}C_{pen}^{1/2}C_{trace}^{-1/2}C_{inv}^{-1/2}\left(\frac{\kappa}{2\gamma_5}|u'|_{1,\Omega_K}^2+\frac{\gamma_5}{2}\|\tau_K^{1/2}\mathcal{P}_K'\left(\boldsymbol{a}\cdot\nabla\left(\bar{u}+u'\right)\right)\|_{0,\Omega_K}^2\right)\end{aligned} \tag{8.45}$$

where $\gamma_5>0$ is another arbitrarily chosen positive number. For the second remaining term, we have

$$\begin{aligned}\left|\int_{\Gamma_K}u'\kappa\nabla z'\cdot\boldsymbol{n}\right| &\leq \left(C_{pen}^{1/2}\kappa^{1/2}h_K^{-1/2}\|u'\|_{0,\Gamma_K}\right)\left(C_{pen}^{-1/2}h_K^{1/2}\kappa^{1/2}\|\nabla z'\cdot\boldsymbol{n}\|_{0,\Gamma_K}\right)\\ &= C_\tau^{1/2}\left(\frac{C_{pen}\kappa}{2\gamma_6 h_K}\|u'\|_{0,\Gamma_K}^2+\frac{\gamma_6}{2}\|\tau_K^{1/2}\mathcal{P}_K'\left(\boldsymbol{a}\cdot\nabla\left(\bar{u}+u'\right)\right)\|_{0,\Omega_K}^2\right)\end{aligned} \tag{8.46}$$

where $\gamma_6>0$ is yet another arbitrarily chosen positive number. For the last remaining term, we integrate by parts, resulting in

$$\int_{\Omega_K}z'\left(\nabla\cdot(\kappa\nabla\bar{u})\right)=-\int_{\Omega_K}\kappa\nabla\bar{u}\cdot\nabla z'+\int_{\Gamma_K}\kappa\nabla\bar{u}\cdot\boldsymbol{n}z'. \tag{8.47}$$

The two terms on the right-hand-side are then easily bound as before, yielding the inequality

$$\begin{aligned}\left|\int_{\Omega_K}z'\left(\nabla\cdot(\kappa\nabla\bar{u})\right)\right| \leq\ & C_\tau^{1/2}\left(\frac{\kappa}{2\gamma_7}|\bar{u}|_{1,\Omega_K}^2+\frac{\gamma_7}{2}\|\tau_K^{1/2}\mathcal{P}_K'\left(\boldsymbol{a}\cdot\nabla\left(\bar{u}+u'\right)\right)\|_{0,\Omega_K}^2\right)\\ &+C_\tau^{1/2}C_{pen}^{1/2}C_{trace}^{-1/2}C_{inv}^{-1/2}\left(\frac{\kappa}{2\gamma_8}|\bar{u}|_{1,\Omega_K}^2+\frac{\gamma_8}{2}\|\tau_K^{1/2}\mathcal{P}_K'\left(\boldsymbol{a}\cdot\nabla\left(\bar{u}+u'\right)\right)\|_{0,\Omega_K}^2\right)\end{aligned} \tag{8.48}$$

where $\gamma_7 > 0, \gamma_8 > 0$ are two final arbitrarily chosen positive numbers. Collecting all of the above inequalities, we obtain the composite inequality

$$\mathbf{B}(\mathbf{U}^h, \mathbf{Z}^h) \geq C_1 \sum_{K=1}^{n_{el}} \|\tau_K^{1/2} \mathcal{P}'_K \left(\boldsymbol{a} \cdot \nabla \left(\bar{v} + v'\right)\right)\|^2_{0,\Omega_K} - C_2 \kappa |\bar{v}|^2_{1,\Omega}$$
$$- \sum_{K=1}^{n_{el}} \left(\left(C_3 \kappa + C_4 \kappa_{art}\right) |v'|^2_{1,\Omega_K} + C_5 \frac{C_{pen} \kappa}{h_K} \|v'\|^2_{0,\Gamma_K} + C_6 \|a_n^{1/2} v'\|^2_{0,\Gamma_K} \right) \tag{8.49}$$

wherein

$$C_1 = 1 - \frac{C_\tau^{1/2}}{2} \left((\gamma_1 + \gamma_6 + \gamma_7) + C_{art}^{1/2} C_{inv}^{1/2} \gamma_2 + C_{trace}^{1/2} \gamma_3 + C_{pen}^{1/2} C_{trace}^{-1/2} C_{inv}^{-1/2} \left(\gamma_4 + \gamma_5 + \gamma_8\right) \right)$$

$$\begin{aligned}
C_2 &= \frac{C_\tau^{1/2}}{2\gamma_2} + \frac{C_\tau^{1/2} C_{pen}^{1/2} C_{trace}^{-1/2} C_{inv}^{-1/2}}{2\gamma_8} \\
C_3 &= \frac{C_\tau^{1/2}}{2\gamma_1} + \frac{C_\tau^{1/2} C_{pen}^{1/2} C_{trace}^{-1/2} C_{inv}^{-1/2}}{2\gamma_5} \\
C_4 &= \frac{C_\tau^{1/2} C_{art}^{1/2} C_{inv}^{1/2}}{2\gamma_3} \\
C_5 &= \frac{C_\tau^{1/2} C_{pen}^{1/2} C_{trace}^{-1/2} C_{inv}^{-1/2}}{2\gamma_4} + \frac{C_\tau^{1/2}}{2\gamma_6} \\
C_6 &= \frac{C_\tau^{1/2} C_{trace}^{1/2}}{2\gamma_3}.
\end{aligned}$$

We now assume that γ_1 through γ_8 are chosen sufficiently small to guarantee that $C_1 > 0$. Note that we can choose such constants independent of the problem parameters and the mesh size. This choice in turn defines the constants C_2 through C_6. We are now in a position to define a suitable group test function $\mathbf{V}^h = (\bar{v}, v') \in \boldsymbol{\mathcal{V}}^h$. Namely, we select $\bar{v} = \bar{u}$ and $v' = u' + C_{lin} z'$ where

$$C_{lin} = \frac{1}{8} \min_{2 \leq i \leq 6} \left\{ \frac{1}{C_i} \right\}. \tag{8.50}$$

Then, by Theorem 8.3.1 and (8.49), it follows that

$$\mathbf{B}(\mathbf{U}^h, \mathbf{V}^h) \geq C_{bound} \|\mathbf{U}^h\|^2_S \tag{8.51}$$

with

$$C_{bound} = \min \left\{ \frac{1}{8}, C_1 C_{lin} \right\} \tag{8.52}$$

and

$$\|\mathbf{V}^h\|_S \leq C_v \|\mathbf{U}^h\|_S \tag{8.53}$$

with $C_v = 1 + C_{lin} C_z$. Thus the desired condition holds with $\beta = C_{bound}/C_v$ independent of the problem parameters $\boldsymbol{a}$ and κ and the mesh size h. ∎

We now introduce one more assumption. This assumption guarantees that our methodology is at least as stable as the SUPG method for steady scalar transport, as is shown in Corollary 4.3.

Assumption 3: *The following inequality holds for each element $\Omega_K \in \mathcal{M}$:*

$$\|\tau_K^{1/2} \boldsymbol{a} \cdot \nabla \left(\bar{v} + v'\right)\|_{0,\Omega_K}^2 \leq C_{SUPG} \left(\kappa_{art} |v'|_{1,\Omega_K}^2 + \|\tau_K^{1/2} \mathcal{P}_K' \left(\boldsymbol{a} \cdot \nabla \left(\bar{v} + v'\right)\right)\|_{0,\Omega_K}^2\right)$$

where $C_{SUPG} > 0$ is a positive constant independent of the problem parameters $\boldsymbol{a}$ and κ and the mesh size h.

Corollary 8.3.3 Provided Assumptions 1, 2, and 3 hold, the following inf-sup stability result is satisfied:

$$\inf_{\mathbf{U}^h \in \boldsymbol{\mathcal{V}}^h} \sup_{\mathbf{V}^h \in \boldsymbol{\mathcal{V}}^h} \frac{\mathbf{B}(\mathbf{U}^h, \mathbf{V}^h)}{\|\mathbf{U}^h\|_{SUPG} \|\mathbf{V}^h\|_{SUPG}} \geq \beta_{SUPG} > 0$$

where

$$\begin{aligned} \|\mathbf{V}^h\|_{SUPG}^2 &= \kappa |\bar{v}|_{1,\Omega}^2 + \sum_{K=1}^{n_{el}} \left(\left(\kappa + \kappa_{art}\right) |v'|_{1,\Omega_K}^2 + \frac{C_{pen}\kappa}{h_K} \|v'\|_{0,\Gamma_K}^2 + \|a_n^{1/2} v'\|_{0,\Gamma_K}^2 \right) \\ &\quad + \sum_{K=1}^{n_{el}} \|\tau_K^{1/2} \boldsymbol{a} \cdot \nabla \left(\bar{v} + v'\right)\|_{0,\Omega_K}^2 \end{aligned}$$

for every $\mathbf{V}^h \in \boldsymbol{\mathcal{V}}^h$ and β_{SUPG} is a positive constant independent of the problem parameters $\boldsymbol{a}$ and κ and the mesh size h.

There remains the question of whether or not we can expect Assumption 3 to be satisfied for a given finite element discretization. The following lemma demonstrates that Assumption 3 is indeed satisfied if the discontinuous subscale solution space is sufficiently rich and the artificial diffusivity is chosen in an intelligent manner.

Lemma 8.3.4 Assumption 3 is satisfied provided that one of the following two conditions is satisfied:

C1: It holds that $\boldsymbol{a} \cdot \nabla \left(\bar{v} + v' \right) \in \mathcal{V}'_{disc}$ for every $(\bar{v}, v') \in \boldsymbol{\mathcal{V}}^h$.

C2: It holds that $\boldsymbol{a} \cdot \nabla \bar{v} \in \mathcal{V}'_{disc}$ for every $\bar{v} \in \overline{\mathcal{V}}$ and Assumption 2 is satisfied with $C_{art} > 0$.

Proof We write

$$\| \tau_K^{1/2} \boldsymbol{a} \cdot \nabla \left(\bar{v} + v' \right) \|_{0,\Omega_K}^2 = \| \tau_K^{1/2} \mathcal{P}'_K \left(\boldsymbol{a} \cdot \nabla \left(\bar{v} + v' \right) \right) \|_{0,\Omega_K}^2 + \| \tau_K^{1/2} \left(\mathcal{I} - \mathcal{P}'_K \right) \left(\boldsymbol{a} \cdot \nabla \left(\bar{v} + v' \right) \right) \|_{0,\Omega_K}^2$$

where $\mathcal{I}$ is the identity operator. If Condition C1 holds, it follows that

$$\| \tau_K^{1/2} \left(\mathcal{I} - \mathcal{P}'_K \right) \left(\boldsymbol{a} \cdot \nabla \left(\bar{v} + v' \right) \right) \|_{0,\Omega_K}^2 = 0$$

and consequently the lemma is satisfied with $C_{SUPG} = 1$. If Condition C2 holds, we instead have

$$\begin{aligned} \| \tau_K^{1/2} \left(\mathcal{I} - \mathcal{P}'_K \right) \left(\boldsymbol{a} \cdot \nabla \left(\bar{v} + v' \right) \right) \|_{0,\Omega_K}^2 &= \| \tau_K^{1/2} \left(\mathcal{I} - \mathcal{P}'_K \right) \left(\boldsymbol{a} \cdot \nabla v' \right) \|_{0,\Omega_K}^2 \\ &\leq \tau_K \| \boldsymbol{a} \cdot \nabla v' \|_{0,\Omega_K}^2 \\ &\leq \tau_K \| \boldsymbol{a} \|_{0,\infty,\Omega_K} |v'|_{1,\Omega_K}. \end{aligned}$$

As Assumption 2 is satisfied with $C_{art} > 0$, it follows that

$$\| \tau_K^{1/2} \left(\mathcal{I} - \mathcal{P}'_K \right) \left(\boldsymbol{a} \cdot \nabla \left(\bar{v} + v' \right) \right) \|_{0,\Omega_K}^2 \leq \frac{C_\tau}{C_{art}} \kappa_{art} |v'|_{1,\Omega_K}$$

and consequently the lemma is satisfied with $C_{SUPG} = \max \left\{ 1, \frac{C_\tau}{C_{art}} \right\}$. ∎

Suppose that the imposed velocity field is a polynomial function of degree q over each element $\Omega_K \in \mathcal{M}$. Then, for the case of a finite element mesh of simplices, we see that $\boldsymbol{a} \cdot \nabla \bar{v}$ is a polynomial function of degree $k+q-1$ over each element and $\boldsymbol{a} \cdot \nabla v'$ is a polynomial function of degree k_f+q-1 over each element. Consequently, if $k_f \geq p + q - 1$ and $q \leq 1$, then Condition C1 of Lemma 4.4 is satisfied, and if only $k_f \geq p + q - 1$ is satisfied but C_{art} is chosen to be a positive number, then Condition C2 of Lemma 4.4 is satisfied. For a continuous piecewise linear finite element discretization with discontinuous piecewise linear subscales, we see that Condition C1 of Lemma

4.4 is satisfied for a piecewise linear velocity field. Alternately, for a continuous piecewise quadratic finite element discretization with discontinuous piecewise linear subscales, we see that Condition C1 of Lemma 4.4 is satisfied for a piecewise constant velocity field. By enriching the subscale space to discontinuous piecewise quadratic subscales, we find Condition C1 of Lemma 4.4 is satisfied again for a piecewise linear velocity field.

Lemma 4.4 provides a general guideline for how to choose the polynomial degree of the subscale space. Nonetheless, we have observed our methodology often returns accurate and stable results even when the conditions of the lemma are not satisfied. In particular, we have observed our methodology is stable if we employ smooth splines for our coarse-scale solution and discontinuous piecewise bi-linear finite elements for our subscale solution. We anticipate that Lemma 4.4 holds in this case, though such an analysis is beyond the scope of the current work.

Our final theorem demonstrates that our method exhibits optimal convergence rates with respect to the SUPG norm provided Assumptions 1, 2, and 3 hold.

Theorem 8.3.5 Suppose that the exact solution satisfies the smoothness condition $u \in H^{p+1}(\Omega)$ and Assumptions 1, 2, and 3 hold. Then, the error $\mathbf{E} = (u - \bar{u}, -u')$ satisfies the *a priori* estimate

$$\|\mathbf{E}\|^2_{SUPG} \leq C_{apriori} \sum_{K=1}^{n_{el}} \left(\|\boldsymbol{a}\|_{0,\infty,\Omega_K} h_K^{2p+1} + \kappa h_K^{2p} \right) |u|^2_{p+1,\Omega_K},$$

where $C_{apriori}$ is a positive constant independent of the problem parameters $\boldsymbol{a}$ and κ and the mesh size h.

Proof Let $\tilde{u} \in \overline{\mathcal{V}}$ be an interpolation function which we will define later, and let us split the error into two components, a method error defined as $\mathbf{E}^h = (\tilde{u} - \bar{u}, -u') = (e^h, e')$ and an interpolation error defined as $\boldsymbol{\eta} = (u - \tilde{u}, 0) = (\eta, 0)$. Our first objective is to bound the method error by the interpolation error. By Corollary 4.3, we have that

$$\beta_{SUPG} \|\mathbf{E}^h\|_{SUPG} \leq \sup_{\mathbf{V}^h \in \boldsymbol{\mathcal{V}}^h} \frac{\mathbf{B}(\mathbf{E}^h, \mathbf{V}^h)}{\|\mathbf{V}^h\|_{SUPG}}. \tag{8.54}$$

Furthermore, it is readily shown that our method is consistent, that is, $\mathbf{B}(\mathbf{E}, \mathbf{V}^h) = 0$, so we further

have that

$$\beta_{SUPG}\|\mathbf{E}^h\|_{SUPG} \leq \sup_{\mathbf{V}^h \in \boldsymbol{\mathcal{V}}^h} \frac{-\mathbf{B}(\boldsymbol{\eta}, \mathbf{V}^h)}{\|\mathbf{V}^h\|_{SUPG}}. \tag{8.55}$$

We now require a bound on the term $\mathbf{B}(\boldsymbol{\eta}, \mathbf{V}^h)$. Direct substitution results in

$$\mathbf{B}(\boldsymbol{\eta}, \mathbf{V}^h) = \bar{B}(\eta, \bar{v}) + C'(\eta, v'). \tag{8.56}$$

We can bound the first term on the right hand side of (8.56) as

$$\begin{aligned} |\bar{B}(\eta, \bar{v})| &\leq \left| \int_\Omega \eta \boldsymbol{a} \cdot \nabla \bar{v} \right| + \left| \int_\Omega \kappa \nabla \eta \cdot \nabla \bar{v} \right| \\ &\leq \sum_{K=1}^{n_{el}} \left(\left\| \tau_K^{-1/2} \eta \right\|_{0,\Omega_K} \left\| \tau_K^{1/2} \boldsymbol{a} \cdot \nabla \bar{v} \right\|_{0,\Omega_K} + \kappa \left| \eta \right|_{1,\Omega_K} \left| \bar{v} \right|_{1,\Omega_K} \right). \end{aligned} \tag{8.57}$$

The second term on the right hand side of (8.56) requires more care. We first integrate by parts to obtain

$$\begin{aligned} C'(\eta, v') &= \sum_{K=1}^{n_{el}} \int_{\Omega_K} v' \left(\boldsymbol{a} \cdot \nabla \eta - \nabla \cdot (\kappa \nabla \eta) \right) \\ &= \sum_{K=1}^{n_{el}} \left(- \int_{\Omega_K} \eta \boldsymbol{a} \cdot \nabla v' + \int_{\Gamma_K} \eta v' a_n + \int_{\Omega_K} \kappa \nabla \eta \cdot \nabla v' - \int_{\Gamma_K} \kappa \nabla \eta \cdot \boldsymbol{n} v' \right). \end{aligned} \tag{8.58}$$

To proceed, we require bounds for each of the four terms on the right hand side of (8.58). The first and third terms are easily bounded as before, yielding

$$\left| \int_{\Omega_K} \eta \boldsymbol{a} \cdot \nabla v' \right| \leq \left\| \tau_K^{-1/2} \eta \right\|_{0,\Omega_K} \left\| \tau_K^{1/2} \boldsymbol{a} \cdot \nabla v' \right\|_{0,\Omega_K} \tag{8.59}$$

$$\left| \int_{\Omega_K} \kappa \nabla \eta \cdot \nabla v' \right| \leq \kappa \left| \eta \right|_{1,\Omega_K} \left| v' \right|_{1,\Omega_K}. \tag{8.60}$$

Similarly, we can bound the second and fourth terms like

$$\left| \int_{\Gamma_K} \eta v' a_n \right| \leq \left\| a_n^{1/2} \eta \right\|_{0,\Gamma_K} \left\| a_n^{1/2} v' \right\|_{0,\Gamma_K} \tag{8.61}$$

$$\left| \int_{\Gamma_K} \kappa \nabla \eta \cdot \boldsymbol{n} v' \right| \leq \kappa \left\| \nabla \eta \cdot \boldsymbol{n} \right\|_{0,\Gamma_K} \left\| v' \right\|_{0,\Gamma_K}. \tag{8.62}$$

Collecting (8.56)-(8.62) and applying the Cauchy-Schwarz inequality, we obtain the composite inequality

$$\frac{|\mathbf{B}(\boldsymbol{\eta}, \mathbf{V}^h)|}{\|\mathbf{V}^h\|_{SUPG}} \leq \left(\sum_{K=1}^{n_{el}} \left(2 \left\| \tau_K^{-1/2} \eta \right\|_{0,\Omega_K}^2 + 2\kappa \left| \eta \right|_{1,\Omega_K}^2 + \left\| a_n^{1/2} \eta \right\|_{0,\Gamma_K}^2 + \frac{\kappa h_K}{C_{pen}} \left\| \nabla \eta \cdot \boldsymbol{n} \right\|_{0,\Gamma_K}^2 \right) \right)^{1/2}.$$

Combining the above expression with (8.55), we finally obtain the method error bound

$$\|\mathbf{E}^h\|^2_{SUPG} \leq \beta^{-1/2}_{SUPG} \sum_{K=1}^{n_{el}} \left(2 \left\| \tau_K^{-1/2} \eta \right\|^2_{0,\Omega_K} + 2\kappa \left| \eta \right|^2_{1,\Omega_K} + \left\| a_n^{1/2} \eta \right\|^2_{0,\Gamma_K} + \frac{\kappa h_K}{C_{pen}} \left\| \nabla \eta \cdot \boldsymbol{n} \right\|^2_{0,\Gamma_K} \right). \tag{8.63}$$

Now suppose we have chosen the interpolant $\tilde{u}$ to be a "best" interpolant such that the following local interpolation estimates hold for every element $\Omega_K \in \mathcal{M}$:

$$\begin{aligned} \|\eta\|^2_{0,\Omega_K} &\leq C_{shape} h_K^{2p+2} |u|^2_{p+1,\Omega_K} \\ |\eta|^2_{1,\Omega_K} &\leq C_{shape} h_K^{2p} |u|^2_{p+1,\Omega_K} \\ \|\eta\|^2_{0,\Gamma_K} &\leq C_{shape} h_K^{2p+1} |u|^2_{p+1,\Omega_K} \\ \|\nabla \eta \cdot \boldsymbol{n}\|^2_{0,\Gamma_K} &\leq C_{shape} h_K^{2p-1} |u|^2_{p+1,\Omega_K} \end{aligned}$$

where $C_{shape} > 0$ is a positive constant independent of the mesh size but possibly dependent on the mesh regularity and coarse-scale polynomial degree k [40]. It then follows that

$$\begin{aligned} \left\| \tau_K^{-1/2} \eta \right\|^2_{0,\Omega_K} &= \tau_K^{-1} \|\eta\|^2_{0,\Omega_K} \\ &\leq C_{shape} C_\tau^{-1} \max \left\{ \frac{\|\boldsymbol{a}\|_{0,\infty,\Omega_K}}{h_K}, \frac{C_{inv}\kappa}{h_K^2} \right\} h_K^{2p+2} |u|^2_{p+1,\Omega_K} \qquad (8.64) \\ \kappa \left| \eta \right|^2_{1,\Omega_K} &\leq C_{shape} \kappa h_K^{2p} |u|^2_{p+1,\Omega_K} \qquad (8.65) \\ \left\| a_n^{1/2} \eta \right\|^2_{0,\Gamma_K} &\leq \|\boldsymbol{a}\|_{0,\infty,\Omega_K} \|\eta\|^2_{0,\Gamma_K} \\ &\leq C_{shape} \|\boldsymbol{a}\|_{0,\infty,\Omega_K} h_K^{2p+1} |u|^2_{p+1,\Omega_K} \qquad (8.66) \\ \frac{\kappa h_K}{C_{pen}} \left\| \nabla \eta \cdot \boldsymbol{n} \right\|^2_{0,\Gamma_K} &\leq C_{shape} C_{pen}^{-1} \kappa h_K^{2p} |u|^2_{p+1,\Omega_K}. \qquad (8.67) \end{aligned}$$

Combining (8.64)-(8.67) with the method error bound (8.63) yields

$$\|\mathbf{E}^h\|^2_{SUPG} \leq C_{method} \sum_{K=1}^{n_{el}} \left(\|\boldsymbol{a}\|_{0,\infty,\Omega_K} h_K^{2p+1} + \kappa h_K^{2p} \right) |u|^2_{p+1,\Omega_K} \tag{8.68}$$

where

$$C_{method} = \beta^{-1/2}_{SUPG} C_{shape} \left(2C_\tau^{-1} + C_{pen}^{-1} + 2 \right).$$

The interpolation error may be bounded in a similar manner, resulting in

$$\|\boldsymbol{\eta}\|_{SUPG}^2 \leq C_{interpolation} \sum_{K=1}^{n_{el}} \left(\|\boldsymbol{a}\|_{0,\infty,\Omega_K} h_K^{2p+1} + \kappa h_K^{2p} \right) |u|_{p+1,\Omega_K}^2 \tag{8.69}$$

where $C_{interpolation} > 0$ is a positive constant independent of the mesh size but possibly dependent on the mesh regularity and coarse-scale polynomial degree k. The desired result follows by combining (8.68) and (8.69) with the decomposition $\mathbf{E} = \mathbf{E}^h + \boldsymbol{\eta}$. ∎

Note remarkably that the error estimate characterized by Theorem 5.5 is completely independent of the subscale polynomial degree. Consequently, the subscales act purely to stabilize the coarse-scale solution and have virtually no impact on solution accuracy. This is one of the main messages of the current work: it is possible to stabilize a high-order numerical method with a low-order, but stable, numerical method.

It should also be remarked that while the constants appearing in all of the above estimates are independent of the problem parameters $\boldsymbol{a}$ and κ and the mesh size h, they are possibly dependent on mesh regularity, the coarse-scale polynomial degree k, and the subscale polynomial degree k_f. A more delicate analysis is required to obtain dependencies with respect to these variables. This would be useful, for instance, in the context of a boundary layer application wherein a highly skewed mesh should be employed near solid boundaries.

8.4 Numerical Results

We finish this chapter by applying our methodology to a collection of two-dimensional steady and unsteady transport problems. All of the following results were obtained by applying the method of discontinuous subscales to isogeometric Non-Uniform Rational B-splines (NURBS) discretizations on uniform grids [81]. These discretizations employ C^{p-1}-continuous piecewise tensor-product polynomials or rational functions of degree k. For $k = 1$, isogeometric NURBS discretizations correspond to standard bilinear finite elements, while for $k > 1$, isogeometric NURBS discretizations exhibit enhanced continuity as compared to standard tensor-product finite elements. For more in-

formation on NURBS-based isogeometric analysis, refer to [49]. Throughout, we used the following values for C_{pen} and κ_{art}:

$$C_{pen} = 4\left(k_f + 1\right)^2 \tag{8.70}$$

and

$$\kappa_{art} = \frac{h_K \left|\boldsymbol{a}\right|}{6k_f} \tag{8.71}$$

where k_f is the subscale polynomial degree and h_K is the mesh size for a given element $\Omega_K \in \mathcal{M}$. These are inspired by theoretical estimates for the trace and inverse constants associated with a discontinuous subscale discretization [74, 139]. Note that these values are simpler than the ones proposed in the previous section, but we have found that they still yield stable and accurate results.

8.4.1 Steady Manufactured Solution

We begin by considering a simple manufactured solution $u\left(x, y\right) = \sin\left(\pi x\right)\sin\left(\pi y\right)$ to the steady scalar transport problem. This solution is realized on the domain $\Omega = [0,1]\times[0,1]$ by setting the velocity to $\boldsymbol{a} = \left(\sqrt{2}/2, \sqrt{2}/2\right)$, setting the forcing to

$$f\left(x, y\right) = \frac{\pi\sqrt{2}}{2}\left(\cos\left(\pi x\right)\sin\left(\pi y\right) + \sin\left(\pi x\right)\cos\left(\pi y\right)\right) + \pi^2\kappa\left(2\sin\left(\pi x\right)\sin\left(\pi y\right)\right), \tag{8.72}$$

and applying homogeneous Dirichlet boundary conditions along the entire domain boundary. To ensure the problem is advection-dominated, the diffusion is set to $\kappa = 10^{-6}$. The problem is then characterized by the Péclet number $Pe = \frac{|\boldsymbol{a}|L}{\kappa} = 10^6$ where L is the length of the domain. Numerical solutions are calculated on grids of 2×2, 4×4, 8×8, 16×16, 32×32, 64×64, and 128×128 elements for coarse-scale polynomial degrees $k = 1, 2$ and subscale polynomial degrees $k_f = 1, 2$. The L^2-norms of the error in the coarse-scale solution and the subscale solution are presented in Fig. 8.1. We observe that both the coarse-scale and subscale solutions converge optimally under mesh refinement.

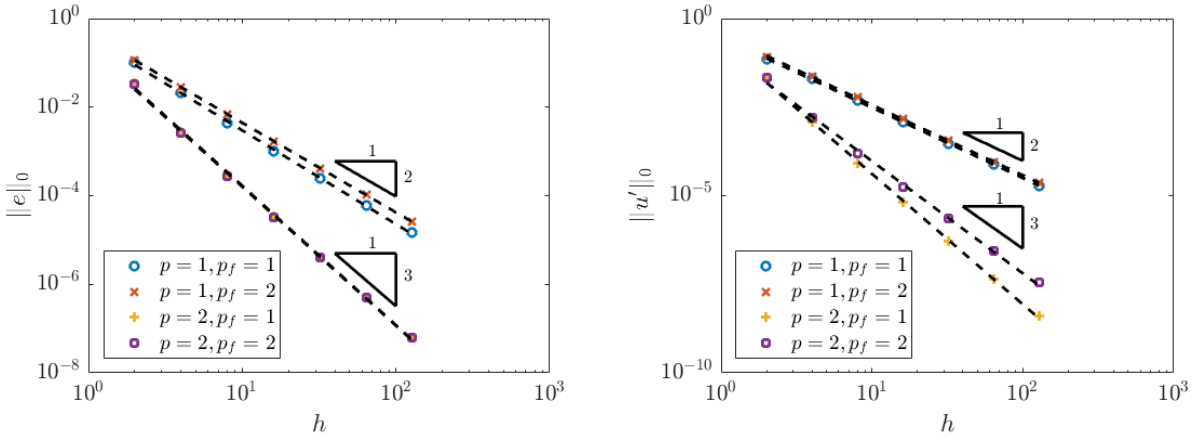

(a) L2-norm of error in coarse scales

(b) L2-norm of fine scales

Figure 8.1: Convergence for steady manufactured solution for varying polynomial degrees.

8.4.2 Steady Advection Skew to the Mesh

We next consider the classical two-dimensional advection skew to mesh problem. This problem is graphically depicted in Fig. 8.2. The Péclet number for the problem is $Pe = 10^6$, so the problem is advection-dominated. Throughout this subsection, we select $\theta = 45°$.

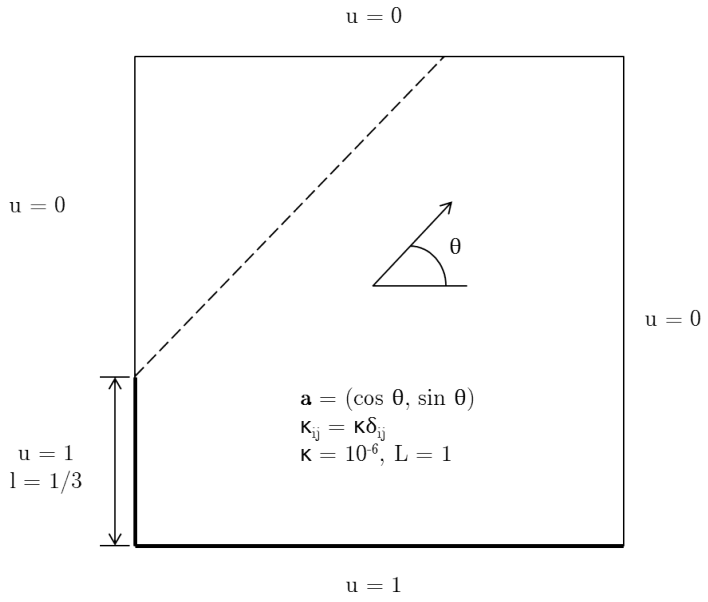

Figure 8.2: Problem setup for the two-dimensional advection skew to the mesh problem.

First, we explore the effect of mesh refinement. Solutions on uniform NURBS meshes with 32×32, 64×64, and 128×128 elements for both $k = 1$ and $k = 2$ are computed and compared. For each of the cases, the subscale polynomial degree is chosen to be $k_f = 1$. A representative solution for $k = 2$, $k_f = 1$, and a 64×64 mesh is shown in Fig. 8.3.

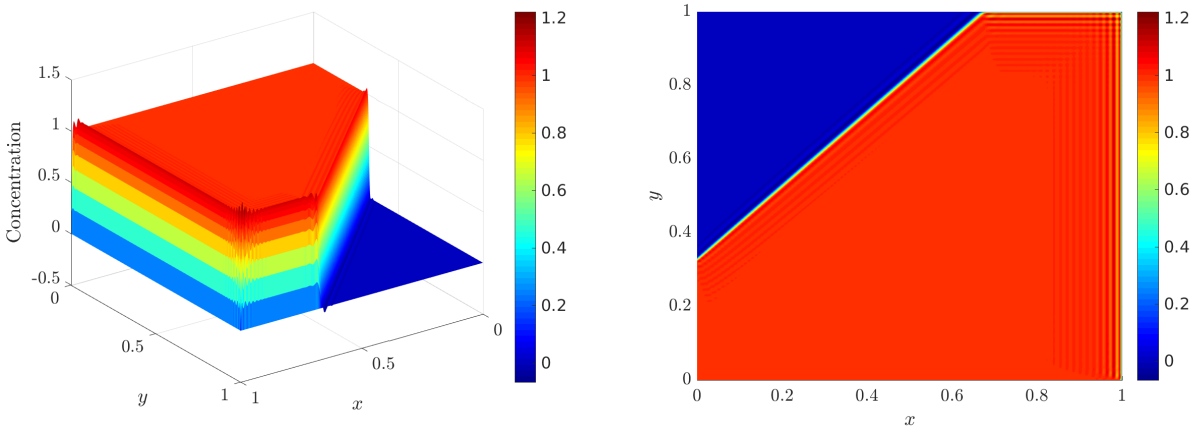

(a) Isometric view

(b) Overhead view

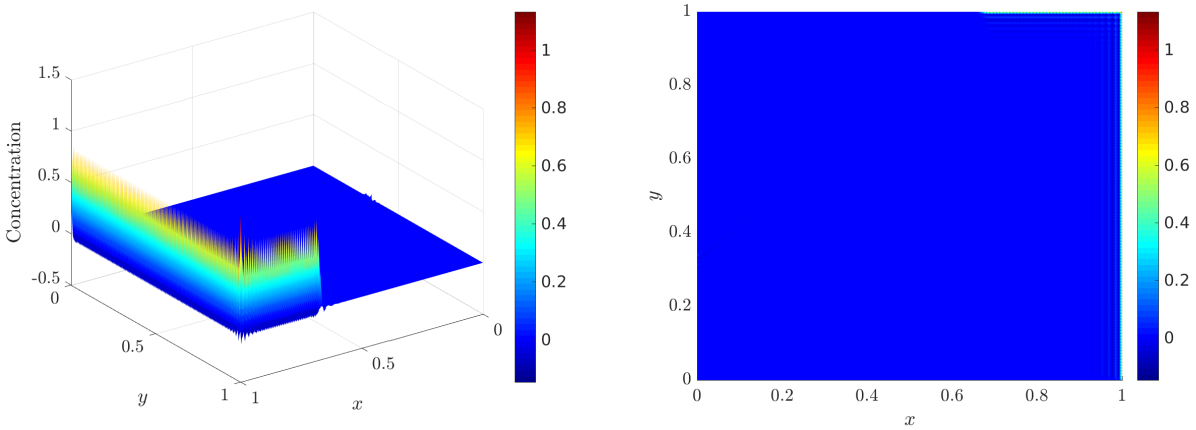

(c) Isometric view

(d) Overhead view

Figure 8.3: Coarse-scale (top) and subscale (bottom) solutions for the advection skew to the mesh problem for $k = 2$, $k_f = 1$, and $h = 1/64$.

The effect of mesh refinement is illustrated by comparison of the obtained solutions along the slice $y = 0.7$ in Fig. 8.4. The results are as expected. Refinement of the mesh allows for a more accurate representation of the boundary and internal layers. The results are polluted by the presence of oscillations near the boundary and internal layers, but for $k = 1$, these oscillations

are limited to a region of one or two elements away from the layers. For $k = 2$, the oscillations do infiltrate further into the domain, but it is our experience that these oscillations are not due to method instability but rather the fact that we are trying to fit the sharp gradients present in the boundary and internal layers. As isogeometric NURBS discretizations exhibit a high level of continuity, any oscillations due to overfitting such gradients are expected to extend into the domain in analogy with Gibbs' phenomena. Nonetheless, the oscillations decay in magnitude away from the layers and are still limited to a region of a fixed number of elements away from the layers. As we will later see, these oscillations can be greatly suppressed through the use of weak enforcement of Dirichlet boundary conditions.

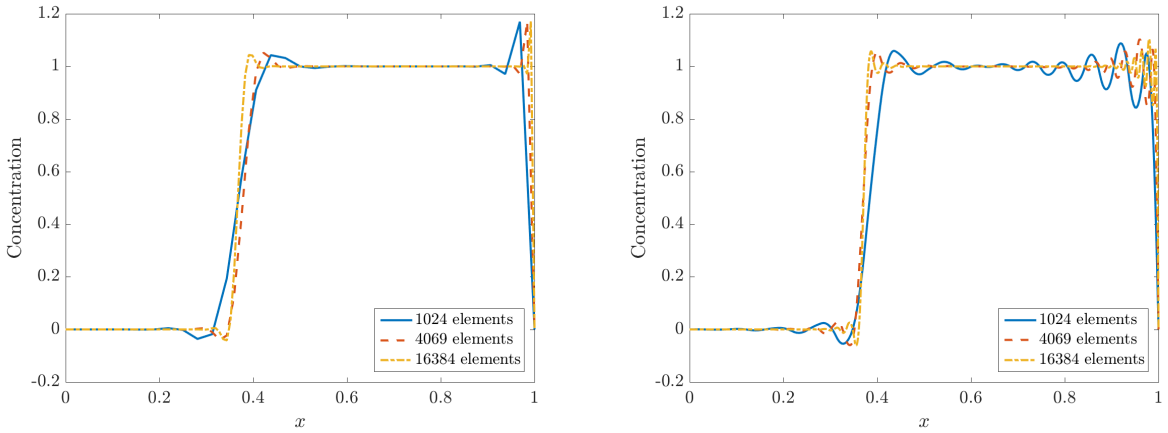

(a) Coarse-scale solution for $k = 1$, $k_f = 1$, and varying mesh size.

(b) Coarse-scale solution for $k = 2$, $k_f = 1$, and varying mesh size.

Figure 8.4: Coarse-scale solution along $y = 0.7$ for varying mesh sizes and coarse-scale polynomial degrees.

We now explore the effect of degree elevation. First, we examine the effect of coarse-scale degree elevation. Solutions for $k = 1, 2, 3$ with $k_f = 1$ on a uniform NURBS mesh with 64×64 elements are computed and compared. The effect of coarse-scale degree elevation is illustrated by comparison of the obtained solutions along the slice $y = 0.7$ in Fig. 8.5. Note that each of the coarse-scale solutions are able to capture the internal and boundary layers, and the coarse-scale solutions associated with higher polynomial degrees exhibit sharper representations of the

layers. However, the coarse-scale solutions associated with higher polynomial degrees also exhibit oscillations in the regions near the internal and boundary layers due to overfitting and Gibbs' phenomena. Next, we explore the effect of subscale degree elevation. Solutions for $k = 2$ with $k_f = 1, 2, 3$ are computed on a uniform NURBS mesh with 64×64 elements and compared. The effect of fine-scale degree elevation is illustrated by comparison of the obtained solutions along the slice $y = 0.7$ in Fig. 8.5. From the figure, it is seen that the choice of subscale polynomial degree does not greatly affect the coarse-scale solution. Consequently, it is recommended that one choose the lowest possible subscale polynomial degree in order to stabilize the higher-order coarse-scale solution at minimal computational cost.

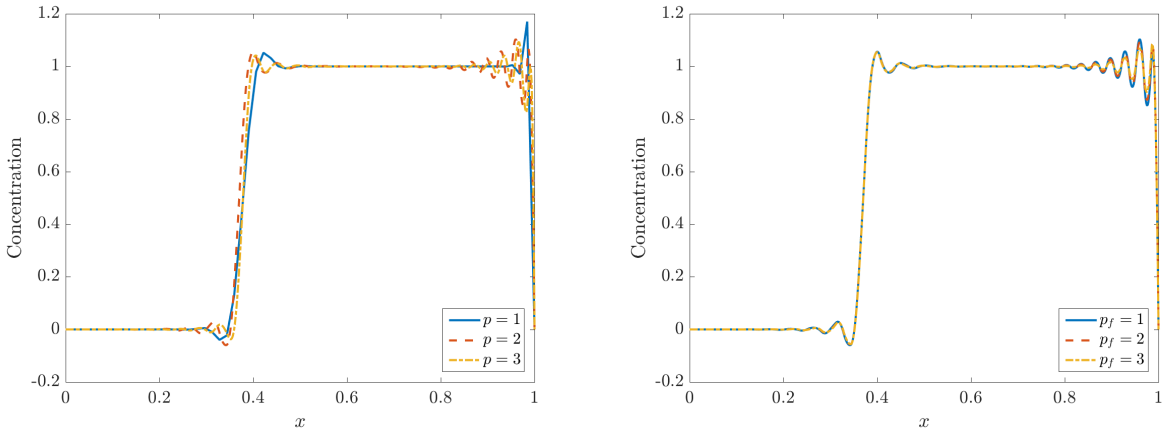

(a) Coarse-scale solution for $k_f = 1$, $h = 1/64$, and varying coarse-scale polynomial degrees.

(b) Coarse-scale solution for $k = 2$, $h = 1/64$, and varying subscale polynomial degrees.

Figure 8.5: Coarse-scale solution along $y = 0.7$ for varying coarse-scale and subscale polynomial degrees.

Heretofore, we have enforced the Dirichlet boundary conditions on the coarse-scale solution field in a strong manner. However, it has been noted in recent work that greatly enhanced results may be obtained by instead imposing these in a weak manner using a combination of upwinding and Nitsche's method [14, 15]. The resulting coarse-scale governing equation takes the form:

Coarse-Scale Governing Equation with Weak Boundary Condition Treatment:

$$\begin{aligned}
&\int_\Omega \frac{\partial \bar{u}}{\partial t}\bar{v} - \int_\Omega \left(\bar{u}+u'\right)\boldsymbol{a}\cdot\nabla\bar{v} + \int_\Omega \kappa\nabla\bar{u}\cdot\nabla\bar{v} + \int_{\Gamma_N} a_n\bar{u}\bar{v} \\
&- \int_{\Gamma_D} \kappa\nabla\bar{u}\cdot\boldsymbol{n}\bar{v} - \int_{\Gamma_D} \bar{u}\kappa\nabla\bar{v}\cdot\boldsymbol{n} + \sum_{K=1}^{n_{el}} \int_{\Gamma_K\cap\Gamma_D} \frac{C_{Nitsche}\kappa}{h_K}\bar{u}\bar{v} + \int_{\Gamma_D} a_n^+\bar{u}\bar{v} \\
&= \int_\Omega f\bar{v} + \int_{\Gamma_N} h\bar{v} - \int_{\Gamma_D} g\kappa\nabla\bar{v}\cdot\boldsymbol{n} + \sum_{K=1}^{n_{el}} \int_{\Gamma_K\cap\Gamma_D} \frac{C_{Nitsche}\kappa}{h_K} g\bar{v} - \int_{\Gamma_D} a_n^- g\bar{v} \\
&\qquad\qquad\qquad\qquad\qquad\qquad\qquad\qquad\qquad\qquad\qquad\qquad \text{for all } \bar{v}\in\bar{\mathcal{V}}
\end{aligned} \tag{8.73}$$

In the above equation, $C_{Nitsche}$ is a penalty constant that must be chosen sufficiently large for method stability, $a_n^+ = (\boldsymbol{a}\cdot\boldsymbol{n})^+ = \max\{\boldsymbol{a}\cdot\boldsymbol{n}, 0\}$, and $a_n^- = (\boldsymbol{a}\cdot\boldsymbol{n})^- = \min\{\boldsymbol{a}\cdot\boldsymbol{n}, 0\}$. Herein, we choose $C_{Nitsche} = 4p$. It should be mentioned that the discontinuous subscale model remains untouched if the Dirichlet boundary conditions on the coarse-scale solution are imposed weakly.

To assess the effect of weak boundary condition enforcement, we have computed solutions using both using strongly-enforced and weakly-enforced Dirichlet boundary conditions with $k = 2$ and $k_f = 1$ on a uniform NURBS mesh with 64×64 elements. The effect of boundary condition enforcement is illustrated by comparison of the obtained solutions along the slice $y = 0.7$ in Fig. 8.6. Note from the figure that there no longer remain any oscillations near the boundary layer if one employs a weak boundary condition enforcement. Moreover, while there remain oscillations near the internal layer, these oscillations are small in magnitude and limited to a region of a small number of elements away from the layer. Consequently, it is strongly advised to weakly enforce Dirichlet boundary conditions along portions of the boundary where a layer is expected.

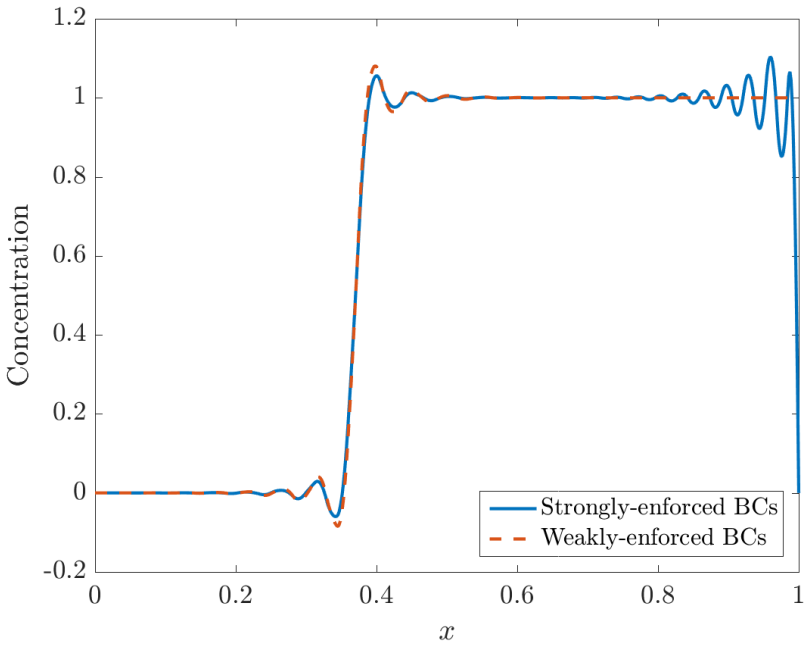

Figure 8.6: Coarse-scale solution along $y = 0.7$ for varying boundary-condition enforcement with $k = 2$, $k_f = 1$, and $h = 1/64$.

8.4.3 Steady Advection in a Quarter-annulus

We next consider a problem posed on a non-square geometry, namely the advection of a Gaussian curve in a quarter annulus. This problem is graphically depicted in Fig. 8.7. Here, r_i is the inner radius of the annulus and r_o is the outer radius of the annulus and they are chosen to be $r_i = 1$ and $r_o = 2$. The flow field for this problem is chosen to be $\boldsymbol{a} = (y, -x)$ and the diffusivity is chosen as $\kappa = 1 \times 10^6$ such that the problem is advection-dominated. Dirichlet boundary conditions are strongly enforced on the lower boundary of the annulus with

$$g\left(x, y = 0\right) = \frac{1}{\sigma\sqrt{2\pi}} \exp\left(\frac{(-x-\mu)^2}{2\sigma^2}\right), \tag{8.74}$$

where $\sigma = 0.05$ and $\mu = -1.5$. Traction-free Neumann boundary conditions are prescribed on the other three boundaries.

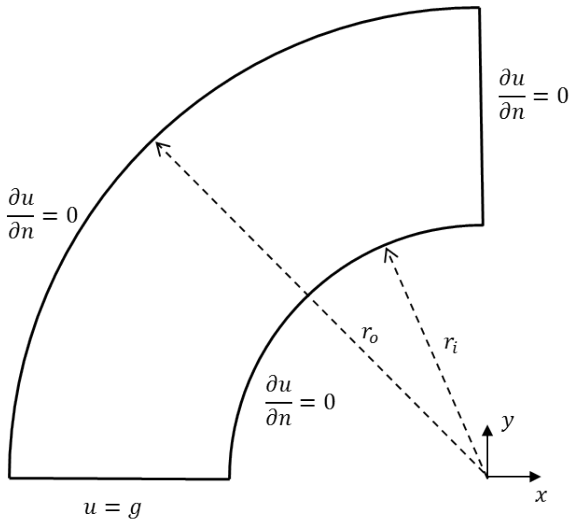

Figure 8.7: Problem setup for the advection in a quarter-annulus problem.

A typical solution corresponding to $k = 2$, $k_f = 1$, and a NURBS mesh of 64×64 elements is displayed in Fig. 8.8. From the figure, it is clear that the method is able to very accurately capture the solution free of oscillations on the curved geometry.

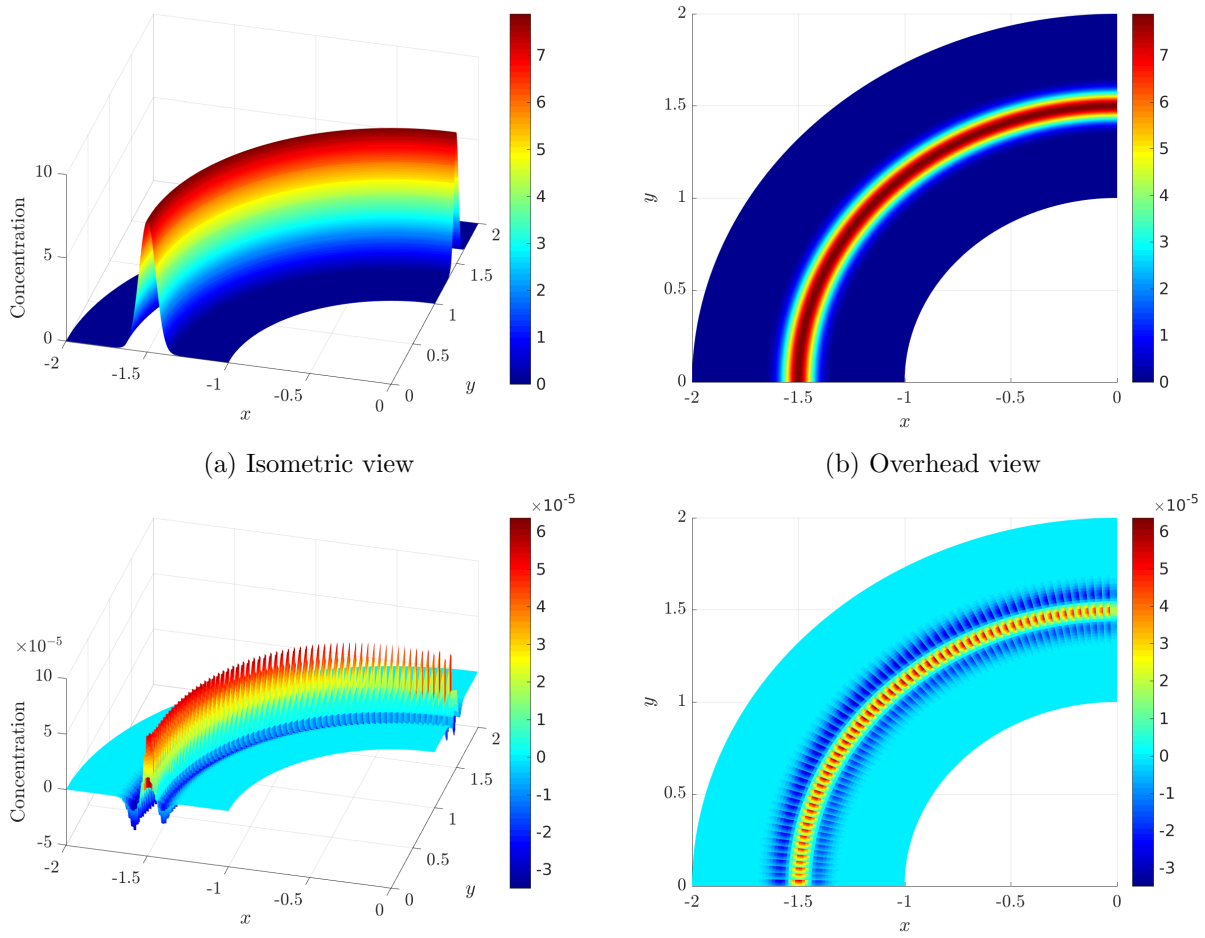

(a) Isometric view

(b) Overhead view

(c) Isometric view

(d) Overhead view

Figure 8.8: Coarse-scale (top) and subscale (bottom) solutions for the advection in a quarter-annulus problem for $k = 2$, $k_f = 1$, and a NURBS mesh of 64×64 elements.

8.4.4 Unsteady Advection of a Gaussian Hill

We now consider an unsteady scalar transport problem, namely the advection of a Gaussian hill in a rotating flow field. For this problem, the domain is $\Omega = [0,1] \times [0,1]$ and the flow field is given as $\boldsymbol{a} = (y - 0.5, x - 0.5)$. The initial scalar field is given as

$$u(x, y, 0) = \exp\left(-\frac{1}{2\sigma}\left((x - 0.5)^2 + (y - 0.25)^2\right)\right), \tag{8.75}$$

where $\sigma = 0.065$, and Dirichlet boundary conditions are strongly enforced along the entire boundary of the domain. Numerical solutions are calculated on a 64×64 NURBS mesh with coarse-scale polynomial degree $k = 2$ and subscale polynomial degree $k_f = 1$. Both the dynamic and quasi-static discontinuous subscale models were employed to stabilize the solution. Time-integration is carried out with the generalized-alpha method using a time step of $\Delta t = 0.005$ and $\rho_\infty = 1$ such that $\alpha_m = 0.5$, $\alpha_f = 0.5$, and $\gamma = 0.5$. The small time step is chosen such that the only source of error is spatial error.

Establishing the initial condition for this problem takes some care, and the approach differs between the dynamic and quasi-static models. For the quasi-static model, we do not require a time-history of the discontinuous subscale solution. Thus, only an initial condition for the coarse-scale solution field is required, and this is established through an L^2-projection of the exact initial condition. For the dynamic model, a time-history of the discontinuous subscale solution is required. Consequently, after an initial condition for the coarse-scale solution field is obtained, an initial condition for the discontinuous subscale solution is established through an L^2-projection of the difference between the exact initial condition and the coarse-scale initial condition.

8.4.4.1 Results for the Quasi-static Discontinuous Subscale Model

We first display results obtained using the quasi-static discontinuous subscale model. In Fig. 8.9, the concentration along the centerline of the hill (found at $y = 0.25$) is plotted for the initial solution and the solution after 1, 5, and 10 full revolutions ($t = 6.28, 31.40, 62.80$, respectively). It is clear that the method is able to preserve the hill with very high accuracy even after several

rotations. After one rotation, the peak is reduced to 0.997, representing a numerical dispersion of the peak of 0.3%. After ten rotations, the peak is reduced to 0.969, representing a numerical dispersion of the peak of 3.1%. There is also some slight skewing of the solution in the downwind direction.

8.4.4.2 Results for the Dynamic Discontinuous Subscale Model

We next display results obtained using the dynamic discontinuous subscale model. In Fig. 8.9, the concentration along the centerline of the hill (found at $y = 0.25$) is plotted for the initial solution and the solution after 1, 5, and 10 full revolutions ($t = 6.28, 31.40, 62.80$, respectively). Like the quasi-static model, it is clear that the method is superb in preserving the hill. After one rotation, the peak is reduced to 0.996, representing a numerical dispersion of the peak of 0.4%. After ten rotations, the peak is reduced to 0.965, representing a numerical dispersion of the peak of 3.5%. Again, like the quasi-static model, there is some slight skewing of the solution in the downwind direction. Curiously, the magnitude of the subscale solution is three orders less for the dynamic model than the quasi-static model, but the two models produce very similar results both quantitatively and qualitatively.

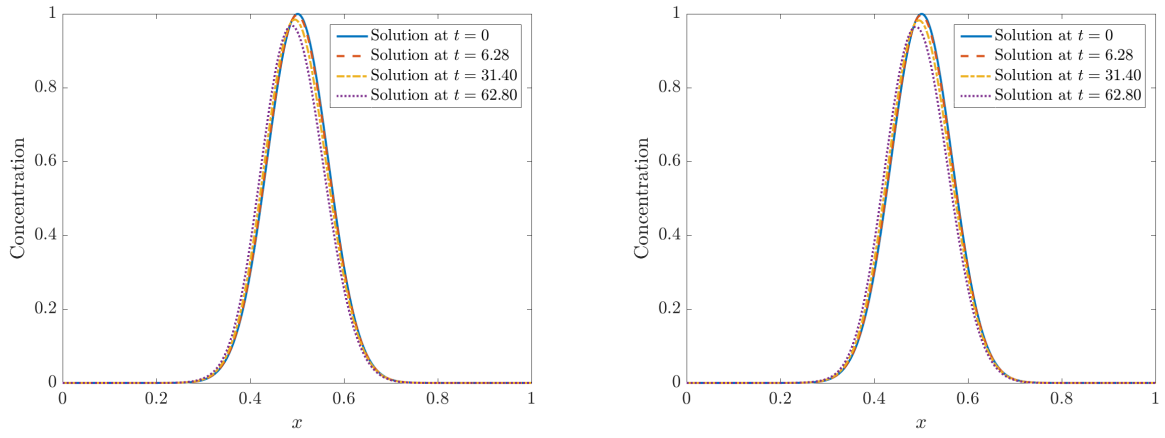

(a) Coarse-scale solution for the quasi-static model (b) Coarse-scale solution for the dynamic model

Figure 8.9: Coarse-scale solution for the unsteady advection of a Gaussian hill problem along $y = 0.25$ for $k = 2$, $k_f = 1$, and $h = 1/64$.

8.4.5 Unsteady Advancing Front

We finish by returning back to the advection skew to the mesh problem but in an unsteady context. Namely, we initialize the scalar field to be zero everywhere except at the Dirichlet boundary where the initial condition meets the specified boundary condition. We then let the solution evolve according to the problem specifications in Fig. 8.2. Since we expect a boundary layer to form for this problem, we elect to enforce the Dirichlet conditions in a weak fashion. For all our numerical results, a uniform NURBS mesh with 64×64 square elements was employed with a coarse-scale polynomial degree of $k = 2$ and a subscale polynomial degree of $k_f = 1$. Time-integration is carried out using the generalized-alpha method using a time step of $\Delta t = 0.01$ and $\rho_\infty = 1$ such that $\alpha_m = 0.5$, $\alpha_f = 0.5$, and $\gamma = 0.5$. We compute and compare solutions using both the dynamic and quasi-static discontinuous subscale models.

8.4.5.1 Results for the Quasi-static Discontinuous Subscale Model

Solutions for the advancing front problem solved with the quasi-static discontinuous subscale model at representative time steps of $t = 0, 0.51, 2.01$ are shown in Figs. 8.10 and 8.11. The coarse-scale solution converges to the steady-state solution as expected. The coarse-scale solution is quite accurate in the eyeball norm, though at each time step, minor oscillations are present near the internal layer similar to what was observed in the steady skew to the mesh problem. Additionally, the magnitude of the oscillations in the fine-scale solution at the final time-step correspond to roughly the same magnitude of the oscillations observed in the steady problem. This is expected, since we expect the steady state subscale solution to coincide with the subscale solution in the steady problem.

8.4.5.2 Results for the Dynamic Discontinuous Subscale Model

Solutions for the advancing front problem solved with the dynamic discontinuous subscale model at representative time steps of $t = 0, 0.51, 2.01$ are shown in Figs. 8.10 and 8.11. Again, the coarse-scale solution is quite accurate and converges to the steady-state solution as expected,

and minor oscillations are present near the internal layer similar to what was observed in the steady skew to the mesh problem. Surprisingly, the magnitude of the subscale solution is much smaller than the subscale solution computed using the quasi-static discontinuous subscale model at intermediate times, yet the obtained numerical results for the coarse-scale solution field are qualitatively and quantitatively similar. The coarse-scale solution field for the dynamic model does exhibit fewer oscillations than the coarse-scale field for the quasi-static model, particularly away from the boundary layer (e.g., near the spatial location $(x, y) = (1, 1)$ at time $t = 2.01$).

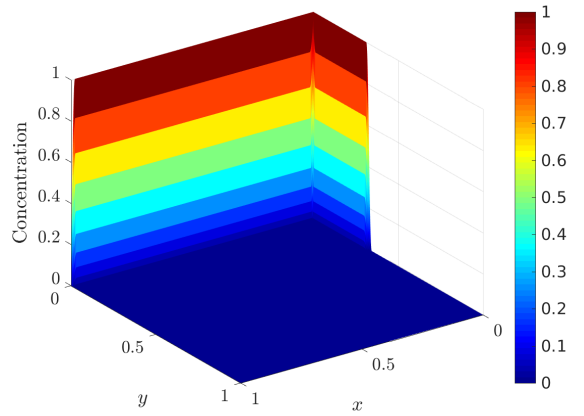

(a) Quasi-static model result at $t = 0$

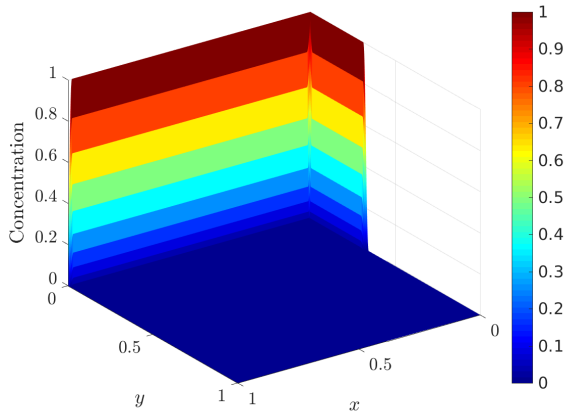

(b) Dynamic model result at $t = 0$

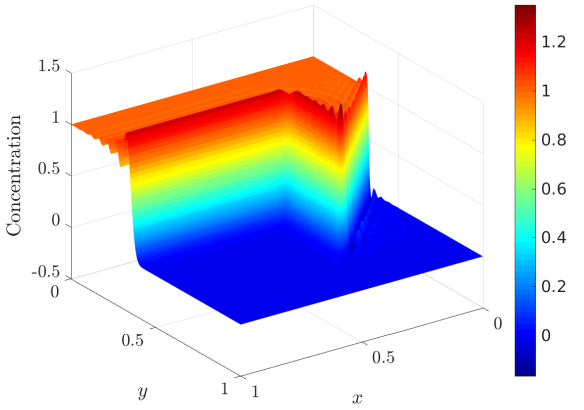

(c) Quasi-static model result at $t = 0.51$

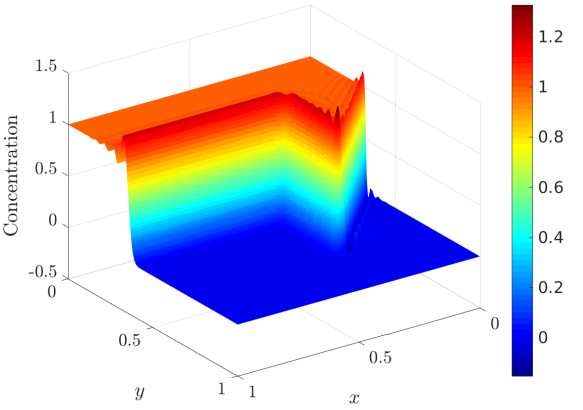

(d) Dynamic model result at $t = 0.51$

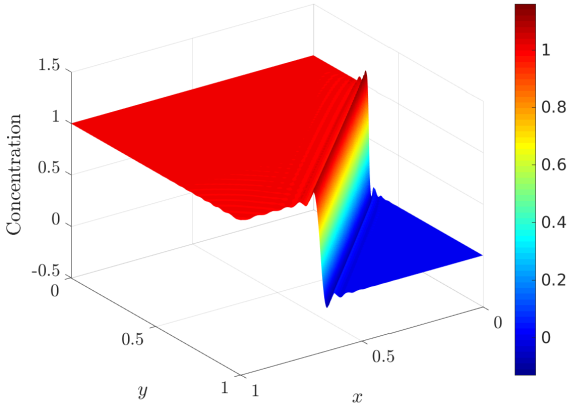

(e) Quasi-static model result at $t = 2.01$

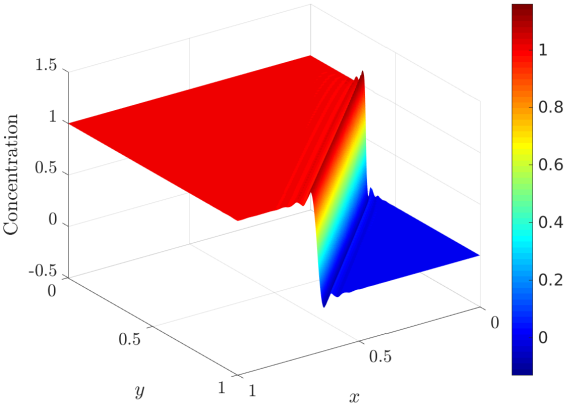

(f) Dynamic model result at $t = 2.01$

Figure 8.10: Coarse-scale solutions for the unsteady advancing front problem for $k = 2$, $k_f = 1$, and $h = 1/64$ at $t = 0, 0.51, 2.01$.

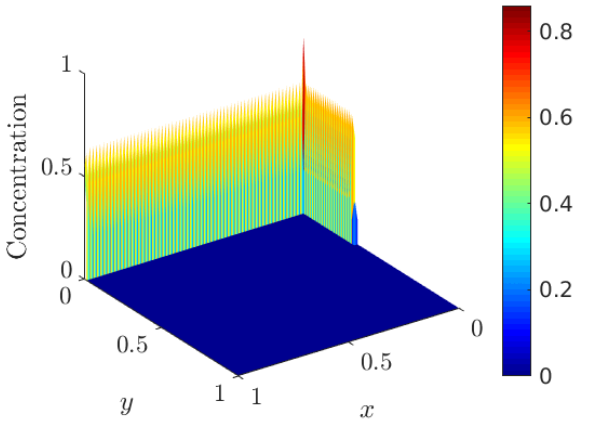

(a) Quasi-static model result at $t = 0$

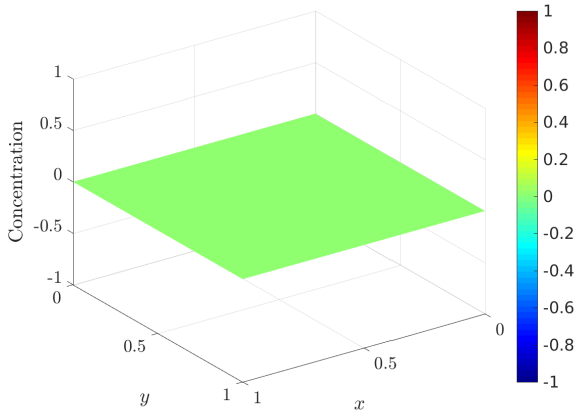

(b) Dynamic model result at $t = 0$

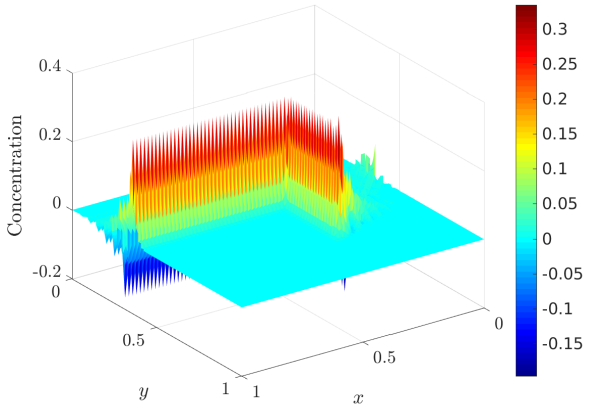

(c) Quasi-static model result at $t = 0.51$

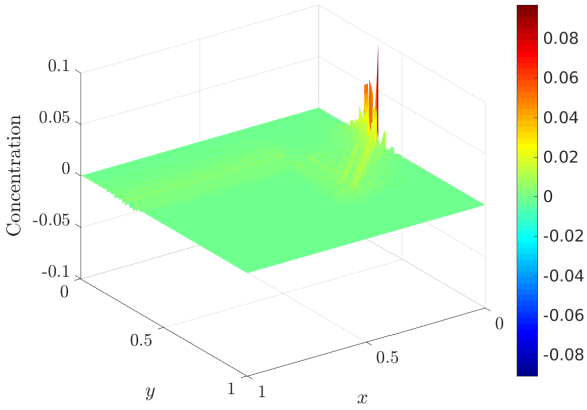

(d) Dynamic model result at $t = 0.51$

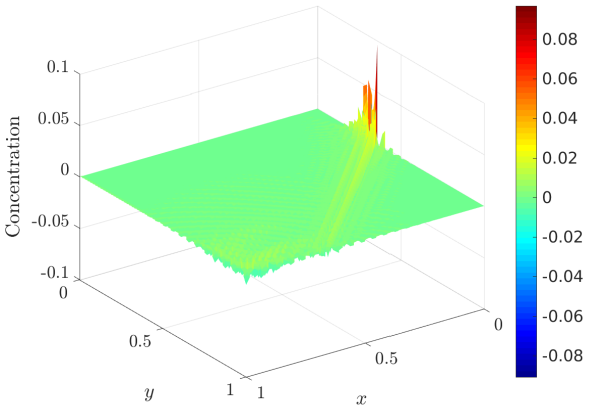

(e) Quasi-static model result at $t = 2.01$

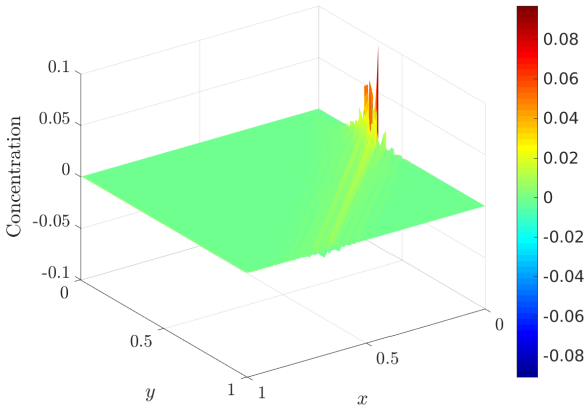

(f) Dynamic model result at $t = 2.01$

Figure 8.11: Subscale solutions for the unsteady advancing front problem for $k = 2$, $k_f = 1$, and $h = 1/64$ at $t = 0, 0.51, 2.01$.

8.5 Differential Subgrid Vortex Models

Encouraged by the positive results demonstrated for scalar transport, we wish to extend the concept of differential subgrid-scale modeling to LES of turbulent flows. Thus a new class of *differential subgrid vortex* models is proposed here. Using this approach, it is possible to account for effects such as advection and diffusion of the fine-scales. As a result, it is expected that these models will exhibit superior accuracy and stability over existing subgrid modeling methods. In subsections 8.5.1 and 8.5.1, we present two candidate differential subgrid vortex models for LES of turbulent flows.

8.5.1 Quasi-static Differential Subgrid Vortex Model

In the quasi-static differential subgrid vortex model, we approximate the fine-scale velocity as

$$\begin{aligned} \bar{\mathbf{u}} \cdot \nabla \mathbf{u}' - \nu \Delta \mathbf{u}' + \nabla p' &= -\text{Res}_m \left(\bar{\mathbf{u}}, \bar{p} \right) \quad \text{over} \quad \Omega_e \\ \nabla \cdot \mathbf{u}' &= 0 \quad \text{over} \quad \Omega_e, \end{aligned} \tag{8.76}$$

subject to the same boundary conditions as (5.16). The method of subgrid vortices is used to solve (8.76), solving the element fine-scale equation using a divergence-conforming discontinuous formulation with weakly-imposed Dirichlet boundary conditions [15].

8.5.2 Dynamic Differential Subgrid Vortex Model

In the dynamic differential subgrid vortex model, we seek to improve the approximation provided by the quasi-static differential subgrid vortex model by including the time evolution of the fine-scale velocity. The resulting approximation for the fine-scale velocity is

$$\begin{aligned} \frac{\partial \mathbf{u}'}{\partial t} + \bar{\mathbf{u}} \cdot \nabla \mathbf{u}' - \nu \Delta \mathbf{u}' + \nabla p' &= -\text{Res}_m Bazilevs07b \left(\bar{\mathbf{u}}, \bar{p} \right) \quad \text{over} \quad \Omega_e \\ \nabla \cdot \mathbf{u}' &= 0 \quad \text{over} \quad \Omega_e, \end{aligned} \tag{8.77}$$

subject to the same boundary conditions as (5.16). As in the quasi-static differential subgrid vortex model, the method of subgrid vortices is used to solve (8.76), solving the element fine-scale equation using a divergence-conforming discontinuous formulation.

Chapter 9

Multigrid Methods

Despite the promise of divergence-conforming discretizations for the spatial discretization of fluid flow problems, very little research has been conducted so far in the area of efficient linear solvers for these discretizations. In fact, only the performance of Krylov subspace methods in conjunction with block preconditioners has been investigated in prior work [46, 47]. In this chapter, we introduce an optimally efficient linear solution procedure for divergence-conforming discretizations of the generalized Stokes and Oseen problems. It should be noted that there are many different candidates in this regard. For instance, there exist efficient physics-based splitting methods such as the inexact Uzawa algorithm [56]. However, these techniques rely on suitable Schur complement approximations which can be difficult to design in the context of generalized Oseen flow. Alternatively, one can employ a multigrid method in conjunction with a Vanka smoother [134], a Uzawa smoother [68], or a Braess-Sarazin smoother [22]. While these techniques generally do not require accurate Schur complement approximations, they typically involve specially tuned relaxation parameters. Perhaps more concerning is the fact that all of the aforementioned procedures do not return a pointwise-divergence free velocity field unless the linear solver is fully converged.

To overcome the issues associated with the aforementioned linear solution procedures, we present a geometric multigrid methodology which relies upon Schwarz-style smoothers [53] in conjunction with specially defined overlapping subdomains that respect the underlying topological structure of the generalized Stokes and Oseen problems. This methodology is inspired by multi-

grid and auxiliary space preconditioning methodologies for divergence-conforming discontinuous Galerkin formulations of Stokes flow [6, 98, 99, 97] and multigrid methodologies for compatible finite element discretizations of Darcy and Maxwell problems [5, 76]. We prove that our methodology yields a pointwise divergence-free velocity field independent of the number of pre-smoothing steps, post-smoothing steps, grid levels, or cycles in a V-cycle implementation. We also demonstrate by numerical example that our methodology is optimally efficient and robust in that it exhibits convergence rates independent of the grid resolution and flow parameters for the generalized Stokes problem as well as the generalized Oseen problem, provided it is not advection-dominated.

9.1 Temporal Discretization of the Navier-Stokes Equations and the Generalized Stokes and Oseen Problems

To motivate the need for efficient linear solvers for the generalized Stokes and Oseen problems, we first demonstrate how such problems arise through semi-implicit temporal discretization of the incompressible Navier-Stokes equations subject to homogeneous Dirichlet boundary conditions, first introduced in (2.1). To discretize (2.1) in time, we first define a sequence of time instances $t_0 < t_1 < t_2 < \ldots < t_N$ such that $t_0 = 0$ and $t_N = T$, and we denote the velocity and pressure solutions at the n^{th} time instance as $\mathbf{u}^{(n)}$ and $p^{(n)}$ respectively for $n = 0, \ldots, N$. We further define $t_{n+1/2} = \frac{t_n + t_{n+1}}{2}$. Without loss of generality, we assume that the time instances are equi-spaced, and we define the time step size to be $\Delta t = t_{n+1} - t_n$. The velocity solution at $N = 0$ is given by $\mathbf{u}^{(0)} = \mathbf{u}_0$, while to find the velocity and pressure solutions at each subsequent time instance, we must discretize the Navier-Stokes problem in time. We discuss two demonstrative semi-implicit temporal discretization schemes herein, though the proceeding discussion also applies to other semi-implicit temporal discretization schemes[1] .

Let us first consider the standard Crank-Nicolson/Adams-Bashforth scheme [75]. In this

[1] With a fully implicit time discretization scheme, one must turn to a nonlinear solution procedure such as Newton's method. However, with Newton's method, one solves a sequence of generalized Oseen problems. Hence, the multigrid methodology discussed here can also be employed to solve these problems.

approach, a central difference approximation of the unsteady term and linear interpolation approximations of the diffusive and pressure force terms are employed:

$$\begin{aligned}
\frac{\partial \mathbf{u}}{\partial t}(t_{n+1/2}) &\approx \frac{\mathbf{u}^{(n+1)} - \mathbf{u}^{(n)}}{\Delta t} \\
\Delta \mathbf{u}(t_{n+1/2}) &\approx \frac{\Delta \mathbf{u}^{(n+1)} + \Delta \mathbf{u}^{(n)}}{2} \\
\nabla p(t_{n+1/2}) &\approx \frac{\nabla p^{(n+1)} + \nabla p^{(n)}}{2}
\end{aligned}$$

The advection term at $t_{n+1/2}$ is alternatively approximated using Taylor-series expansions involving time instances t_{n-1} and t_n, resulting in[2]

$$(\mathbf{u} \cdot \nabla \mathbf{u})(t_{n+1/2}) \approx \frac{3}{2}\mathbf{u}^{(n)} \cdot \nabla \mathbf{u}^{(n)} - \frac{1}{2}\mathbf{u}^{(n-1)} \cdot \nabla \mathbf{u}^{(n-1)}$$

Collecting the above approximations, we find that the resulting generalized Stokes system holds for each $n = 0, \ldots, N-1$:

$$\begin{aligned}
\sigma \mathbf{u}^{(n+1)} - \nu \Delta \mathbf{u}^{(n+1)} + \nabla p^{(n+1)} &= \mathbf{f}_{GS}^{(n+1)} \quad \text{for } \mathbf{x} \in \Omega \\
\nabla \cdot \mathbf{u}^{(n+1)} &= 0 \quad \text{for } \mathbf{x} \in \Omega \\
\mathbf{u}^{(n+1)} &= \mathbf{0} \quad \text{for } \mathbf{x} \in \Gamma
\end{aligned} \tag{9.1}$$

where $\sigma = \sigma = {}^2/\Delta t$ and

$$\mathbf{f}_{GS}^{(n+1)} = \mathbf{f}(t_{n+1/2}) + \sigma \mathbf{u}^{(n)} - 3\mathbf{u}^{(n)} \cdot \nabla \mathbf{u}^{(n)} + \mathbf{u}^{(n-1)} \cdot \nabla \mathbf{u}^{(n-1)} + \nu \Delta \mathbf{u}^{(n)} - \nabla p^{(n)}. \tag{9.2}$$

The above generalized Stokes system is reaction-dominated for small time step sizes and diffusion-dominated for large time step sizes. We demonstrate later that our geometric multigrid methodology is robust for both of these regimes.

The advantage of the Crank-Nicolson/Adams-Bashforth scheme [9, 50] is that the advection term is handled in a purely explicit manner. After spatial discretization, this leads to a symmetric matrix problem. However, the disadvantage of the scheme is that it is stable only if the time-step is chosen sufficiently small as to satisfy a CFL condition. With this in mind, we next consider

[2] This approximation is not properly defined for $n = 0$. Consequently, the approximation is replaced by $\mathbf{u}^{(n)} \cdot \nabla \mathbf{u}^{(n)}$ for $n = 0$ in practice.

an unconditionally stable semi-implicit scheme introduced by Guermond [73]. In this scheme, the unsteady, diffusive, and pressure force terms are approximated as before, but the advection term is approximated as follows[3] :

$$(\mathbf{u}\cdot\nabla\mathbf{u})\,(t_{n+1/2}) \approx \left(\frac{3}{2}\mathbf{u}^{(n)} - \frac{1}{2}\mathbf{u}^{(n-1)}\right)\cdot\nabla\left(\frac{\mathbf{u}^{(n+1)}+\mathbf{u}^{(n)}}{2}\right).$$

Note that the advection velocity is approximated in an explicit manner while the gradient is approximated in an implicit manner. Collecting the above approximations, we find that the resulting generalized Oseen system holds for each $n = 0, \ldots, N-1$:

$$\begin{aligned} \sigma\mathbf{u}^{(n+1)} + \mathbf{a}^{(n+1)}\cdot\nabla\mathbf{u}^{(n+1)} - \nu\Delta\mathbf{u}^{(n+1)} + \nabla p^{(n+1)} &= \mathbf{f}_{GO}^{(n+1/2)} \quad \text{for } \mathbf{x}\in\Omega \\ \nabla\cdot\mathbf{u}^{(n+1)} &= 0 \quad \text{for } \mathbf{x}\in\Omega \\ \mathbf{u}^{(n+1)} &= \mathbf{0} \quad \text{for } \mathbf{x}\in\Gamma \end{aligned} \tag{9.3}$$

where $\sigma = 2/\Delta t$, $\mathbf{a}^{(n+1)} = \frac{3}{2}\mathbf{u}^{(n)} - \frac{1}{2}\mathbf{u}^{(n-1)}$, and

$$\mathbf{f}_{GO}^{(n+1)} = \mathbf{f}(t_{n+1/2}) + \sigma\mathbf{u}^{(n)} - \mathbf{a}^{(n+1)}\cdot\nabla\mathbf{u}^{(n)} + \nu\Delta\mathbf{u}^{(n)} - \nabla p^{(n)}. \tag{9.4}$$

In constrast with the generalized Stokes system obtained earlier, the above system admits different behavior based on not only the scalars σ and ν but also the advection velocity $\mathbf{a}^{(n+1)}$. We demonstrate later that our geometric multigrid methodology is robust for this system provided it is not advection-dominated. This holds if a CFL-like condition is satisfied.

9.2 Spatial Discretization of the Generalized Stokes and Oseen Problems

Now that we have motivated the need for efficient linear solvers for the generalized Stokes and Oseen problems, we turn to the question of spatial discretization. In this section, we present a mixed Galerkin discretization for the generalized Stokes and Oseen problems.

[3] This approximation is also not properly defined for $n = 0$. Consequently, the approximation is replaced by $\mathbf{u}^{(n)}\cdot\nabla\left(\left(\mathbf{u}^{(n)}+\mathbf{u}^{(n+1)}\right)/2\right)$ for $n = 0$ in practice.

9.2.1 Weak Formulation of the Generalized Stokes and Oseen Problems

To begin, we must state a weak formulation for the generalized Stokes and Oseen Problems. We strictly consider the case of homogeneous Dirichlet boundary conditions without loss of generality. As in Chapter 2, we utilize the velocity and pressure test spaces $\mathbf{H}_0^1(\Omega)$ and $L_0^2(\Omega)$ and we assume $\sigma, \nu \in \mathbb{R}_+$, $\mathbf{a} \in \mathbf{H}_0^1(\Omega)$, and $\mathbf{f} \in \mathbf{L}^2(\Omega)$. Additionally, we assume that the advection velocity is divergence-free, that is, $\nabla \cdot \mathbf{a} \equiv 0$. With these assumptions in hand, the weak form of the generalized Stokes or Oseen problem is stated as follows: Find $\mathbf{u} \in \mathbf{H}_0^1(\Omega)$ and $p \in L_0^2(\Omega)$ such that

$$a(\mathbf{v}, \mathbf{u}) - b(\mathbf{v}, p) + b(\mathbf{u}, q) = \ell(\mathbf{v}) \tag{9.5}$$

for all $\mathbf{v} \in \mathbf{H}_0^1(\Omega)$ and $q \in L_0^2(\Omega)$ where

$$a(\mathbf{v}, \mathbf{u}) := \begin{cases} \displaystyle\int_\Omega \sigma \mathbf{v} \cdot \mathbf{u} \; d\Omega + \int_\Omega \nu \nabla \mathbf{v} : \nabla \mathbf{u} \; d\Omega & \text{generalized Stokes} \\ \displaystyle\int_\Omega \sigma \mathbf{v} \cdot \mathbf{u} \; d\Omega + \int_\Omega \mathbf{v} \cdot (\mathbf{a} \cdot \nabla \mathbf{u}) \; d\Omega + \int_\Omega \nu \nabla \mathbf{v} : \nabla \mathbf{u} \; d\Omega & \text{generalized Oseen} \end{cases}$$

$$b(\mathbf{v}, p) := \int_\Omega (\nabla \cdot \mathbf{v}) \, p \; d\Omega$$

$$\ell(\mathbf{v}) := \int_\Omega \mathbf{v} \cdot \mathbf{f} d\Omega$$

9.2.2 Mixed Galerkin Approximation of the Generalized Stokes and Oseen Problems

To discretize in space using a mixed Galerkin formulation, we first must specify finite-dimensional approximation spaces for the velocity and pressure fields. We denote these spaces as $\mathbf{V}_h \subset \mathbf{H}_0^1(\Omega)$ and $\mathrm{Q}_h \subset L_0^2(\Omega)$ respectively, where we opt to use isogeometric B-spline spaces as described in Chapter 3. With approximation spaces defined, the mixed Galerkin formulation of the generalized Stokes or Oseen problem is stated as follows: Find $\mathbf{u}_h \in \mathbf{V}_h$ and $p_h \in \mathrm{Q}_h$ such that

$$a(\mathbf{v}_h, \mathbf{u}_h) - b(\mathbf{v}_h, p_h) + b(\mathbf{u}_h, q_h) = \ell(\mathbf{v}_h) \tag{9.6}$$

for all $\mathbf{v}_h \in \mathbf{V}_h$ and $q \in \mathrm{Q}_h$.

9.3 B-spline Refinement

One more concept needs to be introduced before proceeding forward, namely the concept of B-spline refinement. For a fixed set of polynomial degrees, B-spline refinement is carried out by a process referred to as knot insertion [71]. In the univariate setting, we start with a particular knot vector Ξ and then insert a sequence of knots to arrive at a refined knot vector $\tilde{\Xi}$ such that $\Xi \subset \tilde{\Xi}$. The B-spline basis functions associated with the original knot vector, denoted as $\left\{\hat{N}_{i_p}(\xi)\right\}_{i=1}^{n}$, can be represented as linear combinations of the basis functions associated with the refined knot vector, denoted as $\left\{\tilde{N}_{i,p}(\xi)\right\}_{i=1}^{\tilde{n}}$, using a transformation matrix $\mathbf{T}$. This relationship is expressed mathematically as

$$\hat{N}_{i,p}(\xi) = \sum_{j=1}^{\tilde{n}} [\mathbf{T}]_{ij} \tilde{N}_{j,p}(\xi)$$

for $i = 1, \ldots, n$. Consequently, if a B-spline function takes the form

$$\hat{u}(\xi) = \sum_{i=1}^{n} \hat{u}_i \hat{N}_{i,p}(\xi),$$

it can be alternately be represented as

$$\hat{u}(\xi) = \sum_{j=1}^{\tilde{n}} \tilde{u}_j \tilde{N}_{j,p}(\xi),$$

where

$$\tilde{u}_j = \sum_{i=1}^{n} [\mathbf{T}]_{ij} \hat{u}_i$$

for $j = 1, \ldots, \tilde{n}$. Figure 9.1 depicts the action of knot insertion for univariate quadratic B-splines. B-spline refinement in the multivariate setting (including the compatible B-spline setting) is carried out in a tensor-product fashion, and the transformation matrix $\mathbf{T}$ takes the same form in both the parametric domain and the physical domain. There exist a variety of algorithms capable of performing knot insertion [71, 112, 131] which can be used to construct the transformation matrix $\mathbf{T}$, so we do not discuss this construction further.

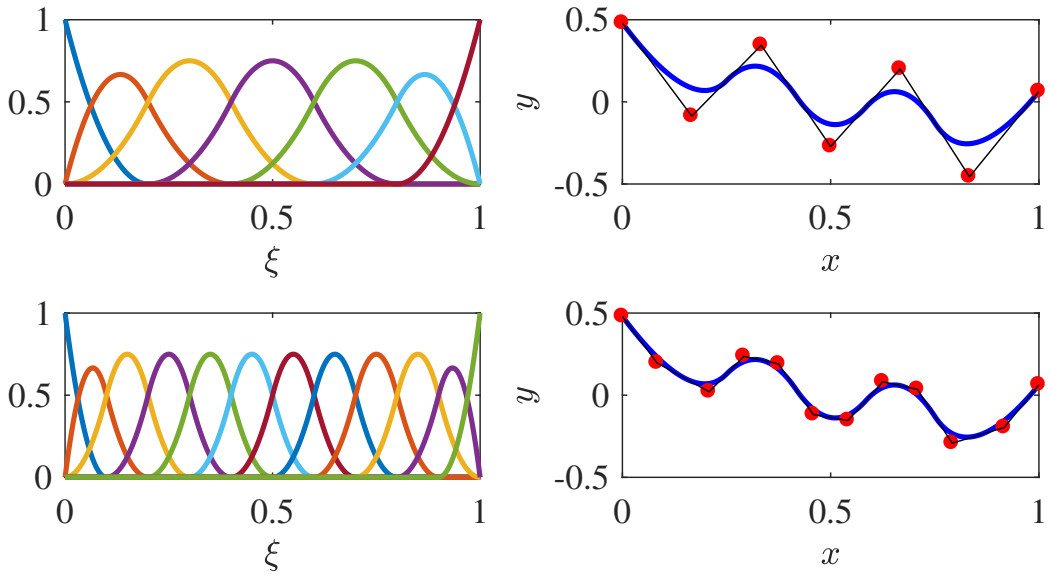

Figure 9.1: The action of knot insertion for univariate quadratic B-splines. Top Left: The original quadratic B-spline basis with $\Xi = (0, 0, 0, .2, .4, .6, .8, 1, 1, 1)$. Top Right: A B-spline function expressed in terms of the original quadratic B-spline basis. Bottom Left: The refined quadratic B-spline basis with $\tilde{\Xi} = (0, 0, 0, .1, .2, .3, .4, .5, .6, .7, .8, .9, 1, 1, 1)$ (bottom, left). Bottom right: The same B-spline function as illustrated in the top right panel but expressed in terms of the refined quadratic B-spline basis.

9.4 A Structure-preserving Geometric Multigrid Methodology

At last, we are ready to present our geometric multigrid methodology for divergence-conforming discretizations of the generalized Stokes and Oseen problems. We begin this section by reviewing the basics of the geometric multigrid approach as well as the required components in the setting of a divergence-conforming discretization. Then, we introduce the Schwarz-style smoothers which our methodology leans upon. We then show that our methodology preserves the divergence-free constraint on the velocity field and that it effectively ellipticizes the underlying system of interest. We limit our discussion to the V-cycle algorithm, though our approach can also be applied within a W-cycle or Full Multigrid framework [31].

9.4.1 Nested B-spline Stokes Complexes, Intergrid Transfer Operators, and the V-Cycle Algorithm

Assume that we have a sequence of nested B-spline Stokes complexes that have been obtained through knot insertion. We denote the discrete velocity and pressure spaces associated with this sequence as $\{\mathbf{V}_\ell\}_{\ell=0}^{n_\ell}$ and $\{\mathrm{Q}_\ell\}_{\ell=0}^{n_\ell}$ respectively where n_ℓ is the number of levels, and we note that

$$\mathbf{V}_0 \subset \mathbf{V}_1 \subset \ldots \subset \mathbf{V}_{n_\ell}$$

$$\mathrm{Q}_0 \subset \mathrm{Q}_1 \subset \ldots \subset \mathrm{Q}_{n_\ell}$$

and

$$\nabla \cdot \mathbf{V}_\ell = \mathrm{Q}_\ell$$

for each $\ell = 0, \ldots, n_\ell$. Level $\ell = 0$ corresponds to the coarsest mesh while level $\ell = n_\ell$ corresponds to the finest mesh. The action of knot insertion not only allows for B-spline refinement, but it also provides the intergrid transfer operators associated with a geometric multigrid method. Namely, we can build prolongation operators

$$P_\ell^v : \mathbf{V}_\ell \to \mathbf{V}_{\ell+1} \quad \text{and} \quad P_\ell^q : \mathrm{Q}_\ell \to \mathrm{Q}_{\ell+1}$$

for $\ell = 0, \ldots, n_\ell - 1$ using the construction provided in Subsection 9.3. We encode the action of these prolongation operators in the matrices $\mathbf{P}_\ell^v$ and $\mathbf{P}_\ell^q$ such that the following refinement operations hold:

$$\mathbf{N}_{i,\ell}^v(\boldsymbol{\xi}) = \sum_j [\mathbf{P}_\ell^v]_{ji} \mathbf{N}_{j,\ell+1}^v(\boldsymbol{\xi})$$

$$N_{i,\ell}^q(\boldsymbol{\xi}) = \sum_j [\mathbf{P}_\ell^q]_{ji} N_{j,\ell+1}^q(\boldsymbol{\xi})$$

for $\ell = 0, \ldots, n_\ell - 1$, where $\left\{\mathbf{N}_{i,\ell}^v\right\}_{i=1}^{n_{v,\ell}}$ and $\left\{N_{i,\ell}^q\right\}_{i=1}^{n_{q,\ell}}$ denote the velocity and pressure B-spline basis functions associated with level ℓ. Moreover, the degrees of freedom associated with pressure

and velocity fields on the ℓ^{th} level can be transferred to the $(\ell+1)^{\text{st}}$ level via the expressions:

$$\mathbf{u}_{\ell+1} = \mathbf{P}_\ell^v \mathbf{u}_\ell$$

$$\mathbf{p}_{\ell+1} = \mathbf{P}_\ell^q \mathbf{p}_\ell.$$

As is standard with a Galerkin formulation, restriction operators are constructed as the adjoint or transpose of the prolongation operators, namely $R_{\ell+1}^v = (P_\ell^v)^*$, $R_{\ell+1}^q = \left(P_\ell^q\right)^*$, $\mathbf{R}_{\ell+1}^v = (\mathbf{P}_\ell^v)^T$, and $\mathbf{R}_{\ell+1}^q = \left(\mathbf{P}_\ell^q\right)^T$ for $\ell = 0, \ldots, n_\ell - 1$. Finally, we define a prolongation matrix $\mathbf{P}_\ell$ for the full group variable such that

$$\mathbf{U}_{\ell+1} = \begin{bmatrix} \mathbf{u}_{\ell+1} \\ \mathbf{p}_{\ell+1} \end{bmatrix} = \begin{bmatrix} \mathbf{P}_\ell^v & \mathbf{0} \\ \mathbf{0} & \mathbf{P}_\ell^q \end{bmatrix} \begin{bmatrix} \mathbf{u}_\ell \\ \mathbf{p}_\ell \end{bmatrix} = \mathbf{P}_\ell \mathbf{U}_\ell$$

for $\ell = 0, \ldots, n_\ell - 1$. The corresponding restriction matrix for level ℓ is given by $\mathbf{R}_{\ell+1} = (\mathbf{P}_\ell)^T$.

We need a few more components before stating the multigrid V-cycle algorithm for our discretization scheme. First of all, we need to form the matrix system associated with the finest level, $\mathbf{KU} = \mathbf{F}$. We then form the system matrices associated with coarser levels via the relation $\mathbf{K}_\ell = \mathbf{R}_{\ell+1}\mathbf{K}_{\ell+1}\mathbf{P}_\ell$ for $\ell = 0, \ldots, n_\ell - 1$ where $\mathbf{K}_{n_\ell} = \mathbf{K}$. Second of all, we need to choose a smoother for each level ℓ which we encode in a smoothing matrix $\mathbf{S}_\ell$, and and we need to select a number of pre-smoothing steps ν_1 and post-smoothing steps ν_2. Third of all, we need to choose a suitable initial guess $\mathbf{U}$ for the solution on the finest level. Then, one V-cycle corresponds to a single call of the form $\text{MGV}(n_\ell, \mathbf{U}, \mathbf{F})$ to the recursive function defined below [31].

Algorithm 1 Multigrid V-Cycle Algorithm

function MGV$(\ell, \mathbf{U}, \mathbf{F})$
  if $\ell = 0$ **then**
    $\mathbf{U} = \mathbf{K}_\ell^{-1}\mathbf{F}$ ▷ Exact System Solution
  else
    for $i = 1$ to ν_1 **do**
      $\mathbf{U} \leftarrow \mathbf{U} + \mathbf{S}_\ell^{-1}(\mathbf{F} - \mathbf{K}_\ell\mathbf{U})$ ▷ Pre-Smoothing
    end for
    $\mathbf{G} = \mathbf{R}_\ell(\mathbf{F} - \mathbf{K}_\ell\mathbf{U})$ ▷ Restriction of Residual to Coarse Grid
    $\Delta\mathbf{U} = \mathbf{0}$ ▷ Coarse Grid Correction Initialization
    MGV$(\ell - 1, \Delta\mathbf{U}, \mathbf{G})$ ▷ Coarse Grid Correction Evaluation
    $\mathbf{U} \leftarrow \mathbf{U} + \mathbf{P}_{\ell-1}\Delta\mathbf{U}$ ▷ Update of Solution
    for $i = 1$ to ν_2 **do**
      $\mathbf{U} \leftarrow \mathbf{U} + \mathbf{S}_\ell^{-1}(\mathbf{F} - \mathbf{K}_\ell\mathbf{U})$ ▷ Post-Smoothing
    end for
  end if
end function

Note that the solution $\mathbf{U}$ is updated within the algorithm stated above. Hence, additional V-cycles simply correspond to additional calls of the form MGV$(n_\ell, \mathbf{U}, \mathbf{F})$.

9.4.2 Overlapping Schwarz Smoothers on Compatible Subdomains

At this juncture, we have not yet determined what smoother to employ. We turn to the use of overlapping Schwarz smoothers [53] with specially chosen overlapping subdomains which respect the underlying topological structure of the generalized Stokes and Oseen problems [99]. Namely, for each level ℓ, we define a collection of subdomains $\{\Omega_{i,\ell}\}_i$ where each individual subdomain is defined as the support of a discrete streamfunction basis function in the two-dimensional setting:

$$\Omega_{i,\ell} := \operatorname{supp}\left(N_{i,\ell}^{\psi}\right)$$

and a discrete vector potential basis function in the three-dimensional setting:

$$\Omega_{i,\ell} := \operatorname{supp}\left(\mathbf{N}_{i,\ell}^{\psi}\right).$$

It is easily seen that the subdomains form a cover of the physical domain, that is

$$\overline{\Omega} = \bigcup_i \Omega_{i,\ell}.$$

For each subdomain, we define discrete velocity and pressure subspaces $\mathbf{V}_{i,\ell} \subset \mathbf{V}_\ell$ and $\mathrm{Q}_{i,\ell} \subset \mathrm{Q}_\ell$, respectively, as

$$\mathbf{V}_{i,\ell} := \{\mathbf{v}_h \in \mathbf{V}_\ell : \text{supp } \mathbf{v}_h \subseteq \Omega_{i,\ell}\} \quad \text{and} \quad \mathrm{Q}_{i,\ell} := \{q_h \in \mathrm{Q}_\ell : \text{supp } q_h \subseteq \Omega_{i,\ell}\}.$$

In the two-dimensional setting, we define a discrete streamfunction subspace for each subdomain as

$$\Psi_{i,\ell} := \{\psi_h \in \Psi_\ell : \text{supp } \psi_h \subseteq \Omega_{i,\ell}\}$$

and in the three-dimensional setting, we define a discrete vector potential subspace for each subdomain as

$$\boldsymbol{\Psi}_{i,\ell} := \{\boldsymbol{\psi}_h \in \boldsymbol{\Psi}_\ell : \text{supp } \boldsymbol{\psi}_h \subseteq \Omega_{i,\ell}\}.$$

The degrees of freedom associated with all of the aforementioned subspaces are illustrated in the two-dimensional case in Figure 9.2 for two separate subdomains.

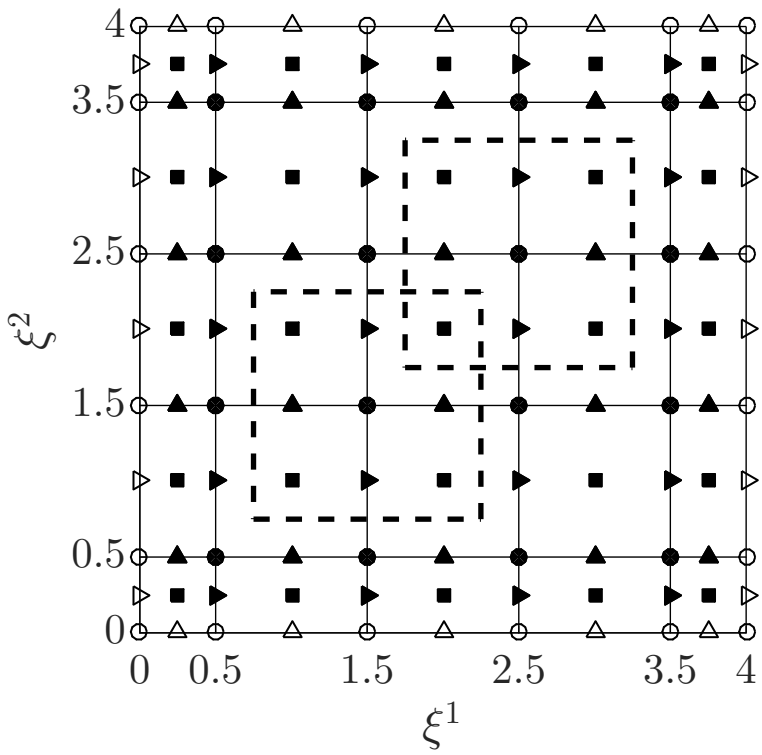

Figure 9.2: The degrees of freedom associated with two example subdomains in the parametric domain $\hat{\Omega}$. Filled circles (●) denote streamfunction degrees of freedom, triangles (►, ▲) denote velocity degrees of freedom, and filled squares (■) denote pressure degrees of freedom. Hollow markers indicate degrees of freedom associated with boundary conditions.

By construction, $\dim(\Psi_{i,\ell}) = 1$ in the two-dimensional setting and $\dim(\boldsymbol{\Psi}_{i,\ell}) = 1$ in the three-dimensional setting. Moreover, $\dim(\mathbf{V}_{i,\ell}) = 4$ and $\dim(\mathrm{Q}_{i,\ell}) = 3$ in both the two- and three-dimensional settings[4] . Thus, the subspaces associated with each subdomain form the following exact discrete Stokes complex in the two-dimensional setting:

$$0 \longrightarrow \Psi_{i,\ell} \xrightarrow{\vec{\nabla}^{\perp}} \mathbf{V}_{i,\ell} \xrightarrow{\vec{\nabla}\cdot} \mathrm{Q}_{i,\ell} \longrightarrow 0 \tag{9.7}$$

and the following exact discrete Stokes complex in the three-dimensional setting:

$$0 \longrightarrow \boldsymbol{\Psi}_{i,\ell} \xrightarrow{\vec{\nabla}\times} \mathbf{V}_{i,\ell} \xrightarrow{\vec{\nabla}\cdot} \mathrm{Q}_{i,\ell} \longrightarrow 0. \tag{9.8}$$

Thus, as previously suggested, our choice of subdomains indeed respects the underlying topological structure of the generalized Stokes and Oseen problems.

[4] From Figure 9.2, it appears that $\dim(\mathrm{Q}_{i,\ell}) = 4$. However, the functions in $\mathrm{Q}_{i,\ell}$ must satisfy a zero average constraint, so the dimension is one less than what is observed from the figure.

With our subdomains defined, we can now describe our choice of smoothers, namely additive and multiplicative Schwarz smoothers using our prescribed subdomains. In this direction, let $\mathbf{E}_{i,\ell}^v$ and $\mathbf{E}_{i,\ell}^q$ denote the velocity and pressure subdomain restriction matrices for a given level ℓ and subdomain i that take the full set of velocity and pressure degrees of freedom associated with level ℓ and map them to the set of pressure and velocity degrees of freedom associated with the subdomain $\Omega_{i,\ell}$. Additionally, let

$$\mathbf{E}_{i,\ell} := \begin{bmatrix} \mathbf{E}_{i,\ell}^v & \mathbf{0} \\ \mathbf{0} & \mathbf{E}_{i,\ell}^q \end{bmatrix}$$

denote the subdomain restriction matrix for a given level ℓ and subdomain i for the full group variable. Then, the action of the additive Schwarz smoother is defined through

$$\mathbf{S}_\ell^{-1} = \eta \left(\sum_i \mathbf{E}_{i,\ell}^T (\mathbf{E}_{i,\ell} \mathbf{K}_\ell \mathbf{E}_{i,\ell}^T)^{-1} \mathbf{E}_{i,\ell} \right), \tag{9.9}$$

where $\eta \in (0,1)$ is a suitably chosen scaling factor [98], while the action of the multiplicative Schwarz smoother is defined through

$$\mathbf{S}_\ell^{-1} = \left[\mathbf{I} - \prod_i \left(\mathbf{I} - \mathbf{E}_{i,\ell}^T (\mathbf{E}_{i,\ell} \mathbf{K}_\ell \mathbf{E}_{i,\ell}^T)^{-1} \mathbf{E}_{i,\ell} \mathbf{K}_\ell \right) \right] \mathbf{K}_\ell^{-1}. \tag{9.10}$$

The additive and multiplicate Schwarz smoothers are generalizations of the classical Jacobi and Gauss-Seidel smoothers, and indeed they can be implemented in an efficient, iterative manner. For both of these smoothers, a sequence of local matrix problems of the form

$$\mathbf{K}_{i,\ell} \mathbf{U}_{i,\ell} = \mathbf{F}_{i,\ell} \tag{9.11}$$

where $\mathbf{K}_{i,\ell} = \mathbf{E}_{i,\ell} \mathbf{K}_\ell \mathbf{E}_{i,\ell}^T$ must be solved. It is easily seen that

$$\mathbf{K}_{i,\ell} = \begin{bmatrix} \mathbf{A}_{i,\ell} & -\mathbf{B}_{i,\ell} \\ \mathbf{B}_{i,\ell}^T & \mathbf{0} \end{bmatrix}$$

where

$$\mathbf{A}_{i,\ell} = \mathbf{E}_{i,\ell}^v \mathbf{A}_\ell \left(\mathbf{E}_{i,\ell}^v \right)^T$$
$$\mathbf{B}_{i,\ell} = \mathbf{E}_{i,\ell}^v \mathbf{A}_\ell \left(\mathbf{E}_{i,\ell}^q \right)^T.$$

Thus, with both the additive and multiplicative Schwarz smoothers, a discrete generalized Stokes or Oseen problem is solved for each subdomain. In the next subsection, we further clarify this interpretation in a variational setting. With the additive Schwarz smoother, the subdomain problems are solved independently, and their respective solutions are summed together and multiplied through by a scaling factor as indicated above. With the multiplicative Schwarz smoother, the subdomain problems are solved in a sequential fashion in analogy with the Gauss-Seidel smoother.

9.4.3 Preservation of the Divergence-free Constraint

Now that we have presented our choice of smoother, we demonstrate that our geometric multigrid methodology preserves the divergence-free constraint on the velocity field. Provided that the initial guess for the V-cycle algorithm satisfies the divergence-free constraint, it is sufficient to show that each smoothing step provides velocity updates that are divergence-free. One application of either the additive or multiplicative Schwarz smoother at level ℓ is akin to solving a collection of local subdomain problems of the form: Find $\delta\mathbf{u}_{i,\ell} \in \mathbf{V}_{i,\ell}$ and $\delta p_{i,\ell} \in \mathrm{Q}_{i,\ell}$ such that

$$a_h(\mathbf{v}_h, \delta\mathbf{u}_{i,\ell}) - b(\mathbf{v}_h, \delta p_{i,\ell}) + b(\delta\mathbf{u}_{i,\ell}, q_h) = \ell(\mathbf{v}_h) - a_h(\mathbf{v}_h, \mathbf{u}_h) + b(\mathbf{v}_h, p_h) - b(\mathbf{u}_h, q_h) \tag{9.12}$$

for all $\mathbf{v}_h \in \mathbf{V}_{i,\ell}$ and $q_h \in \mathrm{Q}_{i,\ell}$ where $\mathbf{u}_h$ and p_h are the approximate discrete velocity and pressure solutions. For the additive Schwarz smoother, the approximate discrete velocity and pressure solutions are updated following the solution of all of the local problems according to

$$\mathbf{u}_h \leftarrow \mathbf{u}_h + \eta \left(\sum_i \delta\mathbf{u}_{i,\ell} \right)$$

$$p_h \leftarrow p_h + \eta \left(\sum_i \delta p_{i,\ell} \right)$$

while for the multiplicative Schwarz smoother, the approximate discrete velocity and pressure solutions are updated following the solution of each individual local problem according to

$$\mathbf{u}_h \leftarrow \mathbf{u}_h + \delta\mathbf{u}_{i,\ell}$$

$$p_h \leftarrow p_h + \delta p_{i,\ell}.$$

For each subdomain problem, if the approximate discrete velocity solution is divergence-free, it holds that

$$b(\delta\mathbf{u}_{i,\ell}, q_h) = 0$$

for all $q_h \in \mathrm{Q}_{i,\ell}$. Since $\mathrm{Q}_{i,\ell} = \nabla \cdot \mathbf{V}_{i,\ell}$, we can select $q_h = \nabla \cdot \delta\mathbf{u}_{i,\ell}$ to find

$$\|\nabla \cdot \delta\mathbf{u}_{i,\ell}\|^2_{L^2(\Omega)} = b(\delta\mathbf{u}_{i,\ell}, q_h) = 0$$

and thus the solution to the local problem is also divergence-free. Thus, if the initial guess for the V-cycle algorithm satisfies the divergence-free constraint, each subsequent application of the Schwarz smoother at any given level ℓ preserves the divergence-free constraint as well.

9.4.4 Efficacy of the Structure-preserving Geometric Multigrid Methodology

We conclude here with a short discussion of the efficacy of our geometric multigrid methodology. We restrict our discussion to the three-dimensional setting without loss of generality. Recall that the spaces $\mathbf{\Psi}_{i,\ell}$, $\mathbf{V}_{i,\ell}$, and $\mathrm{Q}_{i,\ell}$ form a discrete Stokes complex for a given level ℓ and subdomain i. Thus, we can express the velocity solution $\delta\mathbf{u}_{i,\ell} \in \mathbf{V}_{i,\ell}$ to (9.12) in terms of the curl of a vector potential $\delta\boldsymbol{\psi}_{i,\ell} \in \mathbf{\Psi}_{i,\ell}$ provided the velocity is divergence-free, and this vector potential can be obtained via the reduced subdomain problem: Find $\delta\boldsymbol{\psi}_{i,\ell} \in \mathbf{\Psi}_{i,\ell}$ such that

$$a_h(\nabla \times \boldsymbol{\zeta}_h, \nabla \times \delta\boldsymbol{\psi}_{i,\ell}) = \ell(\nabla \times \boldsymbol{\zeta}_h) - a_h(\nabla \times \boldsymbol{\zeta}_h, \mathbf{u}_h) \tag{9.13}$$

for all $\boldsymbol{\zeta}_h \in \mathbf{\Psi}_{i,\ell}$. This is precisely the subdomain problem associated with the global semi-elliptic generalized Maxwell problem with hyperresitivity [17]: Find $\boldsymbol{\psi} \in \mathbf{\Psi}_h$ such that

$$a_h(\nabla \times \boldsymbol{\zeta}^h, \nabla \times \boldsymbol{\psi}^h) = \ell(\nabla \times \boldsymbol{\zeta}^h) \tag{9.14}$$

for all $\boldsymbol{\zeta}^h \in \mathbf{\Psi}_h$. It is known that a geometric multigrid methodology based on the use of Schwarz smoothers posed on structure-preserving subdomains is optimally convergent for Maxwell problems [5]. Consequently, we can expect that at least the discrete velocity solutions will converge in our approach.

9.5 Numerical Results

We now present a series of numerical tests illustrating the effectiveness of our proposed geometric multigrid methodology. Each of the tests correspond to problems with homogeneous Dirichlet boundary conditions applied along the entire domain boundary. In our discretization scheme, no-penetration boundary conditions are enforced strongly and no-slip boundary conditions are enforced weakly using a penalty constant of $C_I = 4(p-1)$ where p is the polynomial degree which is taken to be equal in each parameteric direction. It should be noted that p refers to the polynomial degree of the discrete streamfunction space in the two-dimensional case and the discrete scalar potential space in the three-dimensional case. Hence, for $k = 2$, the discrete pressure fields are piecewise bilinear/trilinear B-splines rather than piecewise biquadratic/triquadratic B-splines. Maximally smooth B-splines defined on uniform knot vectors are utilized throughout.

For all of the following tests, we define convergence as the number of V-cycles required to reduce the initial residual by a factor of 10^6. We always initialize the V-cycle algorithm using a random initial guess which satisfies the divergence-free constraint on the velocity field. For each V-cycle, one pre-smoothing and two post-smoothing steps are employed using either the multiplicative or additive Schwarz smoother. For the additive Schwarz smoother, a scaling factor of $\eta = 0.5$ is employed.

For all the problems presented here, a single element is used for the coarsest mesh and we investigate the convergence behavior for various levels of refinement. We report on the convergence behavior of our method for both the generalized Stokes and Oseen problems as well as a selection of different problem parameters, polynomial degrees, domain geometries, and number of spatial dimensions (2D and 3D). With respect to problem parameters, we consider the ratios between reaction and diffusion and advection and diffusion, which we express through a Damköhler number (Da) and a Reynolds number (Re). We define these numbers as:

$$Da = \frac{\sigma L^2}{\nu} \quad \text{and} \quad Re = \frac{|\mathbf{a}|L}{\nu}.$$

where $\mathbf{a}$ is the advective velocity and L is a characteristic length scale, both of which are taken to

be one throughout.

9.5.1 Two-dimensional Generalized Stokes Flow in a Square Domain

We first consider a two-dimensional generalized Stokes problem posed on the square domain $(0,1)^2$. In particular, we consider a forcing

$$\mathbf{f} = \sigma\mathbf{u} - \nu\Delta\mathbf{u} + \nabla p \tag{9.15}$$

corresponding to the following manufactured solution [33]:

$$\mathbf{u} = \begin{bmatrix} 2e^x(-1+x)^2x^2(y^2-y)(-1+2y) \\ (-e^x(-1+x)x(-2+x(3+x))(-1+y)^2y^2 \end{bmatrix} \tag{9.16}$$

$$\begin{aligned} p = (&-424 + 156e + (y^2-y)(-456 + e^x(456 + x^2(228 - 5(y^2-y)) \\ &+ 2x(-228 + (y^2-y)) + 2x^3(-36 + (y^2-y)) + x^4(12 + (y^2-1))))). \end{aligned} \tag{9.17}$$

The velocity field associated with this exact solution is plotted in Figure 9.3.

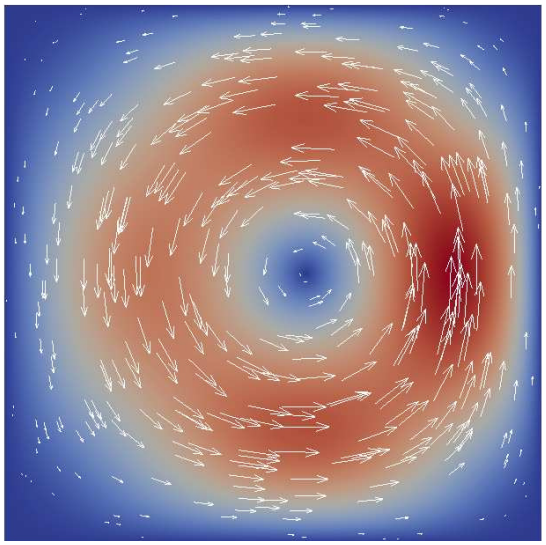

Figure 9.3: Velocity field for the unit square generalized Stokes problem.

We first present convergence results for our multigrid method using the multiplicative Schwarz smoother and polynomial degrees $k = 2$ and $k = 3$ in Table 9.1. It is clear that for a given polynomial order, the convergence behavior is robust with respect to both the number of levels of refinement and the problem parameters. We also observe that as polynomial order is increased, the convergence behavior deteriorates, albeit slightly. This is consistent with previously observed behavior for isogeometric analysis [67, 78, 77].

Table 9.1: Number of V(1,2) cycles required for convergence for the unit square generalized Stokes problem using the multiplicative Schwarz smoother and $k = 2, 3$.

	$k = 2$			$k = 3$		
n_ℓ	DOFs	$Da = 1$	$Da = 1000$	DOFs	$Da = 1$	$Da = 1000$
1	33	3	2	56	6	6
2	85	5	4	120	12	14
3	261	5	5	320	13	13
4	901	6	5	1008	12	12
5	3333	6	5	3536	13	13
6	12805	7	6	13200	13	13
7	50181	7	6	50960	13	13
8	198661	7	6	200208	13	13
9	790533	7	7	793616	13	13
10	3153925	7	7	3160080	13	13

We next present convergence results for our multigrid method using the additive Schwarz smoother and polynomial degree $k = 2$ in Table 9.2. As expected, overall convergence is slower with additive Schwarz than with multiplicative Schwarz, although in this case the method is still robust with regard to both the number of levels of refinement and the problem parameters.

Table 9.2: Number of V(1,2) cycles required for convergence for the unit square generalized Stokes problem using the additive Schwarz smoother and $k = 2$.

n_ℓ	DOFs	$Da = 1$	$Da = 1000$
1	33	5	4
2	85	12	9
3	261	15	14
4	901	16	15
5	3333	16	16
6	12805	16	16
7	50181	16	16
8	198661	16	16
9	790533	16	16
10	3153925	16	16

9.5.2 Two-dimensional Generalized Stokes Flow in a Quarter Annulus

We next consider a two-dimensional generalized Stokes problem posed on a quarter annulus. The domain is described in Figure 9.4 where $r_i = 0.075$ and $r_o = 0.225$. We consider a manufactured solution achieved by mapping the solution presented in (9.16)-(9.17) to the quarter-annulus domain using a quadratic rational Bézier parametric mapping and appropriate push-forward operators. The velocity field associated with the exact solution is also plotted in Figure 9.4.

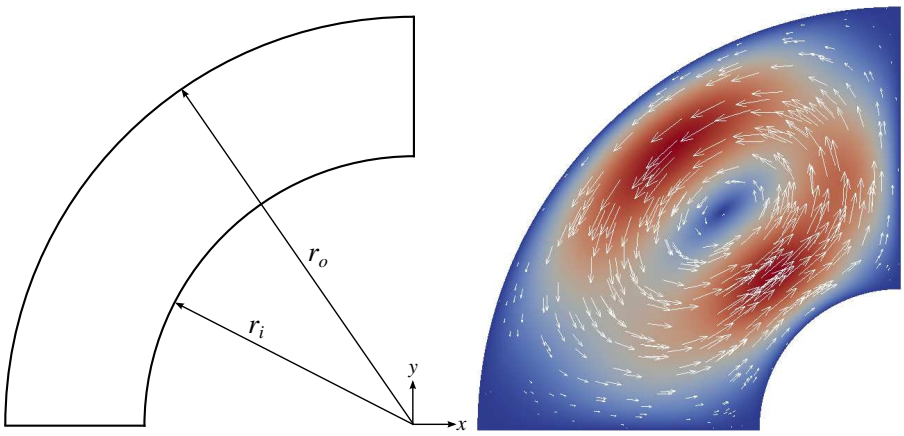

Figure 9.4: Domain description (left) and velocity field (right) for the quarter annulus generalized Stokes problem.

We present convergence results for our multigrid method using the multiplicative Schwarz smoother and polynomial degree $k = 2$ in Table 9.3. Compared with the square domain, the number of V-cycles required for convergence is larger. However, the method is still robust with respect to both the number of levels of refinement and the problem parameters.

Table 9.3: Number of V(1,2) cycles required for convergence for the quarter annulus generalized Stokes problem using the multiplicative Schwarz smoother and $k = 2$.

n_ℓ	DOFs	$Da = 1$	$Da = 1000$
1	33	2	2
2	85	3	3
3	261	8	7
4	901	16	15
5	3333	24	24
6	12805	26	26
7	50181	31	31
8	198661	34	34
9	790533	34	34
10	3153925	34	34

9.5.3 Three-dimensional Generalized Stokes Flow in a Cube Domain

We next consider a three-dimensional generalized Stokes problem posed on the unit cube $(0,1)^3$. In particular, we consider a forcing

$$\mathbf{f} = \sigma\mathbf{u} - \nu\Delta\mathbf{u} + \nabla p \tag{9.18}$$

corresponding to the following manufactured solution [61]:

$$\mathbf{u} = \nabla \times \boldsymbol{\Psi} \tag{9.19}$$

$$\boldsymbol{\psi} = \begin{bmatrix} x(x-1)y^2(y-1)^2z^2(z-1)^2 \\ 0 \\ x^2(x-1)^2y^2(y-1)^2z(z-1) \end{bmatrix} \tag{9.20}$$

$$p = \sin(\pi x)\sin(\pi y) - \frac{4}{\pi^2} \tag{9.21}$$

Streamlines colored by velocity magnitude associated with the exact solution are plotted in Figure 9.5.

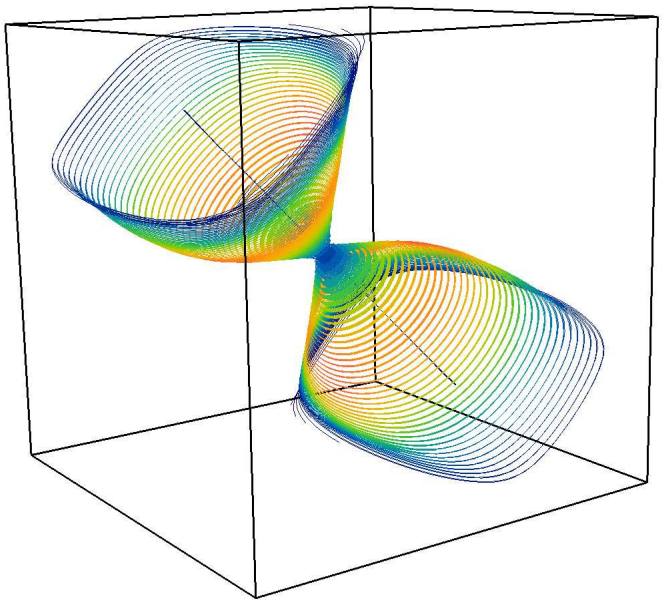

Figure 9.5: Streamlines colored by velocity magnitude for the unit cube generalized Stokes problem.

We present convergence results for our multigrid method using the multiplicative Schwarz smoother and polynomial degrees $k = 2$ and $k = 3$ in Table 9.4. Convergence appears to be much quicker in the three-dimensional setting. Notably, one V-cycle appears to be sufficient to reduce the residual by six orders of magnitude for a sufficient number of levels for both $k = 2$ and $k = 3$ and irrespective of the Damköhler number. We believe this may be due to the fact each velocity degree of freedom is updated twice as many times in each iteration of the smoother in the three-dimensional case as compared to the two-dimensional case.

Table 9.4: Number of V(1,2) cycles required for convergence for the unit cube generalized Stokes problem using the multiplicative Schwarz smoother and $k = 2, 3$.

	$k = 2$			$k = 3$		
n_ℓ	DOFs	$Da = 1$	$Da = 1000$	DOFs	$Da = 1$	$Da = 1000$
1	135	1	1	304	2	4
2	575	1	1	972	1	1
3	3159	2	2	4300	1	1
4	20519	1	1	24300	1	1
5	147015	1	1	160684	1	1
6	1111175	1	1	1163052	1	1

9.5.4 Three-dimensional Generalized Stokes Flow in a Hollow Cylinder Section

The final generalized Stokes problem considered in this paper is a three-dimensional problem posed on a hollow cylinder section. The domain for this problem is simply the quarter annulus from before extruded in the z-direction by a depth of $d = 0.1$. We consider a manufactured solution achieved by mapping the solution presented in (9.19)-(9.21) to the hollow cylinder section domain using a quadratic rational Bézier parametric mapping and appropriate push-forward operators. Streamlines colored by velocity magnitude associated with the exact solution are plotted in Figure 9.6.

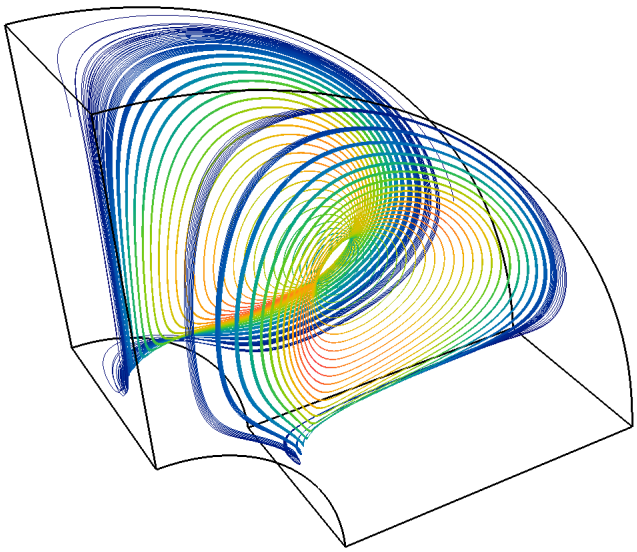

Figure 9.6: Streamlines colored by velocity magnitude for the hollow cylinder generalized Stokes problem.

We present convergence results for our multigrid method using the multiplicative Schwarz smoother and polynomial degree $k = 2$ in Table 9.5. Incredibly, one V-cycle again appears to be sufficient to reduce the residual by six orders of magnitude for a sufficient number of levels irrespective of the Damköhler number.

Table 9.5: Number of V(1,2) cycles required for convergence for the hollow cylinder generalized Stokes problem using the multiplicative Schwarz smoother and $k = 2$.

n_ℓ	DOFs	$Da = 1$	$Da = 1000$
1	135	1	1
2	575	1	2
3	3159	2	2
4	20519	1	1
5	147015	1	1
6	1111175	1	1

9.5.5 Two-dimensional Generalized Oseen Flow in a Square Domain

We now turn our attention to the generalized Oseen problem. We first consider a two-dimensional generalized Oseen problem posed on the square domain $(0, 1)^2$. We manufacture a solution with a forcing

$$\mathbf{f} = \sigma\mathbf{u} + \mathbf{a} \cdot \nabla\mathbf{u} - \nu\Delta\mathbf{u} + \nabla p \tag{9.22}$$

where $\mathbf{u}$ and p are defined as in (9.16)-(9.17) such that the resulting solution is the same as the unit square generalized Stokes problem. Note that the advection velocity is taken to be the manufactured velocity field.

We present convergence results for our multigrid method using the multiplicative Schwarz smoother, polynomial degree $k = 2$, and various Reynolds and Damköhler numbers in Table 9.6. When Reynolds number is low, the advection terms become negligible, and thus the method performs as it did on the 2D generalized Stokes problem. As the Reynolds number is increased, the advection term becomes more significant. In this case, we have observed favorable convergence behavior as long as the Damköhler number is at least as large as the Reynolds number. When the system becomes advection-dominated, on the other hand, the multigrid method fails to converge. We expect that improved results may be obtained through the use of an alternative smoother which respects the directionality of the advection velocity.

Table 9.6: Number of V(1,2) cycles required for convergence for the unit square generalized Oseen problem using the multiplicative Schwarz smoother and $k = 2$.

		$Re = 1$		$Re = 100$
n_ℓ	DOFs	$Da = 1$	$Da = 1000$	$Da = 1000$
1	33	3	2	2
2	85	5	4	3
3	261	5	5	4
4	901	6	5	9
5	3333	6	5	13
6	12805	7	6	15
7	50181	7	6	11
8	198661	7	6	7
9	790533	7	7	7
10	3153925	7	7	7

9.5.6 Three-dimensional Generalized Oseen Flow in a Cube Domain

We conclude by considering a three-dimensional generalized Oseen problem posed on the unit cube $(0, 1)^3$. We manufacture a solution with a forcing

$$\mathbf{f} = \sigma\mathbf{u} + \mathbf{a} \cdot \nabla\mathbf{u} - \nu\Delta\mathbf{u} + \nabla p \tag{9.23}$$

where $\mathbf{u}$ and p are defined as in (9.19)-(9.21) such that the resulting solution is the same as the unit cube generalized Stokes problem. As with the two-dimensional generalized Oseen problem, the advection velocity is take to be the manufactured velocity field.

We present convergence results for our multigrid method using the multiplicative Schwarz smoother, polynomial degree $k = 2$, and various Reynolds and Damköhler numbers in Table 9.7. The same trends that were observed for the two-dimensional case are observed here as well. Namely, when the system is not advection dominated, we achieve excellent convergence behavior. Also, as was the case with the generalized Stokes flow, the three-dimensional case exhibits improved convergence as compared to the two-dimensional case.

Table 9.7: Number of V(1,2) cycles required for convergence for the unit cube generalized Oseen problem using the multiplicative Schwarz smoother and $k = 2$.

		$Re = 1$		$Re = 100$
n_ℓ	DOFs	$Da = 1$	$Da = 1000$	$Da = 1000$
1	135	1	2	2
2	575	1	2	2
3	3159	2	3	3
4	20519	1	2	2
5	147015	1	1	3
6	1111175	1	1	3

Chapter 10

Conclusions and Future Work

10.1 Conclusions

In this dissertation, a novel paradigm for the large eddy simulation of turbulent flows utilizing residual-based subgrid modeling has been presented. By combining divergence-conforming discretizations with residual-based subgrid modeling, an LES-like simulation capability which addresses many of the shortcomings of classical LES approaches has been developed. Furthermore, this method contains no "tunable" parameters, and thus extends generally across various classes of flow. Numerical results demonstrate that the method matches the performance of classical LES models for homogeneous turbulence, but outperforms classical LES models for transitional flows and wall-bounded turbulent flows. The dynamic VMS model is found to be strangely insufficient for $k = 1$, but shows excellent results for $k = 2$ for all of the flows presented here. In constrast, the dynamic RBEV model is effective even for $k = 1$, and demonstrates reasonable results throughout, but is less accurate than the dynamic VMS model for $k = 2$. The quasi-static residual-based models using the classical definition for τ_{uns} are inadequate for semi-implicit time-integration which require very small time steps, but an alternate formulation for τ_{uns} which is less sensitive to the time step is demonstrated to make the quasi-static models as effective as the dynamic models.

Additionally, a differential variational multiscale method, referred to as the method of discontinuous subscales, has been presented. This method is based on approximating the residual-free

bubbles using a discontinuous Galerkin formulation. Stability and convergence results for the methodology were determined and the applicability of the model to scalar transport problems was demonstraetd through a collection of numerical examples. It is observed that the method is accurate, displaying optimal convergence rates with respect to mesh refinement, and stable in the advective-limit. It is also demonstrated that, somewhat surprisingly, lowest-order discontinuous subscale approximations are sufficient to stabilize high-order coarse-scale approximations in the context of isogeometric analysis. Furthermore, two differential subgrid vortex models have been proposed, which extends the method of discontinuous subscales to the realm of LES modeling.

Finally, a structure-preserving geometric multigrid methodology for isogeometric compatible discretizations of the generalized Stokes and Oseen problems has been presented. This methodology relies upon Schwarz-style smoothers in conjunction with specially chosen subdomains. It was proven that the methodology yields a pointwise divergence-free velocity field independent of the number of pre-smoothing steps, post-smoothing steps, grid levels, or cycles in a V-cycle implementation, and the efficiency and robustness of the methodology was demonstrated by numerical example. Specifically, it was found that the methodology exhibits convergence rates independent of the grid resolution and flow parameters for the generalized Stokes problem as well as the generalized Oseen problem, provided it is not advection-dominated. It was also discovered that, somewhat surprisingly, the methodology exhibits improved convergence rates in the three-dimensional setting as compared with the two-dimensional setting.

10.2 Ongoing and Future Work

There are many promising areas for continued research in residual-based subgrid-scale modeling for turbulence and linear solver technology. With regard to residual-based subgrid-scale modeling, demonstrating the performance of the VMS and RBEV models for rotating flow is currently underway. The Taylor-Couette flow problem for $Re = 8000$ has been implemented and initial simulations to validate the code have been conducted. A representative solution using the

quasi-static VMS model is presented in Fig. 10.1. We plan to run a parameter study for this problem similar to what was presented here for the Taylor-Green vortex and the turbulent channel in order to assess the accuracy of the residual-based models for rotating flow. Additionally, continued improvements to the models presented here can be made. Pursuing additional stabilization techniques is expected to make the VMS models more effective for the linear case and improve the performance of the RBEV models. We also seek improvements to the quasi-static models in order to achieve the same performance as the dynamic models at less computational expense. In terms of discontinuous subscale approaches, there are also several avenues for continued work. The first avenue is the design of discontinuous subscale approaches which yield coarse-scale solutions satisfying positivity and monotonicity constraints. This can be achieved through the use of discontinuity capturing operators [93, 94] or by directly embedding the constraints within the variational multiscale framework [58]. The second avenue of research in this area is the design of discontinuous subscale approaches for LES-type turbulence modeling. Two such models are presented here and in future work they will be implemented, analyzed, and demonstrated. While lowest-order discontinuous subscale approximations were found to stabilize coarse-scale approximations in the context of scalar transport, it is expected that such approximations will not be sufficient to yield accurate representations of the subgrid stress tensor for turbulent incompressible flows [138]. It is anticipated that improved LES turbulence models may be attained through adaptive refinement of the discontinuous subscale approximation space. It is also expected to be fruitful to extend and apply residual-based LES turbulence methodologies to multi-physics problems, including coupled flow transport, fluid-structure interaction, and magnetohydrodynamics.

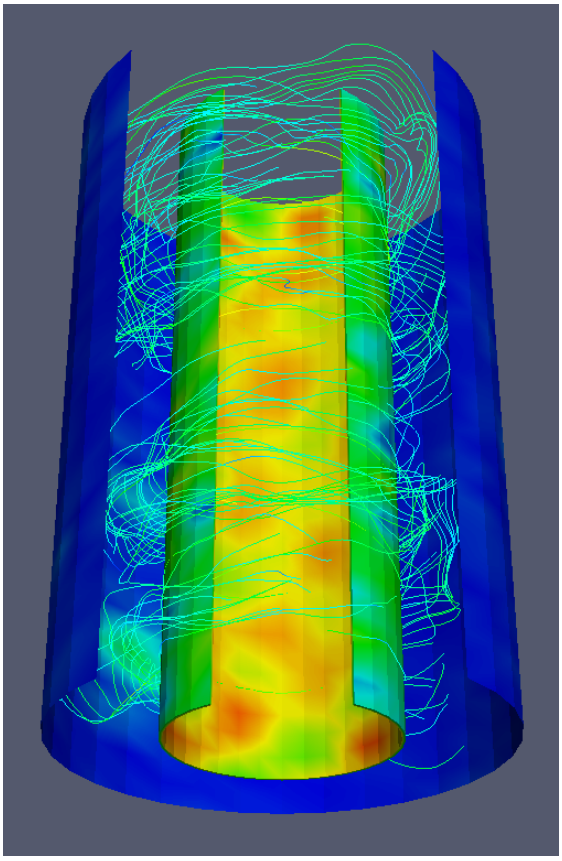

Figure 10.1: Simulation of Taylor-Couette flow for $Re = 8000$ with $k = 2$ and $k_f = 1$ on a domain of 32^3 elements. Velocity contours on and near the inner and outer cylinder walls and streamlines colored by velocity magnitude. Quasi-static VMS model.

With regards to linear solvers, a full mathematical analysis of the presented geometric multigrid methodology is planned. It is anticipated that this analysis will largely follow the same program of work as laid out in a recent geometric multigrid paper for divergence-conforming discontinuous Galerkin formulations of Stokes flow [98]. Additionally, the method can be extended to advection-dominated Oseen problems. In this setting, it is expected that upwind-based line smoothers will be required [105]. Third, it is planned to extend our methodology to multi-patch geometries and adaptive isogeometric compatible discretizations [37, 92]. Initial results in this area are quite encouraging. Finally, as is planned with future work for residual-based LES turbulence models, it is also planned to extend the structure-preserving geometric multigrid methodology to the same classes of multi-physics problems as previously mentioned.

Bibliography

[1] Wall-adapting local eddy viscosity (WALE) model. In ANSYS Fluent Theory Guide.

[2] E. Anderson, Z. Bai, C. Bischof, S. Blackford, J. Demmel, J. Dongarra, J. Du Croz, A. Greenbaum, S. Hammarling, A. McKenney, and D. Sorensen. LAPACK Users' Guide. Society for Industrial and Applied Mathematics, Philadelphia, PA, third edition, 1999.

[3] D. N. Arnold. An interior penalty finite element method with discontinuous elements. SIAM Journal on Numerical Analysis, 19:742–760, 1982.

[4] D. N. Arnold, F. Brezzi, B. Cockburn, and L. D. Marini. Unified analysis of discontinuous Galerkin methods for elliptic problems. SIAM Journal on Numerical Analysis, 39:1749–1779, 2002.

[5] D. N. Arnold, R. S. Falk, and R. Winther. Multigrid in $H(div)$ and $H(curl)$. Numerische Mathematik, 85(2):197–217, 2000.

[6] B. Ayuso de Dios, F. Brezzi, L. D. Marini, J. Xu, and L. Zikatanov. A simple preconditioner for a discontinuous Galerkin method for the Stokes problem. Journal of Scientific Computing, 58(3):517–547, 2014.

[7] I. Babuška. Error-bounds for finite element method. Numerische Mathematik, 16(4):322–333, 1971.

[8] S. Balay, S. Abhyankar, M. F. Adams, J. Brown, P. Brune, K. Buschelman, L. Dalcin, V. Eijkhout, W. D. Gropp, D. Kaushik, M. G. Knepley, L. Curfman McInnes, K. Rupp, B. F. Smith, S. Zampini, H. Zhang, and H. Zhang. PETSc users manual. Technical Report ANL-95/11 - Revision 3.7, Argonne National Laboratory, 2016.

[9] F. Bashforth and J. C. Adams. Theories of Capillary Action. Cambridge University Press, London, 1883.

[10] Y. Bazilevs and I. Akkerman. Large eddy simulation of turbulent Taylor-Couette flow using isogeometric analysis and the residual–based variational multiscale method. Journal of Computational Physics, 229:3402–3414, 2010.

[11] Y. Bazilevs, V. M. Calo, J. A. Cottrell, T. J. R. Hughes, A. Reali, and G. Scovazzi. Variational multiscale residual-based turbulence modeling for large eddy simulation of incompressible flows. Computer Methods in Applied Mechanics and Engineering, 197:173–201, 2007.

[12] Y. Bazilevs, V. M. Calo, T. J. R. Hughes, and Y. Zhang. Isogeometric fluid-structure interaction: Theory, algorithms, and computations. Computational Mechanics, 43:3–37, 2008.

[13] Y. Bazilevs, L. Beirao de Veiga, J. A. Cottrell, T. J. R. Hughes, and G. Sangalli. Isogeometric analysis: Approximation, stability and error estimates for h-refined meshes. Mathematical Models and Methods in Applied Sciences, 16:1031–1090, 2006.

[14] Y. Bazilevs and T. J. R. Hughes. Weak imposition of Dirichlet boundary conditions in fluid mechanics. Computers and Fluids, 36:12–26, 2007.

[15] Y. Bazilevs, C. Michler, V. M. Calo, and T. J. R. Hughes. Weak Dirichlet boundary conditions for wall-bounded turbulent flows. Computer Methods in Applied Mechanics and Engineering, 196:4853–4862, 2007.

[16] Y. Bazilevs, C. Michler, V. M. Calo, and T. J. R. Hughes. Isogeometric variational multiscale modeling of wall-bounded turbulent flows with weakly enforced boundary conditions on unstretched meshes. Computer Methods in Applied Mechanics and Engineering, 199:780–790, 2010.

[17] D. Biskamp. Nonlinear Magnetohydrodynamics, volume 1. Cambridge University Press, 1997.

[18] P. Bochev, T. J. R. Hughes, and G. Scovazzi. A multiscale discontinuous Galerkin method. Lecture notes in computer science, 3743:84–93, 2006.

[19] M. J. Borden, M. A. Scott, J. A. Evans, and T. J. R. Hughes. Isogeometric finite element data structures based on Bézier extraction of NURBS. International Journal for Numerical Methods in Engineering, 87:15–47, 2011.

[20] J. Boussinesq. Essai sur la théorie des eaux courantes. Mémoires présentés par divers savants â l'Académie des Sciences, 23:1–64, 1977.

[21] M. Brachet, D. Meiron, B. Nickel, and R. Morf. Small-scale structure of the Taylor-Green vortex. Journal of Fluid Mechanics, 130:411–452, 1983.

[22] D. Braess and R. Sarazin. An efficient smoother for the Stokes problem. Applied Numerical Mathematics, 23:3–19, 1997.

[23] F. Brezzi. On the existence, uniqueness and approximation of saddle-point problems arising from Lagrangian multipliers. Revue française d'automatique, informatique, recherche opérationnelle. Analyse numérique, 8(2):129–151, 1974.

[24] F. Brezzi, M. O. Bristeau, L. P. Franca, M. Mallet, and G. Roge. A relationship between stabilized finite element methods and the Galerkin method with bubble functions. Computer Methods in Applied Mechanics and Engineering, 96:117–129, 1992.

[25] F. Brezzi, L. P. Franca, T. J. R. Hughes, and A. Russo. $b = \int g$. Computer Methods in Applied Mechanics and Engineering, 145:329–339, 1997.

[26] F. Brezzi, G. Hauke, D. Marini, and G. Sangalli. Applications of the pseudo residual-free bubbles to the stabilization of convection-diffusion problems. Mathematical Models and Methods in Applied Sciences, 13:445–461, 2003.

[27] F. Brezzi, D. Marini, P. Houston, and E. Süli. Modeling subgrid viscosity for advection-diffusion problems. Computer Methods in Applied Mechanics and Engineering, 190:1601–1610, 2000.

[28] F. Brezzi, D. Marini, and A. Russo. Applications of the pseudo residual-free bubbles to the stabilization of convection-diffusion problems. Computer Methods in Applied Mechanics and Engineering, 166:51–63, 1998.

[29] F. Brezzi and L. D. Marini. Augmented spaces, two-level methods, and stabilizing subgrids. International Journal for Numerical Methods in Fluids, 40:31–46, 2002.

[30] F. Brezzi and A. Russo. Choosing bubbles for advection-diffusion problems. Mathematical Models and Methods in Applied Science, 4:571–587, 1994.

[31] W. L. Briggs, V. E. Henson, and S. F. McCormick. A Multigrid Tutorial. Society for Industrial and Applied Mathematics, Philadelphia, 2000.

[32] A. N. Brooks and T. J. R. Hughes. Streamline upwind/Petrov-Galerkin formulations for convection dominated flows with particular emphasis on the incompressible Navier-Stokes equations. Computer Methods in Applied Mechanics and Engineering, 32:199–259, 1982.

[33] A. Buffa, C. de Falco, and G. Sangalli. Isogeometric analysis: Stable elements for the 2D Stokes equation. International Journal for Numerical Methods in Fluids, 65:1407–1422, 2011.

[34] A. Buffa, T. J. R. Hughes, and G. Sangalli. Analysis of a multiscale discontinuous Galerkin method for convection-diffusion problems. SIAM Journal of Numerical Analysis, 44:1420–1440, 2006.

[35] A. Buffa, J. Rivas, G. Sangalli, and R. Vazquez. Isogeometric discrete differential forms in three dimensions. SIAM Journal on Numerical Analysis, 49:818–844, 2011.

[36] A. Buffa, G. Sangalli, and R. Vazquez. Isogeometric analysis in electromagnetics: B-splines approximation. Computer Methods in Applied Mechanics and Engineering, 199:1143–1152, 2010.

[37] A. Buffa, G. Sangalli, and R. Vázquez. Isogeometric methods for computational electromagnetics: B-spline and T-spline discretizations. Journal of Computational Physics, 257:1291–1320, 2014.

[38] V. M. Calo. Residual-based multiscale turbulence modeling: Finite volume simulations of bypass transition. PhD thesis, Stanford University, 2005.

[39] D. Carati and E. V. Eijnden. On the self-similarity assumption in dynamic models for large eddy simulations. Physics of Fluids, 9:2165–2167, 1997.

[40] P. G. Ciarlet. The Finite Element Method for Elliptic Problems. SIAM, 2002.

[41] B. Cockburn and C.-W. Shu. The local discontinuous Galerkin method for time-dependent convection-diffusion systems. SIAM Journal on Numerical Analysis, 35:2440–2463, 1998.

[42] B. Cockburn and C.-W. Shu. Runge-Kutta discontinuous Galerkin methods for convection-dominated problems. Journal of Scientific Computing, 16:173–261, 2001.

[43] R. Codina, J. Principe, O. Guasch, and S. Badia. Time dependent subscales in the stabilized finite element approximation of incompressible flow problems. Computer Methods in Applied Mechanics and Engineering, 196:2413–2430, 2007.

[44] C. Coley, J. Benzaken, and J. A. Evans. A geometric multigrid method for isogeometric compatible discretizations of the generalized Stokes and Oseen problems. ArXiv e-prints, 2017. https://arxiv.org/abs/1705.09282.

[45] C. Coley and J. A. Evans. Variational multiscale modeling with discontinuous subscales: Analysis and application to scalar transport. ArXiv e-prints, 2017. https://arxiv.org/abs/1705.00082.

[46] A. M. A. Côrtes, A. L. G. A. Coutinho, L. Dalcin, and V. M. Calo. Performance evaluation of block-diagonal preconditioners for the divergence-conforming B-spline discretization of the Stokes system. Journal of Computational Science, 11:123–136, 2015.

[47] A. M. A. Côrtes, L. Dalcin, A. F. Sarmiento, N. Collier, and V. M. Calo. A scalable block-preconditioning strategy for divergence-conforming B-spline discretizations of the Stokes problem. Computer Methods in Applied Mechanics and Engineering, 316:839–858, 2017.

[48] J. A. Cottrell. Isogeometric analysis and numerical modeling of the fine scales within the variational multiscale method. PhD thesis, University of Texas at Austin, 2007.

[49] J. A. Cottrell, T. J. R. Hughes, and Y. Bazilevs. Isogeometric Analysis. Toward Integration of CAD and FEA. Wiley, 2009.

[50] J. Crank and P. Nicolson. A practical method for numerical evaluation of solutions of partial differential equations of the heat conduction type. Mathematical Proceedings of the Cambridge Philosophical Society, 43:50–67, 1947.

[51] J. W. Deardorff. A numerical study of three-dimensional turbulent channel flow at large reynolds numbers. Journal of Fluids Engineering, 41:453–480, 1970.

[52] J. W. Deardorff. The representation of small-scale turbulence in numerical simulation experiments. Journal of Fluids Engineering, 95:429–438, 1973.

[53] V. Dolean, P. Jolivet, and F. Nataf. An Introduction to Domain Decomposition Methods: Algorithms, Theory, and Parallel Implementation. Society for Industrial and Applied Mathematics, Philadelphia, 2015.

[54] S. Dong. DNS of turbulent Taylor-Couette flow. Journal of Fluid Mechanics, 587:373–393, 2007.

[55] J. Douglas and J. P. Wang. An absolutely stabilized finite element method for the Stokes problem. Mathematics of Computation, 52:495–508, 1989.

[56] H. C. Elman and G. H. Golub. Inexact and preconditioned Uzawa algorithms for saddle point problems. SIAM Journal on Numerical Analysis, 31(6):1645–1661, 1994.

[57] J. A. Evans. Divergence-free B-spline discretizations for viscous incompressible flows. PhD thesis, University of Texas at Austin, 2011.

[58] J A.. Evans and T. J. R. Hughes. Enforcement of constraints and maximum principles in the variational multiscale method. Computer Methods in Applied Mechanics and Engineering, 199:61–76, 2009.

[59] J. A. Evans and T. J. R. Hughes. Discrete spectrum analyses for various mixed discretizations of the Stokes eigenproblem. Computational Mechanics, pages 1–8, 2012.

[60] J. A. Evans and T. J. R. Hughes. Explicit trace inequalities for isogeometric analysis and parametric hexahedral finite elements. Numerische Mathematik, 123:259–290, 2013.

[61] J. A. Evans and T. J. R. Hughes. Isogeometric divergence-conforming B-splines for the Darcy–Stokes–Brinkman equations. Mathematical Models and Methods in Applied Sciences, 23(4):671–741, 2013.

[62] J. A. Evans and T. J. R. Hughes. Isogeometric compatible discretizations for viscous incompressible flow. In IsoGeometric Analysis: A New Paradigm in the Numerical Approximation of PDEs, pages 155–193. Springer, 2016.

[63] J.A. Evans and T.J.R. Hughes. Isogeometric divergence-conforming B-splines for the steady Navier–Stokes equations. Mathematical Models and Methods in Applied Sciences, 23(8):1421–1478, 2013.

[64] J.A. Evans and T.J.R. Hughes. Isogeometric divergence-conforming B-splines for the unsteady Navier–Stokes equations. Journal of Computational Physics, 241:141–167, 2013.

[65] L. C. Evans. Partial Differential Equations. American Mathematical Society, Providence, R.I., 2010.

[66] R. S. Falk and M. Neilan. Stokes complexes and the construction of stable finite elements with pointwise mass conservation. SIAM Journal on Numerical Analysis, 51(2):1308–1326, 2013.

[67] K. P. S. Gahalaut, Kraus J. K., and Tomar S. K. Multigrid methods for isogeometric discretization. Computer Methods in Applied Mechanics and Engineering, 253:413–425, 2013.

[68] F. J. Gaspar, Y. Notay, C. W. Oosterlee, and C. Rodrigo. A simple and efficient segregated smoother for the discrete Stokes equations. SIAM Journal on Scientific Computing, 36:1187–1206, 2014.

[69] M. Germano, U. Piomelli, P. Moin, and W. H. Cabot. A dynamic subgrid-scale eddy viscosity model. Physics of Fluids, 3:1760–1765, 1991.

[70] S. Ghosal, T. S. Lund, P. Moin, and K. Akselvoll. A dynamic localization model for lage-eddy simulation of turbulent flows. Journal of Fluid Mechanics, 286:229–255, 1995.

[71] R. N. Goldman and T. Lyche. Knot insertion and deletion algorithms for B-spline curves and surfaces. SIAM, 1992.

[72] J. L. Guermond. Stabilization of Galerkin approximations of transport equations by subgrid modeling. ESAIM: Mathematical Modelling and Numerical Analysis, 33:1293–1316, 1999.

[73] J. L. Guermond. Un résultat de convergence d'ordre deux en temps pour l'approximation des équations de Navier–Stokes par une technique de projection incrémentale. ESAIM: Mathematical Modelling and Numerical Analysis, 33(1):169–189, 1999.

[74] I. Harari and T. J. R. Hughes. What are C and h?: Inequalities for the analysis and design of finite element methods. Computer Methods in Applied Mechanics and Engineering, 97:157–192, 1992.

[75] Y. He and W. Sun. Stability and convergence of the Crank–Nicolson/Adams–Bashforth scheme for the time-dependent Navier–Stokes equations. SIAM Journal on Numerical Analysis, 45(2):837–869, 2007.

[76] R. Hiptmair. Multigrid method for Maxwell's equations. SIAM Journal on Numerical Analysis, 36(1):204–225, 1998.

[77] C. Hofreither, S. Takacs, and W. Zulehner. A robust multigrid method for isogeometric analysis in two dimensions using boundary correction. Computer Methods in Applied Mechanics and Engineering, 316:22–42, 2017.

[78] C. Hofreither and W. Zulehner. Spectral analysis of geometric multigrid methods for isogeometric analysis. In Ivan Dimov, Stefka Fidanova, and Ivan Lirkov, editors, Numerical Methods and Applications: 8th International Conference, NMA 2014, Borovets, Bulgaria, August 20-24, 2014, Revised Selected Papers, pages 123–129. Springer International Publishing, Cham, 2015.

[79] M. C. Hsu, Y. Bazilevs, V. M. Calo, T. E. Tezduyar, and T. J. R. Hughes. Improving stability of stabilized and multiscale formulations in flow simulations at small time steps. Computer Methods in Applied Mechanics and Engineering, 199:828–840, 2010.

[80] T. J. R. Hughes. Multiscale phenomena: Green's functions, the Dirichlet-to-Neumann formulation, subgrid scale models, bubbles, and the origins of stabilized methods. Computer Methods in Applied Mechanics and Engineering, 127:387–401, 1995.

[81] T. J. R. Hughes, J. A. Cottrell, and Y. Bazilevs. Isogeometric analysis: CAD, finite elements, NURBS, exact geometry, and mesh refinement. Computer Methods in Applied Mechanics and Engineering, 194:4135–4195, 2005.

[82] T. J. R. Hughes, G. R. Feijó, L. Mazzei, and J. B. Quincy. The variational multiscale method–a paradigm for computational mechanics. Computer Methods in Applied Mechanics and Engineering, 166:3–24, 1998.

[83] T. J. R. Hughes, L. P. Franca, and M. Balestra. A new finite element formulation for computational fluid dynamics: V. Circumventing the Babuška-Brezzi condition: A stable Petrov-Galerkin formulation of the Stokes problem accommodating equal-order interpolations. Computer Methods in Applied Mechanics and Engineering, 59:85–99, 1986.

[84] T. J. R. Hughes, L. P. Franca, and G. M. Hulbert. A new finite element formulation for computational fluid dynamics: VIII. The Galerkin/least-squares method for advective-diffusive equations. Computer Methods in Applied Mechanics and Engineering, 73:173–189, 1989.

[85] T. J. R. Hughes and M. Mallet. A new finite element formulation for fluid dynamicos: III. the generalized streamline operator for multidimensional advective-diffusive systems. Computer Methods in Applied Mechanics and Engineering, 58:305–328, 1986.

[86] T. J. R. Hughes, L. Mazzei, and K. J. Jansen. Large eddy simulation and the variational multiscale method. Computing and Visualization Science, 3:47–59, 2000.

[87] T. J. R. Hughes, L. Mazzei, A. A. Oberai, and A. A Wray. The multiscale formulation of large eddy simulation: decay of homogeneous isotropic turbulence. Physics of Fluids, 13(2):505–512, 2001.

[88] T. J. R. Hughes, A. A. Oberai, and L. Mazzei. Large-eddy simulation of turbulent channel flows by the variational multiscale method. Physics of Fluids, 13(6):1784–1799, 2001.

[89] T. J. R. Hughes and G. Sangalli. Variational multiscale analysis: the fine-scale Green's function, projection, optimization, localization, and stabilized methods. SIAM Journal on Numerical Analysis, 45:539–557, 2007.

[90] T. J. R. Hughes, G. Scovazzi, P. Bochev, and A. Buffa. A multiscale discontinuous Galerkin method with the computational structure of a continuous Galerkin method. Computer Methods in Applied Mechanics and Engineering, 195:2761–2787, 2006.

[91] J. C. R. Hunt, A. A. Wray, and P. Moin. Eddies, streams, and convergence zones in turbulent flows. Center for Turbulence Research Proceedings of the Summer Program 1988, 1988.

[92] K. A. Johannessen and T. Kumar, M. nd Kvamsdal. Divergence-conforming discretization for Stokes problem on locally refined meshes using LR B-splines. Computer Methods in Applied Mechanics and Engineering, 293:38–70, 2015.

[93] V. John and P. Knobloch. On spurious oscillations at layers diminishing (SOLD) methods for convection-diffusion equations: Part I - A review. Computer Methods in Applied Mechanics and Engineering, 196:2917–2215, 2007.

[94] V. John and P. Knobloch. On spurious oscillations at layers diminishing (SOLD) methods for convection-diffusion equations: Part II - Analysis for P1 and Q1 finite elements. Computer Methods in Applied Mechanics and Engineering, 197:1997–2014, 2008.

[95] C. Johnson. Numerical solution of partial differential equations by the finite element method. Cambridge University Press, Cambridge, 1987.

[96] D. Kamensky, M. C. Hsu, Y. Yu, J. A. Evans, M. S. Sacks, and T. J. R. Hughes. Immersogeometric cardiovascular fluid–structure interaction analysis with divergence-conforming B-splines. Computer Methods in Applied Mechanics and Engineering, 314:408–472, 2017.

[97] G. Kanschat, R. Lazarov, and Y. Mao. Geometric multigrid for Darcy and Brinkman models of flows in highly heterogeneous porous media: A numerical study. Journal of Computational and Applied Mathematics, 310:174–185, 2017.

[98] G. Kanschat and Y. Mao. Multigrid methods for H(div)-conforming discontinuous Galerkin methods for the Stokes equations. Journal of Numerical Mathematics, 23:51–66, 2015.

[99] G. Kanschat and Y. Mao. Multiplicative overlapping Schwarz smoothers for $H(div)$-conforming discontinuous Galerkin methods for the Stokes problem, pages 285–292. Springer International Publishing, Cham, 2016.

[100] G. Karypis and V. Kumar. A fast and high quality multilevel scheme for partitioning irregular graphs. SIAM Journal on Scientific Computing, 20:359–392, 1999.

[101] J. A. Langford and R. D. Moser. Optimal LES formulations for isotropic turbulence. Journal of Fluid Mechanics, 398:321–346, 1999.

[102] A. Leonard. Energy cascade in large-eddy simulations of turbulent fluid flows. Advances in Geophysics, 18:237–248, 1974.

[103] D. K. Lilly. On the application of the eddy viscosity concept in the inertial sub-range of turbulence. NCAR Manuscript 123, 1966.

[104] R. R. Mankbadi, M. E Hayer, and L. A. Povinelli. Structure of supersonic jet flow and its radiated sound. AIAA Journal, 32:987–906, 1994.

[105] D. J. Mavriplis. An assessment of linear versus nonlinear multigrid methods for unstructured mesh solvers. Journal of Computational Physics, 175(1):302–325, 2002.

[106] R. D. Moser, J. Kim, and N. N. Mansour. Direct numerical simulation of turbulent channel flow up to Re=590. Physics of Fluids, 11(4):943–945, 1999.

[107] J. C. Nédélec. Mixed finite elements in $\mathbb{R}^3$. Numerische Mathematik, 35(3):315–341, 1980.

[108] N. C. Nguyen, J. Peraire, and B. Cockburn. An implicit high-order hybridizable discontinuous Galerkin method for linear convection-diffusion equations. Journal of Computational Physics, 228:3232–3254, 2009.

[109] F. Nicoud, H. Baya Toda, O. Cabrit, S. Bose, and J. Lee. Using singular values to build a subgrid-scale model for large eddy simulations. Physics of Fluids, 23(8), 2011.

[110] F. Nicoud and F. Ducros. Subgrid-scale stress modelling based on the square of the velocity gradient tensor. Turbulence and Combustion, 62(3):183–200, 1999.

[111] A. A Oberai, J. Liu, D. Sondak, and T. J. R. Hughes. A residual based eddy viscosity model for the large eddy simulation of turbulent flows. Computer Methods in Applied Mechanics and Engineering, 282:54–70, 2014.

[112] L. Piegl and W. Tiller. The NURBS Book. Springer Science & Business Media, 2012.

[113] U. Piomelli. Large-eddy simulation: Present state and future perspectives. AIAA paper, 98-0534, 1998.

[114] U. Piomelli, W. H. Cabot, P. Moin, and S. Lee. Subgrid-scale backscatter in turbulent and transitional flows. Physics of Fluids, 3:1766–1771, 1991.

[115] U. Piomelli, C. L. Streett, and S. Sarkar. On the computation of sound by large-eddy simulations. Journal of Engineering Mathematics, 32:217–236, 1997.

[116] U. Piomelli, T. A. Zang, C. G. Speziale, and M. Y. Hussaini. On the large-eddy simulation of transitional wall-bounded flows. Physics of Fluids, 2:257–265, 1990.

[117] H. Pitsch. Large-eddy simulation of turbulent combustion. Annual Review of Fluid Mechanics, 38:453–482, 2006.

[118] S. Pope. Turbulent Flows. Cambridge University Press, 2000.

[119] L. Prandtl. Über ein neues formelsystem für die ausgebildete turbulenz. Nachrichten der Akademie der Wissenschaften in Göttingen, Mathematisch-Physikalische, pages 6–19, 1945.

[120] P. Raviart and J. Thomas. A mixed finite element method for second order elliptic problems. Mathematical aspects of finite element methods, pages 292–315, 1977.

[121] O. Reynolds. On the dynamical theory of incompressible viscous fluids and the determination of the criterion. Philosophical Transactions of the Royal Society of London, Series A, 186:123–164, 1895.

[122] G. Sangalli. Capturing small scales in elliptic problems using a residual-free bubbles finite element method. Multiscale Modeling and Simulation, 1:485–503, 2003.

[123] G. Sangalli. A discontinuous residual-free bubble method for advection-diffusion problems. Journal of Engineering Mathematics, 49:149–162, 2004.

[124] A. F. Sarmiento, A. M. A. Cortes, D. A. Garcia, L. Dalcin, N. Collier, and V. M. Calo. PetIGA-MF: A multi-field high-performance toolbox for structure-preserving B-splines spaces. Journal of Computational Science, 18:117–131, 2017.

[125] U. Schumann. Subgrid scale model for finite difference simulations of turbulent flows in plane channels and annuli. Journal of Computational Physics, 18:376–404, 1975.

[126] F. Shakib, T. J. R Hughes, and Z. Johan. A new finite element formulation for computational fluid dynamics: X. the compressible Euler and Navier-Stokes equations. Computer Methods in Applied Mechanics and Engineering, 89:141–219, 1991.

[127] C. W. Shu. Discontinuous Galerkin methods: General approach and stability. Numerical solutions of partial differential equations, pages 149–201, 2009.

[128] J. Smagorinsky. General circulation experiments with the primitive equations. Monthly Weather Review, 91(3), 1963.

[129] C. G. Speziale, B. A. Younis, R. Rubinstein, and Y. Zhou. On consistency conditions for rotating turbulent flows. Physics of Fluids, 10:2108–2110, 1998.

[130] T. E. Tezduyar. Stabilized finite element formulations for incompressible flow computations. Advances in Applied Mechanics, 38:1–44, 1992.

[131] D. C. Thomas, M. A. Scott, J. A. Evans, K. Tew, and E. J. Evans. Bézier projection: a unified approach for local projection and quadrature-free refinement and coarsening of NURBS and T-splines with particular application to isogeometric design and analysis. Computer Methods in Applied Mechanics and Engineering, 284:55–105, 2015.

[132] T. M. van Opstal, J. Yan, C. Coley, J. A. Evans, T. Kvamsdal, and Y. Bazilevs. Isogeometric divergence-conforming variational multiscale formulation of incompressible turbulent flows. Computer Methods in Applied Mechanics and Engineering, 316:859–879, 2017.

[133] W. van Rees, A. Leonard, D. Pullin, and P. Koumoutsakos. A comparison of vortex and pseudo-spectral methods for the simulation of periodic vortical flows at high Reynolds numbers. Journal of Computational Physics, 230:2794–2805, 2011.

[134] S. P. Vanka. Block-implicit multigrid solution of Navier-Stokes equations in primitive variables. Journal of Computational Physics, 65:138–158, 1986.

[135] J. A. Vastano and R. D. Moser. Short-time Lyapunov exponent analysis and the transition to chaos in Taylor-Couette flow. Journal of Fluid Mechanics, 233:83–118, 1991.

[136] P. Vignal, A. Sarmiento, A. M. A. Côrtes, L. Dalcin, and V. M. Calo. Coupling Navier-Stokes and Cahn-Hilliard equations in a two-dimensional annular flow configuration. Procedia Computer Science, 51:934–943, 2015.

[137] A. W. Vreman. An eddy-viscosity subgrid-scale model for turbulent shear flow: Algebraic theory and applications. Physics of Fluids, 16:3670–3681, 2004.

[138] Z. Wang and A. A. Oberai. Spectral analysis of the dissipation of the residual-based variational multiscale method. Computer Methods in Applied Mechanics and Engineering, 199:810–818, 2010.

[139] T. Warburton and J. S. Westhaven. On the constants in *hp*-finite element trace inverse inequalities. Computer Methods in Applied Mechanics and Engineering, 192:2765–2773, 2003.

[140] E. Wilson. The static condensation algorithm. International Journal for Numerical Methods in Engineering, 8:198–203, 1974.

[141] K. S. Yang and J. H. Ferziger. Large-eddy simulation of turbulent obstacle flow using a dynamic subgrid-scale model. AIAA Journal, 31:1406–1413, 1993.

[142] S. L. Yeoh, G. Papadakis, and M. Yianneskis. Determination of mixing time and degree of homogeneity in stirred vessels with large eddy simulation. Chemical Engineering Science, 60:2293–2302, 2005.

[143] I. Yilmaz and L. Davidson. Comparison of SGS models in large-eddy simulation for transition to turbulence in Taylor-Green flow. In Conference on Modelling Fluid Flow, 2015.

[144] Y. Zhiyin. Large-eddy simulation: past, present and the future. Chinese Journal of Aeronautics, 28:11–24, 2015.